TUDelft

Delft University of Technology

Numerical Modelling Of Pile Installation Using Material Point Method

Thi Viet Phuong, Nguyen

Important note
To cite this publication, please use the final published version (if applicable).
Please check the document version above.

Numerical Modelling Of Pile Installation

Using Material Point Method

Numerical Modelling Of Pile Installation
Using Material Point Method

Dissertation

by

Phuong NGUYEN THI VIET

Master of Science in Water Science and Engineering
IHE-UNESCO Institute For Water Education, Delft, Nederland
born in Hanoi, Vietnam.

This dissertation has been approved by the promotors

Composition of the doctoral committee:

Rector Magnificus,	chairperson
Prof. ir. A. F. van Tol,	Delft University of Technology, promotor
Dr. ir. R. B. J. Brinkgreve,	Delft University of Technology, copromotor

Independent members:

Prof. Dr. -Ing. J. Grabe	TU Hamburg
Prof. Dr. -Ing I. Herle	TU Dresden
Prof. Dr. K. G. Gavin	Delft University of Technology
Prof. Dr. M. A. Hicks	Delft University of Technology

Other members:

Dr. ir. A. Rohe,	Deltares, Delft, Netherlands

Dr. ir. A. Rohe has contributed greatly to this doctoral research and dissertation.

Contents

Summary

Structures and buildings built on soft soil require deep foundations often consisting of piles. Through the piles, loads are transferred to deeper soil layers which are capable to mobilise enough bearing capacity for the superstructure. During installation of a displacement pile, the soil around the pile gets distorted which leads to a change of stress, density and soil properties in the distorted zone. The quantification of change in soil properties, soil state and the influenced zone around the pile during installation are yet a remaining uncertainty in geotechnical engineering. This thesis examines the mechanisms that govern pile installation and subsequent loading by numerical analysis. The study focuses on jacked and impact hammer installation techniques in dry and fully saturated sand.

Most current numerical methods, e.g. finite element method (FEM), predicting pile capacity do not take installation effects into account, as the occurring large deformations can lead to mesh distortion and non-converging solutions. Therefore, when modelling pile foundations using FEM, the installation phase is usually not incorporated. As a result of this simplification, the soil behaviour is often not correctly predicted leading to large differences with field measurements. In this study, the material point method (MPM) is employed as a numerical tool to study the installation effects. It has been successfully applied to a wide range of problems in geotechnical engineering. MPM is an advancement of the FEM, in which the continuum body is represented by Lagrangian points. Lagrangian points are called material points (MPs) which move through an Eulerian computational mesh. The MPs carry all physical properties of the continuum, whereas the computational mesh stores no permanent information. Through this approach, MPM combines the best aspects of both Lagrangian and Eulerian formulations while avoiding some of their shortcomings.

An appropriate constitutive model is essential to model the complex soil behaviour near the pile during and after installation. A model used for sand should have a state dependent behaviour which is able to capture the evolution of the state and the corresponding change of properties. Furthermore, the high stress level under the pile tip during installation can cause grain crushing in sand. Therefore the constitutive model should include such material property changes caused by grain crushing. In this thesis, a constitutive model for granular materials which considers grain crushing effects is developed in the framework of hypoplasticity. When grain crushing occurs the behaviour of granular material is usually significantly affected. Several empirical relations between peak strength, uniformity coefficient and stiffness depending on stress level or amount of grain crushing have been derived for sands. Such relations are employed to improve a basic hypoplastic constitutive model based on the changes of stress level or grain size distribution. In the proposed modified hypoplastic model only two additional physical parameters, namely

uniformity coefficient and mean grain size diameter are incorporated. The valida-
tion of the modified model for three different sands under triaxial test conditions
with cell pressures up to 30 MPa is presented, and shows a significantly better
correspondence compared to the original basic hypoplastic model.

The modified hypoplastic model for crushed sand is applied to model the in-
stallation process of a jacked pile in sand. Results from this application show that
simulations with the modified hypoplastic model for crushed sand lead to a signifi-
cantly improved load–displacement behaviour compared to the original hypoplastic
model and better correspondence with the experimental result. Hence, taking into
account grain crushing in the hypoplastic constitutive model can be considered as
one of the important factors to successfully model pile installation as well as pre-
dicting the pile bearing capacity.

Simulations of a jacked pile in dry sand are carried out with MPM and show good
agreement with the centrifuge test results for both the installation process as well
as the static load test (SLT) after installation. The predicted pile capacity given by
MPM simulations is in good agreement with the load–displacement curve suggested
by the Dutch standard (NEN 9997-1, 2016). The validation of MPM simulations with
centrifuge tests and standardised load–settlement curves shows the capability of
the proposed numerical tool for modelling the installation effects.

The changes of stress and density in the surrounding soil during pile penetra-
tion are investigated. During installation of a jacked pile in dry sand, soil is pushed
aside by the pile, which leads to densification around the pile and very high lateral
stresses at the pile tip. As a consequence of the change in soil state after installa-
tion, a significantly higher pile bearing capacity is observed during SLT as compared
to simulations without installation effects. This emphasizes the importance of ac-
counting for installation effects when simulating the SLT and more in general when
predicting pile behaviour.

For impact driven piles in both dry and saturated sand, there is a significant
reduction in the horizontal stress close to the pile shaft compared to the initial
K0 horizontal stress, during dynamic pile installation. In dry sand simulations, for
driven piles, the compaction of the soil around the pile is much larger than that of
the jacked pile due to the cyclic and dynamic shearing which results in lower radial
stress around the pile shaft. However, jacked piles result in higher stiffness and
capacity than driven piles due to the higher radial stress at both pile shaft and pile
toe.

In saturated sand simulations, the influence of pore water pressure on pile in-
stallation processes is significant. An increase of excess pore water pressure around
the pile tip during installation is observed. As a consequence of the effective stress
reaching zero value, the soil shows the tendency to liquefy in the area around the
installed pile. Furthermore, there is almost no compaction of the soil around the
driven pile during installation in comparison to the jacked pile. The comparison
between a jacked pile and an impact driven pile shows the significant influence of
these different installation techniques on the bearing capacity of a pile foundation.

The evolution of the excess pore pressures inside the soil body and the influence
of soil properties on the generation and dissipation of the excess pore pressures

during a rapid pile load test (RLT) are numerically examined by MPM simulations to gain more insight in the excess pore pressure effect on the pile capacity. The results from simulations are in good agreement with measurements in terms of load–displacement curve as well as the generation and dissipation of excess pore pressures at the pile tip during RLT.

Samenvatting

Constructies en gebouwen op zachte ondergrond vereisen paalfunderingen. Door de palen worden de belastingen overgedragen naar de dieper gelegen grondlagen die in staat zijn om voldoende draagkracht te mobiliseren voor de bovenliggende constructie. Tijdens de installatie van een grond-verdringende paal wordt de grond rond de paal verstoord, en dat leidt tot een verandering van de spanning, dichtheid en grondeigenschappen in dit verstoorde gebied. Het kwantificeren van deze verandering in grondeigenschappen, grond toestand en het beïnvloedde gebied rond de paal tijdens installatie vormt nog steeds een blijvende onzekerheid in de geotechniek. Dit proefschrift onderzoekt de mechanismen die de paalinstallatie en de daarop volgende belasting bepalen met behulp van een numerieke analyse. De studie richt zich op installatie technieken voor gedrukte en geheide palen in droog en volledig verzadigd zand.

De meeste huidige numerieke methoden, zoals bijvoorbeeld de eindige elementen methode (EEM), nemen, voor de voorspelling van de paaldraagkracht, installatie effecten niet in beschouwing, aangezien de optredende grote vervormingen tot meshverstoring en niet-convergerende oplossingen kunnen leiden. Daarom wordt de installatie fase doorgaans niet meegenomen wanneer paalfunderingen met EEM gemodelleerd worden. Als gevolg van deze vereenvoudiging wordt het grondgedrag vaak niet juist voorspeld wat tot grote verschillen met veldmetingen leidt. In deze studie wordt de Material Point Method (MPM) als numerieke tool gebruikt om installatie effecten te bestuderen. Deze werd al succesvol toegepast voor een aantal geotechnische vraagstukken. MPM kan als een uitbreiding op de EEM opgevat worden, waarbij grond en constructies voorgesteld worden door Lagrangiaanse punten die door een Eulerse mesh bewegen. De fysieke eigenschappen van het continuüm verblijven in de materiaalpunten tijdens de berekening van de vervormingen, terwijl het Eulerse mesh en zijn Gausspunten geen permanente informatie bevatten. Met deze aanpak combineert MPM de beste aspecten van zowel Lagrangiaanse als Eulerse formuleringen terwijl sommige van hun tekortkomingen vermeden worden.

Een geschikt materiaalmodel is essentieel om complex grondgedrag in de buurt van de paal tijdens en na installatie te kunnen modelleren. Een model dat voor zand gebruikt wordt zou toestandsafhankelijk gedrag moeten kunnen vertonen, dat in staat is om de verandering in toestand en bijbehorende verandering in eigenschappen op te vangen. Bovendien kan het hoge spanningsniveau onder de paalpunt tijdens installatie verbrijzeling van de zandkorrels veroorzaken. In dit proefschrift is een materiaalmodel ontwikkeld voor korrelmateriaal op basis van hypoplasticity dat met effecten van korrelverbrijzeling rekening houdt. Wanneer korrelverbrijzeling plaats vindt wordt het gedrag van korrelmateriaal normaliter significant beïnvloed. Verschillende empirische relaties tussen pieksterkte, uniformiteitscoëfficiënt en stijfheid, afhankelijk van het spanningsniveau of mate van korrelverbrijzeling, zijn af-

geleid voor zand. Deze relaties zijn toegepast om een hypoplastisch basismodel te verbeteren, en gebaseerd op de verandering van spanningsniveau en korrelverdeling. In het voorgestelde aangepaste hypoplastische model komen slechts twee aanvullende fysische parameters voor, namelijk de uniformiteitscoëfficiënt en de gemiddelde korreldiameter. De validatie van het aangepaste model is uitgevoerd voor drie verschillende zanden voor triaxiale testcondities met celdrukken tot 30 MPa, en toont een significant betere overeenkomst dan het originele hypoplastische basismodel.

Het aangepaste hypoplastische model voor verbrijzeld zand is toegepast om het installatie proces van een gedrukte paal in zand te modelleren. Resultaten van deze toepassing geven aan dat simulaties met het aangepaste hypoplastische model voor verbrijzeld zand leiden tot een significant beter last-verplaatsingsgedrag vergeleken met het originele hypoplastische model en betere overeenkomst met de experimentele resultaten. Daarom kan het meenemen van korrelverbrijzeling in het hypoplastische materiaalmodel beschouwd worden als een van de belangrijke aspecten om zowel paalinstallatie succesvol te kunnen modelleren als de paaldraagkracht te voorspellen.

Simulaties van een gedrukte paal in droog zand zijn met MPM uitgevoerd en tonen een goede overeenkomst met resultaten van centrifugeproeven voor zowel het installatieproces als de statische belastingproef (static load test, SLT) na installatie. De door MPM simulaties voorspelde paaldraagkracht is in goede overeenstemming met de last-verplaatsingskromme die door de Nederlandse norm (NEN 9997-1, 2016) voorgesteld wordt. De validatie van MPM simulaties met centrifugeproeven en gestandaardiseerde last-verplaatsingskrommes toont de geschiktheid aan van het voorgestelde numerieke tool om installatie effecten te modelleren.

De veranderingen van spanning en dichtheid in de grond rond de paal tijdens penetratie zijn onderzocht. Tijdens installatie van een gedrukte paal in droog zand wordt grond door de paal zijwaarts gedrukt, en dat leidt tot verdichting rond de paal en zeer hoge horizontale spanningen rond de paalpunt. Ten gevolge van de verandering van de grondtoestand na installatie wordt een significant hogere paaldraagkracht waargenomen tijdens een SLT vergeleken met simulaties zonder installatie effecten. Dat benadrukt het belang om installatie effecten mee te nemen wanneer een SLT gesimuleerd wordt en bij het modelleren van paalgedrag.

Voor geheide palen in zowel droog als verzadigd zand ontstaat een significante verlaging van de horizontale spanningen vlakbij de paalschacht gedurende dynamische paalinstallatie. In simulaties met droog zand voor geheide palen is de grondverdichting rond de paal veel groter dan bij een gedrukte paal, veroorzaakt door de cyclische en dynamische verschuiving, welke in lagere radiale spanningen rond de paalschacht resulteert. Gedrukte palen vertonen daardoor een hogere stijfheid en draagkracht dan geheide palen als gevolg van de hogere radiale spanningen aan zowel paalschacht als –punt.

In simulaties met verzadigd zand is de invloed van de poriënwaterdruk op het paalinstallatie proces significant. Een verhoging van de wateroverspanning rond het paalpunt tijdens installatie wordt waargenomen. Omdat de effectieve spanningen naar nul gaan, vertoont de grond de neiging om te verweken in het gebied rond de

geïnstalleerde paal. Bovendien is er bijna geen verdichting van de grond rond een geheide paal tijdens installatie vergeleken met een gedrukte paal. De vergelijking tussen een gedrukte en een geheide paal toont de significante invloed van deze verschillende installatie technieken op de draagkracht van een paalfundering.

De ontwikkeling van wateroverspanningen in het grondlichaam en de invloed van de grondeigenschappen op de ontwikkeling en dissipatie van de wateroverspanningen tijdens een snelle belastingsproef (rapid load test, RLT) zijn numeriek onderzocht met behulp van MPM simulaties om meer inzicht te krijgen in de effecten van wateroverspanningen op de paaldraagkracht. De resultaten van de simulaties zijn in goede overeenstemming met metingen met betrekking tot zowel de last-verplaatsings kromme als ook de ontwikkeling en dissipatie van wateroverspanningen rond het paalpunt tijdens een RLT.

1

Introduction

1.1. Background

For thousands of years, structures and buildings built on soft soil conditions have been supported by deep foundations consisting of piles. Traditionally, wooden piles were used, however nowadays, most piles are made of reinforced concrete or steel. Through the piles, loads are transferred to deeper soil layers which are capable of mobilizing enough bearing capacity for the support of a superstructure.

The improvement of technology and the development of the equipment used to install piles, have led to a proliferation of pile types and installation methods. Based on installation methods, there are two categories of piles. Firstly, displacement piles: these piles are driven into the ground by impact hammers, either vibrated or hydraulically jacked and no soil is removed but displaced during the pile installation. The installation of the displacement pile significantly changes the soil stresses and properties such as density, strength, and stiffness. Secondly, non-displacement piles (e.g. auger and bored piles): a flight auger is screwed into the ground to the required depth after which concrete is siphoned through the flight auger as it is withdrawn from the ground to form the pile. Another type of non-displacement pile is a bored pile. For these piles the soil is excavated and the bored hole is supported by a steel casing or by a support fluid. During or after concreting the bored hole the support fluid or casing are removed. For the non-displacement pile, the strength and the stiffness of the soil are generally not altered during the installation process and the impact is limited. The installation method influences the soil state and consequently leads to a different behaviour and capacity of displacement and non-displacement piles in an identical soil [1–3]. Hence different values of the factors in the empirical equations for pile design are recommended [2, 3].

This thesis studies the behaviour of displacement piles in sand, primarily by means of numerical simulation. In the research particular attention is given to the jacked pile and the impact-driven pile. Displacement piles driven into the ground by an impact hammer are widely used for offshore and nearshore foundations. On-

shore these piles are used as well but often there are limitations due to the noise nuisance and vibration. Each blow of the ram displaces the pile deeper into the soil until the required depth is reached. Recent developments have allowed the piles to be pushed into the soil with hydraulic jacks. A jacked pile method, also called the "pressed-in method", results in decrease nuisance and a higher capacity and stiffness compared to hammering and vibratory driven techniques [4].

During the installation of a displacement pile, the soil around the pile gets disturbed, leading to a change in the stress and density state of the surrounding soil as well as to a change of the soil properties in the disturbed area close to the pile. The extent of the change of the soil properties, the soil state and the affected area around the pile during installation are a remaining uncertainty in geotechnical engineering. In the geotechnical literature, relatively little attention has been paid to the influence of the installation methods on the behaviour or performance of the pile foundation.

In general, the most important questions regarding the design of the pile foundation are related to the bearing capacity. The bearing capacity of a pile foundation is governed by the soil properties or the soil state. As the soil state is altered by the pile driving process, its effects are accounted for in empirical design methods by the application of certain factors. However, most of these methods only estimate pile bearing capacity and do not consider to model the underlying physical mechanisms and the interaction between the pile and the soil during the installation process. Moreover, the complications of all effects or unusual ground conditions are not included in the prediction of the pile bearing capacity by the empirical methods. Nevertheless, these information is essential to make more reliable predictions of the pile bearing capacity, as well as the influence of the installation on adjacent structures and appropriate load settlement behaviour. In other words, current design methods for pile foundations offer a low reliability [5] and are not based on the physical processes which govern the pile capacity [6].

With the increase in computational power, numerical techniques e.g. Finite Element Method (FEM) have been developed in geotechnical engineering. Nowadays, it is increasingly essential to assess the behaviour (settlements) of piled constructions. For buildings, and in particular in case of a combination of lateral loads of pile groups, the assessment is often executed using FEM models. However, FEM models when modelling pile foundations in the FEM code, do not often incorporate the installation phase. As a result of oversimplification, the soil behaviour is not correctly predicted and consequently leads to a large difference between FE predictions and pile behaviour measurements [7]. In conclusion, a proper simulation of the entire installation process is needed.

In order to improve the prediction of pile and soil behaviour, an analysis of the pile installation and consequence effects should be included in the numerical models. Thus, the main aspects to be considered are:

- Large deformation: When modelling penetration, the numerical framework of a common small strain FEM cannot handle large local deformations occurring during installation. As a result, stress concentrations and mesh distortion occur in such FEM simulations.

- Constitutive model: An appropriate constitutive model is quite important to model the complex soil behaviour near the pile during and after pile installation. The model used for sand should have a state dependent behaviour in which the soil stiffness and strength is dictated by the current state. Furthermore, the high stress level under the pile tip during installation can cause grain crushing in sand. Therefore the constitutive model should include material property changes due to grain crushing.

- Pore water pressure effects: The numerical code should incorporate a coupled material and groundwater description and be able to model the generation and dissipation of pore pressure when a pile is driven into fully saturated soil.

- Dynamic loads: Dealing with wave propagation and cyclic loading are important aspects to be considered in the analysis of the dynamic installation technique.

Hammered pile installation in dry and saturated sand was simulated in this study. An attempt is made to validate this type of simulations by numerical modelling of a number of Rapid Pile Load Tests (RLT) that were performed in a geotechnical centrifuge. The RLTs were chosen to model because in these tests the piles were installed in saturated sand and were loaded by impact. And moreover the conditions were well defined, regarding soil, loading and the deformations were measured as well as the pore pressures in the soil during loading. In the following a short introduction of the different types of pile load tests and the Rapid test in particular is given.

The most reliable method for determining the ultimate bearing capacity is to use results from pile load tests (e.g. static load, dynamic load and rapid load tests) and, most importantly, the tests can be used to validate the numerical simulations. Although static load tests provide the most precise method of evaluation of the bearing capacity [8], they are expensive to set up and time-consuming to undertake. The dynamic testing methods provide an economic alternative for static load testing. However, the high impact load under a considerable short blow can cause sustain damage on the pile [9]. Another drawback of the dynamic testing method is the assumption that an "equivalent static" capacity needs to be derived from the dynamic load test. Hence the rapid load testing is an alternative method to overcome the drawbacks of static and dynamic testing methods [10]. However, there is also ambiguity in obtaining equivalent static results from rapid testing methods because the results need to be interpreted to eliminate the dynamic and rate effects. The most complicated aspects of the interpretation of methods and results are the load rate effect and the effect of excess pore pressure in the soil under and close to the pile toe generated during test [11]. Several empirical reduction factors are suggested to obtain an equivalent static bearing capacity of a pile from the rapid load test. However, well-defined interpretation rules are still required for practical engineering.

1

1.2. Objective of the study

The objective of this study is to examine the mechanisms that govern pile installation and the subsequent loading by numerical analysis.

This study is limited to the jacked and impact hammer installation techniques. As the jacked installation process can be considered as quasi-static loading, hence no dynamic effects and drained conditions are assumed. For the analyses of an impact driven pile and of a rapid pile load test, the dynamic calculations and the consolidation analysis are coupled, and the relative movement of the fluids and solids is considered. Consequently, an evolution of excess pore pressure can be simulated more realistically for partially drained loading conditions.

Hence, for a suitable analysis in this study, it is important to obtain a numerical model that can cope with/manage:

- Large deformations

- Adapted soil properties due to stress and density changes

- High stresses and related crushing

- A two phase medium, with the possibility of full liquefaction

There are several numerical methods which can manage large deformations such as Arbitrary Lagrangian-Eulerian (ALE) schemes, meshless methods (e.g the Smoothed Particle Hydrodynamics (SPH) method) and mesh-based particle methods (e.g. the Material Point Method (MPM)). In this study, MPM is employed as a numerical tool to study the installation effects. It has been successfully employed in modelling a wide range of problems in geotechnical engineering. MPM is an advancement of the FEM, in which the continuum body is represented by Lagrangian points. Lagrangian points are called material points (MPs) which move through an Eulerian computational mesh. The MPs carry all physical properties of the continuum, whereas the computational mesh stores no permanent information. Through this approach, MPM combines the advantages of both mesh-based and point-based approaches while avoiding the shortcomings. The problem of mesh distortion, shown by an updated Lagrangian solution, when dealing with large deformation, or numerical diffusion, associated with the convective terms in Eulerian approach do not appear in MPM. Notwithstanding, as being conceived as an extension of the well developed FEM, MPM can utilise the long tradition and experiences of FEM easily. Another advantage of MPM is that it is less complex and computationally more efficient than point-based methods.

A hypoplastic model is used as the constitutive model for soil. In this study, the behaviour of soil under a high stress level is investigated and a modified constitutive model is developed to account for grain crushing effects.

The simulations results are validated using centrifuge tests and standardised load settlements curves to show the capability of numerical tool in modelling the installation effects. The changes of stress and density in the surrounding soil during pile penetration are investigated. A comparison is made between jacked pile and impact hammer pile to investigate the influence of these different installation

techniques on the bearing capacity of a pile foundation. The evolution of the excess pore pressure inside the soil body and the influence of soil properties on the generation and dissipation of the excess pore pressure during a rapid pile load test are numerically examined to gain insight into the excess pore pressure effect on the pile capacity.

This thesis is part of a larger research project in which the modelling of the pile installation of jacked and driven displacement piles by both physical and numerical models is investigated. The experimental part of the research project provided the centrifuge test data to calibrate the numerical results. The most important application of this research will be to translate the installation effects of driven piles into the embedded pile concept and other numerical models for practical application. In the future, a novel technique may be introduced to describe the installation effects of a driven pile without simulating the penetration process, which would be an enormous gain in terms of computational effort and time in the analyses of driven pile. The results of this research will become applicable for the design of pile foundations in the engineering practice by means of robust implementation in the finite element method.

1.3. Outline

The thesis consists of 8 chapters. First, the literature related to the topic of the thesis is reviewed in Chapter 2. Then the formulations of MPM (Material Point Method) are explained in Chapter 3. The important features of the constitutive model used in the analyses and its modification to deal with grain crushing are presented in Chapter 4. Chapter 5 presents the numerical simulations for modelling the installation process of jacked displacement piles in sand using MPM. A fully dynamic analysis of the impact driven pile in sand, modelled by MPM in both dry and saturated sand is described in chapter 6. Chapter 7 presents the modelling of the rapid load tests for both embedded pile as well as jacked pile. Finally, the results of this study and the recommendations for further research are given in chapter 8.

References

[1] A. Viana da Fonseca and J. Santos, *International prediction event on the behaviour of bored, cfa and driven piles in cefeup/isc'2 experimental site–2003,* Final Report, Instituto Superior Técnico of the Technical University of Lisbon and the Faculty of Engineering of the University of Porto, Portugal (2003).

[2] M. McVay, C. Kuo, and A. Guisinger, *Calibrating resistance factor in the load and resistance factor design of statnamic loading test,* .

[3] P. Hölscher and A. van Tol, *Database of field measurements of slt and rlt for calibration,* In: Rapid Load Testing on Piles, Taylor and Francis , 151 (2008).

[4] A. Deeks, D. White, and M. Bolton, *A comparison of jacked, driven and bored piles in sand,* in *Proceedings of the International Conference on Soil Mechanics and Geotechnical Engineering*, Vol. 16 (AA Balkema Publishers, 2005) p. 2103.

1

[5] F. Chow, *Investigations into the behaviour of displacement piles for offshore structures*, Ph.D. thesis, Ph. D. thesis, University of London Imperial College, London (1997).

[6] M. Randolph, R. Dolwin, and R. Beck, *Design of driven piles in sand,* Geotechnique 44, 427 (1994).

[7] W. Broere and A. F. van Tol, *Modelling the bearing capacity of displacement piles in sand,* Proceedings of the ICE-Geotechnical Engineering 159, 195 (2006).

[8] M. Randolph, *Science and empiricism in pile foundation design,* Geotechnique 53, 847 (2003).

[9] P. Middendorp, P. Bermingham, and B. Kuiper, *Statnamic load testing of foundation piles,* in *Proceedings, Fourth International Conference of Applications of Stress-Wave Theory to Piles, The Hague, Netherlands* (1992) pp. 581–588.

[10] M. Janes—Geotechnica, E. Berminghammer, and H. Ltd, *An innovative approach to load testing of high capacity piles,* in *Piling and Deep Foundations: Proceedings of the International Conference on Piling and Deep Foundations, London, 15-18 May 1989*, Vol. 1 (CRC Press, 1989) p. 409.

[11] N. Huy, *Rapid load testing of piles in sand: effect of loading rate and excess pore pressure*, Ph.D. thesis, Delft University of Technology (2008).

2

Analysis of pile installation
A review

2.1. Introduction

Displacement piles are driven into the ground without removing any soil material during the installation process. The stiffness response and bearing capacity of displacement piles is influenced by the installation method. Although piles are well established as a foundation solution, their behaviour remains one of the largest sources of uncertainty in geotechnical engineering. The physical processes and mechanisms that govern the pile response during installation and the subsequent load tests are still not well known. The pile installation leads to significant changes in soil structure and soil state (void ratio and stress state) in the vicinity of piles which affects their lateral and axial bearing capacity.

This Chapter will present a summary of the installation effects investigated by studying existing experimental research. The main focus is on the effect of pile installation on: the bearing capacity, the stress change in the soil, the density change in the soil and the combined changes in stress state and density change, and the evolution of excess pore pressure under dynamic loading. Then, the different approaches used to predict the pile bearing capacity are presented. Finally, the numerical analysis methods and their difficulty on the modelling of proper soil pile interaction during installation are discussed.

2.2. Previous observations of pile installation

Piles can be installed in different ways. Almost all of the prefabricated piles are driven into the ground with an impact hammer. The kinetic energy from each blow of the ram displaces the pile deeper into the soil. Another alternative is the vibratory driving technique where the pile is forced to penetrate by a heavy vibratory head on top. The vibrations degrade the strength of the surrounding soil and the pile is penetrated due to a heavy vibrator weight. A jacked pile is pushed into the soil with

2
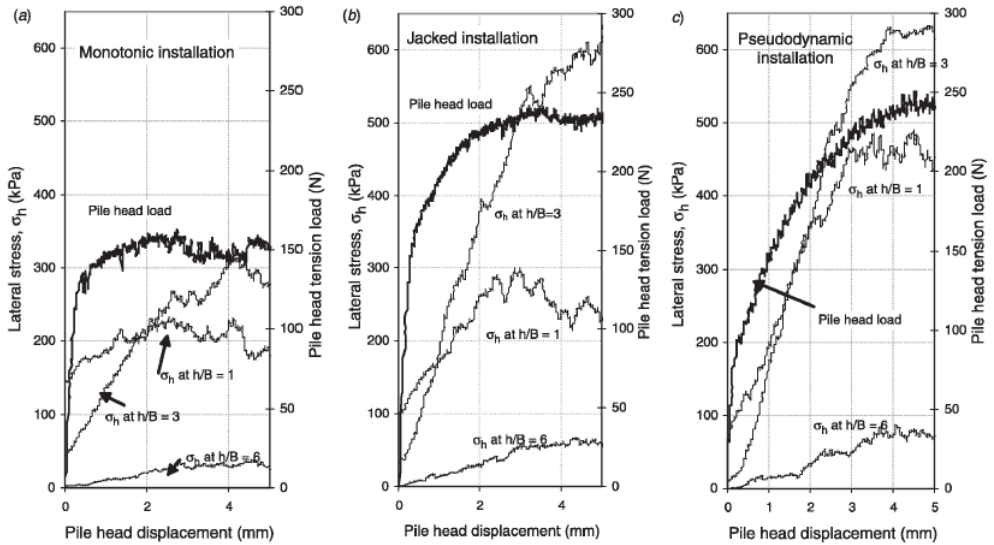
Figure 2.1: Lateral stress variation during static tension load tests after monotonic, jacked and pseudo dynamic installation of piles in fine silica sand. [4].

hydraulic jacks, again the pile displaces the soil. Jacking is characterised by monotonic loading and soil deformation, whereas hammering and vibratory methods are both characterised by cyclic loading, but can yield different capacities [1]. In this section, the pile response after pile installation is compared for jacked and driven piles in order to obtain more insight into the influences of the installation methods and the related pile bearing capacity. Beside, the observations in the stress, density, material change and excess pore pressure during and after different installation methods are addressed as well.

2.2.1. Bearing capacity

In practice a difference in static bearing capacity between jacked, driven and bored pile was found [2, 3]. The capacity of a displacement pile is derived from the pile load tests. For tension piles, the pile bearing capacity is governed by the shaft resistance, whereas, for compression piles the bearing capacity is contributed by both the shaft and the base resistance.

Figure 2.1 plots the development of lateral stresses during the static tension load tests for different installation methods. A difference in load capacity was found when a model pile was installed in a single or in multiple strokes [4]. Clearly, the lateral stresses depend on the installation method and on the instrument level (highest at intermediate level $h/B = 3$)

Typical profiles of before and at ultimate capacity of lateral stress recorded in tension and compression tests are shown in Figure 2.2. The initial lateral stresses acting on the monotonic installed pile were slightly higher than the ones for the jacked and pseudo dynamic installed piles. Yet, the jacked pile yielded a larger static bearing capacity in the compression pile load test than the monotonic and pseudo
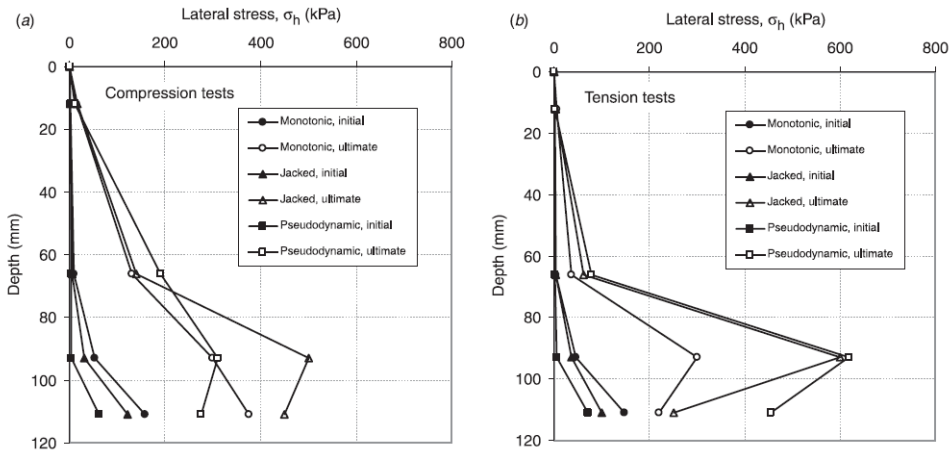
Figure 2.2: Lateral stress profiles before and at ultimate capacity in static load tests [4].

dynamic installed piles. In tension pile load test, the pseudo dynamic installed pile performed similar to the jacked one.

Numerous authors e.g. [4–9] have studied the ratio $\frac{Q_{driven}}{Q_{jacked}}$ in model tests and field tests. The influence of pile installation methods on the ratio of the static bearing capacity of driven and jacked piles $\frac{Q_{driven}}{Q_{jacked}}$ was summarised by Dijkstra [3]. A wide range of values from 0.2 to 2.4 was found for the ratio of $\frac{Q_{driven}}{Q_{jacked}}$. However a very limited amount of tests was considered to obtain such ratio. Moreover, no distinction has been made between compression and tension piles. Dijkstra [3] concluded that the majority of the tests show $\frac{Q_{driven}}{Q_{jacked}} < 1$ or, in other words, the static bearing capacity of jacked piles is higher than that of driven piles, due to the stress build up in the soil during jacking a pile without many unloading cycles as during pile driving [3].

2.2.2. Stress change
This section focusses on the experimental investigation into soil stress change induced by pile installation. Ideally, the stress evolution in the soil during pile installation should be recorded in order to assess the installation effects properly.

In the past, the stress distribution has been qualitatively monitored by using the photo-elastic method in which the soil was substituted by crushed glass or by glass beads. The photo-elastic method was not applicable for natural soils as they are not transparent [3]. Hence, in the centrifuge test of Dijkstra [3], the measurement techniques limited the assessment of stress evolution in natural soil to a point evolution, where the measurement devices were placed. The main results deal with the shape of the shaft friction distribution (exponential or parabolic) and the change of local horizontal stress at a certain depth with an increase of pile displacement.

Two typical shaft friction profiles were plotted [3] in Figure 2.3. Firstly, a profile was expected in which an exponentially increasing shaft friction with depth in homo-

geneous soil (left curve sketched in Figure 2.3) [7, 10–12]. Secondly, a profile with a parabolic shaped increase, with its maximum value located above the pile base (right curve in Figure 2.3) was measured at large acceleration levels ($60g - 100g$) in centrifuge tests [13]. A similar parabolic shaft resistance distribution could also found in the tests with carbonate sand [14]. This indicated that the parabolic shape of the shaft friction profile might be obtained when a considerable particle crushing took place [3]. The measurement of normalized horizontal stress during monotonic installation is shown in Figure 2.4a. σ'_{hm} is the stress recorded during the pile installation. The results indicated that the normalised horizontal stress σ'_{hm}/q_c remained approximately constant throughout the installation at 0.016 with possibly a very slight decrease with increasing depth. σ'_{hm}/q_c ratios are independent of the instrument level (Figure 2.4b). Approximately equal horizontal stress was recorded by each instrument level at 3, 6 and 9 times D from the pile base.

White and Lehane [7] experimentally examined the influences of the installation methods (jacked, pseudo dynamic and monotonic installed pile) on the pile shaft friction by considering the stationary horizontal stress, σ'_{hc}, which was recorded during each installation cycle. For jacked and monotonic installation, this corresponds to a value acting when the pile was unloaded to nominally a zero head load (actually 50 N). For a pseudo-dynamic installation, this was the minimum value recorded during each cycle and occurred close to the moment of a zero pile load head. The profiles of σ'_{hc}, with depths for each installation method, were plotted by [7] (Figure 2.5). As can be seen, the stationary horizontal stress σ'_{hc} decreases when the instrument level h/B increases, which is clear evidence of "friction fatigue". The term "friction fatigue" is the phenomenon showing that the ultimate shaft friction, that can be develop in a given sand horizon, decreases as the pile tip penetrates to deeper level [7]. Furthermore, very low values of σ'_{hc} were recorded on the pseudo-dynamic piles compared with monotonic installation, which may be due to two way cycling during installation. The progressive reduction of σ'_{hc} throughout the cyclic loading was studied by [7] and shown in Figure 2.6 for $h/B = 1$. There is a reduction trend in σ'_{hc} with a number of cycles. During an one way compression load test, the relatively high value of σ'_{hc} reduced to a constant value of about 50 kPa after 30 one-way cycles (which were the cycles of fixed downward displacement followed by unloading to a zero head load) (Figure 2.6a). For the test with two-way cycles (which were the cycles of fixed downward and upward displacement), the horizontal stress σ'_{hc} reduced to zero (Figure 2.6b). White and Lehane [7] concluded that degradation of shaft friction during installation and cyclic loading could be better characterised by the number of cycles rather than by the non-dimensional distance from the pile tip h/D.

Chow [15] studied the stress interactions between two adjacent piles in dense sand. The variation in normalised radial effective stress and shear stress at 4 different distances from the pile tip h_B was shown (Figure 2.7). During the installation of the second pile (at 4.5D center to center to the first pile), a dramatic change in the radial stress σ'_r along the first pile occured: it increased as the pile tip approaches a maximum and then reduced as the tip pass each measurement instruments. The final radial stress values were approximately twice their initial values. The shear
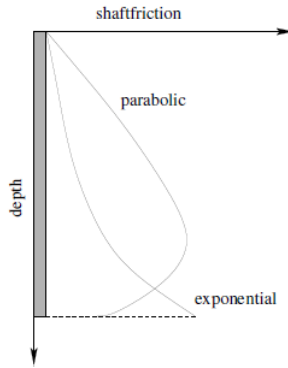
Figure 2.3: Two typical shaft friction profiles; exponentially increasing with depth (left) and parabolic shaped with its maximum value located above the pile base (right) (after [3]).
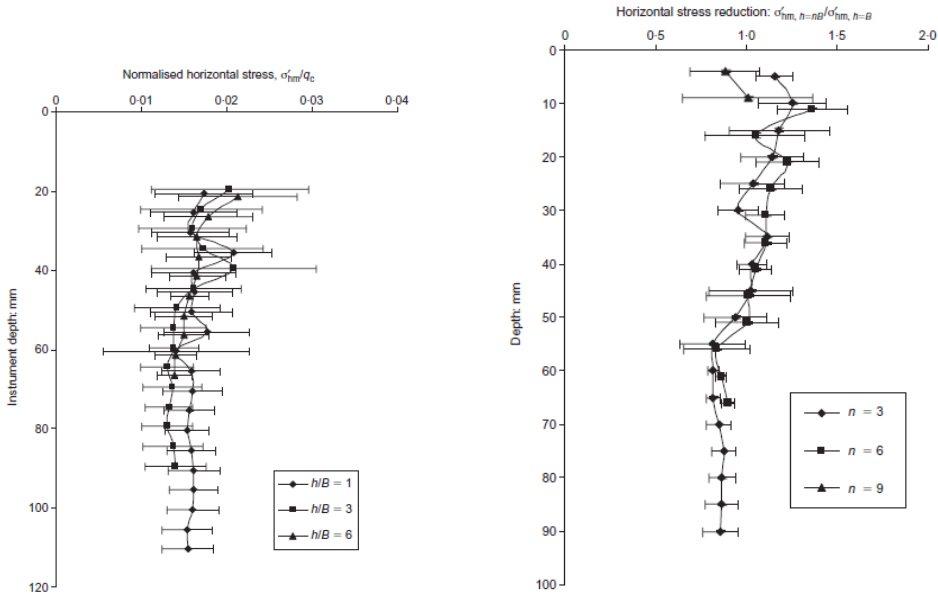
(a) normalised horizontal stress during monotonic installation (mean of all four tests).

(b) reduction in horizontal stress between instruments during monotonic installation (mean of all four tests).

Figure 2.4: Normalised horizontal stress during monotonic installation [7].

stresses became increasingly negative when approaching the pile tip (indicating a downward movement of the soil around the first pile). The shear stresses then became positive (indicating an upward movement of the soil) when the pile tip of the second pile had passed the instruments level of the first pile. The pile load test in Figure 2.8 showed that after the installation of the second pile, the first pile gained 19% in the overall capacity, i.e. a 51% increase in shaft capacity and a stiffer behaviour.
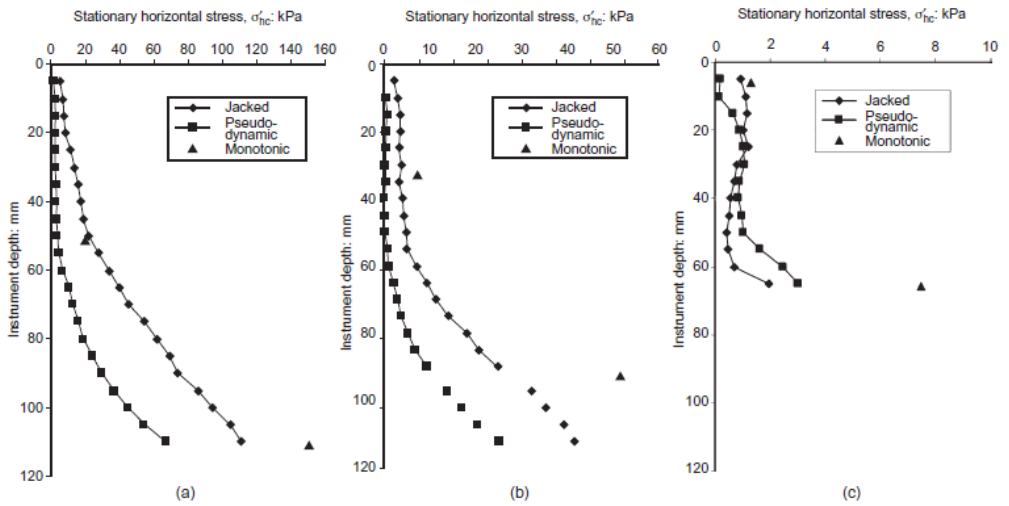
Figure 2.5: Variation of stationary horizontal stress with installation method: (a) $h/B = 1$; (b) $h/B = 3$; (c) $h/B = 6$ ([7]).
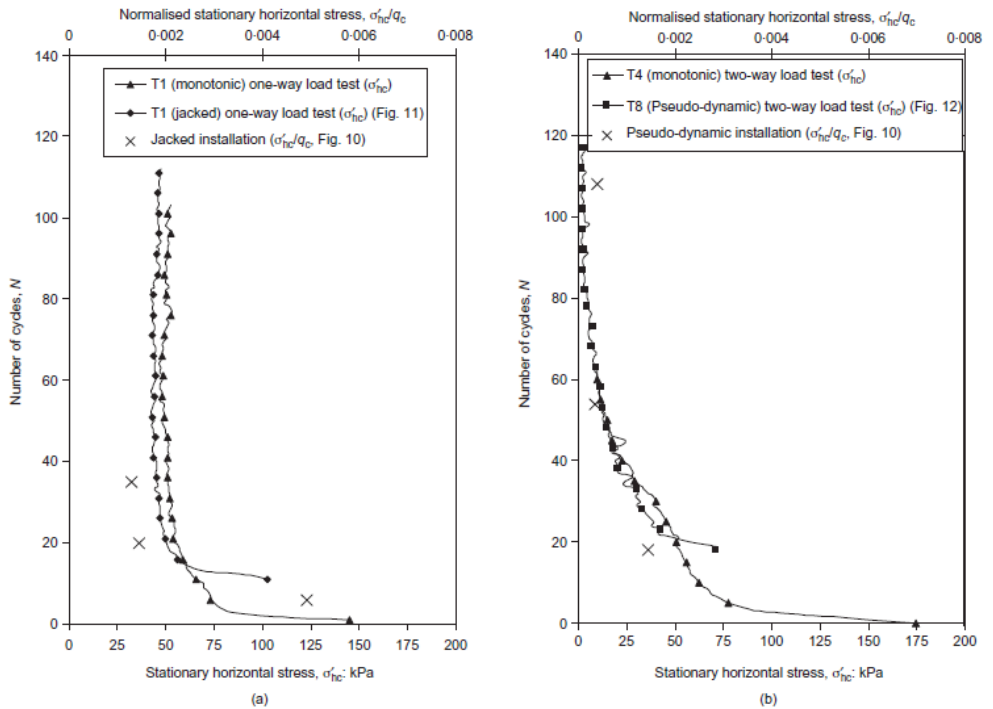
Figure 2.6: Degradation of stationary horizontal stress with cycling at $h/B = 1$ during load tests: (a) one-way compression load test; (b) two-way compression-tension load test ([7]).
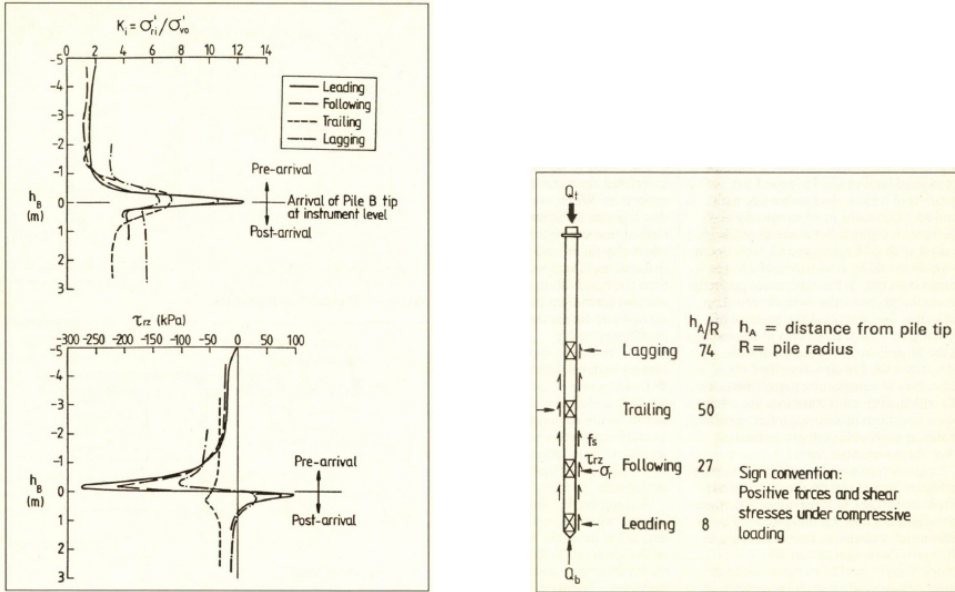
(a) stress measurement against h_B (b) The instrumented pile

Figure 2.7: Normalised radial effective stress and shear stress of the first pile against location of the second pile [15].
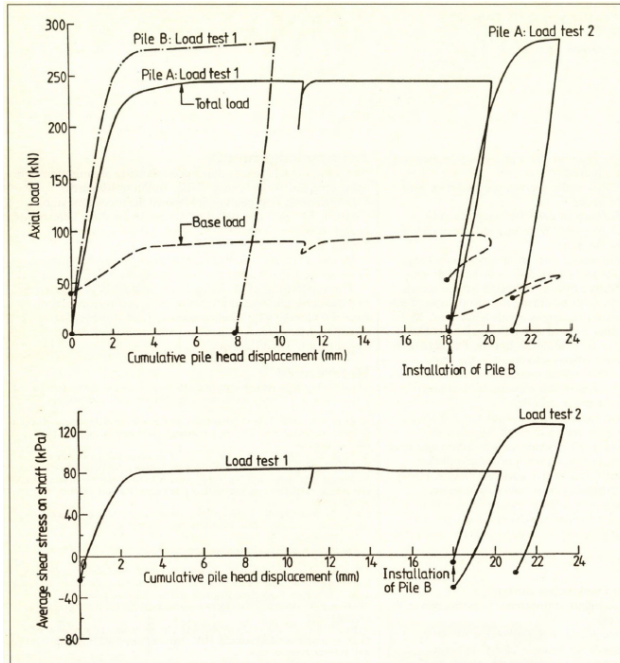
Figure 2.8: Pile tests on the first pile before and after installation of the second pile [15].
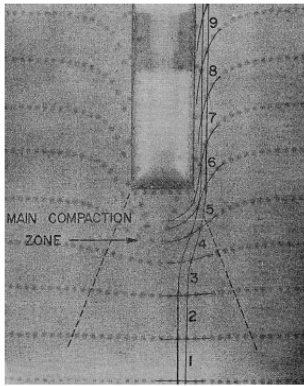
(a) radiograph measurement during jacking [18].

(b) zones of density change around cone penetrometer [16].

Figure 2.9: density change near pile.

2.2.3. Density change

There is a limited amount of experimental work on the investigation of density change due to pile installation. An overview of the existing literature on the qualitative change of the soil density around the pile base and shaft can be found in [3]. The results from literature are separated into plane strain observation and three dimensional observations at low stress levels ($1g$) and at scaled stress levels (Ng).

In almost all of the $1g$ pile tests, loosening was observed near the pile shaft both for initially loose and dense sand (e.g. [16], Figure 2.9b). This loosening near the pile shaft is dilatant behaviour of the soil from the large shear deformation in a narrow band of soil distortion close to the pile shaft [3]. Especially at low horizontal stresses, this failure mechanism can be observed. Such dilative behaviour of the soil near the penetrating pile was also observed at scaled (Ng) stress levels in a centrifuge test by [3], regardless of the density. Figure 2.10 shows the change in porosities for different initial conditions during pile installation at 3 different measurement locations on the model pile. Three instrument levels for the measurement of the density change were installed on the model pile, at 35 mm, 110 mm and 200 mm from the pile tip (i.e. model pile 450 mm in height and 15 mm diameter). Distinct differences in porosity change between the different instrument levels, located at different distances from the pile base, are found in the beginning of the installation phase. These differences tend to become smaller with increased penetration. Regardless of the loose or dense initial conditions, the soil near the pile shaft loosened significantly during monotonic pile jacking in the centrifuge tests [3]. In contrast to higher stress conditions, compression was observed near the pile shaft [17] in the calibration chamber in plane strain conditions. White [17] stated that this was partly due to redistribution of the grains and partly due to crushing. Such compaction resulted in a far field loosening of the soil.

Regarding the density change below the pile base, the results are not consistent. Robinsky and Morrison [18] investigated the soil behaviour around the jacked pile in dry sand with a relative density of $37\% - 57\%$. By using the X-ray method with radiographic equipment, they showed that during installation, the soil below the pile
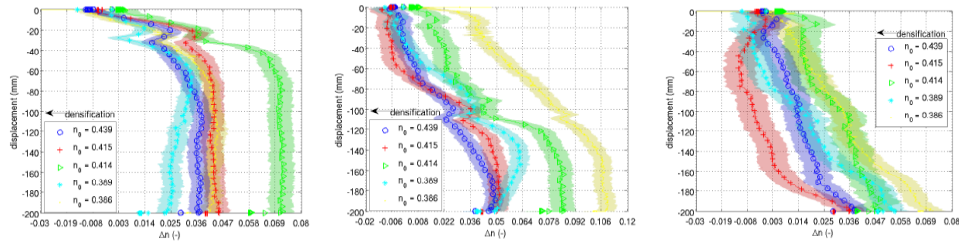
(a) instrument level 1, base   (b) instrument level 1, mid   (c) instrument level 1, upper

Figure 2.10: Change in porosity during pile installation for different initial conditions at different measurement locations (after [3]).

base compacted (Figure 2.9a) while the soil along the pile shaft loosened for both dense and loose sand. The influence zone of installation effects extends up to $5.5D$ from the pile shaft and $4.5D$ under the pile base. Kobayashi and Fukagawa [19] observed loosened soil below the pile base and densified soil along the pile shaft for both loose and dense sand during penetration of a CPT in dry sand. The results are in contrast with those of Robinsky due to the difference in ratio of the pile length over pile diameter (L/D). In the CPT of Kobayashi and Fukagawa, a short and stiff pile of $L/D = 6$ was used (failure mechanism is similar to shallow foundation), whereas in the test of Robinsky, such ratio is about 16 (failure mechanism is similar to deep foundation). Chong [16] investigated the density evolution during model pile installation in dry sand ($L/D = 20$) with a relative density in the range of $40\% - 80\%$ by using thermal conductivity elements. It is found that, for initial dense sand, a loosening of the soil below the pile base is observed, whereas, for initial loose sand the soil under the pile base densified (Figure 2.9b).

Different pile base geometry seems to influence the results in density change during and after pile penetrating. For a pile with a flat base in medium dense sand, the soil under the pile base loosens, whereas a cone shaped pile base shows densification [20]. The influence of the base geometry is small for jacked piles [19].

For initial loose soil condition, most authors found an increase in density below the pile base, except Davidson [21], who reports loosening. However the difference could be caused by the initial condition L/D ratio used in Davidson [21] which was much smaller than the average ratio from the other tests.

2.2.4. Material change

Beside the change in stresses and density during pile installation, material crushing is also observed as a consequence of very high stress under the pile tip [22, 23].

White [24] observed that a "nose cone" formed underneath the pile tip (Figure 2.11b) containing highly crushed sand (zone 3 and 1 in Figure 2.11a show significant particle breakage). The crushed sand was found to flow around the pile shaft (interface zone), to crushed even more, and to infiltrate into the soil. The fine particles within the interface zone are significantly smaller than the void spaces. It offers the possibility of internal migration of fine particles outwards without disturbing the load carrying skeleton of large particles. This migration of particles reduces

2
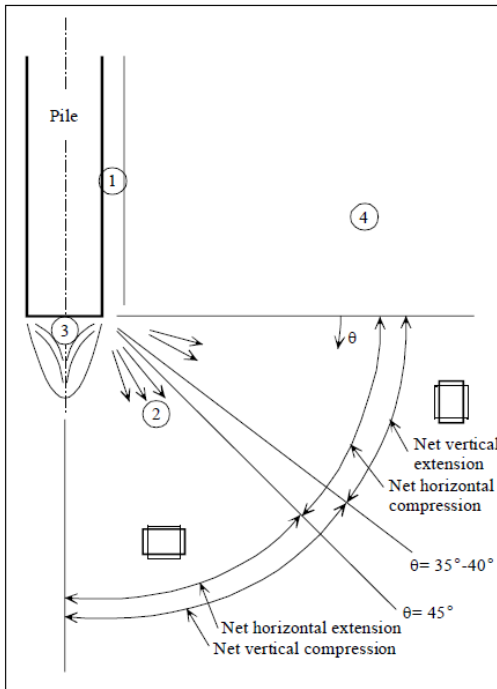
(1) Very dense zone. Significant particle breakage.
    Slight contraction with increasing pile penetration

(2) Very high shear strain reducing with distance
    from pile shoulder, constant with θ

(3) 'Nose cone' of very dense soil. Significant breakage. Not rigid.
    Soil flows through nose cone and around shoulder

(4) Slight densification, decreasing with offset from shaft.
    Horizontal extension with increasing pile penetration

(a) Generalised pattern of strain and particle breakage after pile installation

(b) "nose cone" of soil beneath pile tip

Figure 2.11: Grain crushing in flat pile base.

the amount of material within the interface zone, leading to the remaining particles to repack in a more dense state or to contraction of the interface zone [24].

The relations between the peak strength, the uniformity coefficient and the stiffness of sand, depending on stress level and amount of grain crushing derived for different sands, are reviewed in Chapter 4.

2.2.5. Excess pore water pressure

In fast penetration, especially when the loading rate is faster than the consolidation rate of the soil, the interaction between sand particles and the pore water is significant, and excess pore pressure builds up.

Vesic et al [25] conducted tests to examine the dynamic bearing capacity of footings in dry and submerged sand. They observed a significant increment of bearing capacity in submerged sand. In their explanation, it might be caused by negative pore water pressure, which increased the shear strength of sand and then
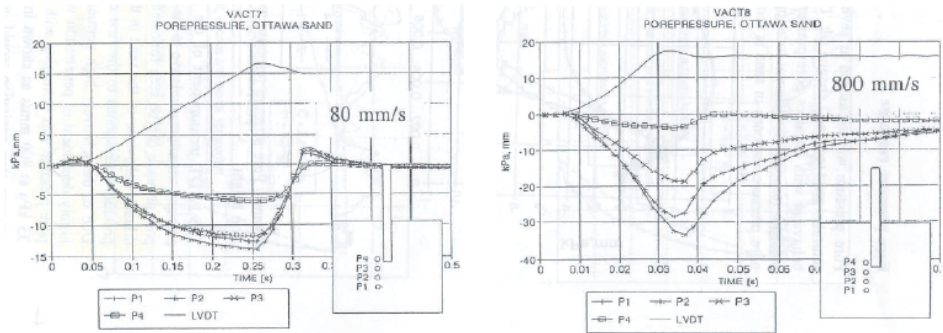
(a) v = 80 mm/s   (b) v = 800 mm/s
Figure 2.12: Pore pressure response in constant rate of penetration tests (after [26]).

the footing capacity.

Eiksund and Nordal [26] performed a series of model pile tests at 1g to measure the excess pore pressure close to the pile tip during constant rate of penetration. Figure 2.12 shows their results of pore pressure measurements at different penetration velocities in a chamber filled with Ottawa sand. In general, the overall pore pressure response is the same: a small increase to a peak positive value is observed initially, but the pore pressure turns into a negative value after approximately 1 mm of model pile movement. Negative pore pressure is caused by dilating behaviour of sand. A higher loading velocity caused a large negative excess pore pressure value (2.12). The largest negative pore pressure measured was approximately -30 kPa, which was extremely small in comparison with the average total stress at a pile tip of 10000 kPa. Therefore it can be concluded that the pore pressure induced by pile penetration had a minor influence on pile bearing capacity [26].

Holscher and Barends [27] measured the excess pore pressure near the pile tip during pile driving, a dynamic load test, and a statnamic load test of a concrete pile with a cross section of $25x25cm^2$. The pile tip was at $18.2m$ below the soil surface and penetrated $3.2m$ into the dense sand layer. Figure 2.13 shows the excess pore pressure as a function of time of the last driving blow, the dynamic test three days later, and the statnamic test five days later. The measurements showed the same pore pressure response during all types of loading. As the pile was loaded, the soil was compressed resulting in the increase of pore pressure, then dilation occurred resulting in a decrease to a negative value of pore pressure. Only the duration of the positive and negative pore pressure phases was very different and related to the duration of the loading. It was not possible to evaluate the importance of excess pore pressure in relation to the pile capacity due to the absence of measured pile head force data [28].

Clayton and Dikran [29] performed dynamic penetration tests with a penetrometer (25 mm diameter) over a distance of 100 mm into saturated sands by repeated blows of a 10 kg weight falling from 430 mm height. Two types of sand, Leighton Buzzard sand (fine sand, $d_{50} = 0.11$ mm) and Woolwich Green sand (well-graded gravelly sand, $d_{50} = 1.0$ mm), were used. The measurements of pore pressure at
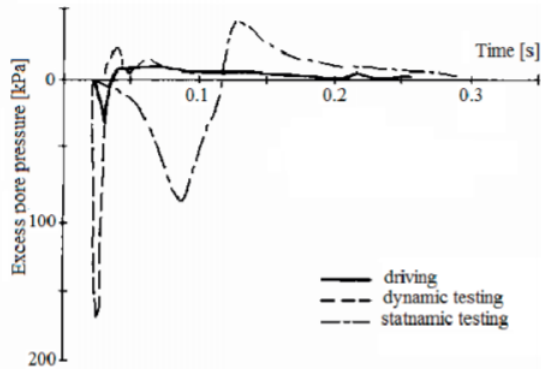
Figure 2.13: Behaviour of excess pore pressure during pile driving and loading [27].

the pile tip (position 1) during one blow as a function of time are shown in Figure 2.15. For fine sand,the sand was initially sheared and the pore pressure dissipates from overpressure (positive pore pressure). For well-graded gravelly sand, the sand was initially compressed then sheared, and a decay of the negative excess pore pressure occurs at the end. The dilative behaviour, at the end of penetrometer motion, occurred in both sand types. The maximum negative pore pressure measured during penetration depended on the position of the transducer. Yagi et al. [30] also showed the changes of pore pressure measured at the cone base during a blow of the hammer (Figure 2.16). For loose sand, just after the blow, a positive peak of pore pressure was observed which suggests compressive soil behaviour under the pile base. In contrast, for dense sand a negative peak of pore pressure appeared which indicated the dilative behaviour of the soil under the pile base. In the loose sand, a remarkable residual pore pressure occurred which is caused by repeated blows and insufficient drainage in the duration of tenths of a second [30].

Huy [31] and Chi [32] conducted a series of centrifuge model pile load tests to study the influence of pore water pressure during rapid load tests and its effect on the widely used unloading point method to derive static pile capacity. The tests confirmed that a rapid load test could overestimate static capacity due to pore water pressure when testing piles in medium to fine sands. Pore pressures during a rapid load test at a maximum displacement of $0.1D$ and at a speed of $280mm/s$ were measured and shown in Figure 2.14. In the field test, the pore pressure transducer was located between the PPT in the pile toe and the PPT3 in the centrifuge test, as can also be seen in Figure 2.14. The underpressure after loading suggested dilatancy followed by consolidation. It is concluded that the centrifuge tests represent realistic behaviour [33].

In conclusion, during pile installation in saturated granular soil, excess pore pressure can build up and depends strongly on the loading time, the contractive or the dilative shearing behaviour of surrounding soil. For the soil at the pile tip, as the pile goes down due to compression of the soil, initially pore pressure increase up to a maximum positive excess pore pressure. If the pile displacement is small enough, the pile motion stops or reverses before shearing occurs, then the excess
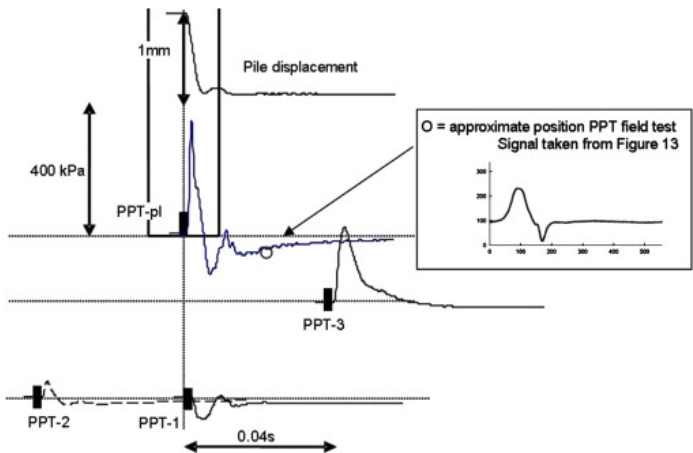
Figure 2.14: Behaviour of excess pore pressure during rapid pile load tests for medium dense sand [31].
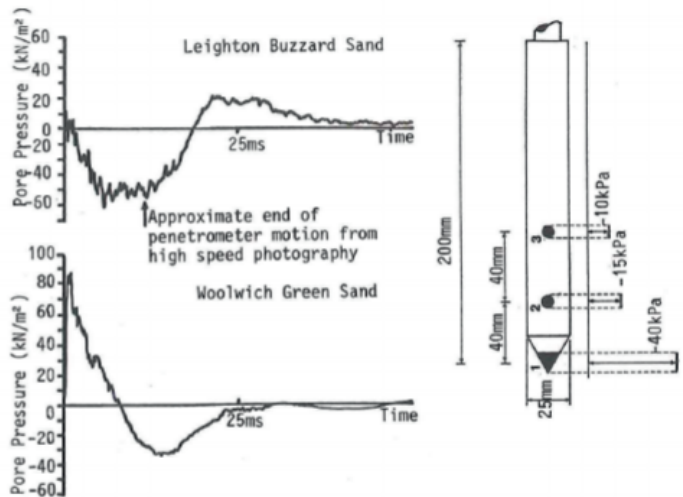
Figure 2.15: Changing of pore pressure during 1 blow at location 1 for Leighton Buzzard sand and Woolwich Green sand [29].

pore pressure dissipates to the static equilibrium. If the pile displacement is large enough that the shearing and dilatancy of the soil occurs and if the loading duration is fast enough that an arrangement of soil particles happens faster than the fluid flow then the excess pore pressure reduces dramatically to a maximum negative value before it dissipates to the static equilibrium [31, 32, 34]. The positive excess pore pressure results in a decrease of the effective stresses and negative excess pore pressure inversely results in higher effective stress levels. Hence clearly, excess pore pressure has an influence on the dynamic and/or rapid resistance by effecting the effective stress under the tip and around the shaft of a penetrometer.

2
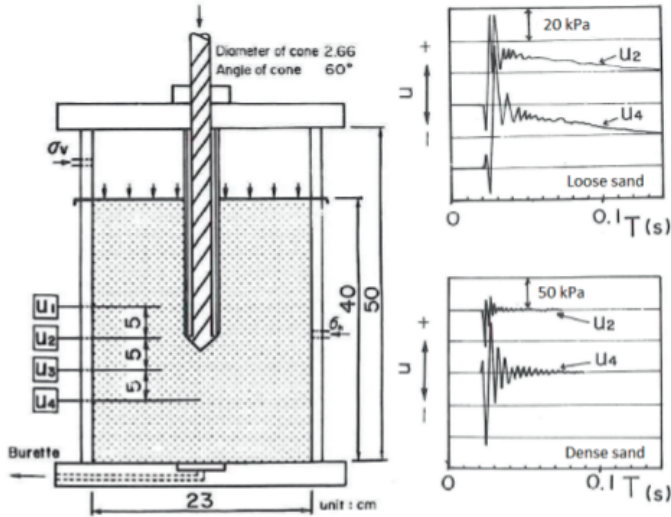
Figure 2.16: Changing of pore pressure during 1 blow of dynamic penetration test [30].

2.3. Bearing capacity prediction in pile design and analysis

In the following sections, two distinct and often used approaches to predict the pile bearing capacity are summarised: (1) The direct limit state methods in which pile bearing capacity correlations are used based on field tests. (2) The indirect limit state methods that use model parameters derived from standard laboratory tests in empirical and analytical methods.

2.3.1. Direct Methods

In the direct limit state methods, the strength of the soil is directly measured and correlated to the pile base and shaft capacity. In practice, these methods have proven to be successful for single piles. The common in-situ measurement instruments used as input value for the design of pile foundations are: the Standard Penetration Test (SPT) and the Cone Penetration Test (CPT). Assuming that the installation effects are the same in all cases, the direct methods include directly the in-situ installation effects arising from the test in the prediction of pile bearing capacity as these tests are penetration tests. However, the installation effects due (different types of) to pile installation may be different than the installation effects in CPT or SPT.

Correlation with CPT data is the most common technique used to estimate the pile capacity. Among the many correlations that have been developed for different subsoil and pile types in the past decades, The Dutch method [35, 36], the French method [37], the Schmertmann method [38] and the Eslami & Fellenius [39] method are the most established. These methods differ mostly in the determination of the representative q_c value for the pile base. The representative q_c value is then multiplied by several factors to account for different influence aspects e.g. the pile type, the pile size, soil density and type, the direction of loading etc.

Recently, new methods have been developed, especially for large diameter offshore piles in sand [40]. In these methods, only the Dutch and French methods directly account for pile installation effects. In some other CPT correlation methods, the influence of pile installation is sometimes lumped together with other corrections in a single empirical reduction factor.

The second group of pile capacity estimation methods is based on a correlation with SPT. An empirical relation between the SPT blow count and pile capacity was presented by Meyerhof [41], in which the installation effects are included in a separate empirical reduction factor for the shaft and base resistance. Such reduction factors have been proposed for driven and bored piles.

2.3.2. Indirect Methods

In indirect methods, the strength and stiffness properties derived from laboratory tests are used as input for the prediction of pile bearing capacity. The bearing capacity factors have been analytically derived from either limit equilibrium methods or cavity expansion methods.

Limit equilibrium analysis uses classical plasticity theory and a predefined slip plane to derive the bearing capacity factors [42]. These factors are combined with the vertical effective stress and the pile base area to predict the static pile base capacity. The shaft resistance of the pile in sand is calculated by estimation of the effective horizontal stress in combination with the effective pile soil friction angle. The effective horizontal stress is derived from the initial effective vertical stress by the coefficient of lateral earth pressure K. The effects of the pile installation process are incorporated in the suggested value for K depending on pile type.

The cavity expansion theory provides useful analytical solutions for determining the tip resistance of a penetrating cone, especially in undrained cohesive soil. Depending on the mechanism of the physical process, the cavity expansion solution assumes either cylindrical or spherical cavity expansion from a finite radius. As the cavity expands to the surface of the pile installed, it mobilizes the surrounding soil and increases the stress level. Hence, the installation stresses are assumed to be simulated. The failure mode considered in cavity expansion is a more realistic failure mode than the simple pre-defined slip planes in a limit equilibrium analysis. Subsequently, the pile bearing capacity is derived by correlating the cavity limit pressure with the cone resistance q_c. The original cavity expansion method was developed for metal research [43] and first introduced in soil mechanics for the analysis of a spherical expansion in associated Mohr-Coulomb material [44]. The method has been extended from small to large strain [45] and from simple elasto-plastic soil models to more advanced constitutive model e.g. hypoplastic model which incorporates dilatancy, contractancy and dependence of stiffness on stress and density [46–48]. The installation effects are considered inherent and therefore, no extra correction for the installation effects is required in the calculation of the bearing capacity. The cavity expansion methods provide a good approximation for the determination of the bearing capacity of a cone or displacement pile. However the results are still of limited value as these methods do not properly simulate the complex soil behaviour near the pile shoulder nor the tip of the CPT or the pile [3].

2.4. Numerical Analysis of pile foundation

However, empirical prediction methods are not as useful for more complex geotechnical problems, where a reliable prediction of the load settlement behaviour is required in, for example, group effects, strong interaction with neighbouring structures or unusual ground conditions. In these cases, a numerical analysis is more suitable as it is not restricted to the study of ultimate bearing capacity (as the direct and indirect methods mentioned above), but provides the probability to expose the calculated stress and strain distribution in the soil around the installed pile and to calculate the stiffness response of the pile. This section gives an overview of numerical methods used to model the process of pile installation and the coupling of dynamic effects and consolidation in the modelling of saturated sand behaviour during penetration.

2.4.1. Numerical methods in pile foundation analysis.

Granular materials can be simulated, either by using a continuum based or by a particle based representation. An example of particle based representation is the Discrete Element Method (DEM), which enables a more realistic modelling of soil medium by simulating the mechanism of the interaction between soil particles; however it is limited to small scale problems. Setting parameters for a DEM model is difficult to achieve in a reliable way as it requires a proper description of the contact between particles. Therefore, continuum models such as the Finite Element Method (FEM) are usually preferred over a discrete representation.

The bearing capacity of piles has first been analysed by FEM in small-strain formulations for cohesive material. Griffiths, Sloan and Randolph [49, 50], amongst others, have assessed the ultimate bearing capacity of foundations using FEM simulations, and De Borst and Vermeer [51] simulated cone penetration in FEM assuming small strain analysis. Although both models provided good basic techniques to determine the pile capacity, the influence of large deformations during the installation process was not taken into account. In such simulations, a pre-embedded cone in an in-situ stress state is forced to reach its ultimate load. The full simulation of the pile installation process is difficult in FEM simulations due to the inability to track large deformations in the soil body and consequently, severe mesh distortion leads to numerical instability. Van Baars, Niekerk and Budwig [52, 53] incorporated the installation effect by loading the boundary of the mesh and applying additional traction loads on the pile shaft. Another way of including installation effects was suggested by Broere and van Tol[54], in which the soil around the pile is pre-stressed with a prescribed displacement before the actual pile bearing capacity calculation is performed. For both above mentioned methods, the magnitude of the additional load or the magnitude of the prescribed displacements is not known a priori, rendering these methods less suitable for predictions. Engin [55, 56] presented a simplified FEM technique to model a jacked pile, the so-called 'Press-Replace' technique. The Press-Replace Method (PRM) enables an engineer to model the installation process of jacked piles as a staged construction process by any finite element code. In PRM, the initial mesh is preserved, while the material properties of the penetrated volume are updated at the beginning of each phase resulting in a

change of the global stiffness matrix without the need for updating the mesh. This makes the calculations faster than large-deformation analysis techniques [55]. The pile and soil responses produced by PRM are in promising agreement with those of Material Point Method (MPM) [57] (the MPM method is briefly explained in the next paragraph). Despite its advantages, PRM has its own limitations as well. Most importantly, it is unable to model the flow of the soil below the pile base and around the peripheral zone of the penetrating pile.

In contrast with the purely Lagrangian and updated Lagrangian methods used in FEM, the Eulerian and Arbitrary Lagrangian-Eulerian (ALE) schemes (e.g. [58, 59]) allow for uncoupling of mesh and material and permit independent movement of the material with respect to the mesh. The difference between the three schemes Lagrangian, Eulerian and ALE is depicted in Figure 2.17. Clearly, in ALE schemes the freedom of movement of computational nodes allows large deformations, so that the mesh entanglement is avoided. One of the most effective ALE methods in modelling penetration problems is the Coupled Eulerian-Lagrangian (CEL) method in which it couples the Lagrangian and Eulerian mesh by a contact description. In CEL, the soil is discretized by an Eulerian mesh, while the pile is discretized by a Lagrangian mesh [60, 61] and the material is allowed to flow in an Eulerian mesh until a contact is detected. This helps to overcome mesh distortion. In the case of re-meshing, however, the mapping of state variables allocated to the material introduces additional inaccuracies into the calculation [62–64]. This has led to the development of meshless methods, such as the Smoothed Particle Hydrodynamics (SPH) method (e.g. [65]), and mesh-based particle methods such as the Material Point Method (MPM). The MPM can be regarded as an extension of a finite element procedure. It uses two types of space discretization: first, the computational mesh, and second, the collection of material points which move through an Eulerian fixed mesh. The material points carry all physical properties of the continuum such as position, mass, momentum, material parameters, strains, stresses, constitutive properties as well as external loads, whereas the Eulerian mesh and its Gauss points carry no permanent information. The advantage of MPM is that the state variables are traced automatically by the material points independent of the computational mesh. Therefore, MPM is well suited for modelling problems with large deformations. More details of the MPM formulation are written in Chapter 3.

2.4.2. Numerical modelling on two-phase problems

Considerable research has been carried out to address problems that involve soil-pore fluid interaction. Such problems are complicated because of the coupled responses of two different phases: the soil skeleton (the solid phase) and the fluid inside the pores of the soil skeleton (the fluid phase). A compression of the soil skeleton induces an increase of pore pressure, whereas, a dilation of the soil skeleton causes a decrease of pore pressure. Taking into account this coupling in the analysis is required to obtain an accurate prediction of the behaviour of two-phase problems, especially in the case of low permeability and fast loading. However, when the permeability is high, and the load is slowly applied, the coupling can be ignored.
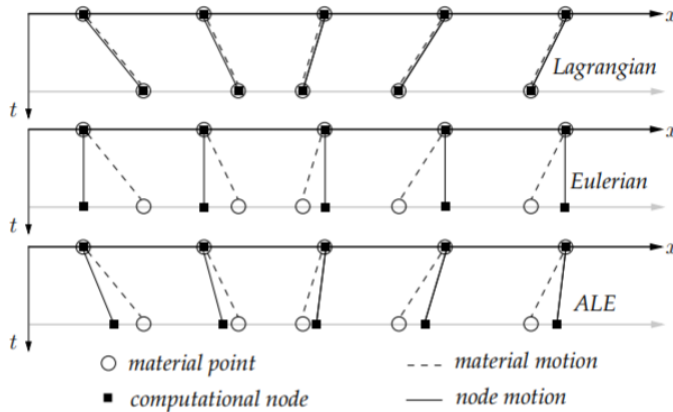
Figure 2.17: One–dimensional illustration of Lagrangian, Eulerian and ALE motions[66]).

The equations describing a two-phase flow were originally developed by Biot [67]. Zienkiewicz & Shiomi [68] and Zienkiewicz et al. [69] were the first to implement the Biot two-phase mixture theory in the FEM in terms of various formulations . Gidaspow[70] gave a comprehensive review of the various formulations within the framework of the mixture theory.

Two common formulations for the implementation of the Biot governing equations are: $v - p$ and $v - w$ formulation (with v is the solid velocity, p is the pore pressure, w is the fluid velocity). For the $v - p$ formulation, inertial effects associated with the relative fluid motion are negligible, and therefore, this formulation is suitable for low frequency loading in porous media (such as landslides, earthquakes or liquefaction phenomena) or in a quasi-static analysis. For the $v - w$ formulation, all inertial effects are included, therefore they are applicable for high frequency phenomena such as blast loading or dynamic rapid pile loading in porous media [71].

A detailed comparison on the finite element algorithms of $v - p$ formulation and $v - w$ formulation was studied by Esch et al. [72]. They concluded that both formulations can capture the undrained wave but the $v - p$ formulation is not able to capture the damp wave. Furthermore, the $v - w$ formulation has the advantage that the algorithm for mapping information between the computational grid nodes and material points for the fluid is virtually identical to that for the solid phase in MPM [64]. For these reasons, the $v - w$ formulation is favoured in this study.

In the $v - w$ formulation, there are 4 unknown variables, i.e. the velocity of the solid phase, the velocity of the water phase, water pressure and the effective stress. The governing equations that are required for the solution of coupled dynamic two-phase problems are presented following Verruijt [73]. The implementation of the $v - w$ formulation in MPM is presented in Chapter 3.

With the use of low-order elements in two-phase problems, the $v - w$ formulation experiences numerical problems (volumetric locking) if the difference in volumetric compressibility of the pore fluid and the solid skeleton is large. When dealing with incompressible fluids, the fractional step method could mitigate the patholog-

ical locking and spurious spatial pressure oscillations [74]. In MPM, the enhanced volumetric strain was found to be useful for accommodating incompressible plastic strains [64].

2.5. Conclusion

In this chapter, current methods to investigate and incorporate pile installation effects are reviewed. Although the effects are quite significant, it is still not possible to experimentally quantify the installation effects as a continuous field experimentally. A large difference among the published results on soil behaviour (i.e., the stress and density change during installation) and the comparison of the bearing capacity from different installation methods is presented.

Not many prediction techniques incorporate installation effects. The current methods for bearing capacity predictions by direct and indirect limit state methods explicitly incorporate the pile installation stage or implicitly with empirical corrections in the correlations. However, most methods only estimate pile bearing capacity and are not able to model the underlying physical mechanism during installation as well as the interaction between the pile and the soil.

In the field of numerical analysis, the difficulties of these methods are the framework considering a large deformation formulation, and the lack of a proper constitutive model including a correct description of the soil behaviour near the pile. The strength and stiffness of soil have a non-linear dependency on the stress and strain level and history. During the installation of a displacement pile in sand, the stress and strain within the deforming soil vary from the in situ stress level and zero strain to tens of MPa stress and of the order of 100% strain [24]. Coop [75] highlighted the lack of understanding of the behaviour of sands at high stress levels as encountered during pile installation. Few triaxial apparatuses operate at the stress level of interest. Existing soil models do not often correctly capture the relevant behaviour. For this reason, the investigation of soil behaviour under high stress as well as the introduction of a modified hypoplastic model for crushed sand are presented in Chapter 4.

In order to gain more insight in installation effects as well as into the mechanism of soil under and around the pile during penetration, numerical investigation of the change of soil state during penetration of jacked and impact hammer pile is conducted using MPM (Chapter 5, 6).

Excess pore pressure occurs during dynamic and rapid penetrations in saturated soils. Accumulation of excess pore pressure along the failure surfaces around the pile may be the main reason for an increase of the rapid resistance over the static resistance. The evolution of the excess pore pressure during the rapid pile load test are numerically investigated in Chapter 7 in order to get a deeper understanding of the excess pore pressure effect on the pile resistance.

For validation, numerical results will be compared with centrifuge test results [31, 32] on modelling pile installation and pile load test.

References

[1] C. I. Mansur and A. H. Hunter, *Pile tests-arkansas river project,* Journal of Soil Mechanics & Foundations Div (1970).

[2] A. Deeks, D. White, and M. Bolton, *A comparison of jacked, driven and bored piles in sand,* in *Proceedings of the International Conference on Soil Mechanics and Geotechnical Engineering*, Vol. 16 (AA Balkema Publishers, 2005) p. 2103.

[3] J. Dijkstra, *On the modelling of pile installation*, Ph.D. thesis (2009).

[4] B. M. Lehane and D. J. White, *Lateral stress changes and shaft friction for model displacement piles in sand,* Canadian Geotechnical Journal 42, 1039 (2005).

[5] A. I. Al-Mhaidib and T. B. Edil, *Model tests for uplift resistance of piles in sand,* Geotechnical Testing Journal 21, 213 (1998).

[6] J. A. Bonita, *The effects of vibration on the penetration resistance and pore water pressure in sands*, Ph.D. thesis, Virginia Tech (2000).

[7] D. White and B. Lehane, *Friction fatigue on displacement piles in sand,* Géotechnique 54, 645 (2004).

[8] A. Yalcin and G. Meyerhof, *The effect of installation on the ultimate resistance of rigid piles under inclined loads in layered sand,* Soils and Foundations 30, 37 (1990).

[9] J. Yang, L. Tham, P. Lee, S. Chan, and F. Yu, *Behaviour of jacked and driven piles in sandy soil,* Géotechnique (2006).

[10] B. Fellenius and A. Altaee, *Critical depth: How it came into being and why it does not exist.* Proceedings of the Institution of Civil Engineers-Geotechnical Engineering 113, 107 (1995).

[11] C. Leung, F. Lee, and N. Yet, *Centrifuge model study on pile subject to lapses during installation in sand,* International Journal of Physical Modelling in Geotechnics 1, 47 (2001).

[12] A. De Nicola, *The performance of pipe piles in sand*, Ph.D. thesis, University of Western Australia (1996).

[13] L. Balachowski, *Différents aspects de la modélisation physique du comportement des pieux: Chambre d'Etalonnage et Centrifugeuse*, Ph.D. thesis (1995).

[14] E. Klotz and M. Coop, *An investigation of the effect of soil state on the capacity of driven piles in sands,* Géotechnique 51, 733 (2001).

[15] F. Chow, *Field measurements of stress interactions between displacement piles in sand,* in *International Journal of Rock Mechanics and Mining Sciences and Geomechanics Abstracts*, Vol. 2 (1996) p. 86A.

[16] F. Chong, *Density changes of sand on cone penetration resistance,* in *Proceedings, 1st International Symposium on Penetration Testing, ISOPT-l, AA Balkema, Rotterdam, the Netherlands*, Vol. 2 (1988) pp. 707–714.

[17] D. White and M. Bolton, *Displacement and strain paths during plane-strain model pile installation in sand,* Géotechnique 54, 375 (2004).

[18] E. Robinsky and C. Morrison, *Sand displacement and compaction around model friction piles,* Canadian Geotechnical Journal 1, 81 (1964).

[19] T. Kobayashi and R. Fukagawa, *Characterization of deformation process of cpt using x-ray tv imaging technique,* in *Third International Conference on Deformation Characteristics of Geomaterials* (2003) pp. 43–47.

[20] E. W. Shublaq, *Soil disturbance due to installation of model piles and pile groups,* Soils and foundations 32, 17 (1992).

[21] J. L. Davidson and A. Boghrat, *Displacements and strains around probes in sand,* in *Geotechnical Practice in Offshore Engineering* (ASCE, 1983) pp. 181–202.

[22] M. Luong and A. Touati, *Sols grenus sous fortes contraintes,* Revue Française de Géotechnique , 51 (1983).

[23] P. V. Lade, J. A. Yamamuro, and P. A. Bopp, *Significance of particle crushing in granular materials,* Journal of Geotechnical Engineering 122, 309 (1996).

[24] D. J. White, *Investigation into the behaviour of pressed-in piles*, Ph.D. thesis, University of Cambridge (2002).

[25] A. Vesic, D. Banks, and J. Woodard, *An experimental study of dynamic bearing capacity of footings on sand,* in *Proceedings of VI International Conference on Soil Mechanics and Foundation Engineering*, Vol. 2 (AA Balkema Rotterdam, 1965) p. 209.

[26] G. Eiksund and S. Nordal, *Dynamic model pile testing with pore pressure measurements,* in *Proc. 5 nd Int. Conf. Application of stress-wave theory to piles, Florida* (1996) pp. 581–588.

[27] P. Holscher and F. Barends, *The relation between soil-parameters and one-dimensional models,* in *Proceedings of the Fourth International Conference on the Application of Stress-Wave Theory to Piles, The Hague, NL, 90 5410 082 6, Balkema, Rotterdam* (1992).

[28] H. Paul, *Dynamical response of saturated and dry soils*, Ph.D. thesis, M. Sc. Thesis, Civil Engineering Department, Delft University of Technology, The Netherlands Google Scholar (1995).

[29] C. Clayton and S. Dikran, *Pore water pressures generated during dynamic penetration testing,* (1982).

[30] N. Yagi, M. Enoki, and R. Yatabe, *Influence of pore water pressure on dynamic and static penetration testings,* in *Proceedings of the 2nd European Symposium on Penetration Testing, ESOPT ll, Amsterdam* (1982) pp. 375–380.

[31] N. Huy, *Rapid load testing of piles in sand: effect of loading rate and excess pore pressure*, Ph.D. thesis, Delft University of Technology (2008).

[32] T. Nguyen, *Modelling of pile load tests in granular soils: Loading rate effects*, Ph.D. thesis, Delft University of Technology (2017).

[33] P. Holscher, A. F. van Tol, and N. Huy, *Rapid pile load tests in the geotechnical centrifuge,* in *the 9th International Conference on Testing and Design Methods for Deep Foundations, Japanese Geotechnical Society* (2012) pp. 257–263.

[34] P. Hölscher, *Field test rapid load testing waddinxveen,* The Netherlands: Deltares (2009).

[35] J. De Kuiter and F. Beringen, *Pile foundations for large north sea structures,* Marine Georesources & Geotechnology 3, 267 (1979).

[36] *NEN-EN 9997-1: 2016 NL: Geotechnical Design - part 1: general Rules*, Nederlands Normalisatie Instituut,, Delft, The Netherlands (2011).

[37] M. Bustamante and L. Gianeselli, *Pile bearing capacity prediction by means of static penetrometer cpt,* in *Proceedings of the 2-nd European symposium on penetration testing* (1982) pp. 493–500.

[38] J. H. Schmertmann, *Guidelines for cone penetration test: performance and design*, Tech. Rep. (United States. Federal Highway Administration, 1978).

[39] A. Eslami and B. H. Fellenius, *Pile capacity by direct cpt and cptu methods applied to 102 case histories,* Canadian Geotechnical Journal 34, 886 (1997).

[40] X. Xu, J. A. Schneider, and B. M. Lehane, *Cone penetration test (cpt) methods for end-bearing assessment of open-and closed-ended driven piles in siliceous sand,* Canadian Geotechnical Journal 45, 1130 (2008).

[41] G. Mayerhof, *Bearing capacity and settlemtn of pile foundations,* Journal of Geotechnical and Geoenvironmental Engineering 102 (1976).

[42] K. Terzaghi, *Theoretical soil mechanics* (Chapman And Hall, Limited.; London, 1951).

[43] R. Hill, *The mathematical theory of plasticity*, Vol. 11 (Oxford university press, 1998).

[44] P. Chadwick, *The quasi-static expansion of a spherical cavity in metals and ideal soils,* The Quarterly Journal of Mechanics and Applied Mathematics 12, 52 (1959).

[45] H. Yu and G. Houlsby, *Finite cavity expansion in dilatant soils: loading analysis,* Geotechnique 41, 173 (1991).

[46] R. Cudmani and V. Osinov, *The cavity expansion problem for the interpretation of cone penetration and pressuremeter tests,* Canadian Geotechnical Journal 38, 622 (2001).

[47] R. O. Cudmani, *Statische, alternierende und dynamische penetration in nicht-bindigen boden* (Institutes fur Bodenmechanik und Felsmechanik der Universitat Fridericiana in Karlsruhe, 2001).

[48] V. Osinov and R. Cudmani, *Theoretical investigation of the cavity expansion problem based on a hypoplasticity model,* International journal for numerical and analytical methods in geomechanics 25, 473 (2001).

[49] D. Griffiths, *Computation of bearing capacity factors using finite elements,* Geotechnique 32, 195 (1982).

[50] S. Sloan and M. F. Randolph, *Numerical prediction of collapse loads using finite element methods,* International Journal for Numerical and Analytical Methods in Geomechanics 6, 47 (1982).

[51] R. De Borst and P. Vermeer, *Possibilites and limitations of finite elements for limit analysis,* Geotechnique 34, 199 (1984).

[52] S. Van Baars and W. Van Niekerk, *Numerical modelling of tension piles,* in *International symposium on beyond 2000 in computational geotechnics* (1999) pp. 237–246.

[53] R. Budwig, *Refractive index matching methods for liquid flow investigations,* Experiments in fluids 17, 350 (1994).

[54] W. Broere and A. F. van Tol, *Modelling the bearing capacity of displacement piles in sand,* Proceedings of the ICE-Geotechnical Engineering 159, 195 (2006).

[55] H. K. Engin, *Modelling pile installation effects: a numerical approach*, Ph.D. thesis (2013).

[56] H. Engin, R. Brinkgreve, and A. van Tol, *Simplified numerical modelling of pile penetration-the press-replace technique,* Int. J. for Num. and Analytical Meth. in Geomech. (2015).

[57] F. S. Tehrani, P. Nguyen, R. B. Brinkgreve, and A. F. van Tol, *Comparison of press-replace method and material point method for analysis of jacked piles,* Computers and Geotechnics 78, 38 (2016).

[58] M. Gadala, *Recent trends in ale formulation and its applications in solid mechanics,* Computer methods in applied mechanics and engineering 193, 4247 (2004).

[59] S. A. Savidis, D. Aubram, and F. Rackwitz, *Arbitrary lagrangian-eulerian finite element formulation for geotechnical construction processes,* Journal of Theoretical and Applied Mechanics 38, 165 (2008).

[60] G. Qiu, S. Henke, and J. Grabe, *Application of a coupled eulerian-lagrangian approch on geomechanical problems involving large deformation,* Computers and Geotechnics 38, 30 (2011).

[61] J. Grabe, T. Pucker, and T. Hamann, *Numerical simulation of pile installation processes in dry and saturated granular soils,* in *International Conference on Numerical Methods in Geotechnical Engineering, NUMGE, Delft, The Netherlands,,* Vol. 1 (CRC Press, 2014) pp. 663–668.

[62] D. Sulsky, Z. Chen, and H. L. Schreyer, *A particle method for history-dependent materials,* Computer Methods in Applied Mechanics and Engineering 118, 179 (1994).

[63] S. Bardenhagen, J. Brackbill, and D. Sulsky, *The material-point method for granular materials,* Computer methods in applied mechanics and engineering 187, 529 (2000).

[64] I. K. Jassim, *Formulation of a Dynamic Material Point Method (MPM) for Geomechanical Problems*, Ph.D. thesis, University of Stuttgart (2013).

[65] J. J. Monaghan, *An introduction to sph,* Computer physics communications 48, 89 (1988).

[66] J. Donea, A. Huerta, J.-P. Ponthot, and A. Rodriguez-Ferran, *Encyclopedia of computational mechanics vol. 1: Fundamentals., chapter 14: Arbitrary lagrangian-eulerian methods,* (2004).

[67] M. A. Biot, *Theory of propagation of elastic waves in a fluid-saturated porous solid. ii. higher frequency range,* The Journal of the acoustical Society of america 28, 179 (1956).

[68] O. Zienkiewicz and T. Shiomi, *Dynamic behaviour of saturated porous media; the generalized biot formulation and its numerical solution,* International journal for numerical and analytical methods in geomechanics 8, 71 (1984).

[69] O. C. Zienkiewicz, A. Chan, M. Pastor, D. Paul, and T. Shiomi, *Static and dynamic behaviour of soils: a rational approach to quantitative solutions. i. fully saturated problems,* Proc. R. Soc. Lond. A 429, 285 (1990).

[70] D. Gidaspow, *Multiphase flow and fluidization: continuum and kinetic theory descriptions* (Academic press, 1994).

[71] O. C. Zienkiewicz, A. Chan, M. Pastor, B. Schrefler, and T. Shiomi, *Computational geomechanics* (Wiley Chichester, 1999).

[72] J. Van Esch, D. Stolle, and I. Jassim, *Finite element method for coupled dynamic flow-deformation simulation,* in *2nd International Symposium on Computational Geomechanics (COMGEO II)*, 1 (2011).

[73] A. Verruijt, *An introduction to soil dynamics*, Vol. 24 (Springer Science & Business Media, 2009).

[74] P. Nithiarasu, *A matrix free fractional step method for static and dynamic incompressible solid mechanics,* International Journal for Computational Methods in Engineering Science and Mechanics 7, 369 (2006).

[75] M. Coop, *The role of high pressure testing in geotechnical research,* (1999).

2

3

The dynamic material point method

In this chapter, the formulation of the Material Point Method (MPM) will be discussed. In section 3.1, the basic concept of MPM is presented. The governing equations and the discretization of the continuum to a cloud of material points are explained in section 3.2 for a single phase material and in section 3.3 for a two phase material involving saturated soil. Section 3.4 continues with approaches to deal with other numerical issues such as volumetric locking when using low-order elements, special boundaries for dissipation of dynamic waves, contact formulation between bodies, moving mesh concept and mass scaling.

3.1. Basic concept of the material point method

3.1.1. Historical development

Originally developed as the Particle-In-Cell method, MPM was initially applied to fluid dynamic problems [1] and later adapted to solid mechanics by Sulsky et al. [2]. In 1996, Sulsky and Schreyer named the method as the Material Point Method and presented its axisymmetric formulation. Więckowski et al. [3] applied the method to simulate the problem of silo discharge, which showed the potential of MPM for simulating flow of granular material. Following this, several MPM analyses to model large deformations in geotechnical problems were performed [4, 5]. , after which it has been widely applied to model many issues in the field of geotechnical engineering, e.g. the failure of a cliff and mass flow through a trapdoor [6]; anchors placed in soil [7]; excavator bucket filling [8]; simulation of experiments related to induced ground deformations [9]; geomembrane response settlement in landfills[10]. MPM has demonstrated to be suitable for penetration problems such as cone penetration test [11], pile installation [12, 13]. The MPM has been also applied to model soil flows, such as the run-out of earthquake-induced slides [14], landslides [15, 16] and dam failures [17]. The application of MPM was then extended to include coupled two-phase behaviour to simulate large deformations in fully saturated soil [18] and in partly saturated soil with groundwater table and

groundwater flow [19]. This MPM formulation is able to capture the physical response of saturated soil under dynamic loading. However, there is only one set of material points is used for both the solid and the liquid phase in this formula; hence it can not capture the groundwater flow, the transition between free surface water and groundwater or the fluid-like behaviour of the soil problems. To overcome such difficulties, a double-point formulation was proposed in [20, 21] and later extended in [22, 23]. The double-point formulation is applied to model several geotechnical problems such as dike failure [24], dam-break floods [25], fluidisation [26].

In this chapter a joint MPM code of the MPM Research Community is used, consisting of the University of Cambridge (UK), UPC Barcelona (Spain), Technical University Hamburg-Harburg (Germany), University of Padova (Italy), Delft University of Technology and Deltares (the Netherlands).

3.1.2. Basic concept

The Material Point Method (MPM) can be regarded as an extension of the Finite Element Method (FEM). It uses two kinds of space discretisations: first, the computational mesh (Eulerian fixed mesh) and second, the collection of material points which move through the computational mesh. Through this approach, MPM combines the best aspects of both Lagrangian and Eulerian formulations while avoiding some shortcoming of them, such as the problem of mesh distortion, shown by an updated Lagrangian solution when dealing with large deformation, or numerical diffusion associated with the convective terms in the Eulerian approach which does not appear in MPM [12].

The material points carry all physical properties of the continuum such as: position, mass, momentum, strains, stresses, constitutive properties as well as external loads, whereas the Eulerian mesh and its Gauss points carry no permanent information. The advantage of MPM is that the state variables are traced automatically by the material points and are carried independently of the computational mesh. Therefore, MPM is well suited for modelling large deformations.

The MPM solution algorithm can be subdivided into three steps: the initialization phase, the Lagrangian phase and the convective phase (Figure 3.1). Firstly, all required information carried by the material points temporarily is transferred to the nodes of the computational background mesh. The discrete equations of motion are initialized. During the Lagrangian phase, the computational mesh is used to determine the incremental solution of the balance equations at its nodes. At the end of this phase, the solution is mapped from the nodes of the computational mesh back to material points. Hence, the state of the material points (velocity, displacement, strain and stress) is updated. In the convective phase the computational mesh is redefined or reset to its initial configuration, while the material points remain the same as at the end of the Lagrangian phase. With the use of information carried by the material points, the solution can be reconstructed on any mesh. Therefore, the computational mesh can be chosen for convenience which is the great advantage of MPM.
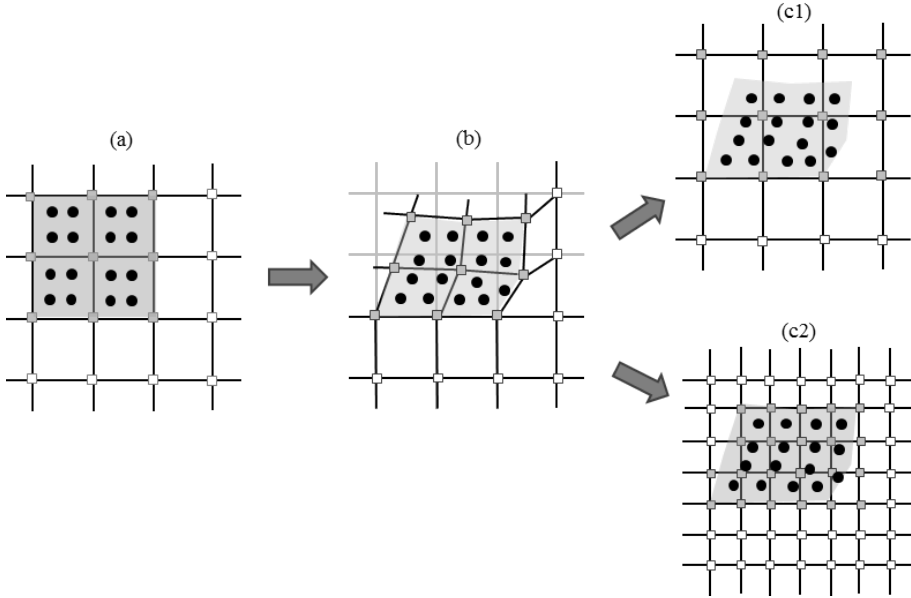
Figure 3.1: The MPM solution algorithm in three steps: a) initialization phase, b) solution of balance equations (Lagrangian phase) and c1) keep the original mesh or c2) redefine a new mesh (convective phase)

3.2. One-phase dynamic material point method

3.2.1. Governing equations

In the MPM, a continuum is considered. The continuum is subject to governing equations which include the conservation of mass, conservation of momentum, conservation of energy, constitutive equations and kinematic constraints. The development of the equations can be found in detail in the literature of continuum mechanics e.g. Malvern[27].

Conservation laws

Consider a continuum that initially occupies region $\Omega^{(0)} \subseteq \mathbb{R}^3$ and region $\Omega \subseteq \mathbb{R}^3$ for time $t > 0$. The region $\Omega^{(0)}$ represents the initial state of the continuum and is referred to as the *initial configuration* or the *undeformed configuration*, whereas the region Ω represents the state of the continuum after deformation, the *current configuration* or the *deformed configuration* respectively (Figure 3.2).

If a material point is initially defined at the position

$$\mathbf{x}^{(0)} = \begin{bmatrix} x_1^{(0)} & x_2^{(0)} & x_3^{(0)} \end{bmatrix}^T \tag{3.1}$$

then its current position

$$\mathbf{x} = \begin{bmatrix} x_1 & x_2 & x_3 \end{bmatrix}^T \tag{3.2}$$

is a function of $\mathbf{x}^{(0)}$ with $\mathbf{x} = \psi(\mathbf{x}^{(0)}, t)$ (superscript T denotes the transpose). The function ψ is used for the transformation from initial to current configuration. It
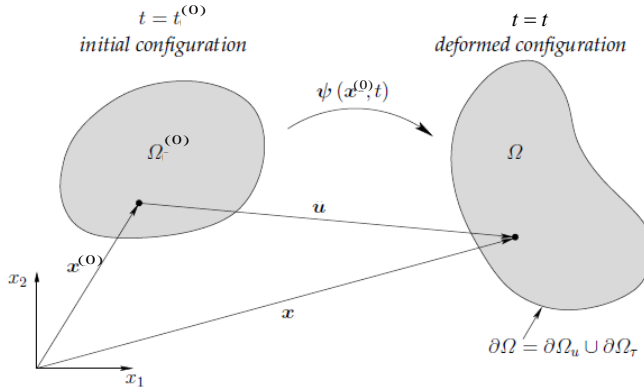
Figure 3.2: The *initial configuration* and the *deformed configuration* (after [12]).

is invertible, such that we may also consider $\mathbf{x}^{(0)}$ to be a function of $\mathbf{x}$ and t as $\mathbf{x}^{(0)} = \psi^{-1}(\mathbf{x}, t)$.

The displacement, velocity and acceleration vectors of a material point are

$$\mathbf{u}(\mathbf{x}, t) = \begin{bmatrix} u_1 & u_2 & u_3 \end{bmatrix}^T,$$
$$\mathbf{v}(\mathbf{x}, t) = \begin{bmatrix} v_1 & v_2 & v_3 \end{bmatrix}^T,$$
$$\mathbf{a}(\mathbf{x}, t) = \begin{bmatrix} a_1 & a_2 & a_3 \end{bmatrix}^T$$

respectively. As indicated in Figure 3.2, the displacement $\mathbf{u}$ can be defined as

$$\mathbf{u}(\mathbf{x}, t) = \mathbf{x} - \mathbf{x}^{(0)} \tag{3.3}$$

and the velocity $\mathbf{v}$ is defined as the material time derivative of the displacement $\mathbf{u}$ as

$$\mathbf{v}(\mathbf{x}, t) = \frac{d}{dt} \mathbf{u}(\mathbf{x}, t) \tag{3.4}$$

The acceleration $\mathbf{a}$ is related to the velocity $\mathbf{v}$ by

$$\mathbf{a}(\mathbf{x}, t) = \frac{d}{dt} \mathbf{v}(\mathbf{x}, t) \tag{3.5}$$

with $\frac{d}{dt} = \frac{\partial}{\partial t}$.

Let ρ be the mass density, σ the Cauchy stress tensor, $\mathbf{b}$ the specific body force, ε the strain tensor and r the internal energy per unit mass in the current configuration. Firstly, conservation of mass involves that

$$\frac{d\rho}{dt} + \rho \nabla \cdot \mathbf{v} = 0 \tag{3.6}$$

where d/dt designates the material derivative, ∇ is the gradient operator and $\nabla \cdot \mathbf{v}$ is the divergence of the vector field $\mathbf{v}$. Equation 3.6 is also referred to as the continuity equation.

Secondly, the Cauchy form of the conservation of linear momentum is given by

$$\rho\frac{d\mathbf{v}}{dt} = \nabla \cdot \boldsymbol{\sigma} + \rho\mathbf{b} \tag{3.7}$$

The conservation of angular momentum implies that the Cauchy stress tensor is symmetric. As the conservation of angular momentum adds no new equation, Equation 3.7 is called the momentum equation.

Finally, if thermal conduction and heat generation are ignored, mechanical energy conservation is ensured by the following equation

$$\rho\frac{dr}{dt} = \boldsymbol{\sigma} : \frac{\varepsilon}{dt} \tag{3.8}$$

Constitutive laws
In order to complete the description of the continuum, a constitutive law relating the strain rates and the stress rates of the material is needed. The strain rate can be determined from the equation

$$\frac{d\varepsilon}{dt} = \frac{1}{2}\Big(\nabla\mathbf{v} + (\nabla\mathbf{v})^{T}\Big) \tag{3.9}$$

The stress will depend on the type of material under consideration. For example, an incrementally linear elasto-plastic model can be written as

$$\frac{d\boldsymbol{\sigma}}{dt} = \mathbf{D} : \frac{d\varepsilon}{dt} \tag{3.10}$$

where $\mathbf{D}$ is the fourth-order constitutive tensor.

3.2.2. Space discretization
In this section, the momentum equation 3.7 is obtained in a discretized form. The weak form and the discrete equations of motion in MPM, which are consistent with those of FEM, are described. The main difference between MPM and FEM is the way the weak form of the momentum equation is integrated in space. FEM uses Gauss points as integration points for space integration, whereas in MPM the space integration is performed using material points instead of Gauss points.

In MPM, two kinds of space discretization are used as illustrated in Figure 3.3. Firstly, the initial configuration of the considered body is based on a collection of material points. Secondly, the entire region where the body is expected to move is discretized by a computational grid. Inside the computational grid, all elements containing material points are active elements. All nodes of active elements are active nodes. When the material points move into an inactive element, this element and its nodes become active.

To define the mass of a material point, the initial configuration domain $\Omega^{(0)}$ is divided into N_p disjointed subdomains Ω_p with $p = 1, 2 \ldots, N_p$, where N_p is the number of material points. Consider that each material point p is assigned initial values of position, velocity, mass, volume and stresses which are denoted as
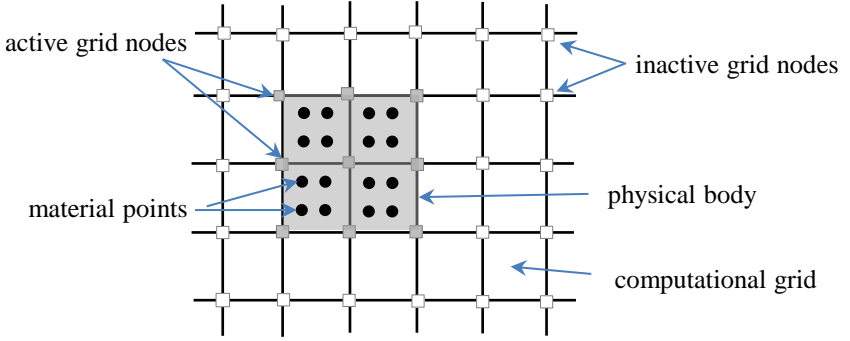
Figure 3.3: Discretization used in the material point method

$\mathbf{x}_p^{(0)}, \mathbf{v}_p^{(0)}, m_p, \Omega_p^{(0)}, \boldsymbol{\sigma}_p^{(0)}$, respectively. The density in the current configuration is given by

$$\rho(\mathbf{x}, t) = \sum_{p=1}^{N_p} m_p \delta(\mathbf{x} - \mathbf{x}_p) \tag{3.11}$$

where δ is the Dirac delta function.

Momentum equation

In order to discretise the momentum equation, the differential equation 3.7 is converted to its weak form and a finite computational grid is chosen in which an approximate solution is searched. This discretization technique is similar to the one applied to the finite element method. To derive the weak formulation, Equation 3.7 is multiplied by a test function, $\mathbf{w}$, and integrated into the domain, yielding

$$\int_\Omega \rho \mathbf{w} \cdot \frac{d\mathbf{v}}{dt} d\Omega = \int_\Omega \mathbf{w} \cdot \nabla \cdot \boldsymbol{\sigma} d\Omega + \int_\Omega \rho \mathbf{w} \cdot \mathbf{b} d\Omega \tag{3.12}$$

Using the Green's divergence theorem, the above equation can be reformulated as

$$\int_\Omega \rho \mathbf{w} \cdot \frac{d\mathbf{v}}{dt} d\Omega = -\int_\Omega \boldsymbol{\sigma} : \nabla \mathbf{w} d\Omega + \int_{\partial\Omega_\tau} \mathbf{w} \cdot \boldsymbol{\tau} dS + \int_\Omega \rho \mathbf{w} \cdot \mathbf{b} d\Omega \tag{3.13}$$

where τ is the surface traction acting on the external boundary. The first term in the weak form of the momentum equation 3.13 represents the inertia, the second one represents the internal force, the third represents the external surface force and the last one represents the body force.

The computational domain is a region which contains the material in Ω and is subdivided into N_e finite elements. The weak form of equation 3.13 is discretized at each time step on this finite computational grid in a similar way as FEM. In the MPM implementation used in this study, the mesh is constructed from 4-noded isoparametric tetrahedral elements in which the same linear functions are used to approximate the field variable when mapping the geometry of the parent domain to the global domain. The finite element shape functions $N_i(\mathbf{x})$ are associated with

the spatial nodes, with coordinate x_i, where $i = 1, 2 ..., N_n$ and N_n is the total number of grid node.

For space discretization, the velocity $\mathbf{v}$ and the test function $\mathbf{w}$ are provided in terms of the interpolation function N and the nodal value as

$$\mathbf{v}(\mathbf{x}, t) = \sum_{i=1}^{N_n} \mathbf{v}_i N_i(\mathbf{x}) \tag{3.14}$$

and

$$\mathbf{w}(\mathbf{x}, t) = \sum_{i=1}^{N_n} \mathbf{w}_i N_i(\mathbf{x}) \tag{3.15}$$

where $\mathbf{v}_i$ and $\mathbf{w}_i$ are the nodal velocity and test functions, respectively, N_i is the nodal shape function. The above equations are substituted into the weak form of the momentum equation 3.13 and utilizing that the test functions are arbitrary, it follows

$$m_i \mathbf{a}_i = \mathbf{f}_i^{ext} - \mathbf{f}_i^{int} \tag{3.16}$$

where m_i is the mass matrix, $\mathbf{a_i}$ is the unknown vector of nodal acceleration, $\mathbf{f}_i^{ext}$ is the vector of external nodal forces, $\mathbf{f}_i^{int}$ is the vector of internal nodal forces and i is the node number. The mapping of velocities from material points to nodes requires inverting the mass matrix to calculate velocities from momentums. In traditional finite element schemes, the consistent mass matrix is usually used. However, inverting the matrix has considerable computational and storage costs. To simplify computations, a lumped mass matrix can be used instead of the consistent mass matrix. The lumped mass matrix is a diagonal matrix with each entry is obtained by summing over the corresponding row of the consistent mass matrix. Using lumped mass matrix allows a fast explicit time integration and storage advantages. On the other hand, the disadvantage of using a lumped mass matrix is some numerical dissipation of kinetic energy [28].

The governing equation of MPM, 3.16, is identical with the formulation of FEM. However, in MPM since the material points move through the mesh, the number of active degrees-of-freedom of the system is changing. Hence, the mass matrix varies with time and requires the computation of a new mass matrix at the beginning of each time step.

The approximation of m_i for the case of lumped mass matrix is as follows:

$$m_i = \sum_{p=1}^{N_p} N_{ip} m_p \tag{3.17}$$

in which the notation $N_{ip} = N_i(\mathbf{x}_p)$ is used. The vector of internal forces is given by

$$\mathbf{f}_i^{int} = \sum_{p=1}^{N_p} \nabla N_{ip} \boldsymbol{\sigma}_p \Omega_p \tag{3.18}$$

The vector of external forces is given by

$$\mathbf{f}_i^{ext} = \mathbf{b}_i + \boldsymbol{\tau}_i \tag{3.19}$$

The first term $\mathbf{b}_i$ is the vector of external body forces, such as gravity which is defined by

$$\mathbf{b}_i = \sum_{p=1}^{N_p} m_p \mathbf{b}(\mathbf{x}_p) N_{ip} \tag{3.20}$$

where $\mathbf{b}(\mathbf{x}_p)$ is the gravity acceleration associated with material point p. The second term of Equation 3.19 is the traction force at the boundary of the domain Ω and evaluated as

$$\boldsymbol{\tau}_i = \int_{\partial \Omega_\tau} N_{ip} \boldsymbol{\tau}(\mathbf{x}) dS \tag{3.21}$$

The nodal velocities are calculated by solving

$$m_i \mathbf{v}_i = \sum_{p=1}^{N_p} m_p N_{ip} \mathbf{v}_p \tag{3.22}$$

These nodal velocities are utilized to find the strain increment as

$$\Delta \boldsymbol{\varepsilon}_p = \frac{\Delta t}{2} \sum_{i=1}^{N_n} \left(\nabla N_{ip} \mathbf{v}_i + (\nabla N_{ip} \mathbf{v}_i)^T \right) \tag{3.23}$$

Then, based on the constitutive relation, the stress increments are calculated at each material point.

3.2.3. Time discretization: Explicit formulation

The motion equation in space discretization form 3.16 is continued to be discretized in time. Basically, in MPM the balance equation is solved on the grid; subsequently the information is used to update the quantities associated with the material points.

Following the space discretization, the mass, velocity at node i and at current time t are found following from equation 3.17

$$m_i^t = \sum_{p=1}^{N_p} m_p^t N_{ip}^t \tag{3.24}$$

and following from equation 3.22

$$\mathbf{v}_i^t = \frac{\sum_{p=1}^{N_p} m_p^t N_{ip}^t \mathbf{v}_p^t}{m_i^t} \tag{3.25}$$

The velocity and the position of the material points need to be updated. There are two approaches of solving Equation 3.16 to advance the state of the continuum

from time t to $t + \Delta t$. The first way was shown in Sulsky et al. [29], in which the nodal acceleration and velocity are calculated and used to update the velocity of material points. The nodal velocity at the end of the time step is calculated as

$$\mathbf{v}_i^{t+\Delta t} = \mathbf{v}_i^t + \Delta t \mathbf{a}_i^t \tag{3.26}$$

The nodal acceleration and velocity are then used to update the velocity and position of the material points as

$$\mathbf{v}_p^{t+\Delta t} = \mathbf{v}_p^t + \Delta t \sum_{i=1}^{N_n} N_{ip}^t \mathbf{a}_i^t \tag{3.27}$$

and

$$\mathbf{x}_p^{t+\Delta t} = \mathbf{x}_p^t + \Delta t \sum_{i=1}^{N_n} N_{ip}^t \mathbf{v}_i^t \tag{3.28}$$

This way of updating velocity and position within the time step is identical to that of the Lagrangian FEM. However, this approach might result in numerical instability as $\mathbf{f}_i^{int}$ can be finite for an infinitesimal nodal mass, m_i [2]. This leads to non-physical nodal accelerations which are used in Equation 3.27. Hence, Sulsky et al. [2] presented an improved method of updating the material points as

$$\mathbf{v}_p^{t+\Delta t} = \mathbf{v}_p^t + \Delta t \sum_{i=1}^{N_n} \frac{N_{ip}^t (\mathbf{f}_i^{int,t} + \mathbf{f}_i^{ext,t})}{m_i^t} \tag{3.29}$$

and

$$\mathbf{x}_p^{t+\Delta t} = \mathbf{x}_p^t + \Delta t \sum_{i=1}^{N_n} \frac{N_{ip}^t \left(\mathbf{v}_i^t m_i^t + \Delta t (\mathbf{f}_i^{int,t} + \mathbf{f}_i^{ext,t}) \right)}{m_i^t} \tag{3.30}$$

In this second way of updating the velocity and position, material points are used, therefore mass conservation is always satisfied. To sum up, Equations 3.16, 3.24, 3.25, 3.29, 3.30 and 3.23 together with appropriate constitutive models are the basic equations used in the explicit MPM algorithm.

The implementation of the MPM solution procedure for one time step is detailed in Appendix A

3.3. Material point method for coupled dynamic two-phase problems

In geotechnical engineering, the problems which involve a fluid in a porous material, e.g. ground water in soil, are crucial. The requirement of coupling solid and fluid phases introduces considerable complexities to the mechanical behaviour of the material and its numerical simulation. The current section focuses on the extension of the MPM to deal with coupled dynamic two-phase problems. The solid velocity - water velocity formulation, so called $\mathbf{v_s} - \mathbf{v_w}$ formulation [30] is used. By

using the velocity of both solid and liquid constituent as the primary unknowns, this formulation was applied to several small and large deformation problems and is able to capture the physical response of saturated soil under dynamic loading [31]. The advantage of using $\mathbf{v_s} - \mathbf{v_w}$ formulation in comparison with the $\mathbf{v} - \mathbf{p}$ formulation (i.e. solid velocity-water pressure) is shown by van Esch et al. [31]. He found that both formulations can capture the undrained wave, but the $\mathbf{v} - \mathbf{p}$ formulation can not accurately capture the damped wave. On the other hand, in $\mathbf{v_s} - \mathbf{v_w}$ formulation, all acceleration terms are considered and the consistency between pressure and stress is automatically ensured.

3.3.1. Governing equations

Conservation of mass

Let us denote $\mathbf{v_s}$ and $\mathbf{v_w}$, the velocity vectors of the solid and water phase, respectively; ρ_s represents the grain density of the solid phase, ρ_w is the water density and n is the porosity. The conservation of mass for solid phase and water phase can be expressed as

$$\frac{d}{dt}[(1-n)\rho_s] + (1-n)\rho_s \nabla \cdot \mathbf{v_s} = 0 \tag{3.31}$$

and

$$\frac{d}{dt}(n\rho_w) + n\rho_w \nabla \cdot \mathbf{v_w} = 0 \tag{3.32}$$

Considering incompressible solid grains and disregarding the spatial variations in densities and porosity, then the expression for the conservation of mass of the solid and water phases Equations 3.31 and 3.32 can be reduced to

$$-\frac{dn}{dt} + (1-n)\nabla \cdot \mathbf{v_s} = 0 \tag{3.33}$$

and

$$n\frac{d\rho_w}{dt} + \rho_w \frac{dn}{dt} + (n\rho_w)\nabla \cdot \mathbf{v_w} = 0 \tag{3.34}$$

Substitute Equation 3.33 into Equation 3.34 to eliminate the term $\frac{dn}{dt}$. It yields

$$n\frac{d\rho_w}{dt} + \rho_w(1-n)\nabla \cdot \mathbf{v_s} + (n\rho_w)\nabla \cdot \mathbf{v_w} = 0 \tag{3.35}$$

The water is assumed to be linearly compressible via the relation

$$\frac{d\rho_w}{dp} = -\frac{\rho_w}{K_w} \tag{3.36}$$

in which, p is the pore pressure and K_w is the bulk modulus of water. Substituting Equation 3.36 into Equation 3.35, the conservation of mass of the saturated soil is expressed as

$$\frac{dp}{dt} = \frac{K_w}{n}\left[(1-n)\nabla \cdot \mathbf{v_s} + n\nabla \cdot \mathbf{v_w}\right] \tag{3.37}$$

Equation 3.37 is also known as a storage equation.

Conservation of momentum

The conservation of momentum of the solid phase is written as

$$(1-n)\rho_s \frac{d\mathbf{v_s}}{dt} = \nabla \cdot \boldsymbol{\sigma}' + (1-n)\nabla \cdot \mathbf{p} + (1-n)\rho_s\mathbf{b} + \frac{n^2\rho_w g}{k}(\mathbf{v_w} - \mathbf{v_s}) \quad (3.38)$$

where $\boldsymbol{\sigma}'$ is the effective stress tensor of saturated soil, k is the hydraulic conductivity of soil or Darcy permeability. The term $n(\mathbf{v_w} - \mathbf{v_s})$ represents the velocity of water with respect to the solid and is also known as the specific discharge.

The conservation of momentum of the water phase is as follows

$$n\rho_w \frac{d\mathbf{v_w}}{dt} = n\nabla \cdot \mathbf{p} + n\rho_w\mathbf{b} - \frac{n^2\rho_w g}{k}(\mathbf{v_w} - \mathbf{v_s}) \quad (3.39)$$

Adding Equation 3.38 into Equation 3.39, the momentum equation of the saturated soil is yielded as

$$(1-n)\rho_s \frac{d\mathbf{v_s}}{dt} + n\rho_w \frac{d\mathbf{v_w}}{dt} = \nabla \cdot \boldsymbol{\sigma} + \rho_{sat}\mathbf{b} \quad (3.40)$$

in which, $\boldsymbol{\sigma} = \boldsymbol{\sigma}' + \mathbf{p}$ is the total stress tensor for saturated soil and $\rho_{sat} = (1-n)\rho_s + n\rho_w$ represents the saturated density.

To sum up, the two momentum equations, i.e. Equation 3.39 for the liquid and Equation 3.40 for the mixture, together with the storage equation 3.37 and the constitutive equation for the soil skeleton, are the governing equations for the coupled two-phase problem.

3.3.2. Discretized equations

The procedure of transforming into the weak form and the space discretization of the momentum equation for two-phase formulation is the same as applied for the single-phase formulation. The detailed solution procedures for discretization in space and time are described in Jassim [12]. In the end, the discrete system of equations can be written as

$$m_{w,i}^t \mathbf{a}_{w,i}^t = \mathbf{f}_{w,i}^{ext,t} - \mathbf{f}_{w,i}^{int,t} - \mathbf{f}_{w,i}^{drag,t} \quad (3.41)$$

$$m_{s,i}^t \mathbf{a}_{s,i}^t = \mathbf{f}_i^{ext,t} - \mathbf{f}_i^{int,t} - \bar{m}_{w,i}^t \mathbf{a}_{w,i}^t \quad (3.42)$$

in which the subscripts s and w indicate solid and water, respectively. No subscripts s or w indicates that the quantity belong to the mixture. $\mathbf{f}_{w,i}^{drag,t}$ is the drag force and defined as

$$\mathbf{f}_w^{drag,t} = \mathbf{Q}^t(\mathbf{v_w}^t - \mathbf{v_s}^t) \quad (3.43)$$

where $\mathbf{Q}$ is a lumped matrix.

It is assumed that the saturated porous medium is represented based on the kinematics of the solid skeleton[32]; therefore, there is no distinction between solid and water material points. Each material points carries the information of both the solid and liquid phase together. The material points move according to the solid movement, while the motion of the liquid is described with respect to the solid motion. The implementation of the MPM solution procedure for one time step of the coupled two-phase problem is given in Appendix B

3.4. Other numerical aspects

3.4.1. Mitigation of volumetric locking

One of the difficulties associated with low-order elements is that they may expose volumetric locking when incompressibility constraints from neighbouring elements are imposed. Volumetric locking can be reduced by means of a Nodal Mixed Discretization (NMD) technique proposed by Detournay [33]. Later, Stolle et al. [34] introduced this technique to 3D dynamic MPM explicit formulation using 4-nodes tetrahedral elements. This technique involves initial determining the strain rates tensor $\dot{\varepsilon}_{ij,e}$ of each element as usual. This strain rate tensor can be partitioned into two components: the volumetric strain rate $\dot{\varepsilon}_{vol,e}\delta_{ij}$ and the deviatoric strain rate $\dot{\varepsilon}_{ij,e}^{d}$ as

$$\dot{\varepsilon}_{ij,e} = \dot{\varepsilon}_{ij,e}^{d} + \frac{1}{3}\dot{\varepsilon}_{vol,e}\delta_{ij} \tag{3.44}$$

in which δ_{ij} is Kronecker delta. The deviatoric strain component remains unchanged during this smoothing technique, while the volumetric strain component is modified by an averaging procedure. The calculation of enhanced volumetric strain includes the following steps:

1. A nodal volumetric strain rate for node i, $\bar{\dot{\varepsilon}}_{vol,i}$, is determined by the weighted averaging volumetric strain rates of all elements attached to node i.

$$\bar{\dot{\varepsilon}}_{vol,i} = \frac{\sum \dot{\varepsilon}_{vol,e}\Omega_e}{\sum \Omega_e} \tag{3.45}$$

   where $\dot{\varepsilon}_{vol,e}$ and Ω_e are the volumetric strain rate and the volume of element e

2. When the volumetric strain rate is computed for each node, the average volumetric strain rate for the 4-node tetrahedral element e, $\bar{\dot{\varepsilon}}_{vol,e}$, is determined as follows:

$$\bar{\dot{\varepsilon}}_{vol,e} = \frac{1}{4}\sum_{i=1}^{4}\bar{\dot{\varepsilon}}_{vol,i} \tag{3.46}$$

   The updated strain rate within an element is computed by means of

$$\bar{\dot{\varepsilon}}_{ij,e} = \dot{\varepsilon}_{ij,e}^{d} + \frac{1}{3}\bar{\dot{\varepsilon}}_{vol,e}\delta_{ij} \tag{3.47}$$

3. The enhanced volumetric strain of the element is then assigned to all material points inside this element.

$$\bar{\dot{\varepsilon}}_{vol}(\boldsymbol{\xi}_p) = \bar{\dot{\varepsilon}}_{vol,e} \tag{3.48}$$

The new strain tensor resulting from the enhancement of volumetric strain is used to calculate the stress tensor according to the constitutive relation.

For situations which encounter the coupled dynamic two-phase problem, the enhanced volumetric strain is applied to both the solid and the water phase. The water pressure rate of a material point p is calculated as

$$\dot{p}(\boldsymbol{\xi}_p) = \frac{K_w}{n}[(1-n)\dot{\varepsilon}_{vol,s}(\boldsymbol{\xi}_p) + n\dot{\varepsilon}_{vol,w}(\boldsymbol{\xi}_p)] \tag{3.49}$$

where $\dot{\varepsilon}_{vol,s}$ and $\dot{\varepsilon}_{vol,w}$ are the volumetric strain rate for the solid and the water phase, respectively. The enhancement procedure of volumetric strain is then applied to calculate the enhanced volumetric strain rate of the solid phase $\bar{\dot{\varepsilon}}_{vol,s}$ and the water phase $\bar{\dot{\varepsilon}}_{vol,w}$ (following Equation 3.45, 3.46, 3.48). Hence, Equation 3.49 yields

$$\dot{p}(\boldsymbol{\xi}_p) = \frac{K_w}{n}[(1-n)\bar{\dot{\varepsilon}}_{vol,s}(\boldsymbol{\xi}_p) + nbar\dot{\varepsilon}_{vol,w}(\boldsymbol{\xi}_p)] \tag{3.50}$$

The effective stress tensor is then updated by the enhanced volumetric strain of the solid phase $\bar{\dot{\varepsilon}}_{vol,s}$.

3.4.2. Dissipation of stress waves

Non-reflecting boundary

In numerical simulations of dynamic problems involving wave propagation, the use of finite mesh leads to reflection of the waves when they reach the boundaries of the mesh. In geomechanics, reflecting waves are not physical and rigid boundaries are mostly numerical artefacts. This problem might be reduced by moving the artificial boundary further away. This is however not always a practical solution as the mesh can become extremely large leading to a substantial increase in the computational effort. A partial solution for this problem was introduced by Lysmer and Kuhlemeyer [35] suggesting a supporting boundary by a dashpot. However, the boundary will continue to deform as long as the dashpot still receives stress from the soil body. In order to limit the deformation of the boundary, a spring is added parallel to the dashpot. Hence, a Kelvin-Voigt type of boundary response is obtained.

When using an absorbing boundary, including dashpots and springs, an additional force term, which is the force of the absorbing boundary $\mathbf{f}^{ab}$, is added to the equation of momentum. For a single-phase analysis, the equilibrium following from Equation 3.16 reads,

$$m_i \mathbf{a}_i = \mathbf{f}_i^{trac} + \mathbf{f}_i^{grav} - \mathbf{f}_i^{int} - \mathbf{f}_i^{ab} \tag{3.51}$$

in which

$$\mathbf{f}_i^{ab} = \int_S \mathbf{N}\boldsymbol{\tau} dS \tag{3.52}$$

where τ is the absorbing boundary traction vector.

The normal traction and shear traction of $\mathbf{f}_i^{ab}$ at the boundary node are t_n and t_s, respectively, they are defined as

$$t_n = \underbrace{c_n \dot{u}_n}_{t_n^{dashpot}} + \underbrace{k_n u_n}_{t_n^{spring}}, \quad t_s = \underbrace{c_s \dot{u}_s}_{t_s^{dashpot}} + \underbrace{k_s u_s}_{t_s^{spring}} \tag{3.53}$$

in which n and s indicate normal and shear components respectively, u is the displacement and $\dot{u}$ is velocity at the boundary node. k_n and k_s are the spring stiffness in normal and shear direction defined as

$$k_n = \frac{E_{oed}}{\delta_n} \qquad k_s = \frac{G}{\delta_s} \qquad (3.54)$$

where E_{oed} is the constrained modulus, G is the shear modulus of the adjacent material. δ is the thickness of the virtual viscous layer to limit the deformation of the boundary. Its value has to be in the range of $0 \leq \delta < \infty$. For $\delta = 0$ the element reduces to a rigid boundary and for $\delta \to \infty$ the element reduces to a dashpot boundary.

c_n and c_s are the dashpot coefficients in normal and shear direction which is determined as

$$c_n = \alpha_n \rho V_p \qquad c_s = \alpha_s \rho V_s \qquad (3.55)$$

in which α_n and α_s are the dimensionless parameters of the dashpot, ρ is the mass density and V_p and V_s are the p-wave speed and s-wave speed of the adjacent material, respectively, and can be determined as

$$V_p = \sqrt{\frac{E_{oed}}{\rho}}, \quad V_s = \sqrt{\frac{G}{\rho}} \qquad (3.56)$$

For a two-phase material analysis, the absorbing boundary is applied to both the solid and the water phase. Therefore, the resulting momentum equations following from Equation 3.51 become

$$m_{w,i}\mathbf{a}_{w,i} = \mathbf{f}_{w,i}^{trac} + \mathbf{f}_{w,i}^{grav} - \mathbf{f}_{w,i}^{int} - \mathbf{f}_{w,i}^{drag} - \mathbf{f}_{w,i}^{ab} \qquad (3.57)$$

$$m_{s,i}\mathbf{a}_{s,i} = \mathbf{f}_i^{trac} + \mathbf{f}_i^{grav} - \mathbf{f}_i^{int} - \bar{m}_{w,i}\mathbf{a}_{w,i} - \mathbf{f}_{s,i}^{ab} - \mathbf{f}_{w,i}^{ab} \qquad (3.58)$$

where $\mathbf{f}_{s,i}^{ab}$ is the force resulting from the absorbing boundary of the soil. The calculation is similar to the Equation 3.52 of the single-phase material analysis. $\mathbf{f}_{w,i}^{ab}$, which is the absorbing boundary of the water phase, is defined as

$$\mathbf{f}_{w,i}^{ab} = \int_S \mathbf{N}^T p_w \mathbf{n} dS \qquad (3.59)$$

where p_w is the water pressure, $\mathbf{n}$ is the surface normal vector.

The water pressure is then calculated as

$$p_w = \frac{K_w}{\delta_w} u_w + \alpha_w \rho_w V_w \dot{u}_w \qquad (3.60)$$

where u_w and $\dot{u}_w$ are the displacement and velocity at the boundary node for water, α_w is the dimensionless dashpot parameter for the absorbing boundary of the water phase, K_w is the bulk modulus of water, δ_w is the spring parameter for

the absorbing boundary of water and V_w is the wave speed of the water which is defined as

$$V_w = \sqrt{\frac{K_w}{\rho_w}} \tag{3.61}$$

As no shear wave exists in water, then V_w indicates the p-wave speed in water.

Local damping

Natural dynamic systems contain some degree of damping due to energy loss as a result of internal friction in the material itself or as a result of particles collision, plasticity, etc. For analyses which aresubject to dynamic loading, the damping in the numerical simulation should reproduce the energy losses as in the natural system. The MPM implementation used in this thesis adopts a local non-viscous damping which is described by Cundall [36] to achieve such convergence. The local damping is applied by introducing the damping force f^{damp} to the system, which is proportional to the out-of-balance force and acts opposite to the direction of the velocity of the considered degree-of-freedom as following

$$ma = f^{trac} + f^{grav} - f^{int} + f^{damp} \tag{3.62}$$

with f^{damp} is the damping force at a considered degree-of-freedom and is defined as

$$f^{damp} = -\alpha |f| sign(v) \tag{3.63}$$

where $f = f^{trac} + f^{grav} - f^{int}$, α is a dimensionless damping factor and v is the velocity at the considered degree-of-freedom. There is no direct relation between α and ζ_d, which is the damping ratio of viscous damping in analytical solution. However, Jassim [12] showed that using a value for local damping $\alpha = 0.157$ results in similar results to that of using a damping ratio of $\zeta_d = 0.05$.

Extending the same concept of local damping for a single-phase material above to a two-phase material, the momentum equation of two-phase material for any degree-of-freedom is then written for the water phase as

$$m_w a_w = f_w^{trac} + f_w^{grav} - f_w^{int} - f_w^{drag} + f_w^{damp} \tag{3.64}$$

and for the solid phase as

$$m_s a_s = f^{trac} + f^{grav} - f^{int} - \bar{m}_w a_w + f_w^{damp} + f_s^{damp} \tag{3.65}$$

in which

$$f_w^{damp} = -\alpha_w |f_w| sign(w) \tag{3.66}$$

with $f_w = f_w^{trac} + f_w^{grav} - f_w^{int}$ and not including the term f_w^{drag}. The reason is, f_w^{drag} representing the drag between the solid and water phase; consequently, it already provides a natural damping. The damping of the solid phase is written as
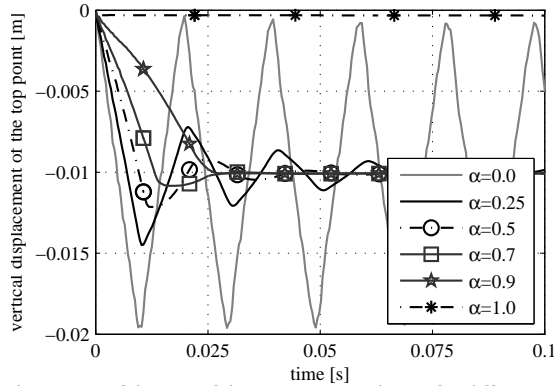
$$f_s^{damp} = -\alpha_s |f - f_w| sign(v) \tag{3.67}$$

Figure 3.4: Vertical displacement of the top of the compression beam for different values of local damping α

where α_s and α_w are dimensionless damping factors for the solid and water phase, respectively; v and w are the velocity of the solid and water at the considered degree-of-freedom, respectively.

An example of one-dimensional axial compressive loading of an elastic column is calculated in single phase using different values of local damping α. The vertical displacement of the top point was recorded as shown in Figure 3.4. For a value of $\alpha = 0.9$, the system is said to be critically damped; for $\alpha > 0.9$ it is over-damped and for $\alpha < 0.9$ it is under-damped. The influence of the damping factor α to the convergence time of the system is shown in Figure 3.5. Hence, it is suggested to use a value of α in the range between 0.7 and 0.9 in order to get a robust damping behaviour. However, it has to be mentioned that for each problem the convergence behaviour has to be thoroughly investigated. High values of α are often used for quasi-static cases to reach static equilibrium (e.g. gravity loading phase). For dynamic systems, only very small values of α are allowed.
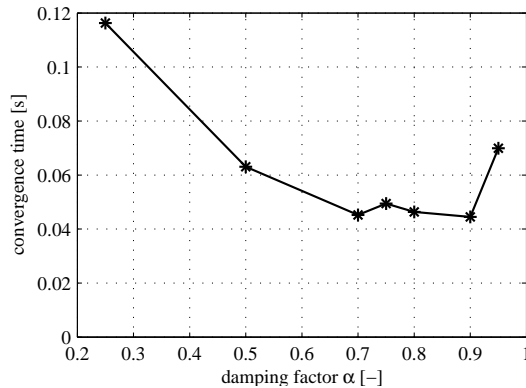

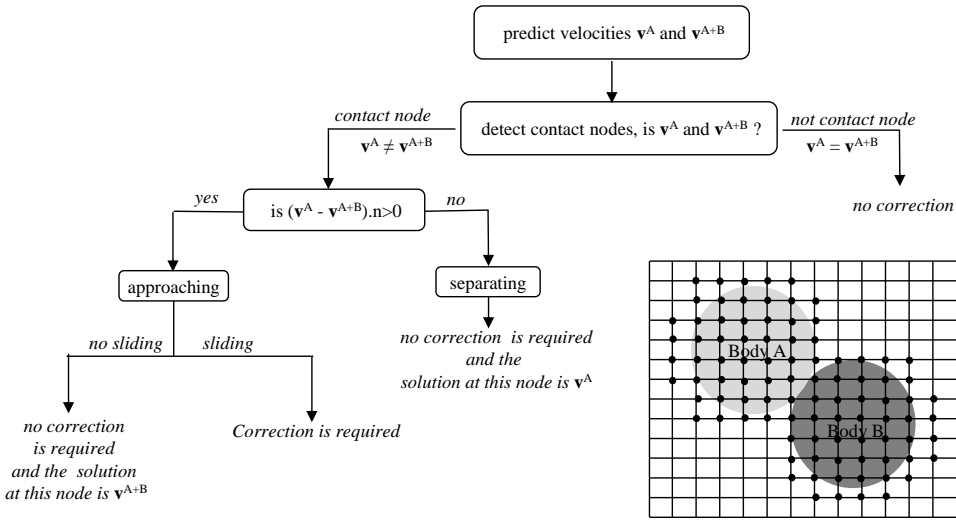Figure 3.5: Dependency of the convergence time of the compression beam simulation on the local damping factor α

Figure 3.6: Flow chart of the contact algorithm for two bodies A and B by [38]

3.4.3. Contact formulation between two bodies

Fomulation

In geotechnical engineering, problems involving soil-structure interaction, e. g. pile penetration into soil, are common. MPM can naturally handle non-slip contact between different bodies without a special algorithm [29]. However, in most geotechnical problems, frictional sliding occurs at the contact surface, and a contact algorithm is required to model it.

In the MPM implementation used in this study, the frictional contact algorithm of Bardenhagen [37] was adopted to model the interaction and frictional sliding between different bodies. With this algorithm, separation between bodies is allowed but not interpenetration. The contact surface is automatically detected and predefined contact surfaces, as well as special contact elements, are not required.

Consider two separated bodies A and B as shown in Figure 3.6 Following the contact algorithm, Equation 3.16 is solved for the combined bodies A and B as well as for each body separately, and yields

$$\mathbf{M}^A \mathbf{a}^A = \mathbf{F}^A, \quad \mathbf{M}^B \mathbf{a}^B = \mathbf{F}^B, \quad \mathbf{M}^{A+B} \mathbf{a}^{A+B} = \mathbf{F}^{A+B} \tag{3.68}$$

Then, the predicted velocities of each single body $\mathbf{v}^A$, $\mathbf{v}^B$ and the system of bodies $\mathbf{v}^{A+B}$ are computed. Contact at a specific node is detected by comparing the velocity of the single body to the velocity of the system of bodies. The considered node is a contact node if these velocities are different. After that, at each considered contact node, the contact is detected to be broken or continued by approaching. Sliding is checked for approaching contact nodes. If sliding occurs a correction of nodal velocity is required. The process of applying the contact algorithm on body A is illustrated in Figure 3.6.

Consider a single body A. Denote $\mathbf{F_n^A}$ and $\mathbf{F_t^A}$ are the normal and tangential

components of the interaction force at a contact node. They are defined as

$$\mathbf{F}_n^A = \frac{m^A}{\Delta t}\mathbf{v}_n, \quad \text{and} \quad \mathbf{F}_t^A = \frac{m^A}{\Delta t}\mathbf{v}_t \tag{3.69}$$

where m^A is the nodal mass of a contact node computed only from body A, $\mathbf{v}_n$ and $\mathbf{v}_t$ are the relative normal and tangential velocities at a contact node and calculated as

$$\mathbf{v}_n = \left((\mathbf{v}^A - \mathbf{v}^{A+B})\cdot\mathbf{n}\right)\mathbf{n} \quad \text{and} \quad \mathbf{v}_t = (\mathbf{v}^A - \mathbf{v}^{A+B}) - \mathbf{v}_n \tag{3.70}$$

In frictional contact, sliding between body A and body B occurs only when $|\mathbf{F}_t^A| > |\mathbf{F}_t^{A,max}|$. In which $|\mathbf{F}_t^{A,max}|$ is the maximum tangential force, which is limited by

$$|\mathbf{F}_t^{A,max}| = \mu|\mathbf{F}_n^A| \tag{3.71}$$

where μ is the friction coefficient.

If sliding occurs, correction of the nodal velocity of body A is required, in which the new nodal velocity can be written as

$$\mathbf{v}_{new}^A = \mathbf{v}^A + \mathbf{c}_n + \mathbf{c}_t \tag{3.72}$$

where $\mathbf{c}_n$ and $\mathbf{c}_t$ are the correction of the normal and tangential component of the velocity respectively. These are derived as

$$\mathbf{c}_n = \left((\mathbf{v}^A - \mathbf{v}^{A+B})\cdot\mathbf{n}\right)\mathbf{n} \quad \text{and} \quad \mathbf{c}_t = -\mu\left((\mathbf{v}^A - \mathbf{v}^{A+B})\cdot\mathbf{n}\right)\mathbf{t} \tag{3.73}$$

Validation
To validate the implementation of the contact algorithm, a problem of two sliding boxes along two inclined planes is considered (see Figure 3.7). The first box is on a $30°$ inclined plane, while the second box is located on a $45°$ inclined plane. The boxes and the floor have the same material properties, i.e. elastic material with Young's modulus $E = 10000$kPa and Poisson's ratio $\nu = 0$.

The boxes start sliding once

$$\omega\sin(\theta) \geq r \tag{3.74}$$

in which, ω is the weight of the box, θ is the incline angle of the sliding plane and r is the resistance tangential force that is calculated in case of frictional contact as

$$r = \mu\omega\cos(\theta) \tag{3.75}$$

Substituting Equation 3.75 into Equation 3.74, it yields

$$\mu \leq \tan(\theta) \tag{3.76}$$

Therefore, a box on an inclined surface will slide if the friction coefficient between the box and the surface $\mu < tan(\theta)$.

For the case $\mu < tan(30°) = 0.57$, both boxes will slide; for $\mu \geq tan(45°) = 1.0$ both boxes stay in rest; consequently, for $tan(30°) < \mu < tan(45°)$, only the lower box will slide. This theoretical relationship can be found back clearly in the results of the MPM calculation as shown in Figure 3.8.
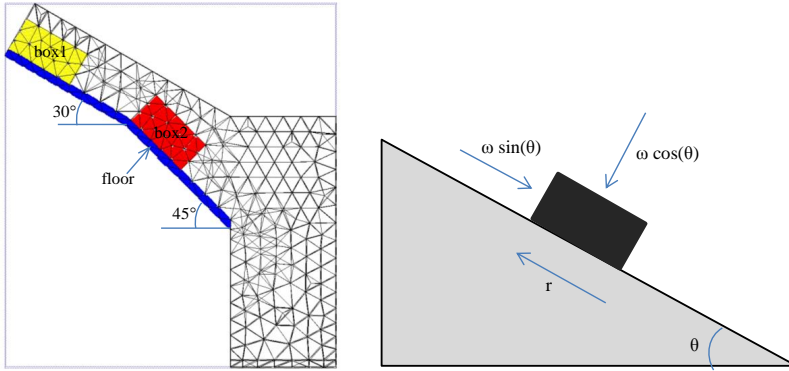
Figure 3.7: a) Geometry of sliding boxes problem generated for MPM calculation and b) forces acting on a sliding box [39].
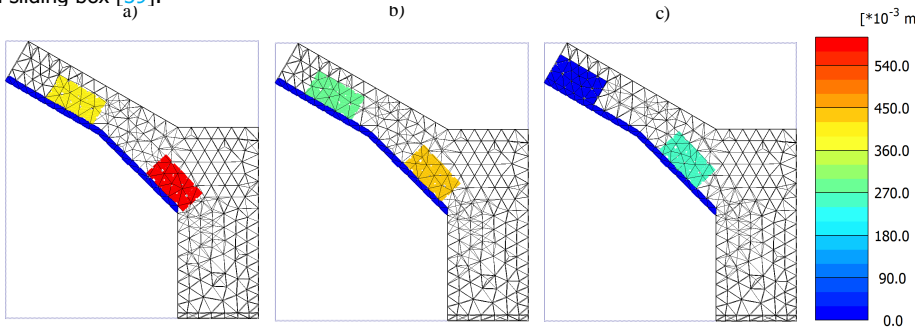

Figure 3.8: Total displacement of material points at the same time step of for different friction coefficients, a) $\mu = 0.0$, b) $\mu = 0.4$, c) $\mu = 0.7$

3.4.4. Moving mesh concept

Consider a rigid pile being pressed into the soil by applying prescribed velocities on the pile head. Accurate computations require a relative dense mesh around the pile tip. However in MPM the pile would move through the mesh and one would need mesh refinement over the complete penetration depth. In order to avoid this, a mesh, which is fixed to the pile so that it moves into the soil, is applied for all simulations in this thesis. Therefore, the fine part of the mesh will always remain around the pile tip.

In the moving mesh concept, the computational domain is divided into a moving mesh and a compressed mesh zone (Figure 3.9). The moving mesh zone is fixed to the pile and moves with the same velocity as the pile during the penetration process. Therefore, the prescribed velocity is applied at the same boundary nodes of the pile head during the calculation process without mapping between material points and nodes.

As a result of the moving mesh, the mesh below the pile tip is compressed with time by the velocity of the pile. This zone is called compressed mesh zone. In contrast to the elements of the moving mesh zone, which always maintain the same shape, elements in the compressed mesh zone are compressed during the
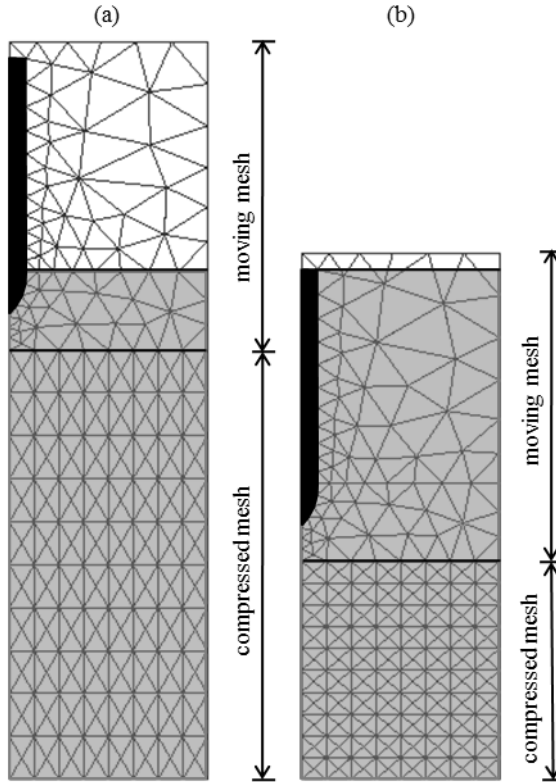
Figure 3.9: Concept of moving mesh for the pile driving problem: a) initial configuration, b) after pile penetration

computation. The amount of compression is distributed linearly with depth so that the nodes at the top surface of the compression zone have the same displacement as the pile and the nodes at the bottom surface have zero displacement. For extremely large deformations the compression mesh zone can be distorted, which can be solved by meshing a wider domain in the compression zone or, if necessary, re-meshing.

An advantage of using the moving mesh concept is that the moving mesh zone can be made fine and this fine mesh is always kept around the pile tip, which is more efficient than generating a fine mesh along the complete penetration depth in the standard formulation of MPM. This fixed mesh to the pile also helps to avoid the occurrence of elements having both pile and soil material points. Moreover, the need of determining a new contact surface between pile and soil is eliminated as the contact nodes always coincide with the geometry of the pile throughout the computation, leading to more accuracy in the contact algorithm.

3.4.5. Mass scaling

Mass scaling can be applied to increase the time step size in problems involving a slow rate of loading. Not the densities nor gravity loading, but only the mass matrices are scaled. Considering β being the dimensionless scale factor, the two momentum equations, Equation 3.41 and 3.42, are modified as

$$\beta m_{w,i}^t \mathbf{a}_{w,i}^t = \mathbf{f}_{w,i}^{ext,t} - \mathbf{f}_{w,i}^{int,t} - \mathbf{f}_{w,i}^{drag,t} \tag{3.77}$$

$$\beta m_{s,i}^t \mathbf{a}_{s,i}^t = \mathbf{f}_i^{ext,t} - \mathbf{f}_i^{int,t} - \beta \bar{m}_{w,i}^t \mathbf{a}_{w,i}^t \tag{3.78}$$

The new time step δt_2 is related to the time step without scaling δt_1 as

$$\Delta t_2 = \sqrt{\beta} \Delta t_1 \tag{3.79}$$

It is noted that in the problems involving consolidation, the use of mass scaling should not affect the consolidation coefficient c_v, which leads to a change of consolidation time. Hence, a reduction of the gravity is necessary

$$c_v = \frac{k}{\gamma_w m_v} = \frac{k}{(\beta \rho_w)(g/\beta)m_v} \tag{3.80}$$

In this thesis, mass scaling is applied to all simulations of pile jacking to improve computational efficiency.

3.5. Conclusion

The MPM - Material Point Method is one of computational methods having the capability of modelling soil-water-structure interaction problems involving large deformations. MPM has been successfully applied to a number of geotechnical engineering problems.

MPM is an advancement of the FEM, in which the continuum body is represented by Lagrangian points. Lagrangian points are called material points (MPs) which move through an Eulerian computational mesh. The MPs carry all physical properties of the continuum, whereas the computational mesh stores no permanent information Through this approach, MPM combines the advantages of both mesh-based and point-based approaches while avoiding the shortcomings, such as the problem of mesh distortion, shownby an updated Lagrangian solution when dealing with large deformation, or the numerical diffusion associated with the convective terms in the Eulerian approach which does not appear in MPM. As being conceived as an extension of FEM, MPM therefore has the advantage of using advanced features that are well established in FEM. Another advantage of MPM compared to other point-based methods is that application of boundary conditions is straightforward since they can be directly applied to the nodes of the background grids as in FEM. Hence, MPM is less complex and computationally more efficient than point-based methods.

One of the disadvantages of the MPM method is that some numerical noise associated with MPM in the numerical results can be observed. It occurs when

3

material points cross element boundaries. The disadvantages could be reduced or eliminated by applying one of the recent extensions to MPM, such as the Generalized Interpolation Material Point Method (GIMP) [40], Convected Particle Domain Interpolation method (CPDI) [41] or the second-order Convected Particle Domain Interpolation method (CPDI2) [42]. Although MPM is quite powerful in simulating geotechnical engineering problems, it is relatively high in computational demand. Furthermore, the implementation of the MPM into available engineering software is relatively complex and is still not commonly used in the geotechnical practise.

References

[1] F. H. Harlow, *The particle-in-cell computing method for fluid dynamics,* Methods in computational physics 3, 319 (1964).

[2] D. Sulsky, S.-J. Zhou, and H. L. Schreyer, *Application of a particle-in-cell method to solid mechanics,* Computer Physics Communications 87, 236 (1995).

[3] Z. Więckowski, S.-K. Youn, and J.-H. Yeon, *A particle-in-cell solution to the silo discharging problem,* International journal for numerical methods in engineering 45, 1203 (1999).

[4] Z. Więckowski, *The material point method in large strain engineering problems,* Computer methods in applied mechanics and engineering 193, 4417 (2004).

[5] Z. Wieckowski, *The material point method in soil mechanics problems,* in *The XXI International Congress of Theoretical and Applied Mechanics* (2004) pp. 3–4.

[6] K. Konagai and J. Johansson, *Two dimensional lagrangian particle finite difference method for modeling large soil deformations,* Doboku Gakkai Ronbunshu 2001, 25 (2001).

[7] C. Coetzee, P. Vermeer, and A. Basson, *The modelling of anchors using the material point method,* International journal for numerical and analytical methods in geomechanics 29, 879 (2005).

[8] C. Coetzee, A. Basson, and P. Vermeer, *Discrete and continuum modelling of excavator bucket filling,* Journal of Terramechanics 44, 177 (2007).

[9] J. Johansson and K. Konagai, *Fault induced permanent ground deformations: experimental verification of wet and dry soil, numerical findings' relation to field observations of tunnel damage and implications for design,* Soil Dynamics and Earthquake Engineering 27, 938 (2007).

[10] S. Zhou, J. Stormont, and Z. Chen, *Simulation of geomembrane response to settlement in landfills by using the material point method,* International journal for numerical and analytical methods in geomechanics 23, 1977 (1999).

[11] L. Beuth, *Formulation and application of a quasi-static material point method*, Ph.D. thesis, University of Stuttgart (2012).

[12] I. K. Jassim, *Formulation of a Dynamic Material Point Method (MPM) for Geomechanical Problems*, Ph.D. thesis, University of Stuttgart (2013).

[13] N. Phuong, A. van Tol, A. Elkadi, and A. Rohe, *Modelling of pile installation using the material point method (mpm),* in *International Conference on Numerical Methods in Geotechnical Engineering, NUMGE, Delft, The Netherlands*, Vol. 1 (CRC Press, 2014) pp. 271–276.

[14] M. Numada, K. Konagai, H. Ito, and J. Johansson, *Material point method for run out analysis of earthquake-induced long-traveling soil flows,* Journal of Earthquake Engineering 27 (2003).

[15] K. Abe, J. Johansson, and K. Konagai, *A new method for the run-out analysis and motion prediction of rapid and long-traveling landslides with mpm,* J Jpn Soc Civil Eng Div C 63, 93 (2007).

[16] S. Andersen and L. Andersen, *Modelling of landslides with the material-point method,* Computational Geosciences 14, 137 (2010).

[17] F. Zabala and E. Alonso, *Progressive failure of aznalcóllar dam using the material point method,* Géotechnique 61, 795 (2011).

[18] I. Jassim, D. Stolle, and P. Vermeer, *Two-phase dynamic analysis by material point method,* International Journal for Numerical and Analytical Methods in Geomechanics 37, 2502 (2013).

[19] K. Abe, K. Soga, and S. Bandara, *Material point method for coupled hydromechanical problems,* Journal of Geotechnical and Geoenvironmental Engineering 140 (2013).

[20] S. S. Bandara, *Material point method to simulate large deformation problems in fluid-saturated granular medium*, Ph.D. thesis, University of Cambridge Cambridge, UK (2013).

[21] S. Bandara and K. Soga, *Coupling of soil deformation and pore fluid flow using material point method,* Computers and Geotechnics 63, 199 (2015).

[22] M. Martinelli and A. Rohe, *Modelling fluidisation and sedimentation using material point method,* in *1st Pan-American Congress on Computational Mechanics* (2015).

[23] M. Martinelli, *Soil-water interaction with material point method. double-point formulation,* Report on EU-FP7 research project MPM-Dredge PIAP-GA-2012 324522 (2016).

[24] M. Martinelli, A. Rohe, and K. Soga, *Modeling dike failure using the material point method,* Procedia Engineering 175, 341 (2017).

3

[25] X. Zhao, D. Liang, and M. Martinelli, *Numerical simulations of dam-break floods with mpm,* Procedia Engineering 175, 133 (2017).

[26] M. Bolognin, M. Martinelli, K. J. Bakker, and S. N. Jonkman, *Validation of material point method for soil fluidisation analysis,* Procedia Engineering 175, 233 (2017).

[27] L. E. Malvern, *Introduction to the Mechanics of a Continuous Medium*, Monograph (1969).

[28] D. Burgess, D. Sulsky, and J. Brackbill, *Mass matrix formulation of the flip particle-in-cell method,* Journal of Computational Physics 103, 1 (1992).

[29] D. Sulsky, Z. Chen, and H. L. Schreyer, *A particle method for history-dependent materials,* Computer Methods in Applied Mechanics and Engineering 118, 179 (1994).

[30] O. C. Zienkiewicz, A. Chan, M. Pastor, B. Schrefler, and T. Shiomi, *Computational geomechanics* (Wiley Chichester, 1999).

[31] J. Van Esch, D. Stolle, and I. Jassim, *Finite element method for coupled dynamic flow-deformation simulation,* in *2nd International Symposium on Computational Geomechanics (COMGEO II)*, 1 (2011).

[32] M. A. Biot, *Theory of propagation of elastic waves in a fluid-saturated porous solid. ii. higher frequency range,* The Journal of the acoustical Society of america 28, 179 (1956).

[33] C. Detournay and E. Dzik, *Nodal mixed discretization for tetrahedral elements,* in *4th international FLAC symposium, numerical modeling in geomechanics. Minnesota Itasca Consulting Group, Inc. Paper*, 07-02 (2006).

[34] D. Stolle, I. Jassim, and P. Vermeer, *Simulation of incompressible problems in geomechanics,* in *Computer Methods in Mechanics* (Springer, 2010) pp. 347–361.

[35] J. Lysmer and R. L. Kuhlemeyer, *Finite dynamic model for infinite media,* Journal of the Engineering Mechanics Division 95, 859 (1969).

[36] P. Cundall, *Distinct element models of rock and soil structure,* Analytical and computational methods in engineering rock mechanics 4, 129 (1987).

[37] S. Bardenhagen, J. Brackbill, and D. Sulsky, *The material-point method for granular materials,* Computer methods in applied mechanics and engineering 187, 529 (2000).

[38] I. Jassim, F. Hamad, and P. Vermeer, *Dynamic material point method with applications in geomechanics,* in *2nd International Symposium on Computational Geomechanics (COMGEO II)* (2011).

[39] *MPM Training course and Workshop 2012 in Delft,* Tech. Rep. (Deltares, Delft, the Netherlands, 2012).

[40] S. Bardenhagen and E. Kober, *The generalized interpolation material point method,* Computer Modeling in Engineering and Sciences 5, 477 (2004).

[41] A. Sadeghirad, R. Brannon, and J. Burghardt, *A convected particle domain interpolation technique to extend applicability of the material point method for problems involving massive deformations,* International Journal for Numerical Methods in Engineering 86, 1435 (2011).

[42] A. Sadeghirad, R. Brannon, and J. Guilkey, *Second-order convected particle domain interpolation (cpdi2) with enrichment for weak discontinuities at material interfaces,* International Journal for Numerical Methods in Engineering 95, 928 (2013).

3

4

Hypoplastic model for grain crushing

4.1. Introduction

Many researches in soil mechanics have focused on soil behaviour at low stress levels which is suitable for most geotechnical engineering problems. However, there are several geotechnical applications which need thorough investigation of high stress conditions, as e.g. high earth dams, deep mine shafts, tunnels, deep well shafts or deep jacked pile foundations. During penetration of a cone or pile in sand, the stress level around the pile tip can vary significantly from very low at rest (i.e. a few kPa) to very high soil stresses which may be up to 70 MPa [2]. As the effective confining stress around the pile increases, the strength of the surrounding soil (such as friction or dilatancy) may reduce. For sands, Bolton [3] attributed this to the grain crushing strength. Yamamuro and Lade [4] and Lade et al. [5] studied the effects of grain crushing in drained and undrained triaxial compression and extension tests at confining stresses between 0.5 MPa and 52 MPa. They concluded that increases in confining stress cause a measured increase in the amount of grain crushing.

Hence, for applications involving large stress variations it is inevitable to have a stress dependent soil model which can be used across a wide stress range and accounts for crushing of soil grains. Daouadij et al. [6, 7] introduced the influence of crushable grain in an elastoplastic model by making the critical state line dependent on the evolution of the grain size distribution. Comparing with experimental data for three different types of materials: a quartzic, calcareous sands and a rockfill material, the model simulations can accurately reproduce the stress-strain behaviour which demonstrates its ability to reproduce the main features of sand behaviour subjected to grain crushing. However, the parameters controlling the amount of grain breakage along a given test have to be determined by curve fitting. Russel and Khalili[8] presented a new bounding surface elastoplastic constitutive model

This chapter has been published in Soil and Foundation [1].

for sands which is suited to a wide range of stress, including grain crushing. In this model, a unique shaped critical state line is defined to capture the three models of plastic deformation observed across a wide range of stresses, including particle re-arrangement, particle crushing and pseudoelastic deformation. A good agreement between model simulations and experimental data from tests subject to five load paths was found. Furthermore, the basic concepts of critical state soil mechanics as well as a nonassociative flow rule commonly used in sand are confirmed to be valid when particle crushing occurs. Later, another bounding surface constitutive model based on Severn-Trent sand model was published, in which the critical state line was extended to include the effect of grain breakage through a grading state index [9]. The effect of crushing was found to shift the critical state line and compression line downwards in the compression plane. As a result, the state parameter tends to increase and the soil feels looser. In 2014, Engin et al. [10] proposed a model which incorporates the effects of grain crushing at high stress levels, and which is a modification of Von Wolffersdorffs hypoplastic model. In this model, the void ratio is modified to be dependent on the uniformity coefficient, which is changing with vertical stress level. Their proposed model can model the suppressed dilatancy at high confinement stress level better than the original model, however, the simula-tion results are not so close with experimental ones. In addition, the performance of the model on the other hand has shown convergence issues during finite element simulations of boundary value problems.

In the first part of this chapter, the relations between peak strength, uniformity coefficient and stiffness of sand depending on stress level and amount of grain crushing derived for different sands based on experimental results in literature are described. Then, a method to modify and improve a basic hypoplastic model in order to describe the behaviour of sand over a wide stress range, especially very high stress levels including grain crushing is developed. For the proposed modified hypoplastic model only two additional well-known physical parameters, namely the uniformity coefficient and the mean grain size are included. Those parameters are straightforward to determine, which is significantly simpler than currently existing models accounting for grain crushing [10, 11]

The proposed modified hypoplastic model is validated using literature data of several triaxial test series for three different sands: Hostun sand in a stress range between 0.1 and 15 MPa [12], Toyoura sand in a stress range between 0.1 and 29.4 MPa [13] and Fontainebleau sand in a stress range between 0.1 and 30 MPa [14].

4.2. Behaviour of sand at high stress levels

4.2.1. Grain size and uniformity

Literature review

Grain size effects play a role in crushing strength, especially in brittle sand grain and rock aggregate. For a given shearing condition, the coarser the granular material is, the higher the grain breakage ratio [15–17]. Ovalle et al. [17] also observed a slight decrease in the shear strength envelope for the coarser material. For instance, the

maximum friction angle decreases about $2°$ to $3°$ for a particle size reduction factor of 4.

Fukumoto [9] conducted one-dimensional compression tests on initially uniformly graded Ottawa sand to determine the grain size distribution at different applied vertical stresses between 7 MPa and 100 MPa. It was observed that with increasing effective vertical stress, the uniformity coefficient increases significantly. Nakata et al. [18, 19] performed high-pressure one-dimensional compression tests on Silica sand samples, both initially uniformly graded and well-graded. They concluded that even for the same material the yielding characteristics depend on the initial grading curve with much more yielding occurring for uniformly graded sands in comparison to well-graded sands. As the material was changing from uniform to well-graded, the nature of grain crushing was changing from catastrophic onset to gradual breakage and rounding off surfaces.

It is observed that the change of the material characteristics can be captured by a change of the shape of the grain size distribution curve, characterized by the uniformity coefficient C_u [18–21] . Moreover the change of uniformity coefficient has a limit value and can be related to a change of applied effective stress . By using the test results of Nakata et al.[18]), Rohe [22] elaborated quantitatively the dependency of the uniformity coefficient on the applied (vertical) stress level characterized by the two stress invariants, namely mean effective stress p' (negative in compression) and deviatoric stress q and generalized as,

$$C_u = \alpha_p p'^2 - \alpha_q q^2 + \beta_p p' - \beta_q q + C_{u0} \tag{4.1}$$

in which α_p and α_q are the factors controlling the quadratic change of uniformity coefficient due to isotropic and deviatoric loading, respectively; β_p and β_q are the factors controlling the linear change of uniformity coefficient due to isotropic and deviatoric loading, respectively and C_{u0} is the reference uniformity coefficient at reference stress σ_{ref}. However, the determination of such factors was not elaborated and the suggested values are valid for a silica sand under one-dimensional compression only.

Table 4.1: Overview of investigated sands.

| N_0	Material	C_{u0}	$d_{50,0}$ [mm]	Test type	Stress level [MPa]	p^{ref} [kPa]	E^{ref} [kPa]	Reference
(1)	Fontainebleau sand	1.5	0.174	triaxial test	$0.1 - 30$	100	57000	[14]
(2)	Hostun sand	1.69	0.32	triaxial test	$0.1 - 15$	50	22727	[12]
(3)	Cambria sand	1.3	1.6	triaxial test	$2.1 - 60$	100	53700	[5]
(4)	Chattahoochee river sand	2.47	0.37	triaxial test	$0.1 - 62$	98	30000	[23]
(5)	Quartz sand	1.83	0.31	triaxial test	$0.1 - 7.8$	115	30000	[8]
(6)	Toyoura sand	1.5	0.23	triaxial test	$0.1 - 49$	98	28023	[13]
(7)	Sacramento river sand	1.57	0.2	triaxial test	$0.1 - 13.7$	98	34000	[24]
(8)	Silica sand	2.17	0.75	oedometer test	$0.1 - 92$			[19]
(9)	Ottawa sand	1.43	0.63	oedometer test	$0.1 - 96.6$			[9]
(10)	Mono quartz sand 1	2	0.36	oedometer test	$0.1 - 50$			[25]
(11)	Mono quartz sand 2	2.36	0.3	oedometer test	$0.1 - 50$			[25]
(12)	Mono quartz sand 3	2.23	0.63	oedometer test	$0.1 - 50$			[25]
(13)	Chattahoochee river sand	2.47	0.37	isotropic compression	$0.1 - 62$			[23]
(14)	Hostun sand	1.69	0.32	oedometer test	$0.1 - 100$			[26]
(15)	Quartz sand	1.83	0.31	oedometer test	$0.1 - 1000$			[27]
(16)	Toyoura sand	1.5	0.23	isotropic compression	$0.1 - 49$			[13]
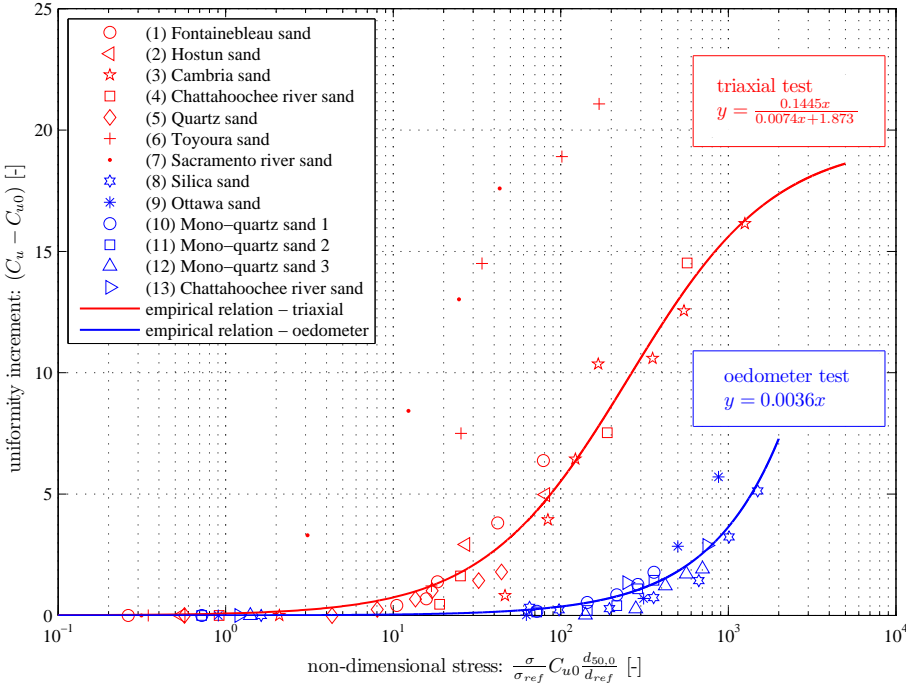
Figure 4.1: Dependency of the uniformity coefficient on the stress level in triaxial compression tests (red) and in one–dimensional compression tests (blue) for various sands listed in Table 4.1.

Generalize the dependency of the uniformity coefficient C_u on stress level

In order to generalize the dependency of the uniformity coefficient C_u on stress level under both triaxial and one-dimensional compression response, the amount of grain crushing for different types of sands is derived with data collected from literature. An overview of investigated sands listing their reference uniformity coefficient C_{u0}, reference grain size diameter $d_{50,0}$, type of test and range of stress level during test is summarized in Table 4.1. Based on the test data the uniformity coefficient C_u is determined for different applied stress levels and illustrated in Figure 4.1. The horizontal axis represents a non-dimensional stress which is the applied stress (vertical effective stress for oedometer test and cell pressure for triaxial test) multiplied by the reference uniformity coefficient C_{u0} and reference mean grain size $d_{50,0}$ in order to account for the influence of initial grain size distribution. σ_{ref} is the reference stress level of 100 kPa. d_{ref} is the reference grain diameter of 1 mm. The vertical axis represents the difference between current uniformity coefficient C_u and reference uniformity coefficient C_{u0} for increasing stress level.

From Figure 4.1 it can be seen that triaxial tests (red markers) result in a higher amount of grain crushing than would occur for oedometer tests (blue markers) which can be attributed to the additional effects of shearing. Most of the sands in triaxial test conditions show a comparable amount of grain crushing, except Toyoura (6) and Sacramento river sand (7). These two sands result in a significant higher amount of crushing. This may be caused by the fact that only the sam-

ples of Toyoura and Sacramento river sand had enough time to achieve maximum densification after applying cell pressure, whereas in the other triaxial tests this issue was not considered. Miura and Yamanouchi [13] found that the porosity of a sand at high pressure was affected not only by the magnitude of the compression pressure but also by its duration. The influence of time on the compressibility of the sand is considerably large when the applied pressure is higher than 29 MPa. Maximum densification could not be reached before 350 or 570 hours for a dense specimen compressed isotropically at a pressure of 30 or 50 MPa). On the other hand, the higher the degree of compression the greater part of grain crushing has been attained [13]. Hence, at the same stress level, for samples of Toyoura and Sacramento river sand such higher values of uniformity coefficient are obtained compared to samples of other sands. For that reason, these two tests on Toyoura and Sacramento river sand are excluded for further study.

According to Figure 4.1, an empirical relation for the dependency of C_u on stress level is suggested as following

- For triaxial response:

$$C_u = \frac{0.1445x}{0.0074x + 1.873} + C_{u0} \tag{4.2}$$

with

$$x = \frac{\sigma_{tx}}{\sigma_{ref}} C_{u0} \frac{d_{50,0}}{d_{ref}} \tag{4.3}$$

in which σ_{tx} is the cell pressure of a triaxial test, the reference pressure σ_{ref} is $100kPa$ and the reference grain diameter d_{ref} is $1mm$.

- For oedometer response:

$$C_u = 0.0036x + C_{u0} \tag{4.4}$$

with

$$x = \frac{\sigma_{oed}}{\sigma_{ref}} C_{u0} \frac{d_{50,0}}{d_{ref}} \tag{4.5}$$

where σ_{oed} is the applied effective vertical stress of a oedometer test.

As the considered sands are mainly Quartz sands, the proposed relation may not be applicable for other types of sand which are more sensitive for crushing such as carbonate sediments, decomposed granite or residual soils. In addition, the effects of particle shape, particle size, initial grading, water content could cause some scatter when different sands are considered.

4.2.2. Minimum and maximum void ratio

Literature review
The maximum void ratio, e_{max}, is the void ratio corresponding to the loosest state of the grain assembly, the minimum void ratio, e_{min}, is the void ratio corresponding to its densest state. Some general properties following from [20, 28, 29] are

Table 4.2: Considered void ratios use to represent the minimum and maximum void ratio

Sand	e_{min}	e_{max}	$e_{dense\ considered}$	$e_{loose\ considered}$
Hostun sand	0.61	0.96	0.67	0.9
Quartz sand			0.68	0.9
Toyoura sand	0.61	0.98	$0.60 - 0.62$	$0.82 - 0.84$
Silica sand	0.63	0.88	$0.60 - 0.63$	0.75

- e_{min} decreases with increasing C_u due to filling of the voids between larger grains by smaller ones. e_{min} decreases with diminishing angularity of grains. e_{min} increases as roundness and sphericity decrease.

- e_{max} decreases with increasing C_u. e_{max} increases as particle roundness and particle sphericity decrease.

Rohe [22] suggested that the change of maximum and minimum void ratio can be related to a change of the uniformity coefficient C_u and the shape of grains as

$$e_{min,max} = f(C_u(R,S)) \tag{4.6}$$

in which R is grain roundness and S is the grain sphericity. However, it is not straightforward to generalise Equation (4.6) for various sands since information on R and S is often missing and complex to determine.

Elaborating empirical correlation between the void ratios and stress level

For the purpose of simplicity, an empirical correlation between the void ratios and stress level is elaborated replacing Equation (4.6). During one dimensional tests, relations between σ_{oed} and the current void ratio are determined for both loosest and densest state of each sand. The loosest state of sand ($e_{loose\ considered}$) is used as reference for e_{max} and the densest state of sand ($e_{dense\ considered}$) is used as reference for e_{min}. Table 4.2 shows the value of void ratio used to build up the relation for e_{min} and e_{max}.

The decrease of minimum and maximum void ratio in oedometer tests for four different sands in Table 1 is quantified and illustrated in Figure 4.2. The horizontal axis represents a non-dimensional stress which is the ratio between applied vertical effective stress of a oedometer test σ_{oed} and reference pressure σ_{ref} of 100 kPa. The vertical axis represents the change of minimum and maximum void ratio for increasing stress level: $\Delta e_{min} = e_{min} - e_{min,0}$ and $\Delta e_{max} = e_{max} - e_{max,0}$.

From Figure 4.2 it can be seen that most of the sands show similar behaviour for stresses ranging between 0 and 100 MPa. Based on that, the following empirical relations are suggested for the change of minimum and maximum void ratio depending on stress level,

$$\Delta e_{min} = \frac{0.0132 \frac{\sigma_{oed}}{\sigma_{ref}}}{0.0159 \frac{\sigma_{oed}}{\sigma_{ref}} + 7.77} \tag{4.7}$$

$$\Delta e_{max} = \frac{0.0072 \frac{\sigma_{oed}}{\sigma_{ref}}}{0.0119 \frac{\sigma_{oed}}{\sigma_{ref}} + 6.37} \tag{4.8}$$
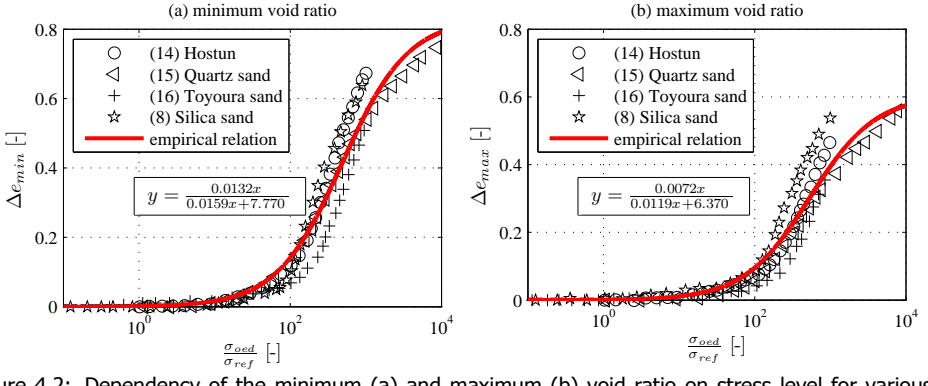
Figure 4.2: Dependency of the minimum (a) and maximum (b) void ratio on stress level for various sands listed in Table 4.1.

These two relations are supposed to be applicable for Quartz sands and restricted for one dimensional loading mode only. The relations between maximum and minimum void ratio and triaxial loading mode are important and should be included in Equations 4.7 and 4.8. However the data needed to buid up such relations is missing, which can be considered in future research.

4.2.3. Peak strength

Various investigations examining soil behaviour in triaxial compression tests at high confining stresses have been carried out in the past. In several conclusions regarding the Mohr-Coulomb secant friction angle at high stresses it is stated that the friction angle in compression decreases with increasing confining stress while approaching an asymptotical limit value at high stress [13, 23]. Other researchers have found that the friction angle in compression tests decreases to a minimum value and then increases to a constant value at higher stress level [4, 12, 24]. It is also found that the volumetric and axial strains at failure in compression tests become more contractive with increasing confining stress [4, 12–14, 23, 24].

Bolton [3] proposed an empirical relation to express that the peak friction angle and dilatancy angle of a sand depend on the stress level. It yields

$$\varphi'_{max} - \varphi'_{crit} = 3I_R \tag{4.9}$$

The maximum dilatancy rate at failure state is defined as,

$$\left(\frac{-\mathrm{d}\varepsilon_{vol}}{\mathrm{d}\varepsilon_{vert}}\right)_{max} = 0.3I_R \tag{4.10}$$

φ'_{max} and φ'_{crit} are the maximum and critical state friction angle respectively, and the relative dilatancy index I_R (non-dimensional value) is defined as,

$$I_R = R_D[Q - \ln(p')] - R \tag{4.11}$$

in which R_D is the relative density of sand and p' is the applied mean effective stress level. Q and R are relative dilatancy indices for which Bolton suggested the
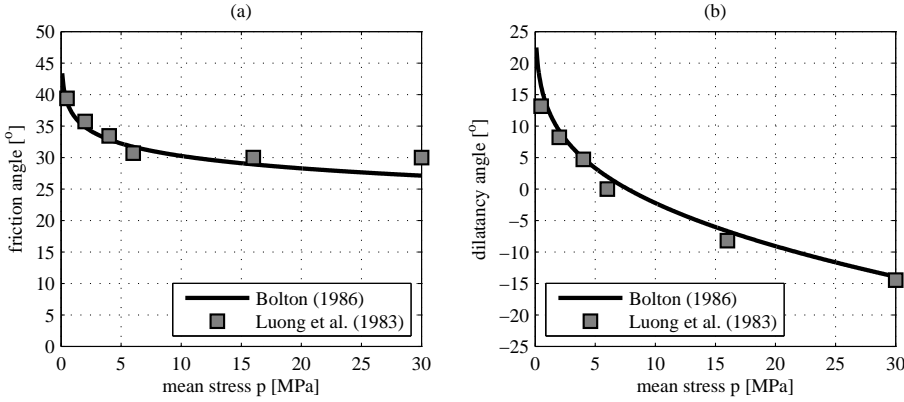
Figure 4.3: Comparison of triaxial test data on Quartz sand (R_D = 95%) at high stress levels [3, 14]. a) relation between stress level and friction angle, b) relation between stress level and dilatancy angle.

values $Q = 10$ and $R = 1$ for Quartz sand. (The value of Q depends on the units taken for p': kPa is used here)

The dilatancy angle can be calculated from drained triaxial tests according to Schanz and Vermeer [30] as follows,

$$\sin\psi = -\frac{\frac{\mathrm{d}\varepsilon_{vol}}{\mathrm{d}\varepsilon_{vert}}}{2 - \frac{\mathrm{d}\varepsilon_{vol}}{\mathrm{d}\varepsilon_{vert}}} \tag{4.12}$$

Combining Equations (4.10) and (4.12), the maximum dilatancy angle can be expressed in the form,

$$\sin\psi = \frac{0.3I_R}{2 + 0.3I_R} \tag{4.13}$$

The triaxial test results of Luong et al. [14] performed on very dense Fontainebleau sand ($e = 0.56, R_D = 95\%$) with different cell pressure levels ranging between 0.5 MPa and 30 MPa are used to evaluate above relationship. Results show that friction angle and dilatancy angle depend on mean stress level and can be calculated based on Bolton's relation 4.11, 4.9 and 4.13. The comparison between results of laboratory triaxial tests and the empirical relation is shown in Figure 4.3. Based on the results it can be concluded that the relations derived by Bolton [3] and Schanz and Vermeer [30] are in good agreement with the triaxial test results and can be used to describe the evolution of strength at high stress levels.

4.2.4. Stress dependency of stiffness

Literature review

Ohde [31] studied the behaviour of sand in compression tests and derived the stress-dependent oedometer modulus following a power law as

$$E = E^{ref}\left(\frac{p}{p^{ref}}\right)^w \tag{4.14}$$

in which E^{ref} is the reference value of stiffness E_{50} at reference pressure p^{ref} (Table 4.1) and w is an exponential factor. Schanz and Vermeer [32] concluded
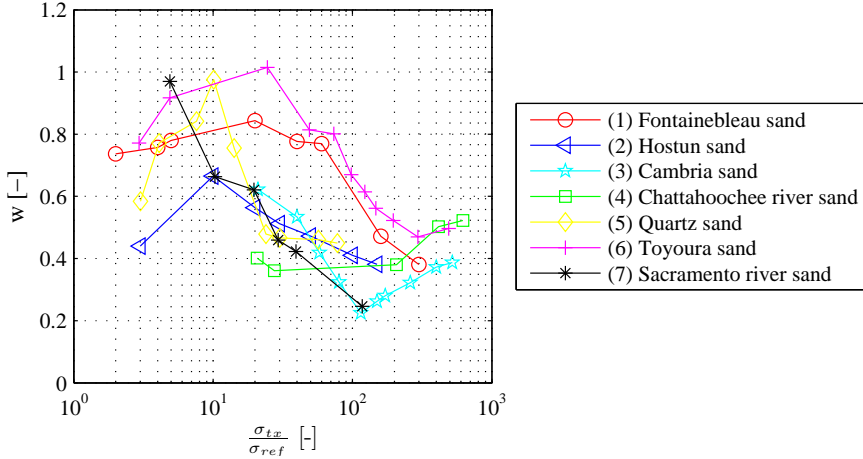
Figure 4.4: Dependency of exponent w (Equation 4.14 on cell pressure level for various granular soils under triaxial test conditions for sands listed in Table 4.1.

that for oedometer and triaxial tests the exponent w is in a range between 0.4 and 0.75 for different types of sands and influenced by the mean grain size d_{50} and the uniformity coefficient C_u. Janke [33] showed that w decreases with decreasing C_u, increasing angularity and increasing d_{50}. According to Herle and Gudehus[34], the value of $w = 0.33$ is considered as a lower bound, corresponding to the behaviour of elastic spheres without rearrangements. $w = 1$ is the upper bound which represents the familiar straight compression line in a semi-logarithmic plot.

Normalised function of stiffness depending on the stress level and grain crushing

To understand the dependency of exponent w on stress level, the value of w is calculated following Equation 4.14, using data from triaxial test results for various sands. The results are illustrated in Figure 4.4. It can be seen that the exponent w is in the range between 0.2 and 1. It is observed that during the increase of confining stress, the exponent w reaches its highest value, after which it reduces significantly towards a minimum and then it may rise somewhat.

Figure 4.5 shows the dependency of w on both stress level and uniformity. The graph can be divided into three zones.

- Zone 1, $(\frac{\sigma_{tx}}{\sigma_{ref}} . C_{u0} . C_u . \frac{d_{50,0}}{d_{ref}}) \leq 5$: w increases due to the densification of soil during loading. Assuming $w = 0.2$ is the lowest value for pressures from 0 to 200 kPa, the increase of w in zone 1 can be estimated as

$$w = (0.179 ln(x) + 0.712)R_D \tag{4.15}$$

  where $x = \frac{\sigma_{tx}}{\sigma_{ref}} . C_{u0} . C_u . \frac{d_{50,0}}{d_{ref}}$ and R_D is the relative density of sand

- Zone 2, $5 < (\frac{\sigma_{tx}}{\sigma_{ref}} . C_{u0} . C_u . \frac{d_{50,0}}{d_{ref}}) \leq 1300$: w reduces significantly. In this zone, the soil starts to be crushed leading to a rapidly increasing C_u. The more
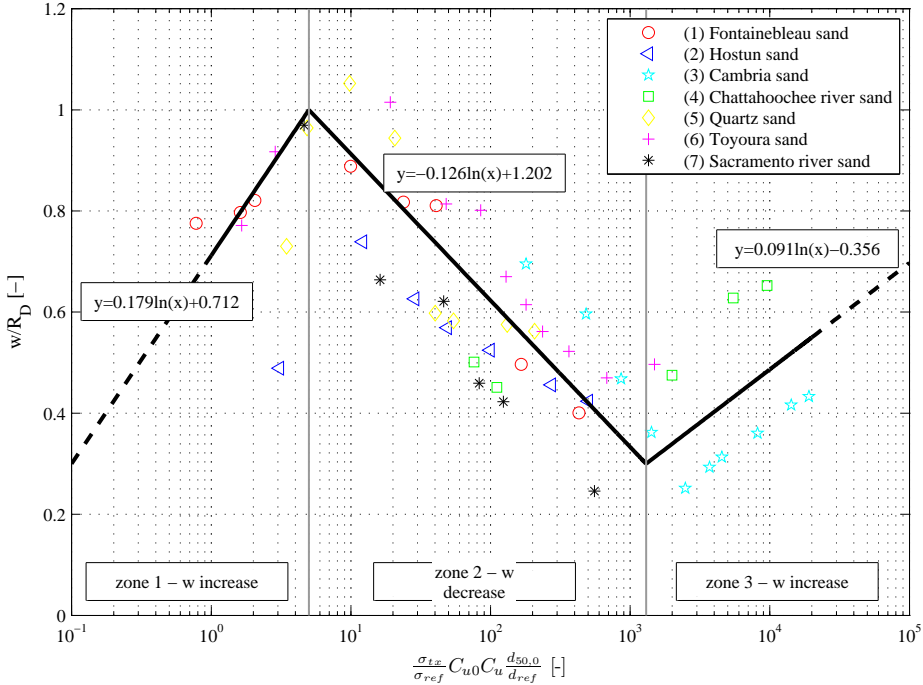
Figure 4.5: Normalised function of w depending on pressure and uniformity.

crushing, the lower value of exponent w is obtained. w can be defined in zone 2 as

$$w = (0.126 ln(x) + 1.202)R_D \quad (4.16)$$

- Zone 3, $(\frac{\sigma_{tx}}{\sigma_{ref}}.C_{u0}.C_u.\frac{d_{50,0}}{d_{ref}}) > 1300$: crushing process is nearly finished, and soil is densifying again, hence a gradual increase of w is observed, which can be defined as

$$w = (0.091 ln(x) - 0.356)R_D \quad (4.17)$$

The empirical relations in Equations (4.15), (4.16) and (4.17) are used to estimate the value of w for increasing stress level and grain crushing for different sands. Hence, the dependency of stiffness on stress level can be calculated following Equation (4.14).

It could be argued that if the data are not enough for a huge scatter in Figure 4.5, then the empirical evidence is limited, but with the used expression for the parameters of influence, there seems to be a trend that indicates three stages in the evolution of the level of stress-dependency of stiffness, which is explained physically. A third order polynomial function could have been used, but instead the authors simply divided the function into three zones, and quantified the function constants based on the limited data. These constants, that are hard-coded in the model, could be updated in the future when more data is taken into consideration.

The purpose here is to identify this trend in stress-level dependency and to describe it at least qualitatively.

To conclude, the empirical relations above are developed to estimate the dependency of the uniformity coefficient, void ratio, strength and stiffness on the stress level. In the following section, the implementation of such relations into a constitutive relationship is introduced.

4.3. Modified hypoplastic model for sand at high stress levels

Hypoplasticity is an anelastic (dissipative) and incrementally nonlinear constitutive theory of granular materials, which requires neither a yield surface nor a decomposition of strain rate into elastic and plastic portion Niemunis [35]. In the framework of hypoplastic constitutive relations dilation, contraction and the dependency of stiffness on stress and density is incorporated. The hypoplastic model was first proposed in 1978 by Kolymbas [36]. It suffered from difficulties in determining the input parameters as well as its physical meaning for such rate type constitutive equation. Until 1991, a solution was proposed by Kolybas [37] which combined the influences of pressure and density into the model. Later in 1996, the pressure-dependent limit void and stress ratios were introduced by Bauer [38] and Gudehus [39] into the hypoplastic relation. This lead to a possible easy and robust way of model parameter determination and consequently, more and more validation of the model with laboratory tests. A shortcoming of the model by Bauer and Gudehus was that it did not predict proper shape of the critical state locus in the octahedral plane. Hence, another modification of the model is attributed to von Wolffersdorff [40], who modified the Lode-angle dependency in such a way that it corresponds to the Matsuoka-Nakai limit surface.

The hypoplastic constitutive model by von Wolffersdorff [40] will be used in this study as the basic model for further development. The Cauchy (effective) stress tensor $\boldsymbol{\sigma}$ and the void ratio e are state variables. It is assumed that the soil is a homogeneous granular body whose state is fully described by these two state variables. The constitutive relation is presented in the form which consists of terms linear in strain rate similar to hypoelasticity as well as additional terms that are nonlinear in strain rate. It is written as

$$\mathring{\boldsymbol{\sigma}} = f_s(\mathbf{L} : \dot{\boldsymbol{\varepsilon}} + f_d \mathbf{N} \parallel \dot{\boldsymbol{\varepsilon}} \parallel) \tag{4.18}$$

with

$$\mathbf{L} = F^2 \dot{\boldsymbol{\varepsilon}} + a^2 \text{tr}(\hat{\boldsymbol{\sigma}} \cdot \dot{\boldsymbol{\varepsilon}})\hat{\boldsymbol{\sigma}} \tag{4.19}$$

$$\mathbf{N} = aF \parallel \dot{\boldsymbol{\varepsilon}} \parallel (\hat{\boldsymbol{\sigma}} + \hat{\boldsymbol{\sigma}}_d) \tag{4.20}$$

it yields

$$\mathring{\boldsymbol{\sigma}} = f_e f_b \frac{1}{\text{tr}(\hat{\boldsymbol{\sigma}}^2)} \left[F^2 \dot{\boldsymbol{\varepsilon}} + a^2 \text{tr}(\hat{\boldsymbol{\sigma}} \cdot \dot{\boldsymbol{\varepsilon}})\hat{\boldsymbol{\sigma}} + f_d aF \parallel \dot{\boldsymbol{\varepsilon}} \parallel (\hat{\boldsymbol{\sigma}} + \hat{\boldsymbol{\sigma}}_d) \right] \tag{4.21}$$

in which $\mathbf{L}$ and $\mathbf{N}$ are the fourth and second order constitutive tensors, respectively, both functions of stress. The first part in Equation 4.18 is the hypoelastic part which linear in $\dot{\varepsilon}$ and the second part is non-linear in $\dot{\varepsilon}$ due to the Euclidean norm of the strain rate tensor $\| \dot{\varepsilon} \| = \sqrt{\mathrm{tr}^2(\dot{\varepsilon})}$.

Further,

$$\hat{\boldsymbol{\sigma}} = \frac{\boldsymbol{\sigma}}{\mathrm{tr}(\boldsymbol{\sigma})} \tag{4.22}$$

is the stress ratio tensor and

$$\hat{\boldsymbol{\sigma}}_d = \hat{\boldsymbol{\sigma}} - 1/3\mathbf{I} \tag{4.23}$$

is the deviatoric part of $\hat{\boldsymbol{\sigma}}$ and $\mathbf{I}$ is the unit tensor.

The scalars a and F, in Equation 4.21 depend on the invariants of the Cauchy stress tensor $\boldsymbol{\sigma}$ and the void ratio e. They determine the Matsuoka-Nakai critical state surface in stress space as

$$a = \frac{\sqrt{3}(3 - \sin\varphi_c)}{2\sqrt{2}\sin\varphi_c} \tag{4.24}$$

in which φ_c is the friction angle in critical states and

$$F = \sqrt{\frac{1}{8}\tan^2\psi + \frac{2 - \tan^2\psi}{2 + \sqrt{2}\tan\psi\cos 3\vartheta} - \frac{1}{2\sqrt{2}}\tan\psi} \tag{4.25}$$

in which the invariants $\tan\psi$ and $\cos 3\vartheta$ read

$$\tan\psi = \sqrt{3}\,\|\hat{\boldsymbol{\sigma}}_d\| \tag{4.26}$$

and

$$\cos 3\vartheta = -\sqrt{6}\frac{\mathrm{tr}(\hat{\boldsymbol{\sigma}}_d^3)}{[\mathrm{tr}(\hat{\boldsymbol{\sigma}}_d^2)]^{\frac{3}{2}}} \tag{4.27}$$

The scalar F specifies the shape of the Matsuoka-Nakai yield function. The critical state surface of this model can be written as

$$f = \frac{1}{2}\|\hat{\boldsymbol{\sigma}}\| - F^2\frac{4\sin\varphi_c}{3(3 - \sin\varphi_c)} \tag{4.28}$$

The pycnotropic functions f_d and f_e in Equation 4.21 are density dependent which are defined as

$$f_d = \left(\frac{e - e_d}{e_c - e_d}\right)^\alpha, \quad f_e = \left(\frac{e_c}{e}\right)^\beta \tag{4.29}$$

and the barotropic function f_b is pressure dependent which is written as

$$f_b = \frac{h_s}{n}\left(\frac{1 + e_i}{e_i}\right)\left(\frac{e_{i0}}{e_{c0}}\right)^\beta\left(-\frac{\mathrm{tr}(\boldsymbol{\sigma})}{h_s}\right)^{1-n}\left[3 + a^2 - \sqrt{3}a\left(\frac{e_{i0} - e_{d0}}{e_{c0} - e_{d0}}\right)^\alpha\right]^{-1} \tag{4.30}$$
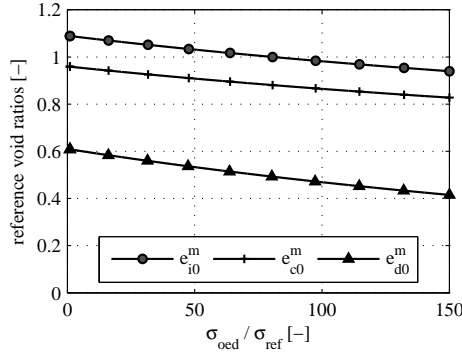
Figure 4.6: Dependency of reference void ratios on stress level (for Hostun sand, $R_D = 90\%$).

in which α, β, n are material factors which are constant in the exponents; h_s is the granular hardness; e_{c0}, e_{d0}, e_{i0} are the critical void ratio, the minimum void ratio and the maximum void ratio at zero mean pressure, respectively. Altogether, there are eight parameters defining the basic hypoplastic model according to von Wolffersdorff [40], i.e. φ_c, h_s, n, e_{d0}, e_{c0}, e_{i0}, α and β.

Such parameters are usually calibrated at low stress levels $(0 - 200$ kPa) for which they are assumed to be constant. As shown in Section 4.2, high stress levels and grain crushing may have a significant influence on the material behaviour. In the following section a method will be introduced to modify the hypoplastic model such that high stress levels and grain crushing behaviour can be considered.

4.3.1. Modified minimum and maximum void ratio

Based on a regression analysis of experimental data of oedometer tests, Section 4.2.2 shows the dependency of the reference void ratio on the applied vertical stress. As a consequence of grain crushing, both minimum and maximum void ratios decrease with the increasing applied stress (see Figure 4.2). Therefore it is proposed to redefine reference void ratios at each stress level to account for grain crushing. Based on the initial values of reference void ratios at zero pressure, e_{d0} and e_{c0}, the generalized form of modified reference void ratios according to Rohe [22] and Engin [10] can be defined as

$$e_{d0}^m = e_{d0} - \Delta e_{min} \tag{4.31}$$

$$e_{c0}^m = e_{c0} - \Delta e_{max} \tag{4.32}$$

and

$$e_{i0}^m = 1.15 e_{c0}^m \tag{4.33}$$

where Δe_{min} and Δe_{max} follow the correlations in Equation (4.7) and (4.8), respectively. The effects of modifying reference void ratios depending on stress levels are shown in Figure 4.6.

4.3.2. Modified parameter α

Herle and Gudehus [34] indicated that the peak state in a triaxial compression test simulation with the hypoplastic model can be controlled by considering the exponent
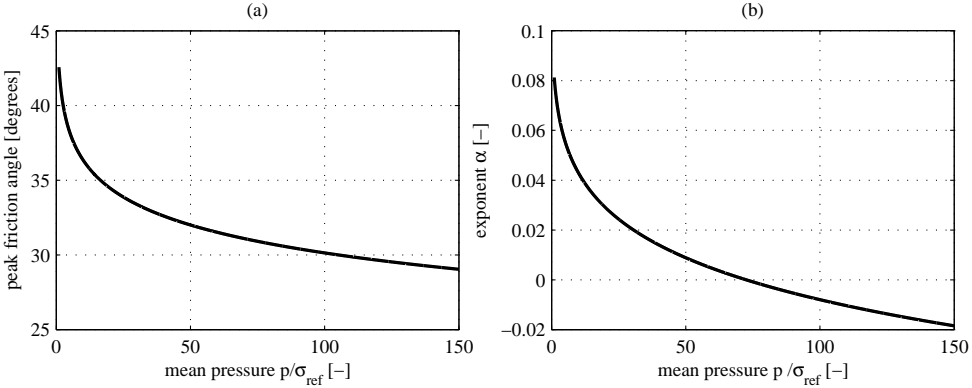
Figure 4.7: Relation between a) friction angle at peak φ_p versus mean pressure p and b) exponent α versus mean pressure p (for Hostun sand, $R_D = 90\%$).

α. They defined the following relation between α and maximum friction angle

$$\alpha = \frac{\ln\left[6\frac{(2+K_p)^2+a^2K_p(K_p-1-\tan\nu_p)}{a(2+K_p)(5K_p-2)\sqrt{4+2(1+\tan\nu_p)^2}}\right]}{\ln((e-e_d)/(e_c-e_d))} \tag{4.34}$$

With the peak ratios

$$K_p = \frac{1+\sin\varphi_p}{1-\sin\varphi_p} \tag{4.35}$$

$$\tan\nu_p = 2\frac{K_p-4+5AK_p^2-2AK_p}{(5K_p-2)(1+2A)} - 1 \tag{4.36}$$

in which

$$A = \frac{a^2}{(2+K_p)^2}\left[1 - \frac{K_p(4-K_p)}{5K_p-2}\right] \tag{4.37}$$

and

$$a = \frac{\sqrt{3}(3-\sin\varphi_c)}{2\sqrt{2}\sin\varphi_c} \tag{4.38}$$

The value of friction angle at peak φ_p is determined following Bolton's Equation (4.9) which is stress dependent. Hence, it is possible to determine α corresponding to each stress level as shown in Figure 4.7 for a reference stress of σ_{ref} = 100 kPa. The value of exponent α reduces significantly with increasing stress level, and can even become negative.

4.3.3. Modified parameter β
Through the factor $f_s = f_e \cdot f_b$ the calculated stiffness modulus E increases with increasing density and stress level [34]. For a measured E corresponding to particular stress level, density and direction of stretching, exponent β can be calculated

from Equation 4.21, thus it follows

$$\beta = \frac{ln\left[E\frac{3+a^2-f_{d0}a\sqrt{3}}{3+a^2-f_d a\sqrt{3}}\frac{e_i}{1+e_i}\frac{n}{h_s}\left(\frac{3p_s}{h_s}\right)^{n-1}\right]}{ln(e_i/e)}$$ (4.39)

Herle and Gudehus [34] suggested to determine parameter β by considering the ratio of stiffness modulus at two different void ratios but at the same stress level. Hence, β is constant and the influence of p_s in the calculation of β is neglected. Using this approach, β is limited to the range of $0 \le \beta \le 2.5$ and $\beta \approx 1$ is obtained for many sands.

For the modified hypoplastic model exponent β is proposed to be defined alternatively. Consider a sand which has the same initial void ratio but at different stress level, Equation (4.39) then becomes

$$\frac{\left(\frac{e_{i1}}{e_1}\right)^{\beta_1}}{\left(\frac{e_{i2}}{e_2}\right)^{\beta_2}} = \frac{E_1}{E_2}\frac{3+a^2-f_{d2}a\sqrt{3}}{3+a^2-f_{d1}a\sqrt{3}}\frac{e_{i1}}{1+e_{i1}}\frac{1+e_{i2}}{e_{i2}}\left(\frac{P_1}{P_2}\right)^{(n-1)}$$ (4.40)

in which the hypoplastic void ratios depend on the mean stress and are defined as

$$\frac{e_i}{e_{i0}} = \frac{e_c}{e_{c0}} = \frac{e_d}{e_{d0}} = \exp\left[-\left(\frac{-\mathrm{tr}\boldsymbol{\sigma}}{h_s}\right)^n\right] = \exp\left[-\left(\frac{-3p_s}{h_s}\right)^n\right]$$ (4.41)

Hence, $f_{d1} = f_{d2}$ and the term $\frac{3+a^2-f_{d2}a\sqrt{3}}{3+a^2-f_{d1}a\sqrt{3}}$ becomes 1.

The relation between stiffness E and mean stress p follows the power law in Equation (4.14). Therefore, $E_1/E_2 = (P_1/P_2)^w$ and Equation (4.40) can be written as

$$\left(\frac{e_{i2}}{e_2}\right)^{\beta_2} = \left(\frac{e_{i1}}{e_1}\right)^{\beta_1}\frac{1+e_{i1}}{e_{i1}}\frac{e_{i2}}{1+e_{i2}}\left(\frac{P_2}{P_1}\right)^{w+n-1}$$ (4.42)

Consider β_1 is the reference value of β which is determined following Herle and Gudehus [34] at a reference mean stress p_1 of 100 kPa, hence

$$\beta_2 = \frac{ln\left[\left(\frac{e_{i1}}{e_1}\right)^{\beta_{ref}}\frac{1+e_{i1}}{e_{i1}}\frac{e_{i2}}{1+e_{i2}}\left(\frac{P_2}{P_{ref}}\right)^{w+n-1}\right]}{ln\left(\frac{e_{i2}}{e_2}\right)}$$ (4.43)

where w is defined by Equations (4.15), (4.16) and (4.17)

The relation between β and mean stress p is shown in Figure 4.8 for Hostun sand. A slight increase in β at low stress level to a peak value of about 2.5 can be observed, after which a significant decrease of β from 2.5 to -2.5 follows.

In summary, a modified hypoplastic model is proposed in such way that parameters e_{c0}, e_{d0}, e_{i0}, α, β are stress dependent. For the basic hypoplastic model, there are eight parameters to be determined: φ_c, h_s, n, e_{c0}, e_{d0}, e_{i0}, α, β. In the modified hypoplastic model, nine parameters need to be determined: φ_c, h_s,
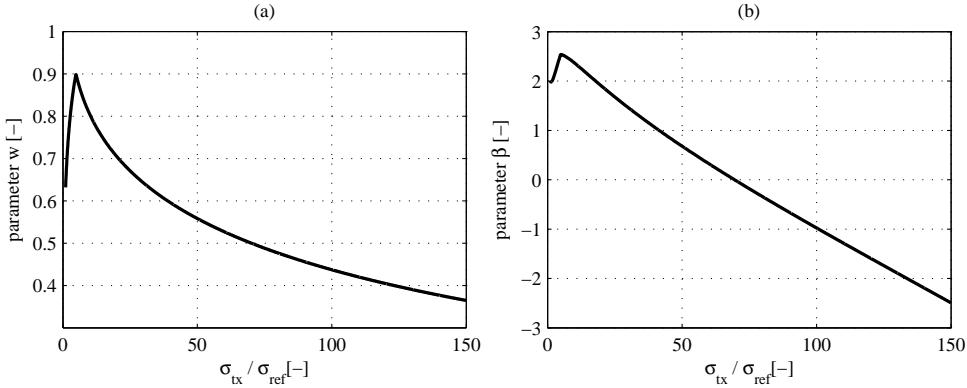
Figure 4.8: Relation between exponent β versus normalised stress p (for Hostun sand, $R_D = 90\%$).

n, e_{c0}, e_{d0}, e_{i0}, β_{ref}, C_{u0} and d_{50} . Parameter α can be eliminated as it is calculated directly from the mean stress level. β_{ref} is the value of β at reference stress level of 100 kPa. C_{u0} and d_{50} are two additional physical input parameters used to account for grain crushing. The determination of standard hypoplastic parameters follows Herle and Gudehus [34].

4.4. Validation of the modified hypoplastic model

The modified hypoplastic model is validated by simulating several triaxial tests for three different sands, i.e. Hostun, Fontainebleau and Toyoura at stress levels between 0.5 and 30 MPa. The modified hypoplastic model is implemented in UMAT format [41] and triaxial test simulations are done using a single Gauss point element test. The numerical results are compared with laboratory test results which are available in literature. The hypoplastic input parameters (which were calibrated for stress levels between 50 and 500 kPa) for the three sands are listed in Table 4.3.

In the previous section, it is suggested to modify the reference void ratios, exponent α and exponent β depending on the stress level. The effects of each parameter adaption are illustrated in Figure 4.9 for Hostun dense sand with relative density of 90%. Note that the simulations are carried out with the original parameters of Table 2 which where determined for the reference stress level. At a cell pressure of 10 MPa, the original hypoplastic model predicts too high peak friction angle and too much dilatancy, whereas in the triaxial test, the friction angle tends towards the critical value and only contractive behaviour is observed. In other words, in the simulation the dense Hostun sand at very high cell pressure behaves in a quite

Table 4.3: Hypoplastic parameters for Hostun sand [34], Toyoura sand [34] and Fontainebleau sand [14].

Parameter	$\varphi_c[°]$	$h_s[MPa]$	n	e_{d0}	e_{c0}	e_{i0}	α	β	C_{u0}	$d_{50}[mm]$
Hostun	32	1000	0.29	0.61	0.96	1.09	0.13	2.0	1.69	0.32
Toyoura	32	120	0.69	0.61	0.98	1.13	0.12	1.0	1.5	0.23
Fontainebleau	32	10000	0.56	0.54	0.94	1.08	0.08	1.2	1.48	0.174
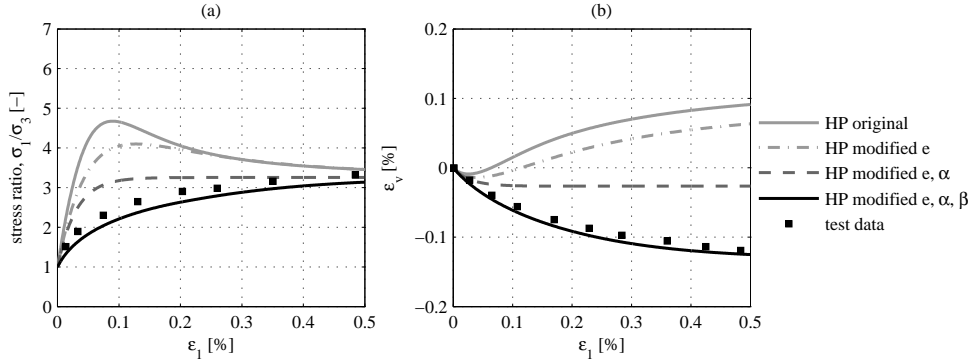
Figure 4.9: Triaxial response of dense Hostun sand ($R_D = 90\%$) at high cell pressures of 10 MPa. Comparison of test result [12] with different hypoplastic model modifications. a) stress ratio versus vertical strain, b) volumetric strain versus vertical strain.

similar way as loose sand. The modification for the reference void ratio suggested by Rohe[22] and Engin [10] only slightly improves the peak strength and dilative behaviour. The modification of α results in quite accurate peak friction angle compared to the test, however, the soil stiffness is still too high. Finally, using also the modification of exponent β, the stiffness and dilative behaviour is reduced significantly to correspond with the test data. Hence, the modified hypoplastic model proposed in the previous section results in simulations which are in good agreement with the triaxial laboratory test results.

More sands at different stress levels were selected to validate the model. Figures 4.10, 4.11 and 4.12 show the comparison between triaxial simulations at increased cell pressure using the original and the modified hypoplastic model with test results for three sands: Hostun sand, Toyoura sand and Fontainebleau sand, respectively. Each figure is divided into three rows, in which the first row shows the laboratory test results (Figure a and b), the second row shows the simulation results using the original hypoplastic model (Figure c and d) and the last one shows the simulation results using the modified hypoplastic model (Figure e and f). In the first column of each figure the relation between stress ratio σ_1/σ_3 and axial strain ε_1 is plotted, and the second column illustrates the relation of volumetric strain ε_v versus axial strain ε_1. For all simulations using the original hypoplastic model of all three sands, there is no contractive behaviour observed even at very high confining stresses (Figure 4.10d, 4.11d and 4.12d). Moreover, the use of a constant value for α in the original hypoplastic model overestimates the peak friction angle, especially at high stress levels, whereas, the modified hypoplastic model results in quite accurate peak strength compared to the test data of all three sands. At very high stress level (larger than 5 MPa) the modified hypoplastic model results in a soil stiffness response that is much softer than for the original hypoplastic model which is quite similar to the test results. From the test data in Figure 4.10a, 4.11a and 4.12a, it is observed that there is a slight reduction of critical state friction angle to lower values with increasing stress level. In the case of Toyoura sand, Figure 4.11a, after reduction to a low value, the critical state friction angle rises somewhat. Hence, further studies are necessary to get a better understanding of the change of the

critical state friction angle when crushing occurs.

To summarise, the validation of the modified hypoplastic model using triaxial test data shows the added value with regard to the original hypoplastic model. This indicates that the modified hypoplastic model considering grain crushing effects is very well suited to model the behaviour of sands for a wide range of stress levels.

4.5. Conclusion

The characteristics of sand at high stress levels and related to grain crushing are analysed. Based on these analyses, it is proposed to modify and improve the hypoplastic constitutive model to account for the influence of grain crushing. In the modified model, two well-known physical parameters, uniformity coefficient C_u and mean grain size diameter d_{50}, are included. Such parameters are straightforward to determine making the proposed model convenient to use.

The empirical relations involving grain-crushing of the modified hypoplastic model are implemented in Plaxis or in MPM as a user defined soil model. A series of triaxial tests on three different sands were used to calibrate and validate the model. Comparison between experimental data and numerical simulations demonstrates that the modified hypoplastic model is capable of predicting both stress and strain accurately.

The modified hypoplastic model for crushed sand is applied to model the installation process of a jacked pile in sand in chapter 5 (section 5.6). Results from this application shows that the simulation with the modified hypoplastic model gives a better correspondence with the experiments than the original hypoplastic model. Hence taking into account grain crushing in the hypoplastic constitutive model can be considered as one of the important factors to successfully model the pile installation as well as predicting the pile bearing capacity.

This study only considers stress dependency of five parameters $\alpha, \beta, e_i, e_c, e_d$ of the hypoplastic model. However, parameters h_s, n and φ_c are most likely influenced by grain crushing and stress level as well [34]. Hence, further investigation should be carried out to improve the model, which may lead to a better correspondence with test data.
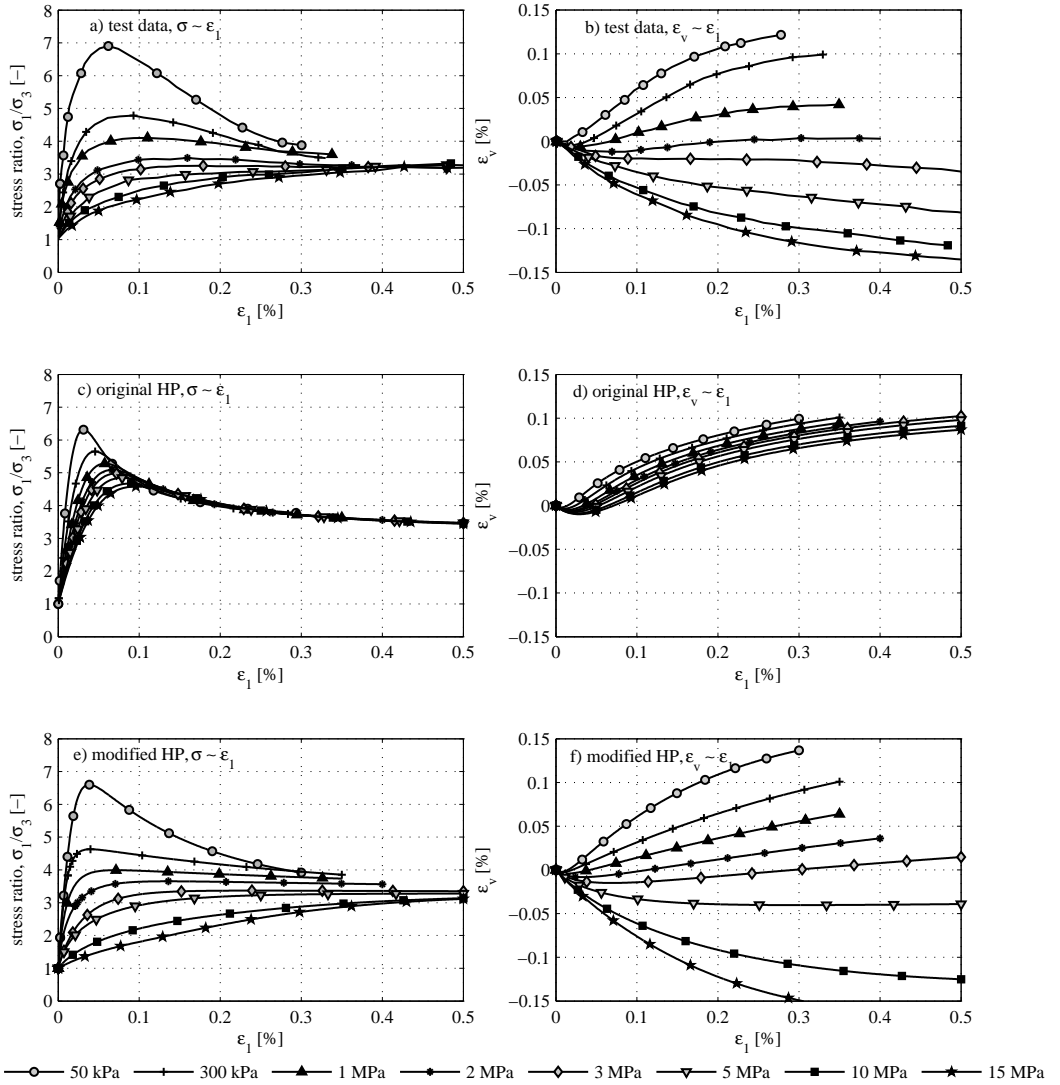
Figure 4.10: Triaxial response of Hostun sand at cell pressures between 50 kPa and 15 MPa, a) and b) are test results [12], c) and d) are simulation results using original hypoplastic model, e) and f) are simulation results using modified hypoplastic model.
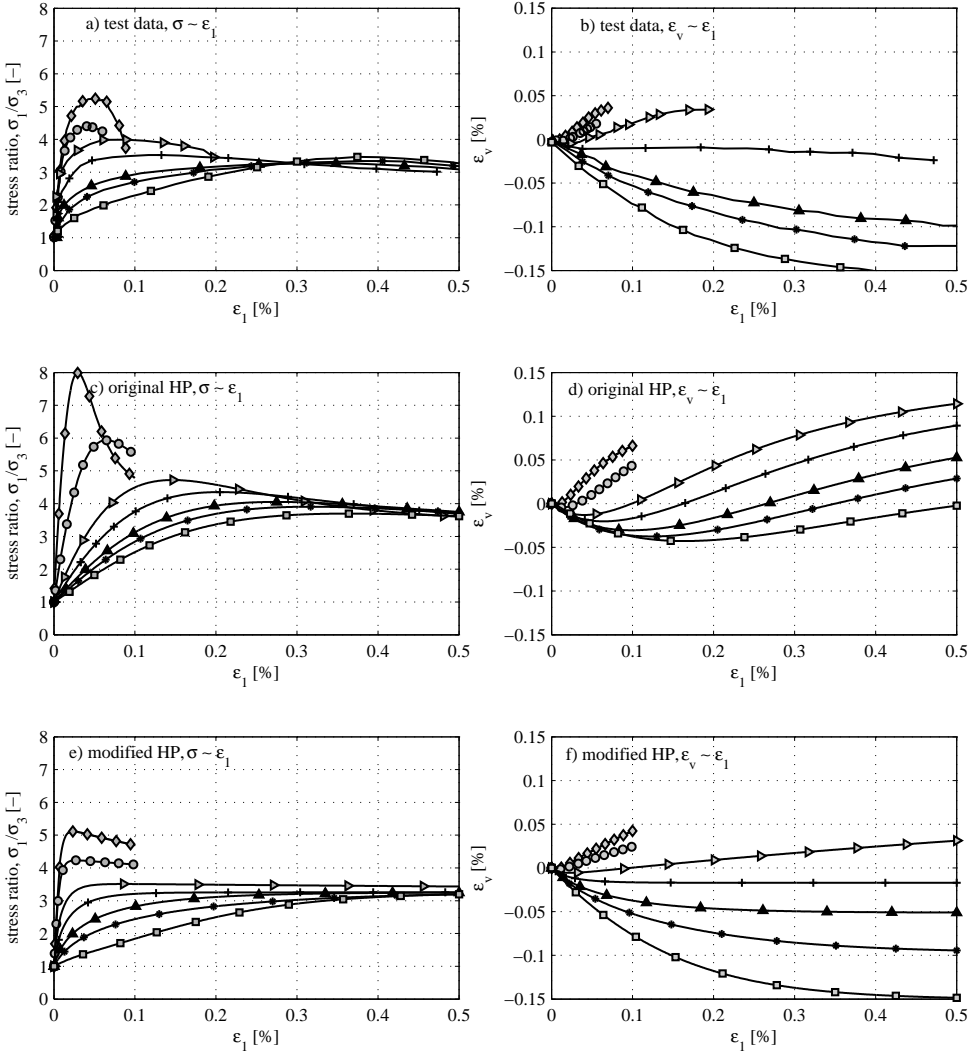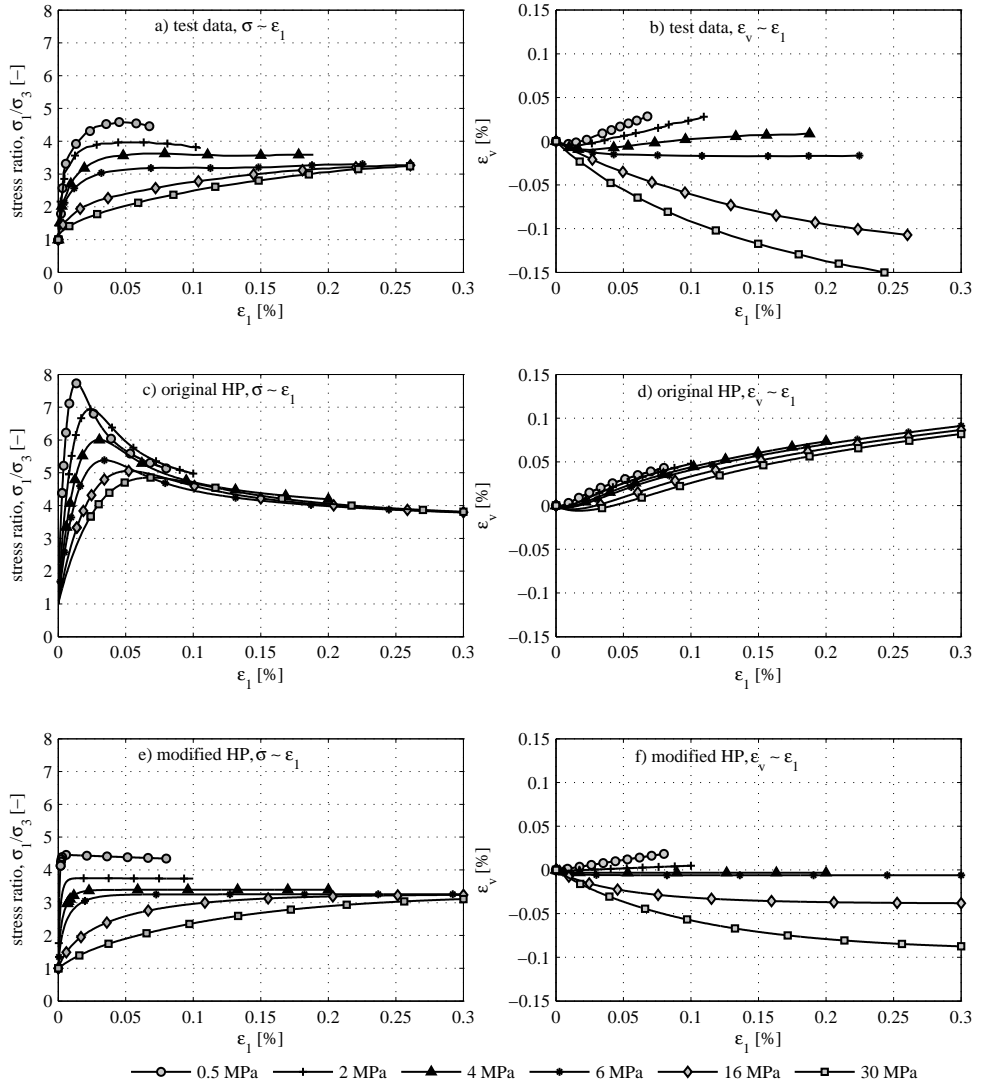
Figure 4.11: Triaxial response of Toyoura sand at cell pressures between 98 kPa and 29400 kPa, a) and b) are test results [13], c) and d) are simulation results using original hypoplastic model, e) and f) are simulation results using modified hypoplastic model.

Figure 4.12: Triaxial response of Fontainebleau sand at cell pressures between 500 kPa and 30 MPa, a) and b) are test results [14], c) and d) are simulation results using original hypoplastic model, e) and f) are simulation results using modified hypoplastic model.

References

[1] N. Phuong, A. Rohe, R. Brinkgreve, and A. van Tol, *Hypoplastic model for crushable sand,* Soils and Foundations 58, 615 (2018).

[2] D. J. Murphy, *Stress, degradation, and shear strength of granular material,* Geotechnical modeling and applications. Gulf Publishing Company, Houston , 181 (1987).

[3] M. Bolton, *The strength and dilatancy of sands,* Geotechnique 36, 65 (1986).

[4] J. A. Yamamuro and P. V. Lade, *Drained sand behavior in axisymmetric tests at high pressures,* Journal of Geotechnical Engineering 122, 109 (1996).

[5] P. V. Lade, J. A. Yamamuro, and P. A. Bopp, *Significance of particle crushing in granular materials,* Journal of Geotechnical Engineering 122, 309 (1996).

[6] A. Daouadji, P.-Y. Hicher, and A. Rahma, *An elastoplastic model for granular materials taking into account grain breakage,* European Journal of Mechanics-A/Solids 20, 113 (2001).

[7] A. Daouadji and P.-Y. Hicher, *An enhanced constitutive model for crushable granular materials,* International journal for numerical and analytical methods in geomechanics 34, 555 (2010).

[8] A. R. Russell and N. Khalili, *A bounding surface plasticity model for sands exhibiting particle crushing,* Canadian Geotechnical Journal 41, 1179 (2004).

[9] T. Fukumoto, *Particle breakage characteristics of granular soils,* Soils and Foundations 32, 26 (1992).

[10] H. Engin, H. Jostad, and A. Rohe, *On the modelling of grain crushing in hypoplasticity,* in *International Conference on Numerical Methods in Geotechnical Engineering, NUMGE, Delft, The Netherlands* (2014).

[11] W. Hu, Z. Yin, C. Dano, and P.-Y. Hicher, *A constitutive model for granular materials considering grain breakage,* Science China Technological Sciences 54, 2188 (2011).

[12] J. L. Colliat-Dangus, J. Desrues, and P. Foray, *Triaxial testing of granular soil under elevated cell pressure,* Advanced triaxial testing of soil and rock, ASTM STP 977, 290 (1988).

[13] N. Miura and T. Yamanouchi, *Compressibility and drained shear characteristics of a sand under high confining pressures,* Technology reports of the Yamaguchi University 1, 271 (1973).

[14] M. Luong and A. Touati, *Sols grenus sous fortes contraintes,* Revue Française de Géotechnique , 51 (1983).

4

[15] N. Marachi, C. Chan, H. Seed, and J. Duncan, *Strength and deformation characteristics of rockfills materials*, Tech. Rep. TE-69-5 (Department of civil engineering, University of California, Berkeley, 1969).

[16] D.-M. Lee, *Angles of friction of granular fills.*, Ph.D. thesis, University of Cambridge (1992).

[17] C. Ovalle, E. Frossard, C. Dano, W. Hu, S. Maiolino, and P.-Y. Hicher, *The effect of size on the strength of coarse rock aggregates and large rockfill samples through experimental data,* Acta Mechanica 225, 2199 (2014).

[18] Y. Nakata, M. Hyodo, A. F. L. Hyde, Y. Kato, and H. Murata, *Microscopic particle crushing of sand subjected to high pressure one-dimensional compression,* Soils and Foundations 41, 69 (2001).

[19] Y. Nakata, Y. Kato, M. Hyodo, A. F. L. Hyde, and H. Murata, *One-dimensional compression behaviour of uniformly granded sand related to single particle crushing strength,* Soils and Foundation 41, 39 (2001).

[20] J. Biarez, P.-Y. Hicher, *et al.*, *Elementary mechanics of soil behaviour: saturated remoulded soils.* (Balkema, Rotterdam, 1994).

[21] M. Coop, K. Sorensen, T. B. Freitas, and G. Georgoutsos, *Particle breakage during shearing of a carbonate sand,* Géotechnique 54, 157 (2004).

[22] A. Rohe, *On the modelling of grain crushing in hypoplasticity*, Tech. Rep. (Delft University of Technology, 2010).

[23] A. S. Vesic and G. W. Clough, *Behavior of granular materials under high stresses,* Journal of Soil Mechanics & Foundations Div (1968).

[24] K. L. Lee and H. B. Seed, *Drained strength characteristics of sands,* Journal of Soil Mechanics & Foundations Div (1967).

[25] F. A. Chuhan, A. Kjeldstad, K. Bjørlykke, and K. Høeg, *Porosity loss in sand by grain crushing, experimental evidence and relevance to reservoir quality,* Marine and Petroleum Geology 19, 39 (2002).

[26] J. L. Colliat-Dangus, *Comportement des matériaux Granulaires sous fortes contraintes*, Ph.D. thesis, Université de Grenoble (1986).

[27] J. A. Yamamuro, P. A. Bopp, and P. V. Lade, *One-dimensional compression of sands at high pressures,* Journal of geotechnical engineering 122, 147 (1996).

[28] T. Youd, *Factors controlling maximum and minimum densities of sands,* Evaluation of Relative Denisty and Its Role in Geotechnical Projects Involving Cohesionless Soils 523, 98 (1973).

[29] G.-C. Cho, J. Dodds, and J. C. Santamarina, *Particle shape effects on packing density, stiffness, and strength: natural and crushed sands,* Journal of Geotechnical and Geoenvironmental Engineering 132, 591 (2006).

[30] T. Schanz and P. Vermeer, *Angles of friction and dilatancy of sand,* Géotechnique 46, 145 (1996).

[31] J. Ohde, *Zur theorie der druckverteilung im baugrund,* (1939).

[32] T. Schanz and P. Vermeer, *On the stiffness of sands,* Géotechnique 48, 383 (1998).

[33] S. Jänke, *Zusammendrückbarkeit und scherfestigkeit nichtbindiger erdstoffe: ihre quantitative ermittlung mit hilfe einfacher kennwerte und feststellung der sie bestimmenden einflussfaktoren,* Baumaschine und Bautechnik 15 (1968).

[34] I. Herle and G. Gudehus, *Determination of parameters of a hypoplastic constitutive model from properties of grain assemblies,* Mechanics of Cohesive-frictional Materials 4, 461 (1999).

[35] A. Niemunis, *Extended hypoplastic models for soils*, Vol. 34 (Inst. für Grundbau und Bodenmechanik, 2003).

[36] D. Kolymbas, *Ein nichtlineares viskoplatisches Stoffgesetz für Böden* (Institut für Bodenmechanik und Felsmechanik, Universität Fridericiana in Karlsruhe, 1978).

[37] D. Kolymbas, *An outline of hypoplasticity,* Archive of Applied Mechanics 61, 143 (1991).

[38] E. Bauer, *Calibration of a comprehensive hypoplastic model for granular materials,* Soils and Foundations 36, 13 (1996).

[39] G. Gudehus, *A comprehensive constitutive equation for granular materials,* Soils and Foundations 36, 1 (1996).

[40] P.-A. von Wolffersdorff, *A hypoplastic relation for granular materials with a predefined limit state surface,* Mechanics of Cohesive-frictional Materials 1, 251 (1996).

[41] G. Gudehus, A. Amorosi, A. Gens, I. Herle, D. Kolymbas, D. Mašín, D. Muir Wood, A. Niemunis, R. Nova, M. Pastor, *et al.*, *The soilmodels. info project,* International Journal for Numerical and Analytical Methods in Geomechanics 32, 1571 (2008).

4

<div style="text-align: right; font-size: 3em;">5</div>

Jacked installation in dry sand

5.1. Introduction

During installation, jacked displacement piles are pushed into the ground leading to a distortion of the surrounding soil. As a result, large shear strains and significant increase of stresses surrounding the pile tip are observed [4]. This complex installation process will substantially influence the bearing capacity of the pile foundation.

In this chapter, numerical simulations are presented for modelling the installation process of jacked displacement piles in sand using the aforementioned MPM Software. Both the Mohr Coulomb model and the hypoplastic model are used as a constitutive model to investigate the differences between those two models. Choosing a suitable constitutive model for the soil plays a crucial role in geotechnical numerical modelling. In this study, the hypoplastic constitutive model in the fomulation of Von Wolffersdorff [5] is used. This model is able to incorporate dilation, contraction and the dependence of stiffness on stress and density. Centrifuge tests [6, 7] showed that very high stresses occur at the pile tip during the installation process. The range of stress may increase up to 100 times the initial value. Under such a large increase of stress in the soil, a decrease in a dilatancy effect caused by the particle crushing is observed, which leads to significant reduction on shear strength of the soil [8–11]. These effects are addressed by adapting the hypoplastic model parameters accordingly in order to successfully simulate a centrifuge test as presented in this work [2]. Two different initial densities of sand are investigated, namely loose ($R_D = 36\%$, e0 = 0.75) and medium-dense sand ($R_D = 54\%$, e0 = 0.68). Afterwards simulations of a static load test following the pile installation process are carried out. The numerical simulation results are compared with results of pile installation and static load test experiments in the centrifuge. It should be noted that a shortcoming of the centrifuge test is, that it captures the size effect due to stress level but not due to the mean grain size in the case of shear localization.

This chapter is part of three papers [1–3].

Table 5.1: Properties of Baskarp sand.

Parameter	Value	Dimension
Density of soil particles	2647	kg/m^3
d_{10}	90	μm
d_{50}	130	μm
d_{90}	200	μm
Minimum porosity	34	$\%$
Maximum porosity	47	$\%$
Friction angle at $R_D = 50\%$	41	degree

However, choosing a pile with large dimensions relative to the grain size can minimize the error of the grain size effect [12]. Moreover, centrifuge tests are preferred to field tests because of the well-defined testing and material conditions compared to the complex characteristics of sand in natural condition. In the last section, MPM results are compared with another method named Press Replace Method (PRM) which is a simple method used in finite element code for simulating boundary-value problems that involves penetration of an object into a continuum.

5.2. Centrifuge test

5.2.1. Test set-up

The performed numerical calculations are based on the geometry of the centrifuge test carried out at Deltares. The centrifuge experiments performed are described in detail in Huy[13] and Holscher et al. [14]. Figure 5.1, shows the test set up. The tests were done in a 0.6 m diameter and 0.79 m high steel container filled with sand (sample height 0.46 m). A loading system with plungers was mounted on top of the container. It consisted of two hydraulic plungers that were installed in a series. The first and largest plunger was fixed on the loading frame, and was used to install the pile in flight to its starting position before the load test program began. The second, smaller plunger which was affixed to the rod of the first plunger was the fast loading plunger and used to perform the model pile load tests. The pile was attached to the second plunger.

The model pile was a steel pile with a length of 0.3 m and a diameter of 0.0113 m. The model pile weighed 0.57 kg. A load cell was placed on the model toe to measure pile toe resistance.

5.2.2. Sample properties & preparation

Soil properties

Baskarp sand with a $d_{50} = 130$ μm was used for the tests. It is widely used in laboratory tests, and its soil parameters have been reported in a variety of literature. Table 5.1 presents the sand's basic properties as determined in laboratory tests [13, 15].
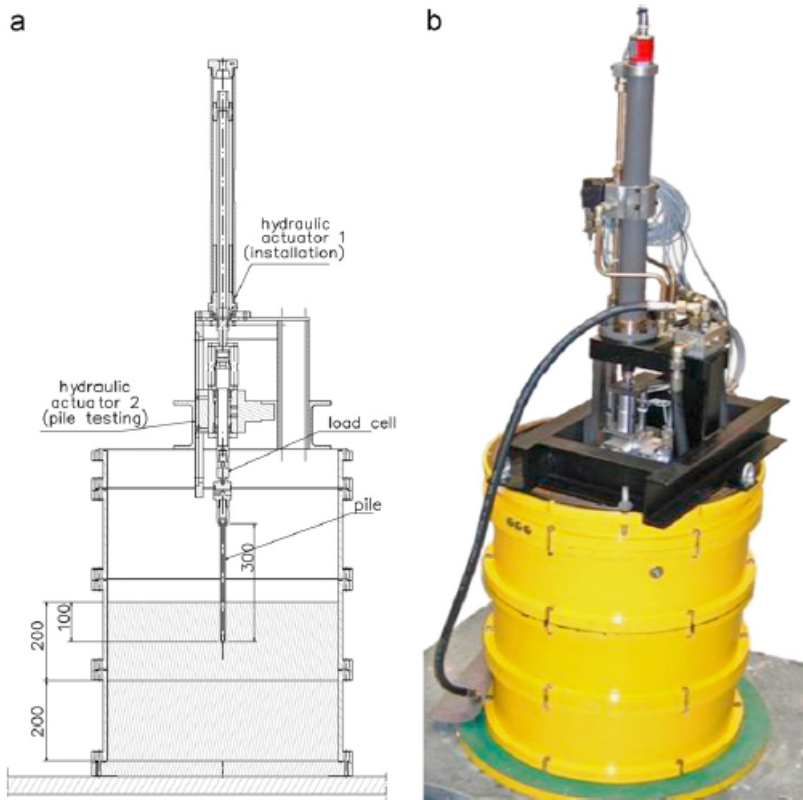
Figure 5.1: Test set up of the centrifuge test ([13]): schematic view (left) and test equipment (right).

Sample preparation

The sand samples with a homogenous sand body at a pre-determined density were prepared following the method of van der Poel and Schenkeveld [16]. The container was first filled with de-aerated water and the pre-determined amount of wet sand was pluviated under the water surface. A very loose sand sample was created. A loaded permeable plate was placed on the surface of the sand sample. The container was lifted a few centimeters above the floor and released. The loose sand sample was then compacted by shock waves to achieve the predetermined relative density. It is possible to prepare a soil sample with a predefined relative density within $1 - 2\%$ accuracy by using this preparation method. In the samples, a viscous fluid was used instead of water to fulfill the scaling rule. In particular the permeability, it was necessary to choose a pore fluid with a viscosity much higher than of water. The saturated water in the prepared sand sample above was replaced by the viscous fluid by using the method of Allard and Schenkeveld[17]. The viscous fluid was first slowly positioned above the saturated sand sample. A vacuum at the bottom of the container was used to extract the water, therefore the viscous fluid penetrated into the sand sample.

Pile installation

During preparation at normal gravity ($1\,g$), the pile was initially embedded at 10 times its diameter ($10D$) below the sand surface. The installation of the model pile started after the centrifuge had been accelerated to a level of $40\,g$. During this installation phase, the pile was installed in-flight to a final depth of $20D$ with a velocity of 1.67×10^{-4} m/s. After the installation phase, a series of static load tests (SLT) was performed to determine the pile capacity with a velocity of 1.67×10^{-6} m/s and an additional displacement of $0.1D$.

The pre-embedment of $10D$ was chosen for practical reasons relating to the test set-up. Earlier centrifuge research ([15]) has shown that after $10D$ penetration, a steady state is achieved in terms of the stress and the deformation field around the pile toe. The pile may therefore be seen as a soil displacement pile in terms of pile toe behaviour.

During each test the following variables were measured: displacement of the pile, the force at the head and the toe of the pile, the pore fluid pressure at the pile toe and the pressure in the four buried transducers.

5.3. Numerical model

The numerical simulations are done with a geometry prototype scale. The detailed geometry of the numerical model is shown in Figure 5.2. The right side boundary is at a distance of $26D$ from the pile center, which is identical to the size of the sample container in the centrifuge experiment. The right side boundary is fixed in the normal direction and free in the other directions. The bottom boundary is fully fixed.

The pile is modelled as a rigid body penetrated into the soil. The shape of the pile tip is flat which is identical to the pile in the centrifuge test. However, the edge of the pile tip in the simulation is slightly curved to avoid numerical difficulties due to locking (Figure 6.3). Additionally, the moving mesh concept (section 3.4.4) is adopted in all simulations.

The simulations are done with one –phase (drained) material behaviour since no change in pore pressure was recorded in the centrifuge tests during the installation process and static load test due to the low applied loading rates.

A contact algorithm (section 3.4.3) is used to model the frictional contact between the pile and the soil. The friction angle of sand against polished steel of the model pile is chosen around $10°$ as suggested by Murray and Geddes [18]. The mobilized wall friction angle may be different along the mantle due to varying stress level. However, for simplification reasons a constant wall friction coefficient along the pile is assumed (e.g. [19, 20]). The chosen value of wall friction coefficient for all simulations in this study is assumed based on the characteristics of a polished steel pile surface, which is $mu = \tan \varphi = 0.194$. The influence of mu on the load-displacement curve is investigated and shown that the value of mu plays an important role on the evolution of total pile shaft force rather than the evolution of total pile tip force (Appendix D.2).

For the simulations in this work, an implementation of MPM is applied in which 4-noded tetrahedral elements with linear interpolation of displacements are used.
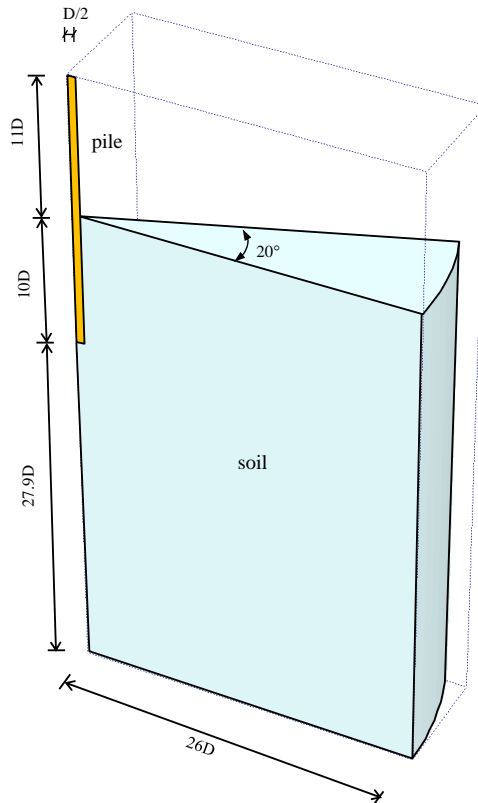
Figure 5.2: Geometry of considered problem

The finite element mesh for the problem is shown in Figure 6.3. This mesh has a total of $26,826$ tetrahedral elements including the initially inactive elements, with a total $152,020$ of material points. The mesh is refined near the pile. The inactive elements above the soil surface may be activated during the calculation process as material points are entering. Although the considered problem is axisymmetric, the simulations are three dimensional due to the nature of the MPM implementation. A $20°$ section of the axisymmetric problem is considered for discretization. It was determined that elements of the background mesh near the vertical axis with an angle smaller than $20°$ could generate numerical inaccuracies due to the extreme aspect ratios.

The stresses in the soil are initiated using the so-called K_0-procedure. The pile which is initially embedded at $10D$ below the soil surface is installed into the soil by $10D$ with a velocity of 0.02 m/s. The penetration of the pile into the soil is modelled by applying a prescribed velocity on the top of the pile. A relaxation phase follows the installation phase. During the relaxation phase, the pile is slowly unloaded until the pile head force becomes zero. Finally, a static load test (SLT) is performed with a velocity of 0.002 m/s. The velocity values used in the numerical analyses is higher than the values used in the centrifuge test to optimize the calculation time. It has
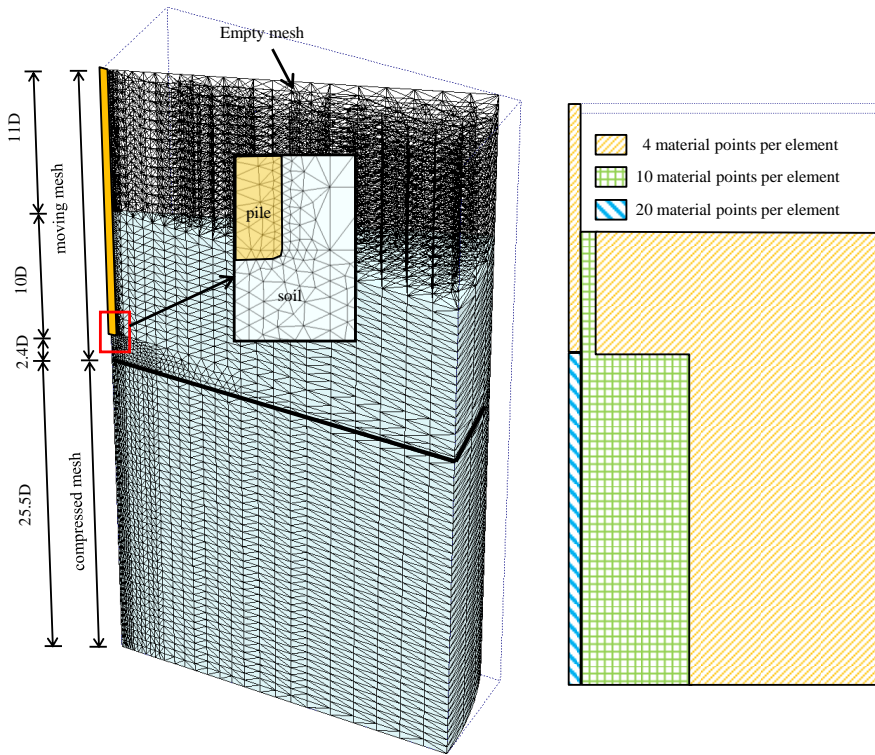
Figure 5.3: Mesh discretization and the distribution of material point method used for numerical analysis with MPM

been confirmed in a parametric study that the velocity used does not significantly influencing the results (Appendix D.1).

The evolution of shear bands in granular bodies is strongly related to the micro –properties of the material. Shear band thickness is influenced by the soil grain size which cannot be modelled properly with the current continuum model. In order to properly describe the behaviour of granular materials with shear localization, MPM may need regularization by using e.g. micro –polar or non –local terms, which is out of the scope of this study.

5.4. Soil model

During the installation process the soil around the pile tip is exposed to (very) high stress levels. According to the centrifuge results, the maximum stress at the pile tip near the end of the installation process is about 8.5 MPa for medium dense sand and 5.5 MPa for loose sand (Figure 5.4). Therefore, the constitutive model used for the numerical simulations must be able to account for an appropriate soil response over a wide range of stress levels.
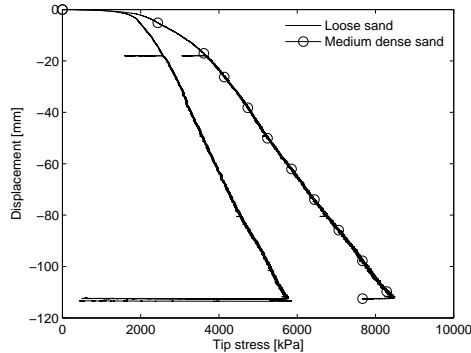
Figure 5.4: Change of stress under the pile tip during installation

5.4.1. Mohr Coulomb model

The value of friction angle and dilation angle with increasing stress level is calculated based on empirical formulas in section 4.2.3 and plotted in Figure 5.5 for both medium dense sand (black line) and loose sand (red line). The horizontal axis shows the range of stress change and the vertical axis shows the corresponding value of friction angel (Figure 5.5a) and dilation angle (Figure 5.5b) at particular stress level. According to that, at a stress level of 8.5 MPa (stress measured under the pile tip for medium dense sand near the end of installation), the maximum friction angle is determined around $30°$ and the dilation angle is slightly negative (around $-4°$). The same value of friction angle and dilation angle is obtained for loose sand at stress level of 5.5 MPa (stress measured under the pile tip for loose sand near the end of installation). These values are significantly lower than the values of friction angle ($37°$) and dilation angle ($12°$) obtained from the triaxial tests at 200 kPa. It is decided to use the same low values for the friction angle ϕ and dilation angle ψ in Mohr-Coulomb model for both medium dense and loose sand to account for the high stress level under the pile tip. Then, the difference between those two sands is only the value of stiffness parameter E. Stiffness increased with depth is used. In this MPM code, it is possible to increase the shear stiffness G (related to the normal stiffness E through Poisson's ratio using elasticity theory $E = 2G(1 + \nu)$ with depth. The increase of shear stiffness with depth takes the form: $G = G0 + Factor * Depth$ (depth from specified soil surface). Where G_0 is the shear stiffness at a reference level (model surface in this case $G_0 = 0$). The stiffness parameter at the bottom of the soil model is estimated based on the correlation $E = 60R_D$ [MPa] proposed by Lengkeek [21].

The material parameters for the Mohr-Coulomb model are summarized in Table 5.2. Such approach of using critical angle of friction φ_c to calculate pile bearing capacity was previously pointed out in literature. For example, Randolph et al. [22] used φ_c in predicting the end bearing capacity of driven pile in sand. [23] found in his FLAC analyses that the angle of friction at any point around the deep pile is not greater than φ_c even in dense sand. The influence of Mohr-Coulomb parameters, E, φ and ψ on the penetration process is examined and reported in appendix D.3. The higher value of soil stiffness or strength parameter, the higher capacity of the
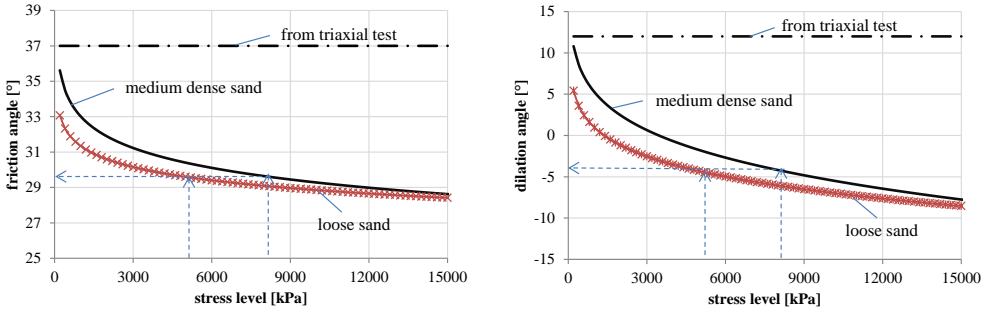
Figure 5.5: Calculated friction and dilation angle used in Mohr-Coulomb model for both medium and loose sand to simulate the pile installation according to Bolton.

Table 5.2: Mohr-Coulomb material parameters for medium dense and loose sand used in the MPM simulations.

Sand	R_D	E [kPa]	ϕ	ψ	c [kPa]	ν
Medium dense	0.54	32400	30°	0°	1.0	0.3
Loose	0.36	21000	30°	0°	1.0	0.3

Table 5.3: Hypoplastic parameters for Baskarp sand (Anaraki, 2008).

Parameter	ϕ_c	h_s [MPa]	n	e_{d0}	e_{c0}	e_{i0}	α	β
Baskarp sand	31°	4000	0.42	0.548	0.929	1.08	0.12	0.96

pile is obtained.

5.4.2. Hypoplastic model

The hypoplastic model as implemented in the MPM code used in this study is based on the formulation of Von Wolffersdorff [5]. This hypoplastic constitutive relationship requires eight basic parameters: granular stiffness h_s, critical friction angle ϕ_c, critical void ratio at zero pressure e_{c0}, minimum and maximum void ratio at zero pressure e_{d0} and e_{i0}, and the constants n, α and β. Anaraki [24] performed experiments on Baskarp sand to determine its hypoplastic material properties which are summarised in Table 5.6. Several simulations of triaxial test were done on both loose and dense sand to validate the hypoplastic parameter set in Table 5.6. Detailed results are shown in Appendix C. Based on the validation with the laboratory tests, the parameter value suggested by Anaraki [24] are reasonable to use for simulation with pressure range from 50 to 200 kPa. However for simulations with high pressure level, it is suggested (Appendix C) to use a lower value of the parameter h_s for loose sand, which is 2 GPa instead of 4 GPa.

As well known in section 4.3, in order to avoid overestimation of the pile base capacity, the dependency of α on high stress level during installation will be considered. In the triaxial compression test, as the cell pressure increase from 200 kPa to 10000 kPa, the value of α shows a significant reduction from 0.12 to -0.03 for medium dense sand and -0.06 for loose sand (Figure 5.7). Therefore, in this chapter, a reduction of α from 0.12 to 0.02 is assumed in all the simulations.
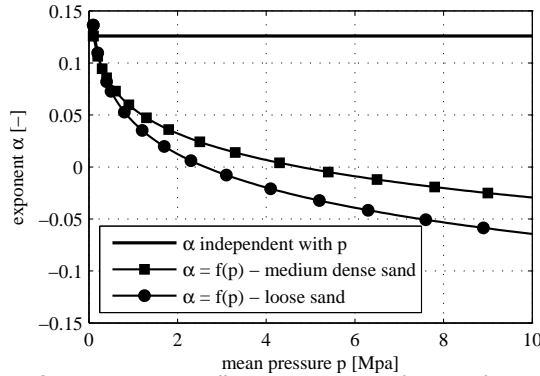
Figure 5.6: Dependency of exponent α on cell pressure in triaxial respond
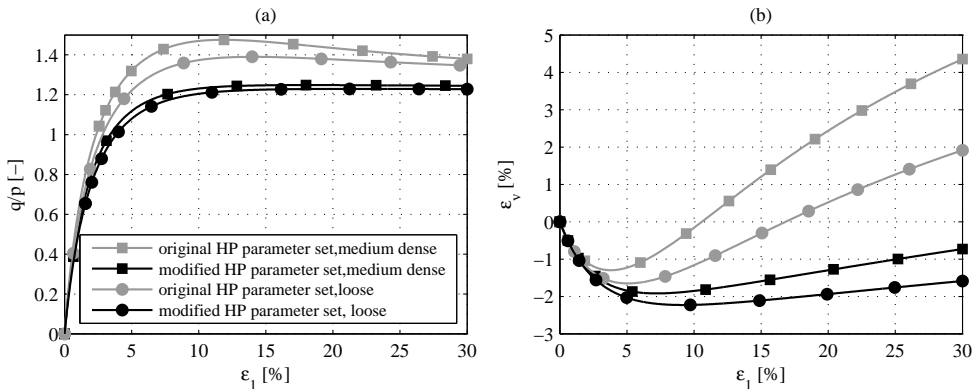
Figure 5.7: Comparison of triaxial element test simulations at 10 MPa on Baskarp sand using the modified hypoplastic parameter set ($\alpha_{modified} = 0.02$) with one using the original parameter set ($\alpha_{original} = 0.12$)

To include the effect of grain crushing, the dependency of void ratio on the stress level is considered according to Rohe [25]. Based on such relations, the maximum, minimum and critical void ratio input are calculated at a vertical stress level of 10 MPa and used for all simulations.

The final suggested hypoplastic parameter set for Baskarp sand in order to get a good response under high stress level in the pile installation simulations is given in Table 5.4. The comparison of triaxial behaviour at confining pressure of 10 MPa between modified and original hypoplastic parameter sets for Baskarp sand is shown in Figure 5.7. The modified parameter set clearly reduces the peak shear strength as well as dilation behaviour at high cell pressure. A parametric study on the influence of the hypoplastic parameters on the penetration analysis has been performed and reported in appendix D.4. Both total pile tip force and total pile shaft force are reduced with the reduction of h_s and n; whereas, the use of lower α only reduces the total pile tip force, but almost no influence on the total pile shaft force.

Parameter set for small strain stiffness in the hypoplastic model is tabulated in Table 5.5. The parameters are determined based on Appendix C.3.

As a conclusion, the standard or original hypoplastic model parameters are not

Table 5.4: Modified parameters for the Hypoplastic model of Baskarp sand used to model centrifuge test

Parameter	ϕ_c	h_s [MPa]	n	e_{d0}	e_{c0}	e_{i0}	α	β
original HP	31°	4000	0.42	0.548	0.929	1.08	0.12	0.96
modified HP$_{\text{medium dense}}$	30°	4000	0.42	0.51	0.88	1.01	0.02	0.96
modified HP$_{\text{loose}}$	30°	2000	0.42	0.51	0.88	1.01	0.02	0.96

Table 5.5: Small strain stiffness parameters of Baskarp sand used in jacking pile simulation

m_R	m_T	R_{max}	β_R	χ
5	2	$1e-4$	1	1

suited for pressures larger than approximately 1 MPa. Furthermore, for extremely high pressures, the soil below the pile is not a granular body anymore due to the breakage of grains. Nevertheless, the hypoplastic constitutive model is able to predict the soil response at high pressures if its parameters are adapted according to the changing of stress level from low to high. The constitutive hypoplastic model in this chapter is improved to account for grain crushing by two difference approaches. Firstly, in section 5.5, the adapted values for $\alpha = 0.02$ which are based on the average stress level during installation is chosen for both medium dense and loose sand. The relevant parameter α is calibrated using high pressure triaxial test results. With such adapted values for α, the effects of grain crushing are accounted for, which significantly helps to improve the constitutive behaviour. Secondly, in section 5.6, the modified hypoplastic model proposed in Chapter 4 is used to model the centrifuge test. This modified hypoplastic model considers stress dependency during pile installation of five parameters $\alpha, \beta, e_i, e_c, e_d$ of the hypoplastic model.

5.5. Results
5.5.1. Load-displacement curve during pile installation
To compare the numerical results with the centrifuge test the evolution of the axial force on the pile head is investigated. In Figure 5.8, the simulation with the original hypoplastic model parameters significantly overestimates the pile head force compared to the experiment results. Simulations with the modified hypoplastic parameter set, using $\alpha = 0.02$, or with proposed Mohr-Coulomb parameters, show a better correspondence with the experiments. This again confirms the importance of taking into account the dependency of friction and dilation angles on the increase of the stress as explained in the previous section.

Figure 5.9 shows in detail the evolution of total pile shaft force, F_s and total pile tip force F_t for different densities and different constitutive model of soil. The curves F_s are nearly similar between medium dense sand and loose sand. Hence the density has no influence on the evolution of the total pile shaft in this case. This is because of the assumption that friction angle and dilatancy angle (in Mohr-Coulomb model) and α (in hypoplastic model) are the same for both medium dense and loose sand. The Mohr-Coulomb model is observed to result in two times higher F_s than the hypoplastic model. This may be due to the assumption of zero dilation in Mohr Coulomb model, then the soil is only compacted along the pile shaft, whereas a
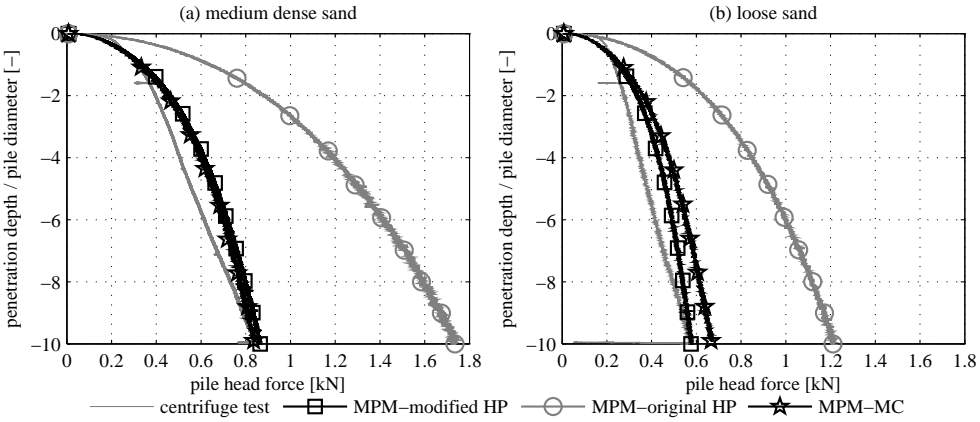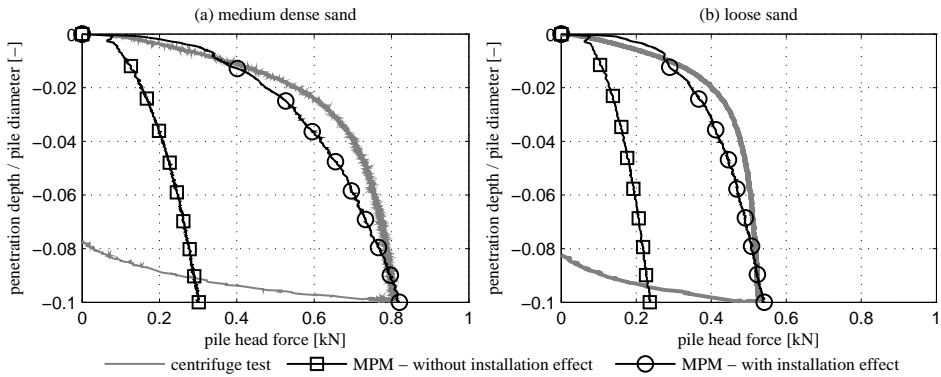
Figure 5.8: Load-displacement curve of the pile head during pile installation for a) medium dense sand ($e = 0.68$, $R_D = 54\%$) and b) loose sand ($e = 0.75$, $R_D = 36\%$). Comparison of centrifuge test results and MPM simulations using Mohr Coulomb model (MPM-MC) and hypoplastic model (MPM-original HP and MPM-modified HP).

5
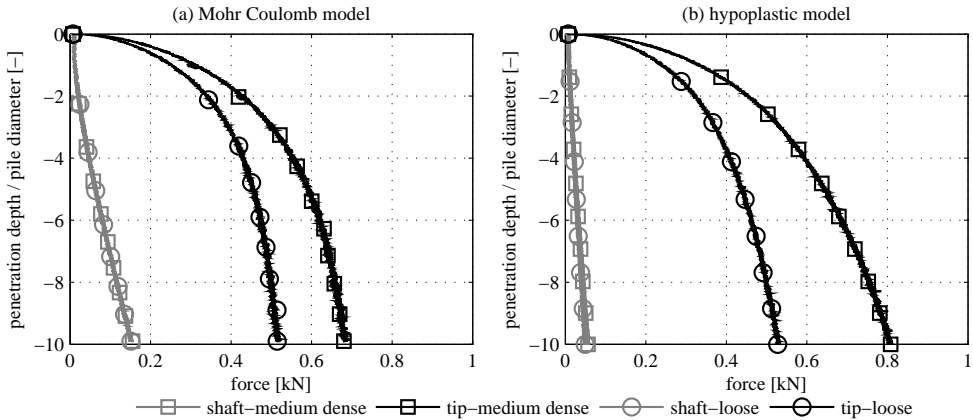
Figure 5.9: Total pile shaft and tip reaction curves obtained during installation for different densities. Comparison of Mohr Coulomb results and hypoplastic results.

loosening zone is observed along the pile shaft of hypoplastic model (section 5.5.4). The ratio between F_t/F_s in Mohr-Coulomb model is 2.7 for loose sand and 3.6 for medium dense sand. This ratio is about 2.5 times higher when using hypoplastic model. While, the centrifuge test gives values of F_t/F_s as 3.6 for loose sand and 4.3 for medium dense sand. Hence the measured ratio from the centrifuge test are in between the given ratios from Mohr-Coulomb model and hypoplastic model.

5.5.2. Load-displacement curve during static load test (SLT)

Validation with centrifuge SLT

After the pile has been installed to a depth of $20D$ and unloaded, a pile load test is carried out. During the unloading phase, the pile head is slowly pulled out at a prescribed velocity of 0.0001 m/s until the pile head force becomes nearly zero. The displacement of the pile head during this phase is less than 0.02D, which cor-
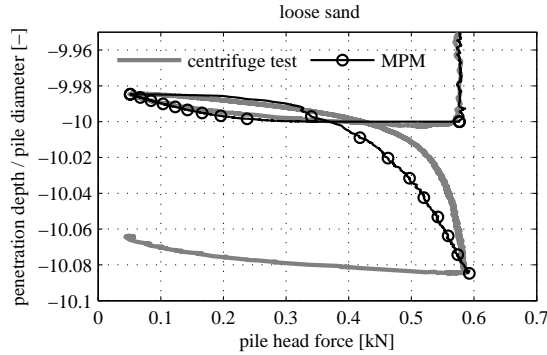
Figure 5.10: Load –displacement curve of the pile head during unloading and reloading phase for loose sand ($e_0 = 0.75$, $RD = 36\%$). Comparison of centrifuge test results and MPM simulations.

Figure 5.11: Load-displacement curve of the pile base during SLT for a) medium dense sand ($e = 0.68$, $R_D = 54\%$) and b) loose sand ($e = 0.75$, $R_D = 36\%$). Comparison of centrifuge test results and MPM simulations.

responds to the centrifuge test (Figure 5.10).

The load-displacement curves of the calculated SLT comparing with the centrifuge tests are plotted in Figure 5.11. It can be seen that the base bearing capacity in the simulation is in good agreement with the centrifuge test results. Although the stiffness of the load-displacement curves during SLT between the simulation and centrifuge test is slightly different, the capacity at $0.1D$ penetration is corresponding well, for both loose and medium dense sand.

Simulations in which the SLT has been performed immediately after the pile is pre-embedded (wished-in-place) $20D$ are also shown in Figure 5.11. Clearly, without considering installation effects the calculated bearing capacity of the pile is significantly lower than the test results. This emphasizes the importance of accounting for installation effects when simulating the SLT. These results could be compared with findings in the literature regarding the ratio between pile capacity of non-displacement and displacement piles. These ratios between the base capacities ranges from 0.18 for loose to 0.33 for dense sand according to a data base in Gavin et al. [26]. The ratios in Figure 5.11 are between 0.31 and 0.34 for the base capacity at a penetration of $10D$.
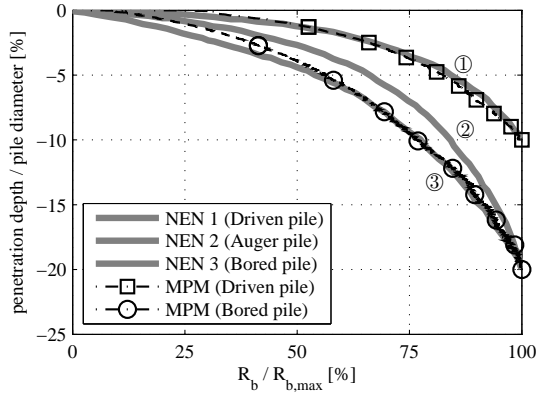
Figure 5.12: Comparing results of the design load test suggested by Dutch code (NEN $9997-2011$) with MPM simulations (R_b is effective stress of pile tip during SLT and $R_{b,max}$ is effective stress of pile tip after SLT).

Validation with Dutch code

The SLT results were compared with the prescribed load displacement curves in NEN $9997-2011$ [27], the Dutch application document of Eurocode 7 with additional requirements which is, to our knowledge, the only Eurocode adaptation that provides (dimensionless) numerical values for load displacements behaviour. The normalised plots given in Figure 5.12 show the relative stiffness of load-displacement curve response from the numerical simulations ($e_0 = 0.68$, $RD = 54\%$) in comparison with the design curves suggested by NEN $9997-2011$. For a reliable design using this code, the ultimate base capacity is determined at $0.1D$ displacement for a driven pile and at $0.2D$ displacement for a bored pile. The resulting normalised base resistance curve of the simulation of the displacement pile SLT is in good agreement with curve 1 for driven piles from the NEN $9997-2011$ code. This demonstrates the importance of including the pile installation in the simulation and using an advanced soil model e.g. hypoplastic model in modeling pile load tests. The curve that simulates the pre-embedded pile shows a good correspondence with the curve suggested by curve 3 for a bored pile in NEN $9997-2011$ code.

5.5.3. Stress state after pile installation

Figure 5.13 shows the comparison of the radial stress distribution after $10D$ penetration between simulation using the Mohr-Coulomb and hypoplastic model. After 10D penetration for both loose and medium dense sand, a significant increase of horizontal stresses due to pile installation is observed. The radial stresses are increased along the pile shaft and with a peak near the pile tip. Two cross sections AA' (close to the pile tip) and BB' (along the pile shaft) are investigated in detail for the change in radial stresses. The radial stresses after $10D$ penetration at a horizontal cross section AA' are plotted in Figure 5.14. Close to the pile, the initial radial stresses are increased by a factor of almost 75 for medium dense sand and a factor of 50 for loose sand. At a distance from the pile center larger than $10D$, no stress changes can be observed for either case.
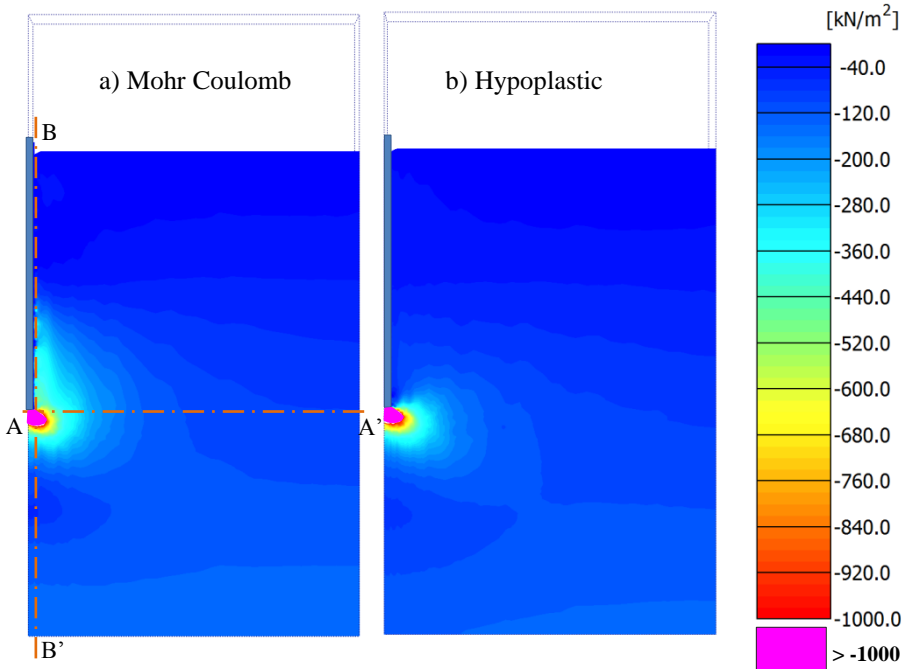
Figure 5.13: Radial stresses after 10D penetration for simulation using a) Mohr Coulomb model and b) hypoplastic model.

There are significant differences in the radial stress distribution in the vertical cross section BB' between the Mohr-Coulomb model and the hypoplastic model (Figure 5.13 and 5.15). It should be noted that, the position of the pile in figure 5.15 is initially at z/D of -10 and at z/D of -20 in the end of penetration process. The radial stresses along the pile shaft after $10D$ installation are 4 to 5 times the initial K_0 value in the case of Mohr-Coulomb model, whereas, only a factor of 1.5 to 2 is observed for the hypoplastic model. Below the pile tip, the horizontal stresses drop down to a value below the K_0 state for both cases. The observed change of radial stresses along a vertical cross section near the pile shaft is in good agreement with Mahutka [28]

5.5.4. Density change after installation

One of the benefits of the hypoplastic model over the Mohr Coulomb model is that it accounts for the change of density during the installation process. The final state of the void ratio after $10D$ penetration is shown in Figure 5.16. The significant densification of the soil around the pile after installation is observed for both medium dense and loose sand, excepting a small dilative zone near the end of the pile shaft and around the corner of the pile. The dilative zone may be explained due to the high shear strains in the soil surrounding the corner pile. Hence, the compaction of the soil close to the pile is superimposed by the shearing process while at a greater distance from the pile corner the compaction is dominant, which is in line with the findings of other researchers ([28]). In Figure 5.17, the distribution of void ratio
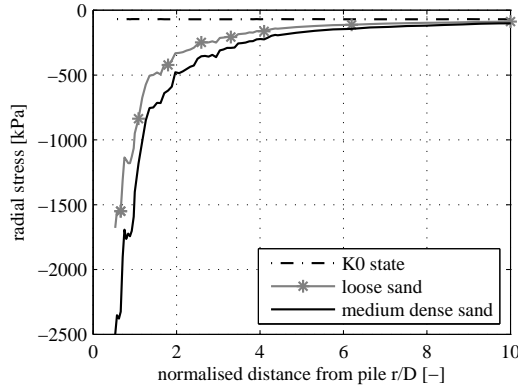
Figure 5.14: Radial stresses after $10D$ penetration at horizontal cross section AA' for medium dense and loose sand, hypoplastic model.
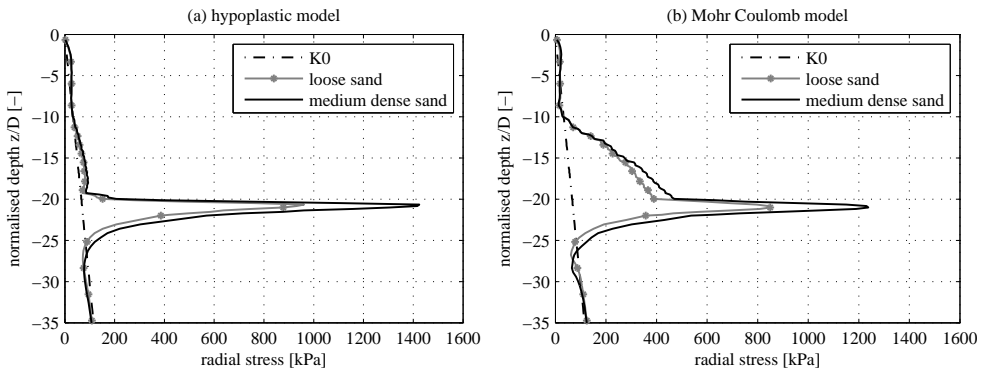
Figure 5.15: Radial stresses after $10D$ penetration at a vertical cross section BB' close to the pile shaft for medium dense and loose sand. MPM simulation with a) hypoplastic model, b) Mohr-Coulomb model

in vertical cross sections at different radial distances from the centre of the pile after $10D$ penetration can be seen for both medium dense sand (Figure 5.17a) and loose sand (Figure 5.17b). It can be seen that for medium dense sand at a distance of $0.5D$ which is next to the pile shaft, the void ratio increases due to dilation is observed almost along the pile shaft whereas, it is only seen in the corner of the pile in the case of loose sand. For both medium dense and loose sand, the lowest void ratio value is found just under the pile tip which is considered as the highest densification zone. The densification reduces gradually with the increasing distance from the pile. At a distance of $10D$ from the centre pile and $5-7D$ below the pile tip, no change in void ratio is observed.

Several horizontal cross sections at different depth $10D$, $15D$, $20D$ and $25D$ from the soil surface are also plotted in Figure 5.18 to obtain the distribution of void ratio after installation in horizontal direction. In general, the disturbance zone due to installation is extended to a distance of about $8D$ from the pile center and no change in void ratio at cross section $25D$ for both loose and medium dense sand. In loose sand, the soil around the pile is compacted for both cross section $10D$, $15D$ and $20D$, whereas, a small dilation is observed near the pile shaft in the case
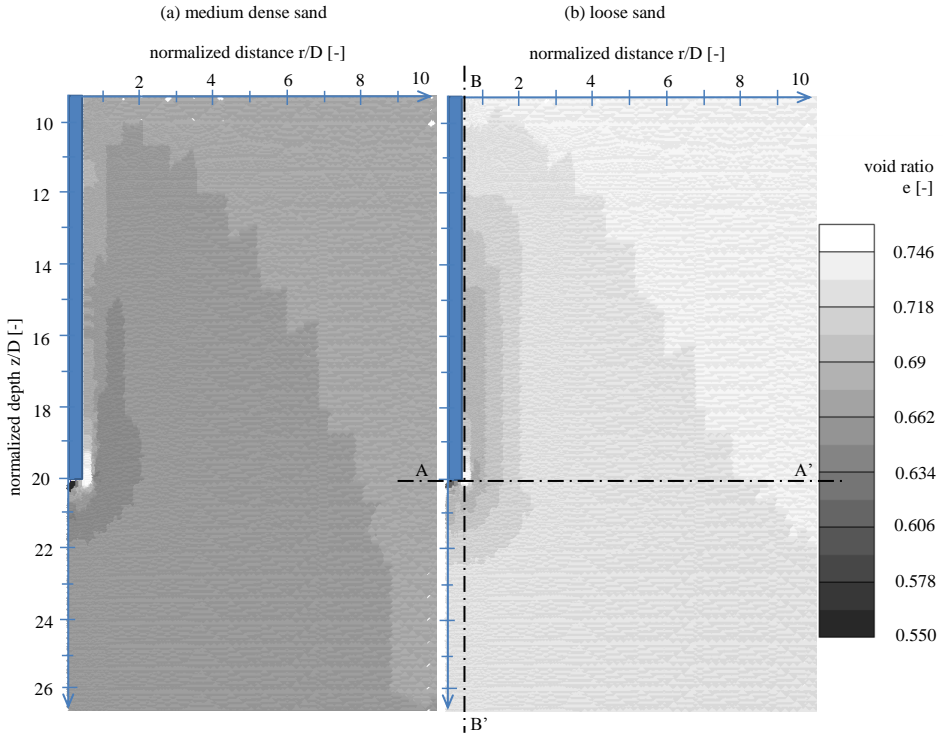
Figure 5.16: Void ratio change after $10D$ penetration. MPM simulation for a) medium dense sand ($e = 0.68$, $R_D = 54\%$) and b) loose sand ($e = 0.75$, $R_D = 36\%$).
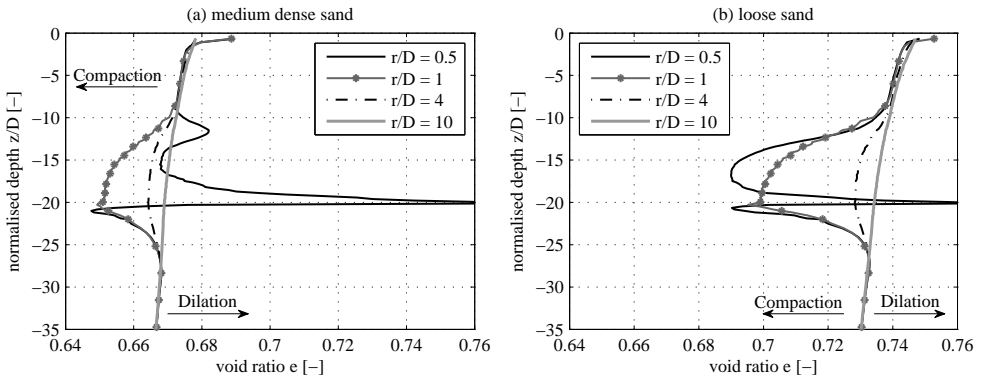
Figure 5.17: Void ratio distribution in vertical cross sections at different radial distances from the center of the pile after $10D$ penetration for a) medium dense sand ($e = 0.68$, $R_D = 54\%$) and b) loose sand ($e = 0.75$, $R_D = 36\%$).

of medium dense sand.

In conclusion, the results in density change after installation seem reasonable but that specific validation is not present, only the overall behaviour (in term of capacity) confirm the results.
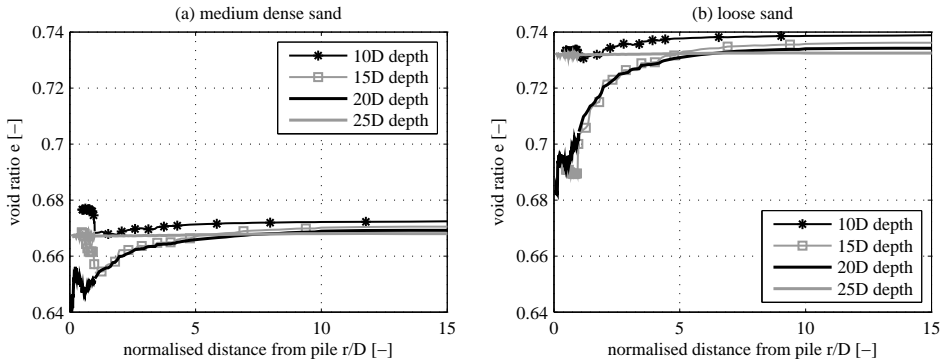
Figure 5.18: Void ratio distribution in horizontal cross sections at different depth after 10D penetration for a) medium dense sand ($e = 0.68$, $R_D = 54\%$) and b) loose sand ($e = 0.75$, $R_D = 36\%$).

5.5.5. Influence of pile tip shape

In this section, the influence of pile tip shape on the installation effect is examined. The flat pile tip used above is compared with the triangular pile tip shape in which the transition from the shaft to the tip is curved (Figure 5.19). Such a smooth shape of the tip is often used in simulation to avoid numerical difficulties due to locking (e.g. [20, 28, 29]).

Displacement of soil around the pile tip:

Figure 5.20 illustrates the differences in calculated horizontal displacement and vertical displacement between flat and triangular pile tip shape after $10D$ pile installation. Under the flat pile tip, the zone ABC has no horizontal displacement and is mainly moving down with the same displacement of the pile. Such a zone is quite similar with the 'nose cone' observation of White et al. [30]. The 'nose cone', which was referred to a highly compressed region below the pile tip, had a central core that is stationary relative to the pile tip. They also observed the soil sliding out from the nose cone and flowing around the shaft of the pile. In contrast, there is no 'nose cone' formed under the triangular pile tip. The vertical displacement of
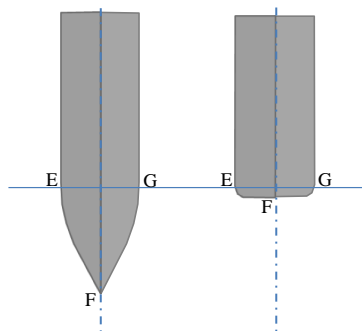
Figure 5.19: Triangular pile tip (left) and flat pile tip (right).
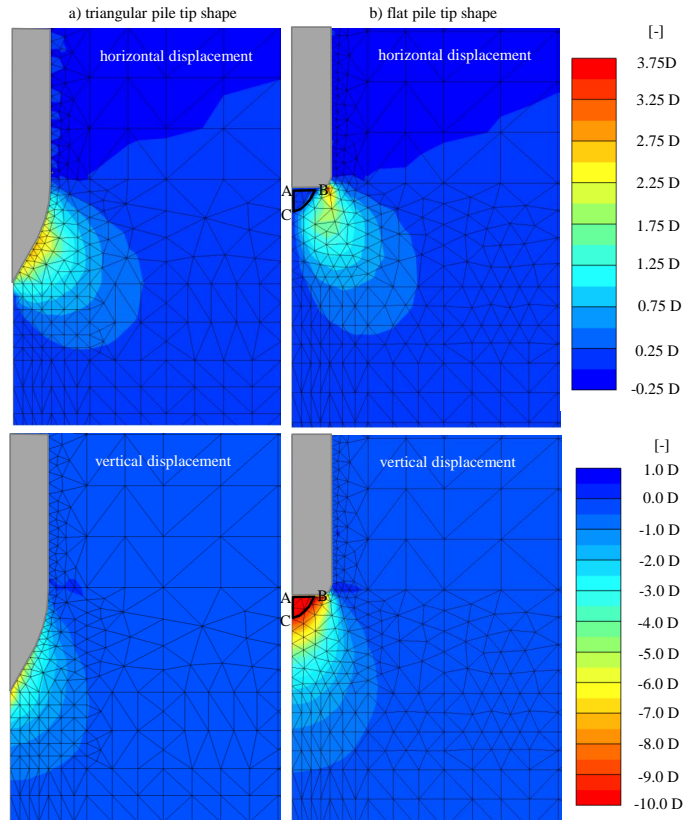
Figure 5.20: Displacement of soil around the pile tip after $10D$ penetration (simulation with loose sand and hypoplastic model).

the soil under the triangular pile tip is much less than the soil under flat pile tip, amounting to about half the displacement of the pile. However, the soil is pushed aside more significantly in the case of triangular pile tip.

Stresses of the soil around the pile tip

The comparison in horizontal and vertical stresses for different pile tip shape is shown in Figure 5.21 The flat pile tip generates very high vertical stress underneath it, which is three times larger than the vertical stress under triangular pile tip. It is clearly reasonable due to a highly densified 'nose cone' formed under flat pile tip. With such high vertical stresses, the flat pile tip results in 25% higher total pile tip force at the end of installation (Figure 5.22a). As the pile shaft forces are nearly the same in both cases (Figure 5.22b), then consequently flat pile tip gives larger bearing capacity than in the case of triangular pile tip. Noted that, the total pile tip force is the sum of vertical nodal forces at all nodes along the curve EFG in Figure 5.19.
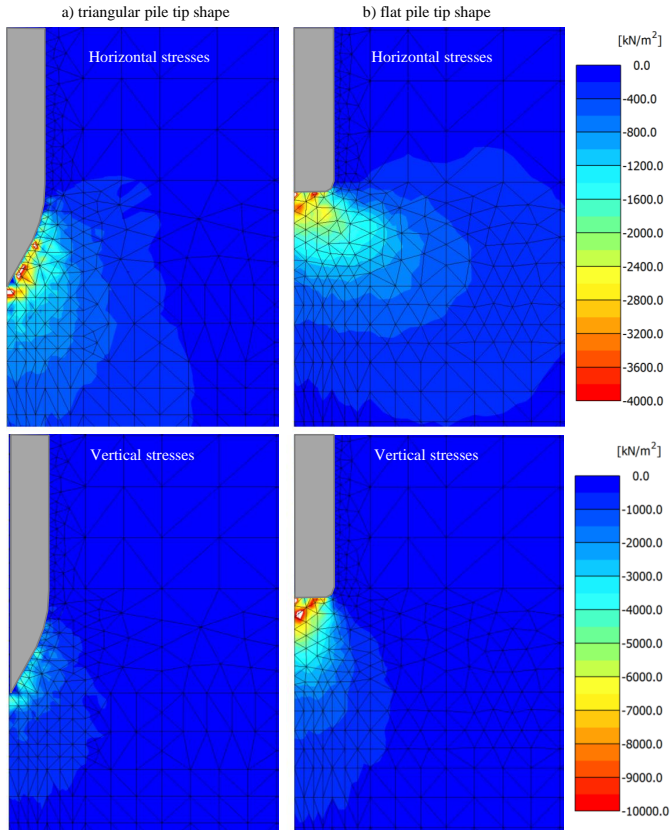
Figure 5.21: Vertical and horizontal stresses of soil around the pile tip after $10D$ penetration (simulation with loose sand and hypoplastic model).
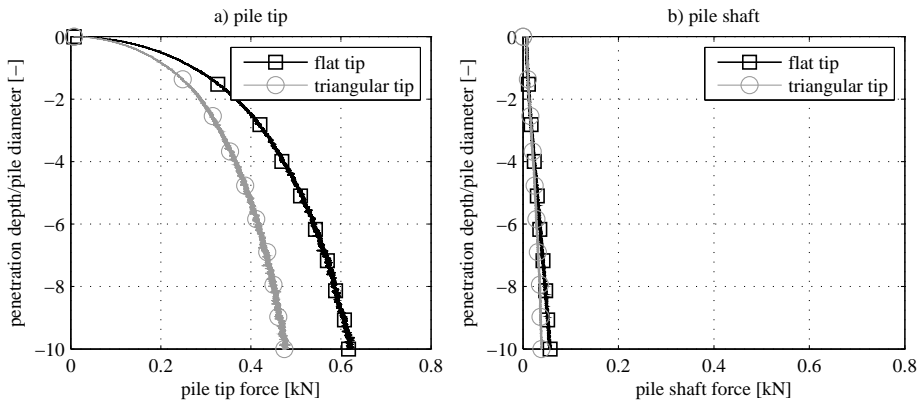
Figure 5.22: Comparison of load-displacement curve of the pile tip during installation between flat and triangular tip shape.
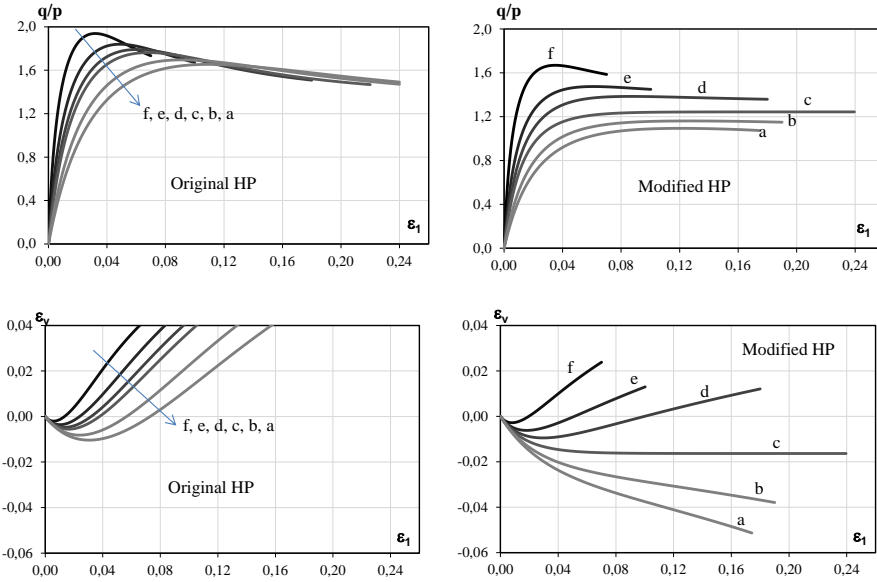
Figure 5.23: Triaxial response of Baskarp sand at elevated cell pressures: $a = 30MPa, b = 16MPa, c = 6MPa, d = 4MPa, e = 2MPa, f = 0.5MPa$. Comparison between original HP and modified HP model.

5.6. Application of the modified hypoplastic model

In this section, the proposed modified hypoplastic model for crushed sand (written in chapter 4) will be used to model the installation process of a jacked pile in sand and compare to the centrifuge results.

The modified hypoplastic model uses the same parameter set of original hypoplastic model and two new added physical parameters which are uniformity coefficient C_{u0} and mean grain size d_{50}. The hypoplastic parameters of Baskarp sand was used in the simulation is listed in Table 5.6. The dependency of parameters $\alpha, \beta, e_i, e_c, e_d$ on stress level is accounted itself inside the proposed modified model automatically. Figure 5.23 compares the triaxial response of Baskarp sand at elevated cell pressure from 0.5 MPa to 30 MPa between original HP and modified HP model. For all simulations using the original HP model, there is no contractive behaviour observed even at very high confining pressure. Moreover, the original HP model gives much higher value of the peak friction angle, especially at high stress levels compared to modified HP. Unfortunately, there is no available triaxial test data of Baskarp sand under high cell pressure level to validate the results given by modified HP.

With increasing stress around the pile tip during installation, the properties of the surrounding sand are significantly influenced as discussed in the previous chap-

Table 5.6: Hypoplastic parameters for Baskarp sand [24].

Parameter	φ_c	h_s [MPa]	n	e_{d0}	e_{c0}	e_{i0}	α	β	C_{u0}	$d_{50}[mm]$
Baskarp sand	30°	4000	0.42	0.548	0.929	1.08	0.12	0.96	1.60	0.13
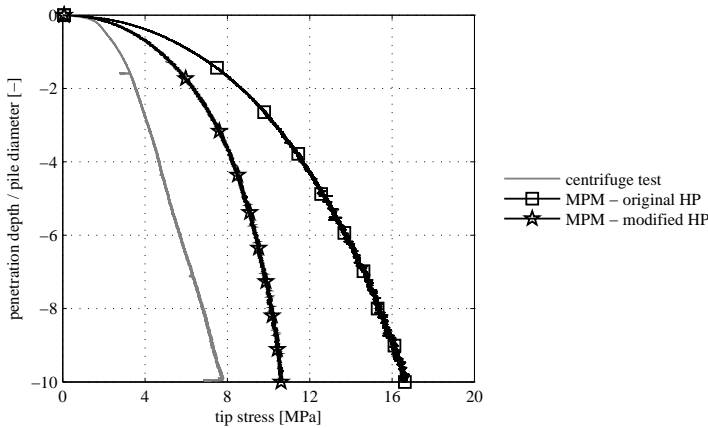
Figure 5.24: Evolution of stress under the pile tip during pile installation in medium dense sand ($R_D = 54\%$). Comparison of centrifuge test results and MPM simulation results using original and modified hypoplastic model.

ter, e.g. a change in grain size distribution or a high reduction in the peak strength and stiffness of soil due to grain crushing. Hence, the simulation with the original hypoplastic model parameters (black line with square markers in Figure 5.24) significantly overestimates the pile tip stress compared to the centrifuge results. The simulation with the modified hypoplastic model (black line with start markers in Figure 5.24) shows a better correspondence with the experiments. Therefore, taking into account grain crushing in the hypoplastic constitutive model can be considered as one of the important factors to successfully model the pile installation as well as predicting the pile bearing capacity.

This study only considers stress dependency of five parameters $\alpha, \beta, e_i, e_c, e_d$ of the hypoplastic model. However, parameters h_s, n and φ_c are most likely influenced by grain crushing and stress level as well [31]. Hence, further investigation should be carried out to improve the model, which may lead to a better correspondence with test data.

5.7. Comparison of Press-Replace Method and Material Point Method for Analysis of Jacked Piles

In this section, installation of jacked piles in sand is simulated using Press-Replace Method (PRM) and Material Point Method (MPM) and the results are compared together. PRM is a simple method based on small deformation theory, which has been solely for simulation of penetration problem such as pile jacking and cone penetration. The simplicity of PRM enables an engineer to model the installation process of jacked piles as a stage construction process by any finite element code. Such a comparison shows if the PRM can be relied upon for the analysis of jacked piles. It also reveals the differences that exist between PRM and MPM. This section is a part of the journal paper: Comparison of Press-Replace Method and Material Point Method for analysis of jacked piles in Computers and Geotechnics [3].

5.7.1. Press Replace Method

The PRM is a simplified approach based on standard finite element (FE) method for simulating boundary-value problems that involve penetration of an object into a continuum. PRM was first introduced by Andersen [32] for simulating the load-controlled penetration of a suction anchor in clay. Recently, Engin [33] successfully used the displacement-controlled PRM to simulate pile and cone penetration in a sandy soil. In PRM, the initial mesh is preserved, while the material properties of the penetrated volume are updated at the beginning of each phase resulting in a change of the global stiffness matrix without the need for updating the mesh. This makes the calculations faster than large-deformation analysis techniques [34]. Despite its advantages, PRM has its own limitations, too; most importantly, it is unable to model the flow of the soil below the pile base, and around peripheral zone of the penetrating pile.

Figure 5.25 illustrates three sequential phases. As shown in Figure 5.25, the penetration path is divided into several slices of thickness t_s. When the pile base (in gray color) is resting on top of slice i, the displacement-controlled axial loading of u_i, equal to the summation of previous displacement and an additional displacement increment, is applied on the pile head. The displacement increment is equal to the thickness of the soil slice t_s. Once the loading stage is completed, the soil material in slice i is replaced by the pile material. This process continues until the pile base reaches to the last slice on the penetration path. PRM is performed within the framework of the small-deformation theory (infinitesimal strain), in which the global stiffness matrix is always formed based on the original (undeformed) geometry of the soil-pile model. In other words, the global stiffness matrix only takes the updated material properties in the clusters (slices) that have switched to the pile material into account. It is noted that in the replace stage, a thin slice of soil is replaced by stiffer elastic material (pile). Therefore, there should be some compensation in the form of straining inside and near the zone that is replaced by the pile material. However, this straining is not achieved in PRM, which relies on small deformation theory, because the amount of the elastic energy is very small compared to the total energy that is spent in the system. The total spent energy is mostly dissipated due to plastic deformation. Therefore, this small compensation of straining is not required. Hence, by not incorporating this straining, the amount of the dissipated energy is slightly overestimated. More details about PRM can be found in [34].

5.7.2. Numerical model

Continuous jacking of a circular cross section pile, with the diameter $D = 0.3$ m, into uniform Baskarp sand is considered in this section. Figure 5.26 shows the problem studied. A thin elastic layer is considered on top of the sand layer to avoid numerical issues due to the tension developed at the surface of the sand layer during the installation process. Detailed finite element mesh, contact problem and soil model for both PRM and MPM are described in [3]
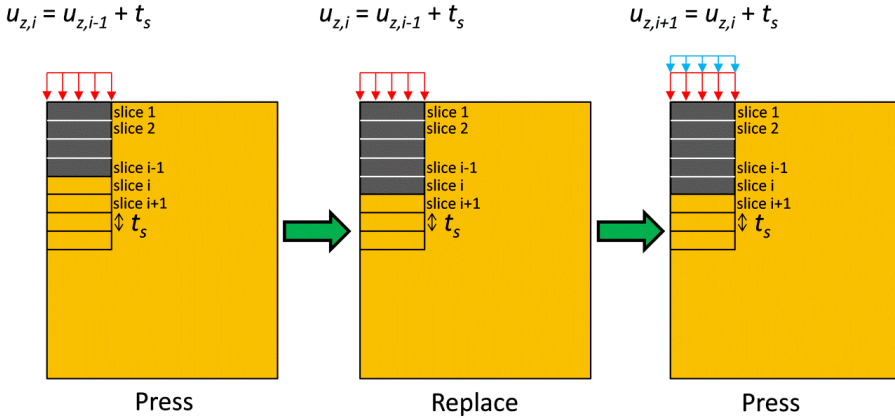
$$u_{z,i} = u_{z,i-1} + t_s \qquad u_{z,i} = u_{z,i-1} + t_s \qquad u_{z,i+1} = u_{z,i} + t_s$$
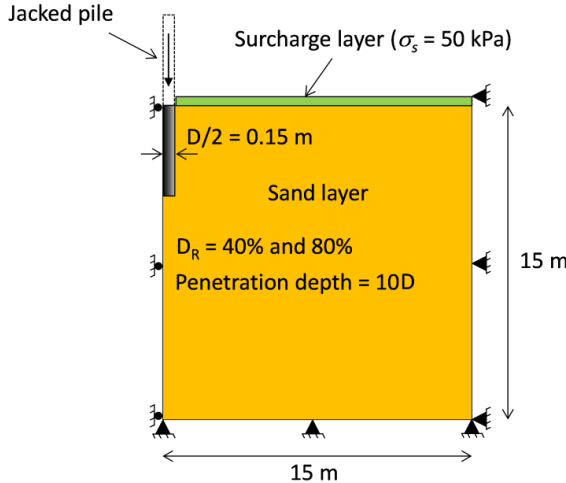

Figure 5.25: Press-Replace technique (after [31]).

Figure 5.26: Geometry and properties of the axisymmetric soil-pile model (after [3]).

5.7.3. Results

The pile was jacked down to $10D$ below the ground level. Figure 5.27 shows the total penetration (installation) resistance and the base resistance mobilized during the penetration for both PRM and MPM.

It is clear from Figure 5.27 that, in general, the total jacking force and the mobilized base resistance computed using PRM are in good agreement with those calculated using MPM. The total jacking force, which is equal to the summation of the base and shaft resistances, obtained from PRM is slightly higher (8% to 14%) than MPM; given that the base resistances from PRM and MPM are very close, it is clear that the shaft resistance obtained from PRM during the pile installation is greater than the one obtained from MPM.

To explore the effect of interface friction at the pile base on the penetration resistance calculated using PRM, an additional analysis with the base interface friction angle of 30° was performed for the dense sand, which is labeled PRM* in Figure
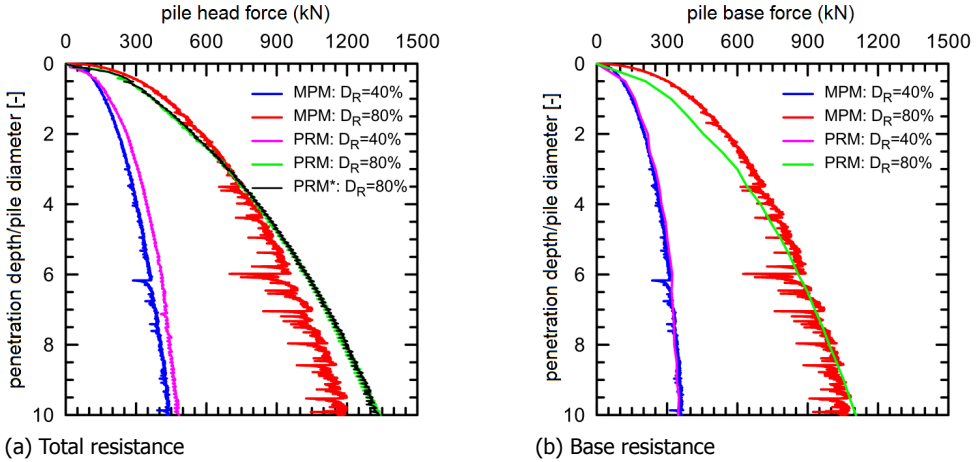
(a) Total resistance

(b) Base resistance

Figure 5.27: Penetration resistance during the pile installation (after [3]).

5.27. It is shown in Figure 5.27(a) that altering the base interface friction angle from 27.5° to 30° has an immaterial effect on the penetration resistance (the associated plots overlap each other), which warrants the use of one interface friction angle at the pile-soil interface for all analyses presented in this paper.

It is shown in Figure 5.28 that as the soil becomes denser the soil extent that undergoes the same radial displacement becomes greater in PRM than in MPM. Figure 5.29 shows that the same observation made for the radial displacement holds for the vertical displacement, too. However, it is shown that in MPM simulation the maximum vertical displacement right below the pile base is greater than PRM. As shown in Figure 5.30, a greater part of the domain of the loose sand undergoes compaction ($e < e_0$) in PRM analysis than in MPM analysis. For the dense sand, both methods show clear soil dilation next to the pile shaft ($e > e_0$), with PRM resulting in more dilation right next to the pile shaft than MPM. This difference between MPM and PRM is the major reason behind predicting higher installation shaft resistance by PRM, compared to MPM. Noted that in Figure 5.30, the PRM results seem 'smoother' than MPM results because MPM results were plotted from raw particle data without any smoothing function, whereas the post processing used in PRM is much more advanced.

Figure 5.31 and Figure 5.32 show the similarity of the radial, vertical stresses around the pile base in PRM and MPM. This explains the similar base resistances observed in Figure 5.27(a).

Once the installation is complete, the pile is unloaded. Then, a numerical static load test (SLT) is performed where a displacement-controlled loading is applied to the pile head until the pile head vertical displacement reaches $0.2D$. Figure 5.33 shows the load-settlement response of SLTs in the loose and dense sands. As shown in Figure 5.33, the load settlement responses obtained from PRM and MPM are in good agreement for the piles installed in the loose sand, while for the piles installed in the dense sand the load predicted by PRM for $0.2D$ pile head settlement in the dense sand is about 9% higher than the MPM. The shaft resistance calculated using
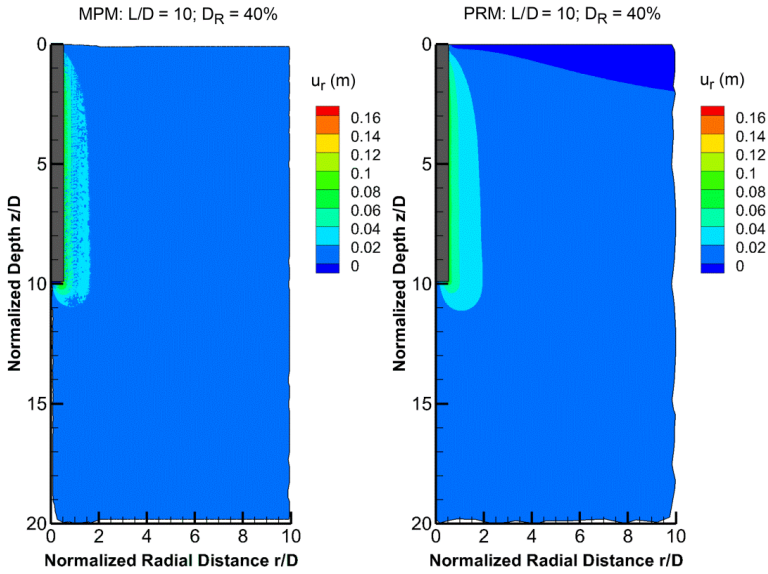
(a) MPM in the loose sand

(b) PRM in the loose sand
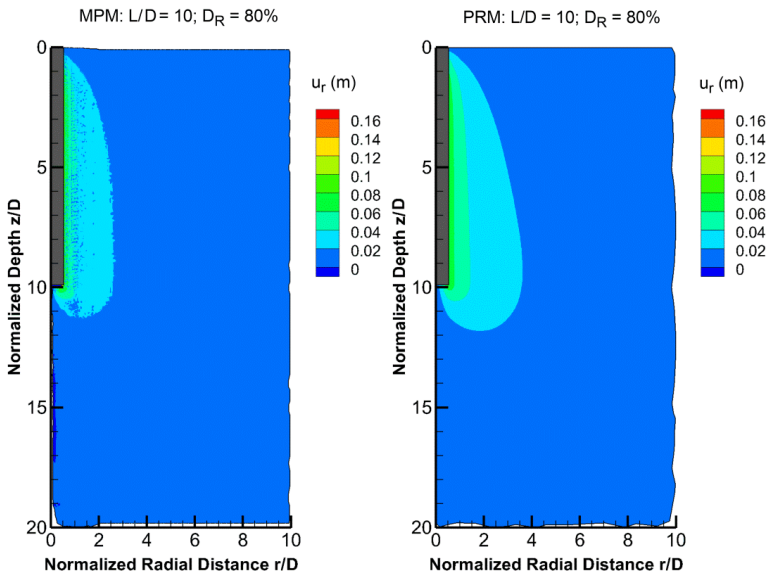
(c) MPM in the dense sand

(d) PRM in the dense sand

Figure 5.28: Radial displacement after $10D$ pile penetration (after [3]).

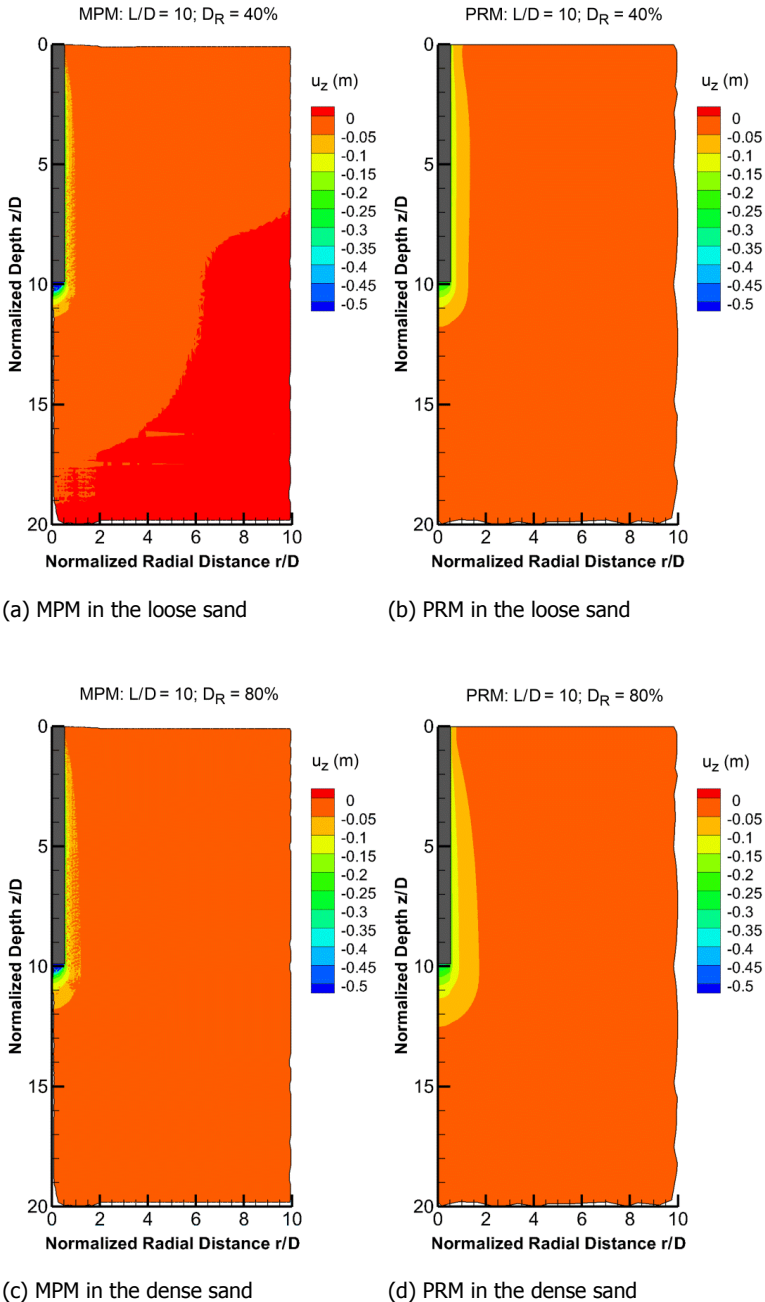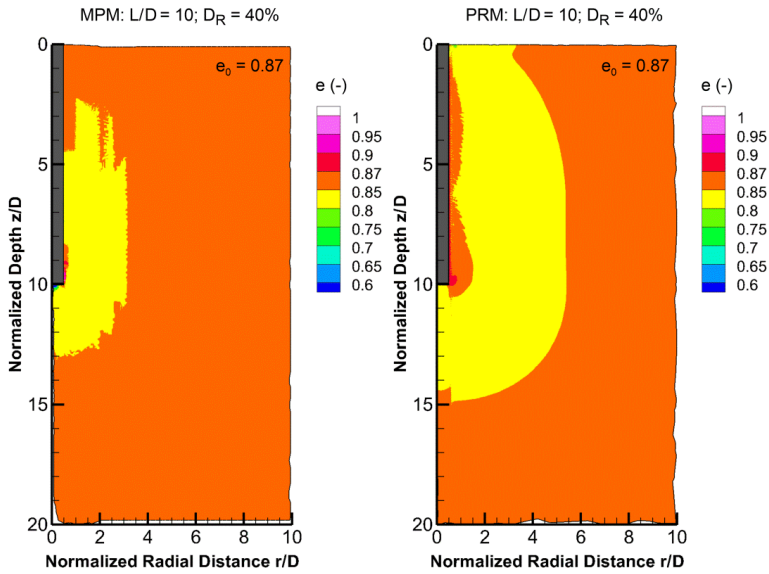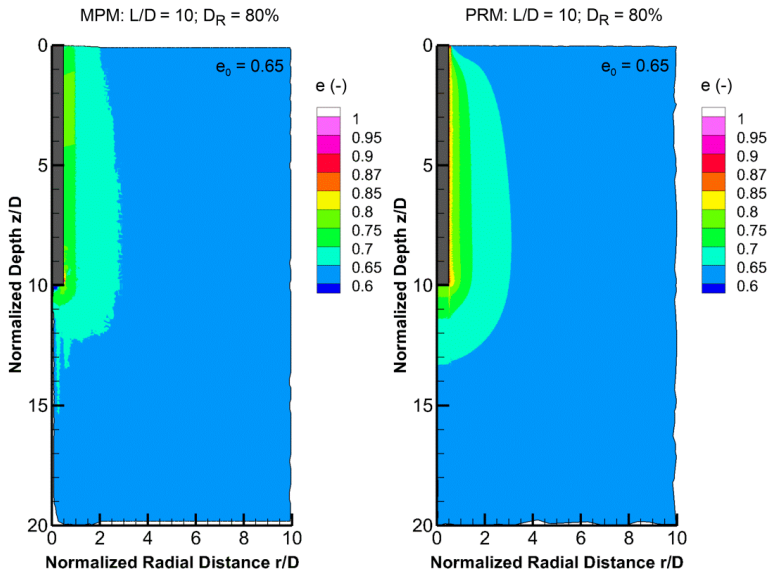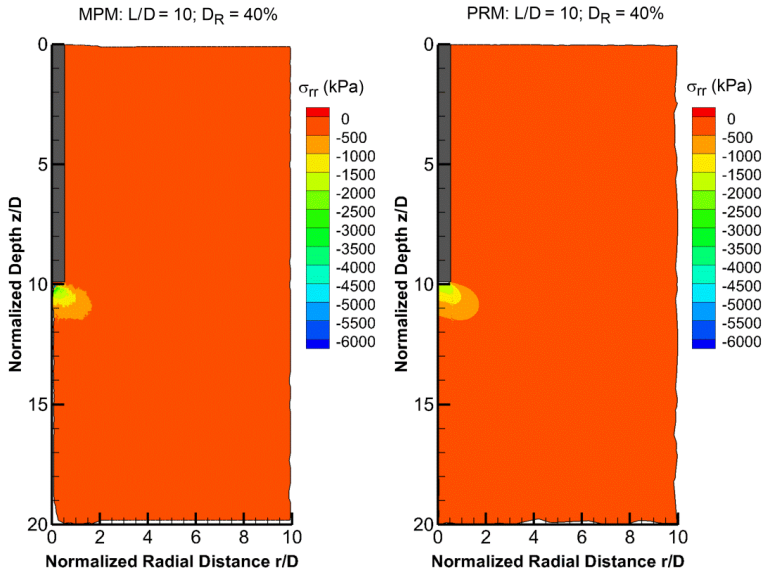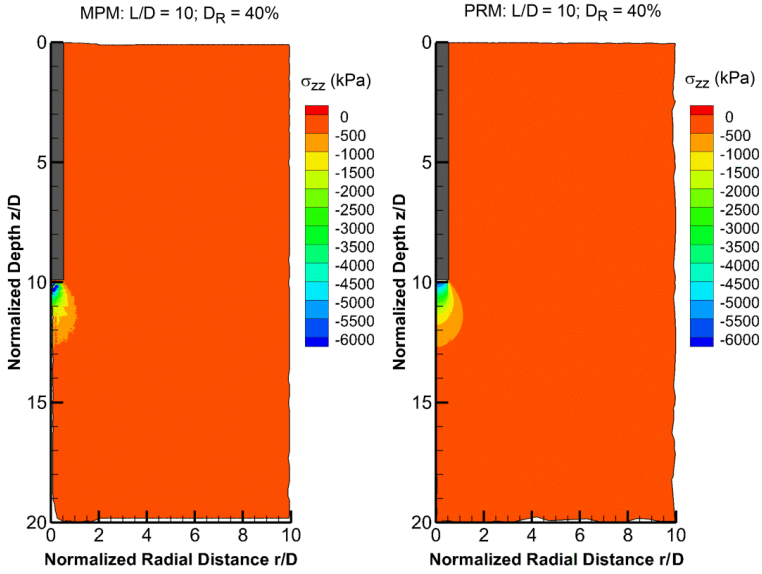PRM is greater than MPM and the base resistance calculated using PRM is lower

(a) MPM in the loose sand

(b) PRM in the loose sand

(c) MPM in the dense sand

(d) PRM in the dense sand

Figure 5.29: Vertical displacement after 10B pile penetration (after [3]).

(a) MPM in the loose sand   (b) PRM in the loose sand

(c) MPM in the dense sand   (d) PRM in the dense sand

Figure 5.30: Void ratio after $10D$ pile penetration (after [3]).

(a) MPM in the loose sand

(b) PRM in the loose sand
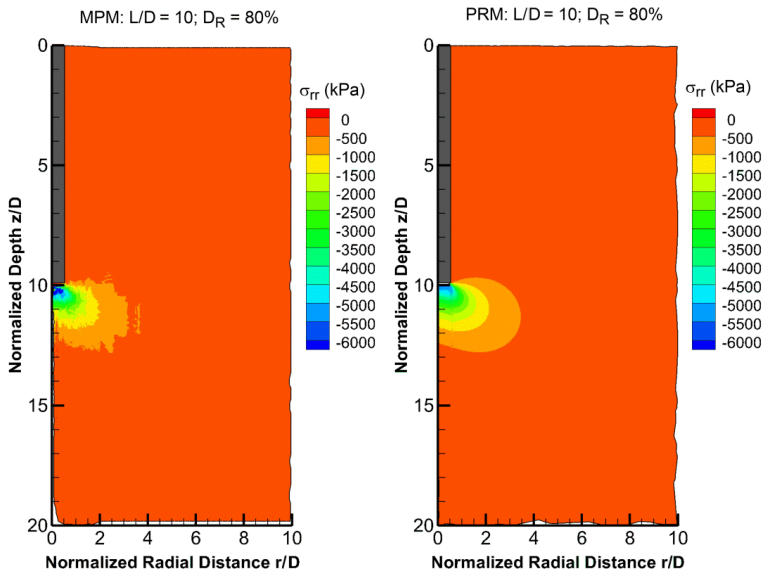
(c) MPM in the dense sand

(d) PRM in the dense sand

Figure 5.31: Radial stress after $10D$ pile penetration (after [3]).

(a) MPM in the loose sand

(b) PRM in the loose sand
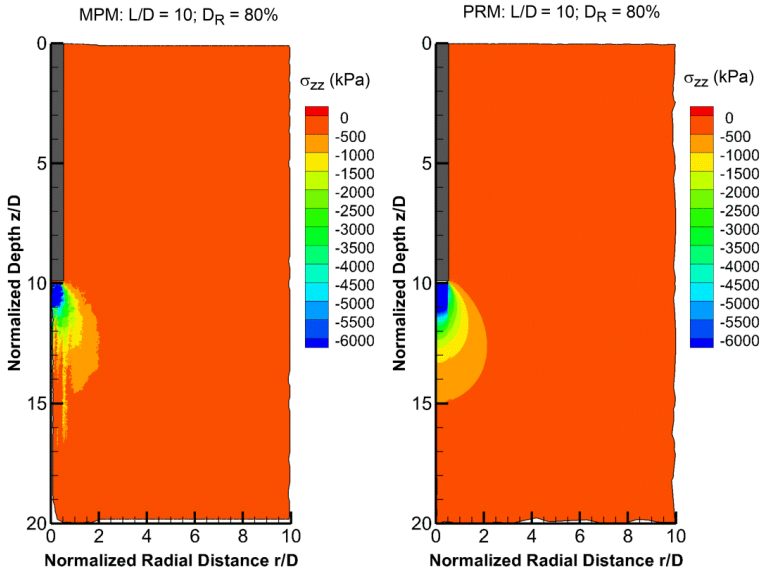
(c) MPM in the dense sand

(d) PRM in the dense sand

Figure 5.32: Vertical stress after 10D pile penetration (after [3]).

(a) Total resistance   (b) Shaft resistance   (c) Base resistance
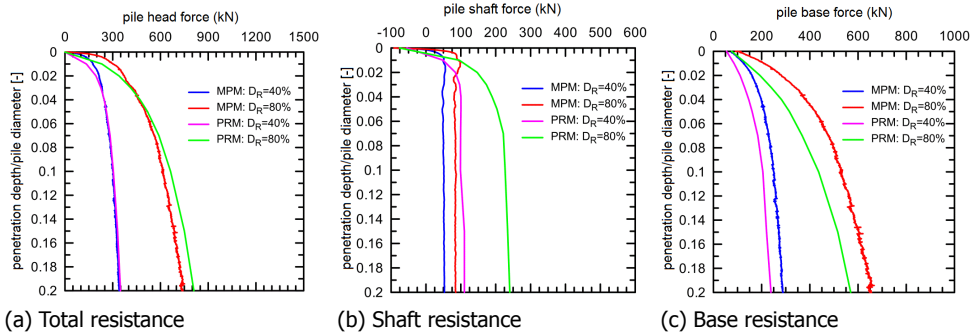
Figure 5.33: Soil resistance during the numerical static load tests (after [3]).

than MPM.

The difference in the shaft and base resistances of PRM and MPM can be attributed to the difference in the state of the soil at the very beginning of the static load tests. One of the parameters that quantifies the state of the soil in this study is the sand void ratio. Figure 5.34 shows the void ratio around the pile base ($2D$ below the pile base and $3D$ away radially from the pile centerline) in the loose and dense sands after unloading the pile at the end of pile installation. There is a clear compaction below the pile base in both loose and dense sands after pile unloading, whereas in PRM this soil compaction is not significant in the loose sand and there is no sign of soil compaction below the pile base in the dense sand. Therefore, it is reasonable to observe higher base resistance in the numerical SLT results of MPM than from those of PRM.

5.8. Conclusion

Several calculations were performed using the material point method (MPM) in order to model the installation process as well as the static load capacity of a jacked displacement pile in sand. The geometry and soil parameters of the simulations were chosen according to a centrifuge test in which the pile was installed in-flight during the test at $40\,g$. The results of the simulations are compared with the centrifuge experiments.

The outcome of the research implies the importance of considering installation effects in numerical simulations when calculating the pile capacity and load settlement behaviour. Moreover, it shows the capability of the used numerical scheme to simulate the installation process of jacked piles in sand. MPM instead of classical FEM, as applied in this study, is well suited to model the large deformations and flow of material occurring during the pile installation process. In order to successfully model the centrifuge test, it is necessary to account for a reduction of the friction and dilation angles at very high stress levels. With this reduction, the MPM simulations show good agreement with the centrifuge test results for both the installation process as well as the static load test (SLT) after the installation both for the simulation with the Mohr Coulomb and hypoplastic model. The numerical analyses of the pile installation show significant differences of the soil stresses and
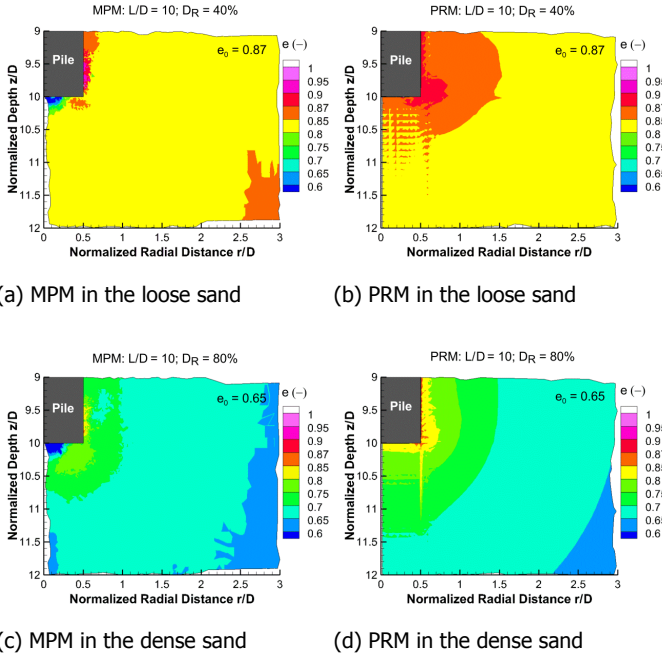
(a) MPM in the loose sand   (b) PRM in the loose sand

(c) MPM in the dense sand   (d) PRM in the dense sand

Figure 5.34: Void ratio around the pile base after unloading (after [3]).

strains around the pile after installation compared with the initial K_0-state. During installation, soil is pushed aside by the pile, which leads to densification around the pile and very high lateral stress at the pile tip. The influence of the installation extends to 8 pile diameters in horizontal direction from the center of the pile and 7 pile diameters below the pile tip. The pile capacity given by MPM simulations results in a good agreement with the load-displacement curve suggested in NEN $9997-2011$ code. As a consequence of the change in soil state after installation, a significantly higher pile bearing capacity is observed during SLT as compared to simulations without installation effects. With this research, the importance of including installation effects in numerical simulations, which aim to determine the bearing capacity of displacement piles and realistic load displacement behaviour, is demonstrated.

The simulation with the modified hypoplastic model for crushed sand (proposed in chapter 4) shows a significant improve load displacement behaviour of the model pile compared to the one using original hypoplastic model and better correspondence with the experiment result. This proposed hypoplastic model considers stress dependency of five parameters $\alpha, \beta, e_i, e_c, e_d$ of the hypoplastic model automatically. However, other parameters e.g. h_s, n and φ_c are most likely influenced by grain crushing and stress level as well. Hence, further investigation should be carried out to improve the model.

Regarding the comparison of PRM and MPM, it was shown that during pile installation PRM can produce jacking force and base resistance that are very close to the

jacking force and base resistance obtained from MPM. Also, it was concluded that in comparison with MPM, PRM results in lower base resistance and higher shaft resistance during pile operational loading (e.g., SLT). At the operational loading stage, PRM simulates a small-strain BVP with the assumption that the geometry of the pile-soil system does not change. But, in MPM, the pile indeed further penetrates into the soil and therefore benefits from increase in the soil bearing capacity due to this penetration. Thus, it can be suggested that PRM yields a conservative base resistance at the operational loading stage in comparison with MPM. The higher shaft resistance and lower base resistance from PRM counterbalance each other and result in the total capacity that is very close to the one predicted by MPM. In a conclusion, PRM as a method that is founded on small-strain finite element method can produce pile and soil responses that are in a promising agreement with those of MPM which is a finite-deformation analysis method. This comparison is important because a realistic and yet efficient simulation of installation of jacked piles is an appealing step towards the design and analysis of this type of displacement piles. Although, PRM is unable to model the flow of the soil below and around the pile during installation process, the simplicity of PRM enables an engineer to model the installation process of jacked piles as a staged construction process by any finite element code.

Having concluded that it is important to take installation effects into account, however simulating the whole penetration process of all piles of a practical application by means of MPM is expensive and not practical in engineering. It is ideal to develop a method to incorporate the installation effects around the wished-in-place pile to account for these effects [34]. Hence, there would be particular efficient and useful due to a significant reduction in computational demand, especially for situation with more than one pile.

References

[1] N. Phuong, A. van Tol, A. Elkadi, and A. Rohe, *Modelling of pile installation using the material point method (mpm),* in *International Conference on Numerical Methods in Geotechnical Engineering, NUMGE, Delft, The Netherlands*, Vol. 1 (CRC Press, 2014) pp. 271–276.

[2] N. Phuong, A. van Tol, A. Elkadi, and A. Rohe, *Numerical investigation of pile installation effects in sand using material point method,* Computers and Geotechnics 73, 58 (2016).

[3] F. S. Tehrani, P. Nguyen, R. B. Brinkgreve, and A. F. van Tol, *Comparison of press-replace method and material point method for analysis of jacked piles,* Computers and Geotechnics 78, 38 (2016).

[4] R. Salgado, J. Mitchell, and M. Jamiolkowski, *Calibration chamber size effects on penetration resistance in sand,* Journal of Geotechnical and Geoenvironmental Engineering 124, 878 (1998).

[5] P.-A. von Wolffersdorff, *A hypoplastic relation for granular materials with a*

predefined limit state surface, Mechanics of Cohesive-frictional Materials 1, 251 (1996).

[6] E. Klotz and M. Coop, *An investigation of the effect of soil state on the capacity of driven piles in sands,* Géotechnique 51, 733 (2001).

[7] J. Dijkstra, W. Broere, and A. F. van Tol, *Density changes near an advancing displacement pile in sand,* in *2nd BGA International Conference on Foundations ICOF* (2008) pp. 545–554.

[8] M. Luong and A. Touati, *Sols grenus sous fortes contraintes,* Revue Française de Géotechnique , 51 (1983).

[9] J. L. Colliat-Dangus, J. Desrues, and P. Foray, *Triaxial testing of granular soil under elevated cell pressure,* Advanced triaxial testing of soil and rock, ASTM STP 977, 290 (1988).

[10] N. Miura and T. Yamanouchi, *Compressibility and drained shear characteristics of a sand under high confining pressures,* Technology reports of the Yamaguchi University 1, 271 (1973).

[11] J. A. Yamamuro and P. V. Lade, *Drained sand behavior in axisymmetric tests at high pressures,* Journal of Geotechnical Engineering 122, 109 (1996).

[12] L. Balachowski, *Différents aspects de la modélisation physique du comportement des pieux: Chambre d'Etalonnage et Centrifugeuse*, Ph.D. thesis (1995).

[13] N. Huy, *Rapid load testing of piles in sand: effect of loading rate and excess pore pressure*, Ph.D. thesis, Delft University of Technology (2008).

[14] P. Holscher, A. F. van Tol, and N. Huy, *Rapid pile load tests in the geotechnical centrifuge,* in *the 9th International Conference on Testing and Design Methods for Deep Foundations, Japanese Geotechnical Society* (2012) pp. 257–263.

[15] J. Dijkstra, *On the modelling of pile installation*, Ph.D. thesis (2009).

[16] J. Van der Poel and F. Schenkeveld, *A preparation technique for very homogenous sand models and cpt research,* in *Centrifuge*, Vol. 98 (1998) pp. 149–154.

[17] M. Allard and F. Schenkeveld, *The delft geotechnics model pore fluid for centrifuge tests,* in *Centrifuge*, Vol. 94 (1994) pp. 133–138.

[18] E. Murray and J. D. Geddes, *Uplift of anchor plates in sand,* Journal of Geotechnical Engineering 113, 202 (1987).

[19] J. Grabe, T. Pucker, and T. Hamann, *Numerical simulation of pile installation processes in dry and saturated granular soils,* in *International Conference on Numerical Methods in Geotechnical Engineering, NUMGE, Delft, The Netherlands,*, Vol. 1 (CRC Press, 2014) pp. 663–668.

5

[20] I. K. Jassim, *Formulation of a Dynamic Material Point Method (MPM) for Geomechanical Problems*, Ph.D. thesis, University of Stuttgart (2013).

[21] H. Lengkeek, *Estimation of sand stiffness parameters from cone resistance,* Plaxis Bulletin Issue (2003).

[22] M. Randolph, R. Dolwin, and R. Beck, *Design of driven piles in sand,* Geotechnique 44, 427 (1994).

[23] M.-w. Gui, *Centrifuge and numerical modelling of pile and penetrometer in sand*, Ph.D. thesis, Cambridge University (1995).

[24] K. E. Anaraki, *Hypoplasticity investigated: parameter determination and numerical simulation*, Master's thesis, Delft University of Technology (2008).

[25] A. Rohe, *On the modelling of grain crushing in hypoplasticity*, Tech. Rep. (Delft University of Technology, 2010).

[26] T. A. Gavin K, Cadogan D and C. P, *The base resistance of non–displacement piles in sand. part i: field tests.* Proceedings of the Institution of Civil Engineers–Geotechnical Engineering 166, 540 (2013).

[27] *NEN-EN 9997-1: 2016 NL: Geotechnical Design - part 1: general Rules*, Nederlands Normalisatie Instituut,, Delft, The Netherlands (2011).

[28] K. Mahutka, F. Konig, and J. Grabe, *Numerical modelling of pile jacking, driving and vibro driving.* in *International conference on Numerical Simulation of Construction Processes in Geotechnical Engineering for Urban Environment* (Bochum, Rotterdam, 2006).

[29] S. Henke and J. Grabe, *Numerical modelling of pile installation,* in *In Proceedings of 17th International Conference on Soil Mechanics and Geotechnical Engineering* (Alexandria, Egypt,, 2009) pp. 1321–1324.

[30] D. White and M. Bolton, *Displacement and strain paths during plane-strain model pile installation in sand,* Géotechnique 54, 375 (2004).

[31] I. Herle and G. Gudehus, *Determination of parameters of a hypoplastic constitutive model from properties of grain assemblies,* Mechanics of Cohesive-frictional Materials 4, 461 (1999).

[32] K. H. Andersen, L. Andresen, H. P. Jostad, and E. C. Clukey, *Effect of skirt-tip geometry on set-up outside suction anchors in soft clay,* in *ASME 2004 23rd International Conference on Offshore Mechanics and Arctic Engineering* (American Society of Mechanical Engineers, 2004) pp. 1035–1044.

[33] H. Engin, R. Brinkgreve, and A. van Tol, *Simplified numerical modelling of pile penetration-the press-replace technique,* Int. J. for Num. and Analytical Meth. in Geomech. (2015).

[34] H. K. Engin, *Modelling pile installation effects: a numerical approach*, Ph.D. thesis (2013).

6

Pile installation in dry and saturated sand

6.1. Introduction

Impact driven piles are widely used in the construction of buildings and infrastructure. In these driving methods, the piles are pushed down by each drop, or blow, of the hammer, until the required penetration depth is achieved. This method of pile installation leads to significant changes in soil structure and soil state in the vicinity of the piles, which affects their bearing capacity. A proper assessment of the size and type of hammer needed to drive the pile to the required depth, as well as an assessment of the probability of pile damage due to high driving stresses, is important.

In the early analysis of pile driving, Smith [1] and Lee et al. [2] applied the one dimensional wave theory to calculate the wave propagation in an elastic rod . However, the prediction results were not accurate enough due to the one-dimensional approximation of soil response. In 1982, Smith and Chow [3] reported considerable differences between the one dimensional analyses and the axisymmetric finite element analyses for driven piles in clay. In 1994, Mabsout and Tassoulas [4] conducted a detailed numerical analysis of pile driving using a finite three-dimensional model, which is handled by two-dimensional analysis due to the axisymmetric nature of the problem. They adopted a frictional contact algorithm to characterize the interaction between soil and structure. They also added transmitting viscous elements to the far field boundaries to mitigate wave reflections [5]. Henke [6, 7] used the three dimensional Finite Element Method (FEM) to investigate the effect of the different pile installation methods of jacking, hammering and vibratory pile driving, on the behaviour of surrounding dry sand. The influence of driving a pile near existing piles was also examined.

Most of the numerical simulations of pile installation processes are performed with dry sand. Modelling the behaviour of soils under pile driving in saturated soils

is a challenge. It requires a method that is capable of modelling large deformation and able to account for the dynamic generation and dissipation of the pore water pressure. Grabe et al. [8] presented the influence of pore water pressure during an installation process of drilled full displacement piles, by using the two phase approach proposed by Hamann & Grabe [9]. Galavi et al. [10] used the material point method to simulate vibratory and impact driving of offshore monopiles, and provided useful insight into pile installation processes. The similarities and differences between the behaviour of jacked piles and that of driven piles are poorly understood, mainly because of the lack of field experience and a high quality load test database. Meyerhof [11] suggested that the shaft capacity of a jacked pile is only one third of that of a driven pile. Chow [12] and the BCP Committee [13] suggested that there is little evidence for this installation effect, and recorded similar behaviour when testing jacked and driven piles. Nauroy and Le Tirant [14] carried out calibration chamber tests in which open- and closed-ended piles were hammered or jacked past a buried total stress cell. They observed that the stress level measured during jacking is approximately one third higher than during hammering. Foray et al. [15] found that jacked piles mobilised 20% greater base resistance than driven piles, but 40% less shaft friction. De Nicola and Randolph [16] conducted centrifuge model tests of jacked and driven pipe piles and revealed comparable base and shaft capacities. Deeks et al. [17] reported that jacked piles behave much stiffer than comparable driven piles. Yang et al. [18] studied the similarities and differences between the behaviour of jacked piles and that of driven piles by conducting a series of full scale field tests on H-piles in sand. They observed that the shaft resistance of jacked piles is generally stiffer and stronger than that of driven piles, whereas the base resistance of jacked piles is weaker than that of driven piles. At a load level of twice the design capacity, the percentage of pile head load carried by base varies from 2% to 10% for jacked piles, whereas for driven piles the percentage varies from 6% to 61%.

In this chapter, a fully dynamic analysis of the impact driven pile in sand is modelled by the Material Point Method (MPM) in both dry and saturated sand. The pile is assumed to behave as linear elastic so that the assessment of its damage is excluded from this study. The hypoplastic model is used to capture the behaviour of sand under cyclic loading. The results after pile installation are compared between jacked and driven piles in order to obtain further insight on the influence of the installation method to the soil state and the pile bearing capacity.

6.2. Numerical model

6.2.1. Converting hammer impact into surface traction

The pile is driven into the ground by a drop hammer with a mass m and the falling height is h. For simplicity, Jassim [5] converted the momentum gained by the hammer during the free fall into surface traction $f(t)$ acting on the pile head with a pre-defined function in time. Figure 6.1 shows an illustration of the hammer drop and the corresponding force function.

Goble and Rausche [19] provided measurements data for the loading function
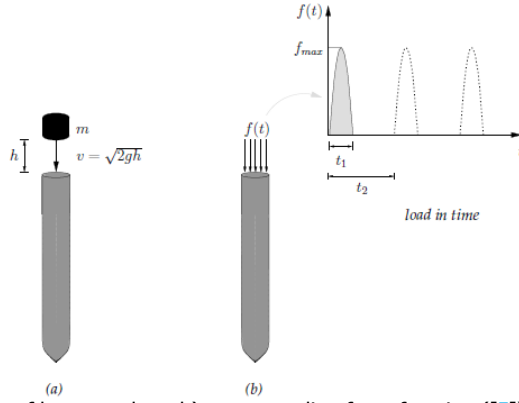
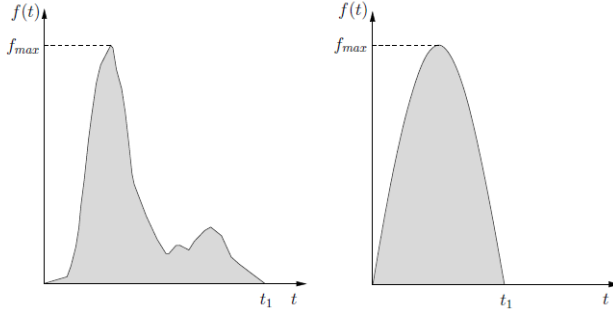Figure 6.1: a) Illustration of hammer drop, b) corresponding force function ([5])

Figure 6.2: The forcing function for pile driving: (left) measured [19] and (right) the approximation to haversine time distribution [5]

shown in Figure 6.2(left), where t_1 is the load duration and f_{max} is the peak load. The function was approximated as a so-called haversine by Jassim [5] (Figure 6.2(right)). For any hammer blow, Jassim [5] suggested to approximate the loading function as

$$f(t) = \begin{cases} f_{max} sin(\frac{\pi t}{t_1}) & \text{if } t \leq t_1 \\ 0 & \text{if } t > t_1 \end{cases} \tag{6.1}$$

where

$$f_{max} = \frac{\pi \eta m \sqrt{2gh}}{2t_1} \tag{6.2}$$

t_1 is the loading duration, f_{max} is the peak load and η represents the hammer efficiency. η is chosen as 64% following Borja [20]. With A being the cross-sectional area of the pile, the peak pressure p_{max} at the pile head is written as

$$p_{max} = \frac{\pi \eta m \sqrt{2gh}}{2t_1 A} \tag{6.3}$$

6.2.2. Numerical model

The detailed geometry of the numerical model is shown in Figure 6.3 (right). The length and depth of the investigated area is $18.5D$ and $32D$ respectively, in which $D = 0.64$ m is the pile diameter. Absorbing boundaries are placed along the lateral outer surface and along the base of the model to absorb waves travelling in both the solid and liquid phase. The formulation of absorbing boundaries is based on the local absorbing boundary, which was first described by Lysmer and Kuhlmeyer [21] and, subsequently, extended by Al-Kafaji [5] to a two-phase formulation by considering separate dashpots for the solid and the liquid phases. The damping coefficients of the dashpots are calculated based on the wave speed in the solid and the liquid phases. The detailed formulation of absorbing boundaries is written in section 3.4.2.

The 4-noded tetrahedral elements with linear interpolation of displacements are used in the simulations. The finite element mesh (shown in Figure 6.3 (left)) has a total of $37,594$ tetrahedral elements including the initially inactive elements, with a total $178,653$ of material points. The mesh is refined near the pile. The inactive elements above the soil surface may be activated during the calculation process as material points are entering. As the simulation of the jacked pile in chapter 5, a $20°$ section of the axisymmetric problem is considered for discretization.

In Chapter 5, the jacked pile is modelled as a rigid body, whereas the impact-driven pile in this chapter is discretised with volume elements in FEM. The jacking process was displacement controlled, while the driving process is load controlled. Hence, it allows to simulate the wave propagation inside the pile as in reality. The shape of the pile tip is flat and slightly curved at the edge to avoid numerical difficulties due to locking (Figure 6.3). The pile is assumed to behave according to the linear elastic constitutive relation, with a Young's modulus of $E = 500[MN/m^2]$, a Poisson's ratio of $\nu = 0$ and a density of $\rho = 2500[kg/m^3]$. To increase the accuracy of results, the moving mesh concept is utilised in which the top part of the mesh moves together with the pile, while the lower part of the mesh is being compressed. This ensures that the refined elements are always located along the pile. More detail on the moving mesh concept is written in Section 3.4.4.

The considered pile is embedded $10D$ below the soil surface. Then an impulse load is applied on top of the pile head, as described in the previous section 6.2.1. The value of impulse load p_{max} applied on the pile head is chosen to get the optimal penetration depth per blow. The loading duration $t_1 = 0.012s$ and the time until the next blow $t_2 = 0.1s$ is used for all simulations.

The stresses in the soil are initiated using the K_0-procedure. A frictional contact formulation (written in Section 3.4.3) is used to prevent interpenetration of pile and soil. The friction coefficient between the pile and the sand is assumed to be 0.174.

Parametric studies on the influence of the damping factor α for pile, skin friction μ, relative density R_D and driving pressure p_{max} are illustrated in Appendix E.

6.2.3. Soil model

The hypoplastic constitutive model of von Wolffersdorff [22] with the extension of intergranular strain by Niemunis and Herle [23] is used. This hypoplastic model
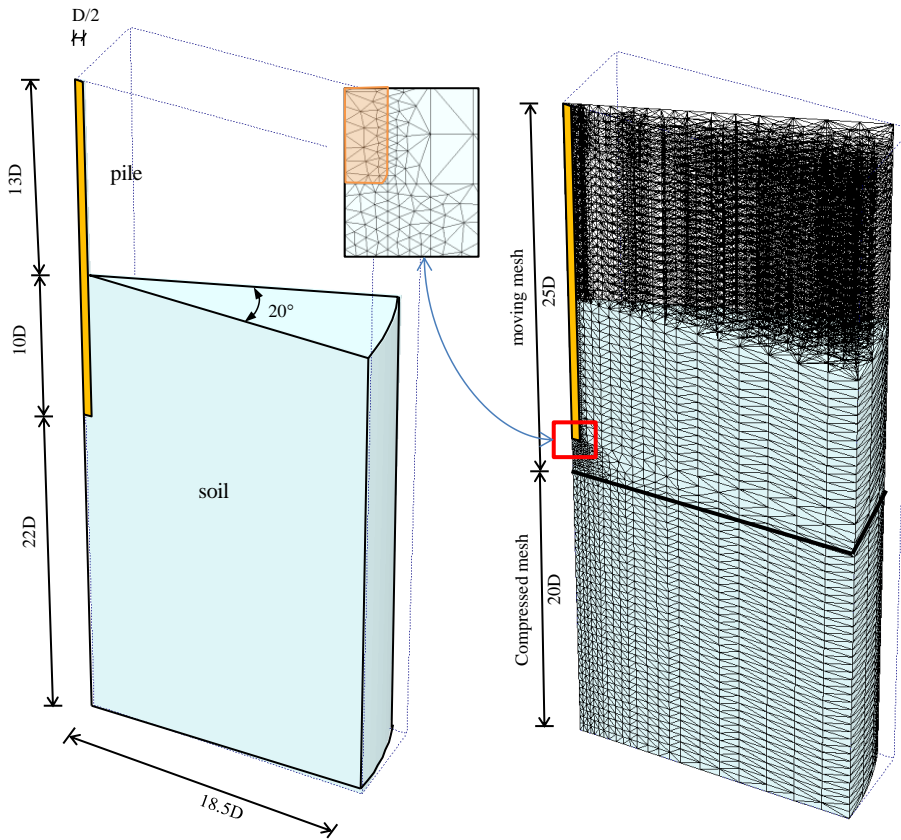
Figure 6.3: Geometry of considered problem and mesh discretization

is able to realistically reproduce the non-linear and inelastic behaviour of granular materials like sand including dilatancy, contractancy, and different stiffnesses for loading and unloading. With the additional state variable of intergranular strain, it is possible to model the accumulation effects and the hysteric material behaviour under cyclic loading which is of particular importance for the dynamic installation processes. Details of the hypoplastic formulation are given in Chapter 4.

For all the calculations of the impact hammer pile in this chapter, the original hypoplastic parameters of Baskarp Sand, listed in Table 5.3, are used. Parameter sets for small strain stiffness in the hypoplastic model are tabulated in Table 5.5.

For simulations of saturated soil, excess pore pressures can develop due to external loading. Soil has a time-dependent behaviour which depends on permeability. To capture such behaviour and the development of excess pore pressure, a two-phase material with partially drained conditions is considered. The $v - w$ formulation is used, where the unknown primary variables are solid velocity v and fluid velocity w. The implementation of the $v - w$ formulation in MPM is presented

Table 6.1: Additional parameters for modelling soil as a two phase material.

Parameter	Value	Description
ρ_s	2647	density of solid grains $[kg/m^3]$
ρ_w	1000	density of water $[kg/m^3]$
K_s	$1 \cdot 10^{15}$	bulk modulus of solid grains $[kN/m^2]$
K_w	81400	bulk modulus of water $[kN/m^2]$
k	$8.85 \cdot 10^{-5}$	hydraulic conductivity $[m/s]$

in Section 3.3. Additional parameters for modelling soil as a two phase material are listed in Table 6.1.

6.3. Numerical results of impact hammer pile installation

Considering a hammer having a mass of $m = 2000[kg]$ dropped from a height of $h = 1[m]$ and a load duration of $t_1 = 0.012[s]$, the corresponding peak pressure at the pile head was found to be $p_{max} \approx 10000[kN/m^2]$. This pressure is applied directly on the pile as a nodal force for the actual modelling of the pile driving process. The time between successive blows is $t_2 = 0.1[s]$, corresponding to a driving frequency of $10[Hz]$.

6.3.1. Pile driving in dry sand

Stress state after pile driving

Figure 6.4 shows the radial stress as a contour plot after 1 blow, 10 blows, 50 blows and 100 blows, respectively, for pile driving in medium dense sand ($R_D = 45\%$). It can be noticed that the radial stresses decrease in the near area of the pile shaft.

Figure 6.5a shows the radial stress for the horizontal cross section in $10D$, $13D$ and $17.5D$ depth, respectively, directly after 100 hits. Figure 6.5b shows the radial stress along the pile and at several distances from the axis of symmetry after 100 blows. It should be noted that the position of the pile in Figure 6.5 is initially at $10D$ and at $16.5D$ at the end of penetration process. During the driving process, a high stress peak occurs at the pile tip, about 3 times the value of the initial K_0 stress. The stress increase reaches down to $3D$ beneath the pile tip for the medium dense sand and spreads out in a radial direction for about $4D$. Along the pile shaft ($r = 0.5D$), the radial stress decreases significantly below the initial K_0 state. Below the pile tip, the radial stress drops down to a value below the K_0 state. At a distance from the pile centre larger than $10D$, no stress changes can be observed.

The observed change of radial stress along the vertical cross section near the pile shaft, as well as the radial stress contour around the driven pile, are in good agreement with simulation results obtained by Mahutka et al. [24]

Density change after pile driving

Figure 6.6 shows the calculated void ratio distribution after 1 blow, 10 blows, 50 blows and 100 blows for a driven pile in medium dense sand. It can be seen that the soil close to the pile is significantly compacted, except for a small dilative zone near
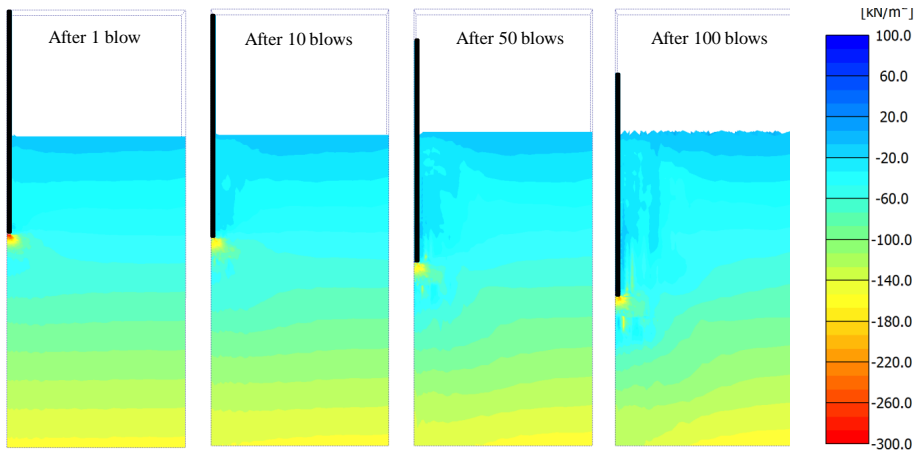
Figure 6.4: Calculated radial stress distribution around the driven pile after 1 blow, 10 blows, 50 blows and 100 blows.
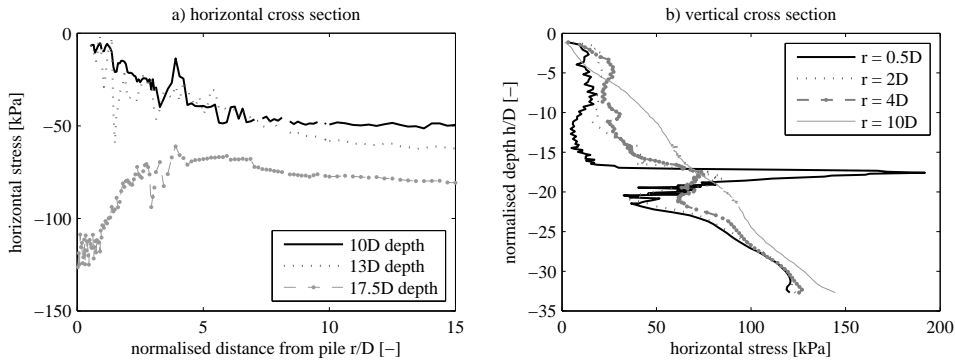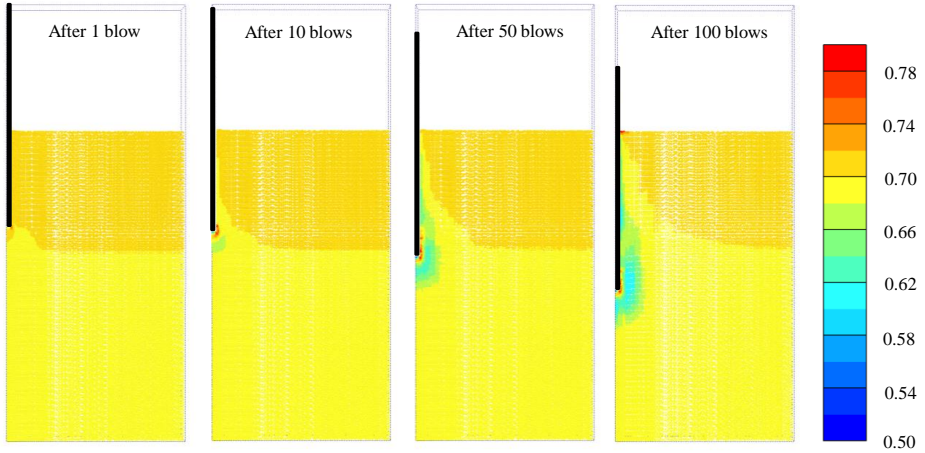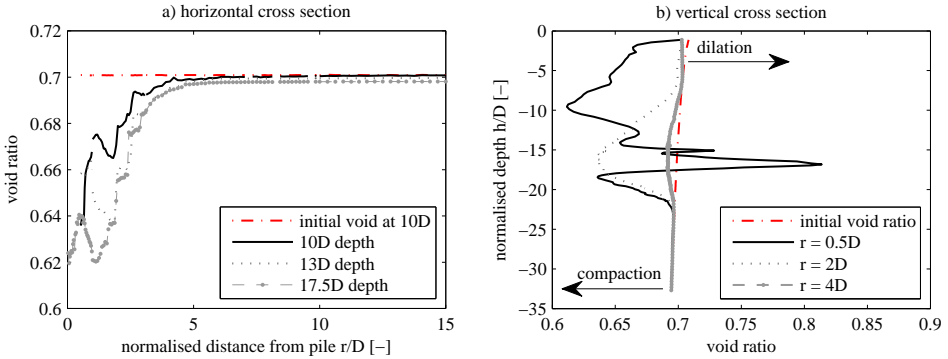

Figure 6.5: Calculated radial stress after 6.5D pile penetration (100 blows) in dry sand for different cross sections: a) horizontal cross section in different depth from the soil surface, b) vertical cross section for different distances to axis of symmetric.

the end of the pile shaft and around the corner of the pile. The soil is compacted in a region of approximately $2D - 2.5D$. The compaction comes mainly from the displacement of the soil and some additional compaction results from cyclic shearing due to the drop impulse [24]. The dilative zone may be explained due to a high shear strain in the soil surrounding the corner pile. Hence, the compaction of the soil close to the pile is superimposed by the shearing process, while at a greater distance from the pile corner the compaction is dominant, which is in line with the findings of other researchers ([24]).

Several horizontal cross sections at different depth: $10D$, $13D$ and $17.5D$ from the soil surface, are plotted in Figure 6.7a to obtain the distribution of the void ratio after 100 blows in horizontal direction. Figure 6.7b shows the change in void ratio after 100 blows for different distances from the axis of symmetry. The pile tip is at the depth of $16.5D$ from the soil surface. In general, the disturbance zone due to pile driving is extended to a distance of about $5D$ from the pile center and no change in void ratio below the depth of $25D$ from the soil surface. The largest

Figure 6.6: Calculated void ratio distribution around the driven pile after 1 blow, 10 blows, 50 blows and 100 blows.

Figure 6.7: Calculated void ratio after 6.5D pile penetration (100 blows) in dry sand for different cross section: a) horizontal cross section in different depth from the soil surface, b) vertical cross section for different distances to axis of symmetric.

compaction can be found at the depth of 10D below the soil surface close to the pile shaft.

6.3.2. Pile driving in saturated sand

Stress state after pile driving

The change of the vertical and horizontal effective stress after 1 blow, 10 blows, 50 blows, 100 blows and 150 blows of a driven pile in saturated medium dense sand is shown in Figure 6.8a, 6.8b. The effective stress near the pile is reduced after blows to approximately zero. Thus, the soil shows the tendency to liquefy in this area. Such behaviour of soil liquefaction was also found in previous numerical studies [8, 10]. The horizontal stress decreases close to the pile shaft during dynamic pile installation has also already been observed in various field tests. Ng et al. [25] and Axelsson [26] both investigated the earth pressure acting on a pile after installation.

Very low effective earth pressure on the pile shaft after the end of pile driving of around $K = 0.07 - 0.3$ was obtained, although pore pressures had already been equalised.

Figure 6.9a shows the calculated radial stress right after 150 blows in saturated medium dense sand for different horizontal cross sections. Figure 6.9b plots the calculated radial stress near the pile shaft and at a different distance from the pile center (note that the pile tip is at $16.5D$ depth). As can be seen, the zone, in which the reduction of radial stress to nearly zero is extended to a distance of about $2.5D$ from the pile center. At a distance between $2.5D - 7D$ from the pile center, a significant increase in radial stress is obtained. The peak value of stress in this zone is at the same level with the pile tip and has a value of about 2 times the initial stress. The influence zone due to installation is about $8D$ from the pile center and $30D$ below the soil surface.

Influence of pore water pressure during and after pile driving

The effective stress reaches a zero value due to an increase of excess pore water pressure around the pile tip during installation. Figure 6.8c shows the distribution of pore water pressure around the pile after 1 blow, 10 blows, 50 blows,100 blows and 150 blows. Clearly, the excess pore water pressure is built up gradually during the pile installation.

Figure 6.10 shows the development of pore water pressure calculated for ten different particles located around the pile during 10 blows. During the loading time of each blow, pore water pressure increases rapidly and then reduces during unloading time for most particles, except for particle 4. Under the pile tip (particle 1, 2, 3), pore water pressure reduces significantly and tensile stress is observed after a few blows, especially at location $1D$ below the pile tip (particle 2). For the rest of particles 4 to 10, there is still some excess pore pressure that remains after each blow which causes excess pore water pressure increase at those locations in time.

Density change after pile driving

The distribution of the void ratio near the driven pile after 1 blow, 10 blows, 50 blows, 100 blows and 150 blows is shown in Figure 6.11. The soil around the pile is slowly densifying after blowing. Almost along the entire pile shaft and under the pile tip, dilation is observed. This also can be seen clearly in Figure 6.12. At the distance of $r = 2D$ from the pile center, soil is compacted, however the amount of compaction is quite small, about 14% of the initial void ratio. The disturbance zone due to installation is extended to a distance of about $4D$ from the pile center and to the depth of $20D$ from the soil surface.

In general, there is almost no compaction of the soil around the driven pile during installation in comparison to the jacked pile, as can be seen in Figure 6.13 a and b. These differences are caused by the appearance of excess pore pressure during installation of an impact hammer pile.
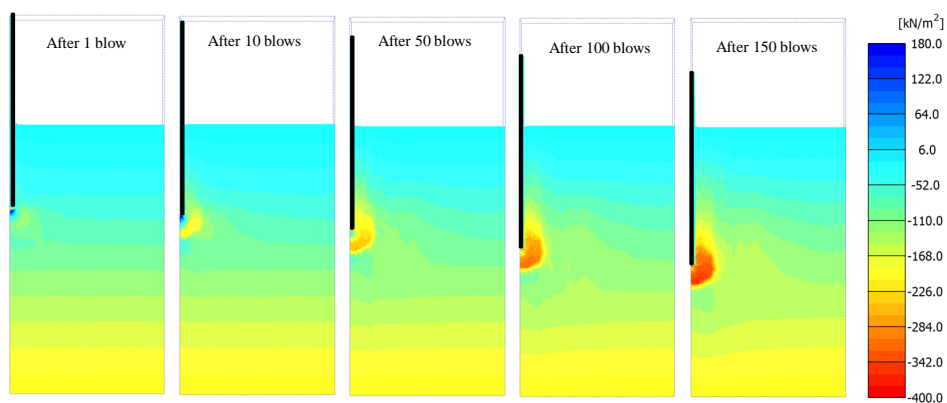
After installation, the simulation is continued with a relaxation phase. During the relaxation phase, there is no load applied on the pile head. As the results of flow balance, the excess pore water pressure around the pile tip is reduced to zero,
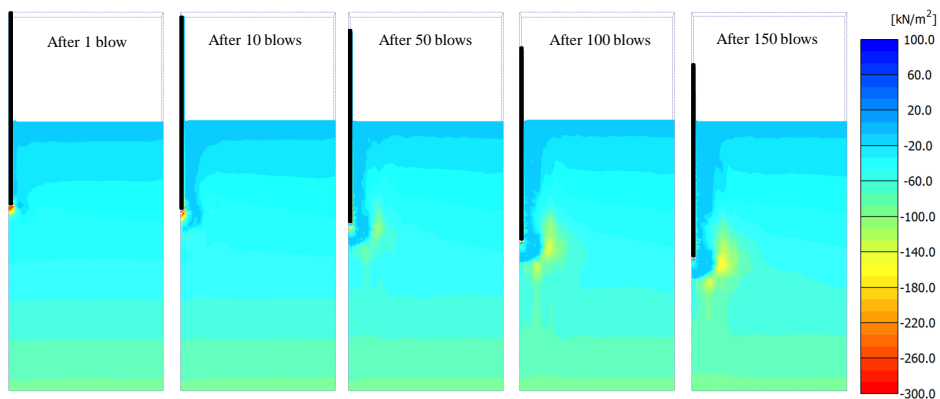
(a) radial effective stress
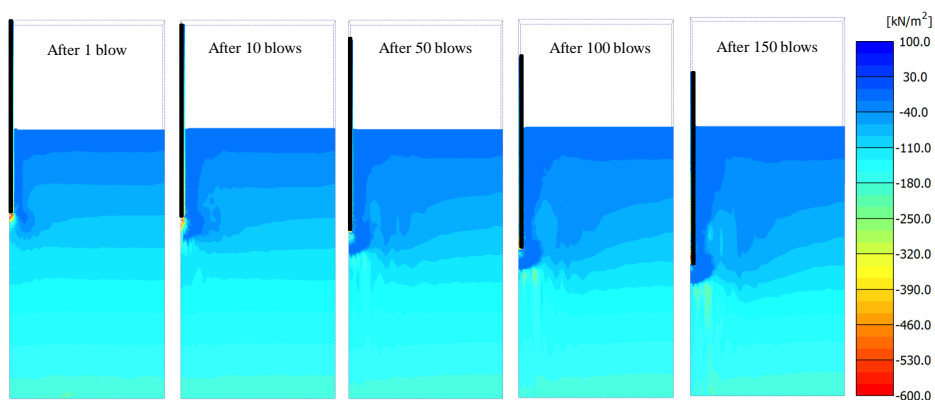
(b) vertical effective stress

(c) pore water pressure

Figure 6.8: Calculated stresses after 1 blow, 10 blows, 50 blows, 100 blows and 150 blows of pile driving in saturated medium dense sand.
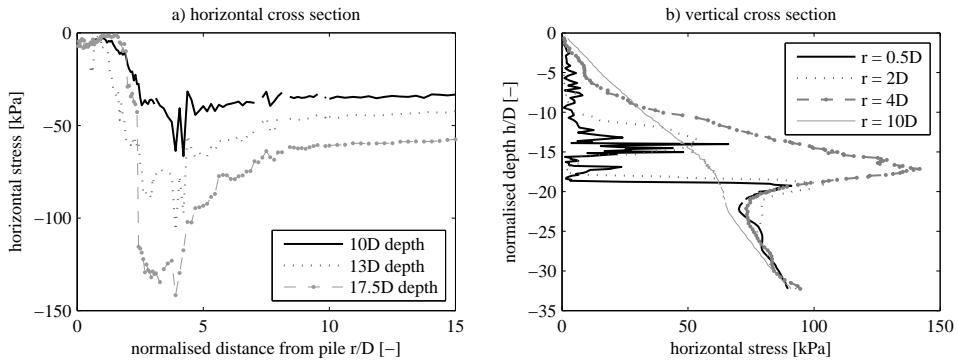
Figure 6.9: Calculated radial stresses after 6.5D pile penetration (150 blows) in saturated sand for different cross sections: a) horizontal cross section in different depth from the soil surface, b) vertical cross section for different distances to axis of symmetric.
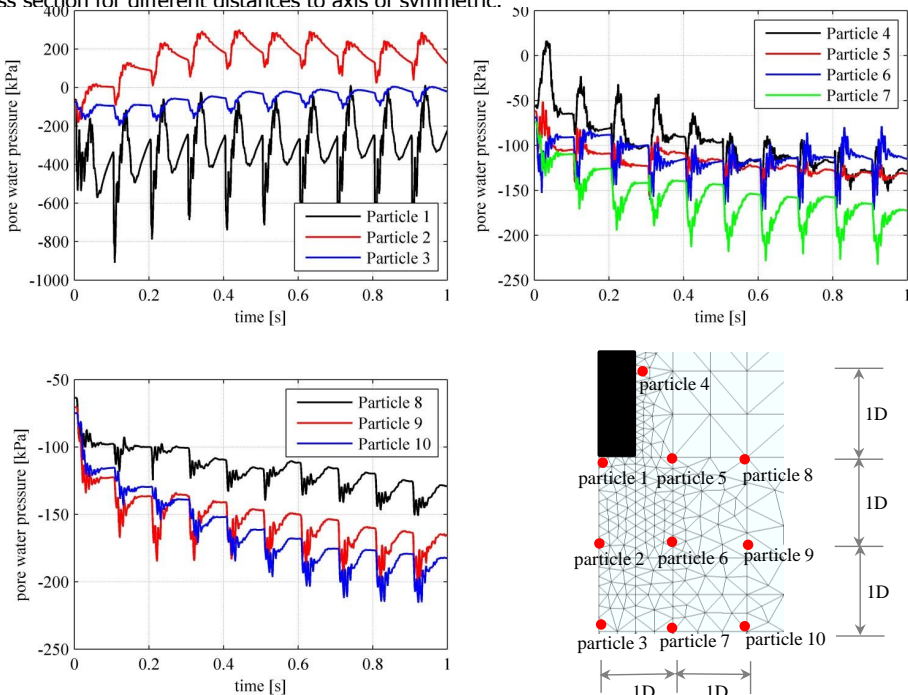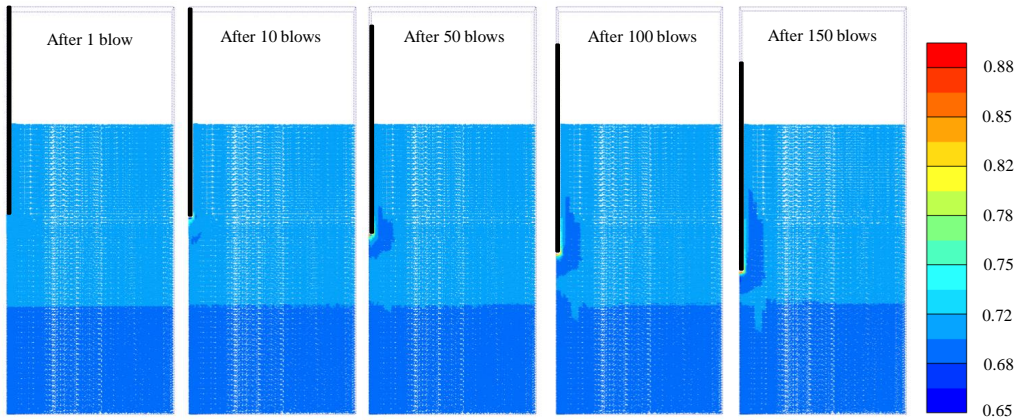

Figure 6.10: Developing of pore pressure during 10 blows for several particles around the pile tip.

leading to the effective stress of the soil being slowly built up. This leads to some compaction of the soil around the driven pile, as shown in Figure 6.13c, but much less than with the jacked pile.

Figure 6.11: Calculated void ratio distribution after 1 blow, 10 blows, 50 blows, 100 blows and 150 blows of pile driving in saturated medium dense sand .
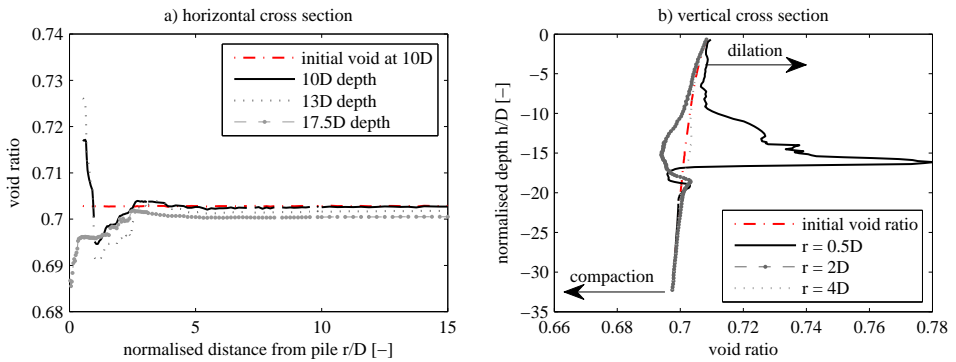
Figure 6.12: Cross section of void ratio after 6.5D pile penetration in saturated sand: a) horizontal cross section, b) vertical cross section.
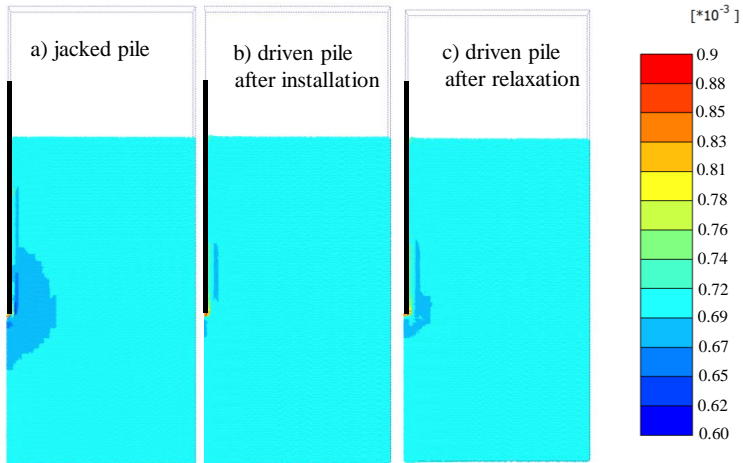
Figure 6.13: Comparison of void ratio distribution between jacked pile and impact hammer pile. Case of medium dense sand ($R_D = 45\%$).

6.4. Comparison of impact hammer pile and jacked pile in dry sand

In this section the results of the simulations of an impact driven pile installed in dry sand are presented and compared with the results of the jacked pile (results from Chapter 5). The detailed geometry of the considered problem and the mesh discretization for numerical analysis of driven pile are the same in Figure 5.2 and 5.3. The diameter of the pile D is $0.452m$. Absorbing boundaries are placed along the lateral outer surface and along the base of the model. The jacked pile is modelled as a rigid body, whereas the driven pile is discretised with a volume element in FEM and assumed to behave according to the linear elastic constitutive relation. The parameters of the pile model are the same as in the previous section. The relative density of the soil is $R_D = 0.36$ and $R_D = 0.54$. The hypoplastic soil parameters as well as additional parameters for modelling two-phase material are the same as in Section 6.2.3.

Figure 6.14 illustrates the difference in radial stress distribution after 4.5D penetration between a jacked and a hammered pile for both loose and medium dense sand. For a jacked pile, there is a significantly increasing radial stress around the pile tip, whereas in hammered pile, the radial stress reduces and reaches zero in some place around the pile tip and shaft.

The vibration of the pile after loading causes the soil around it to compact and to increase in density, which explains the results of the void ratio changing after installation as shown in Figure 6.15, where the soil around the impact driven pile is much more compacted than around the jacked pile.

All installation methods show significant differences concerning radial stress and void ratio after pile installation. From the numerical results it can be stated that the radial stress depends highly on the degree of densification during the installation process. In all cases a certain amount of soil is pushed aside by the pile. In the case, of the jacked pile, there is only a slight densification of the surrounding soil. Because of the monotonic nature of the installation method, the soil is not able to rearrange its grain structure and, as a result, high stress interlockings occur around the pile [24]. In case of the hammered pile driving, the soil is compacted close to the pile shaft due to small cyclic shearing. In this compacted area the soil grains are allowed to rearrange themselves. As a result, the soil near the pile shaft is able to relax and the radial stress decreases [24].

Figure 6.16 compares the load-displacement curve during installation between a hammered pile and a jacked pile for both loose and medium dense sand. it can be seen that, the jacked pile gives about a 4 times higher total bearing capacity than the hammered pile in both cases of relative density. This observation is in good agreement with Deeks et al. and Dijkstra [17, 27]. Deeks et al. [17] found that the stiffness of jacked piles is considerably higher than conventionally driven or bored piles due to the pre-loading of the soil below the base during installation and the presence of residual base load. In their test results, the stiffness of these jacked piles exceeds recommended design stiffness for driven piles by factor of more than 2. Dijkstra [27] summarized through the test performed by various authors
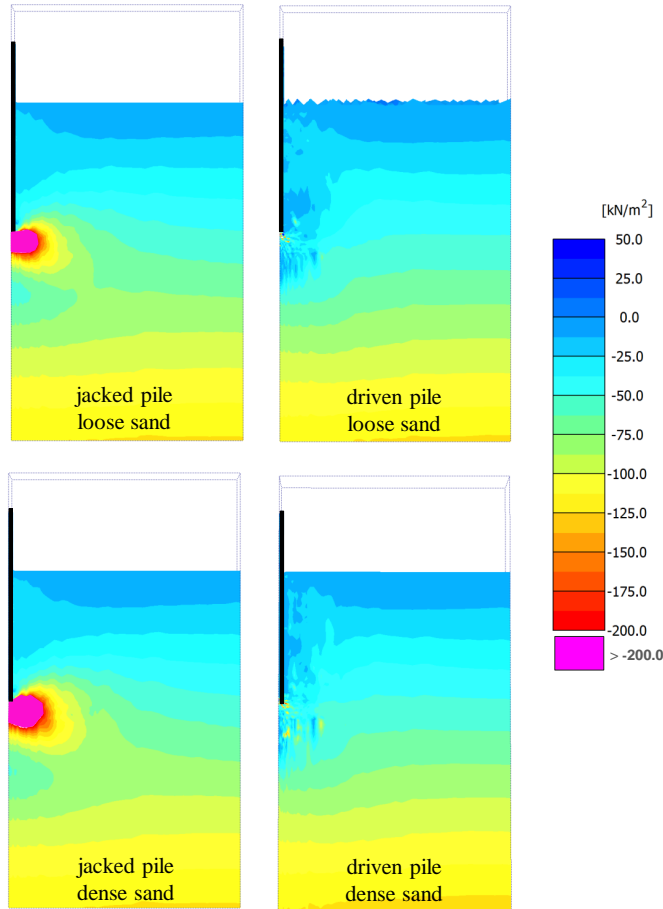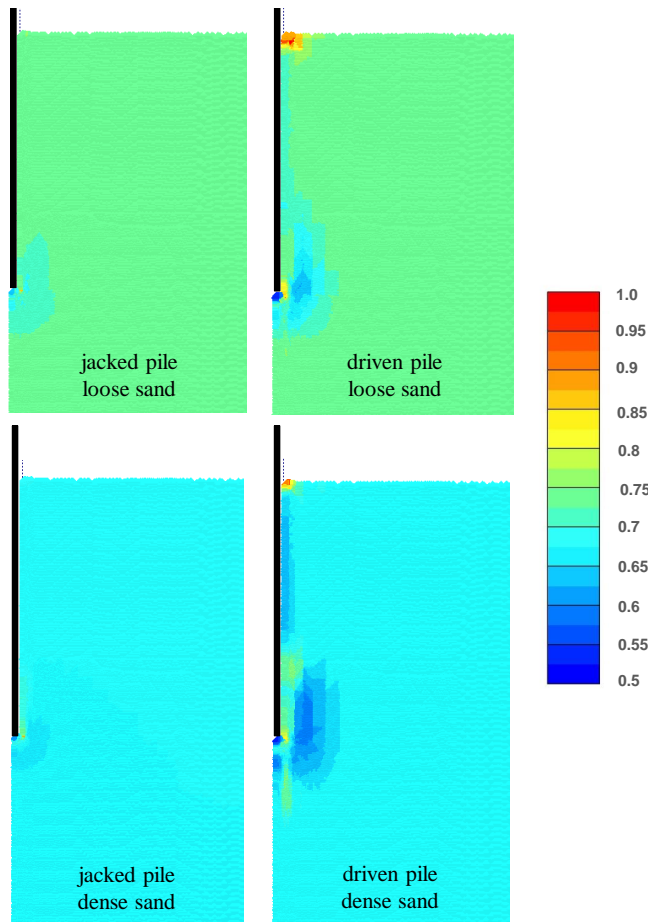
Figure 6.14: Horizontal stress distribution after 4.5D penetration. Comparison between jacked pile and driven pile for both loose and medium dense sand

the ratio Q_{driven}/Q_{jacked} (Q is the static bearing capacity of considered pile). The majority of the tests shows $Q_{driven}/Q_{jacked} < 1$. In other words, the static bearing capacity of jacked piles is higher than that of driven pile.

6.5. Penetration per blow

Figure 6.17 shows the number of blows applied on different simulations and the reached depth. According to the simulation results, it is easier to hammer the pile in dry sand than in saturated sand and, similarly, easier in loose sand than in dense sand. It may be explained as a result of the generation of negative excess pore water pressure appearing under the pile tip during each blow. Figure 6.18c illustrates the generation of pore water pressure for different particle near the pile tip. It can be seen that for both particles under the pile tip (particle 1, 2, 4 and 5), a negative excess pore pressure is obtained during the loading duration. The

Figure 6.15: Void ratio distribution after 4.5D penetration. Comparison between jacked pile and driven pile for both loose and medium dense sand

negative excess pore pressure results in an increase of the effective stresses, which leads to more difficulty to penetrate the pile to a deeper level in the sand.

6.6. Conclusion

A numerical study on impact driving piles in both dry and saturated sand has been presented in this chapter. Complex pile installations processes of impact hammer pile can be simulated using MPM. The influence of pore water pressure on pile installation processes can be taken into account using the two-phase $v - w$ formulation.

For both dry and saturated sand, there is a significant reduction in the horizontal stress close to the pile shaft during dynamic pile installation. This behaviour has also observed in various field tests [25, 26] and numerical studies [8, 10, 24].
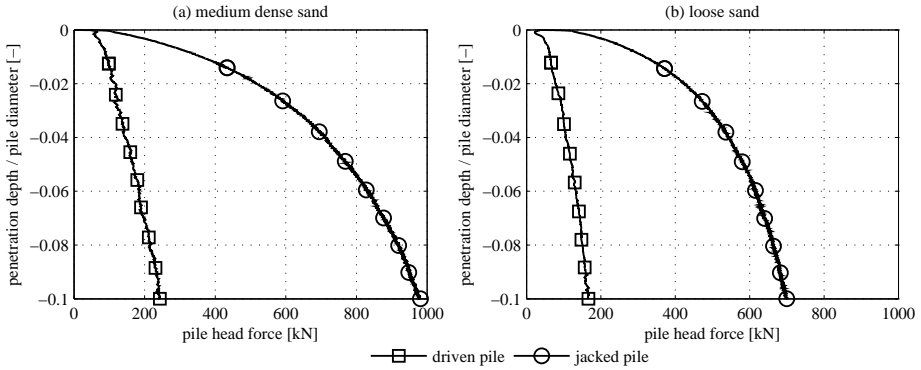
Figure 6.16: Load displacement curve during static load test. Comparison between jacked pile and driven pile for both loose and medium dense sand
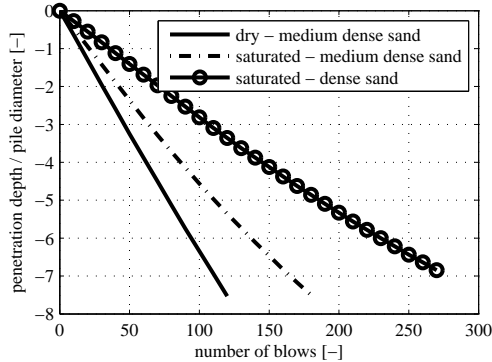
Figure 6.17: Penetration depth per blows, impulse load of 10000 kPa, pile diameter of 0.64 m.

For hammered piles, the compaction of the soil around the pile is much larger than that of the jacked pile due to the cyclic and dynamic shearing which results in lower radial stress around the pile shaft.

Generally, if the volume decrease caused by densification of the soil is higher than the volume of soil pushed away by the pile, a relaxation of the radial stress at the shaft can be expected. If instead the densification is smaller than the displaced soil volume, the radial stress will increase [24]. Hence, in dry sand, jacked piles result in a higher stiffness and capacity than hammered piles due to the higher radial stress at both pile shaft and pile toe.

In saturated sand, the influence of the pore water pressure on the pile installation processes is significant. An increase of excess pore water pressure around the pile tip during installation is observed. As a consequence, as the effective stress reaches zero value, the soil shows the tendency to liquefy in the area around the installed pile. Furthermore, there is almost no compaction of the soil around the driven pile during installation in comparison to the jacked pile.

The investigation of pile installation processes and the estimation of the impact of pile installation processes on surrounding structures are possible due to numerical simulations.
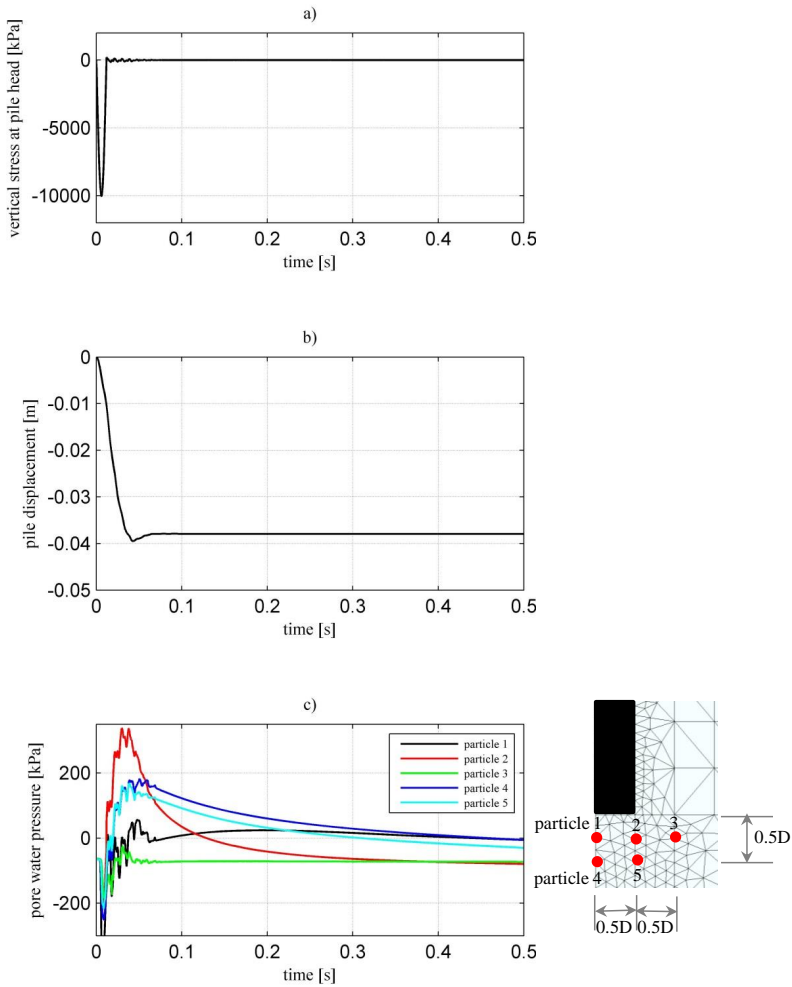
Figure 6.18: Measurement during first blow, a) vertical stress of the pile head vs time, b) pile displacement vs time, c) pore water pressure at different locations vs time.

References

[1] E. A. Smith, *Pile-driving analysis by the wave equation,* American Society of Civil Engineers Transactions (1962).

[2] S. Lee, Y. Chow, G. Karunaratne, and K. Wong, *Rational wave equation model for pile-driving analysis,* Journal of Geotechnical Engineering 114, 306 (1988).

[3] I. Smith and Y. Chow, *Three dimensional analysis of pile drivability,* in *Proc. 2nd Int. Conf. on Numerical Methods in Offshore Piling, Austin, Texas* (1982) pp. 1–19.

[4] M. E. Mabsout and J. L. Tassoulas, *A finite element model for the simulation of pile driving,* International Journal for numerical methods in Engineering 37, 257 (1994).

[5] I. K. Jassim, *Formulation of a Dynamic Material Point Method (MPM) for Geomechanical Problems*, Ph.D. thesis, University of Stuttgart (2013).

[6] S. Henke and J. Grabe, *Numerical modelling of pile installation,* in *In Proceedings of 17th International Conference on Soil Mechanics and Geotechnical Engineering* (Alexandria, Egypt,, 2009) pp. 1321–1324.

[7] S. Henke, *Influence of pile installation on adjacent structures,* International journal for numerical and analytical methods in geomechanics 34, 1191 (2010).

[8] J. Grabe, T. Pucker, and T. Hamann, *Numerical simulation of pile installation processes in dry and saturated granular soils,* in *International Conference on Numerical Methods in Geotechnical Engineering, NUMGE, Delft, The Netherlands,*, Vol. 1 (CRC Press, 2014) pp. 663–668.

[9] T. Hamann and J. Grabe, *A simple dynamic approach for the numerical modelling of soil as a two-phase material,* geotechnik 36, 180 (2013).

[10] V. Galavi, L. Beuth, B. Z. Coelho, F. S. Tehrani, P. Hölscher, and F. Van Tol, *Numerical simulation of pile installation in saturated sand using material point method,* Procedia Engineering 175, 72 (2017).

[11] G. Mayerhof, *Bearing capacity and settlemtn of pile foundations,* Journal of Geotechnical and Geoenvironmental Engineering 102 (1976).

[12] F. Chow, *Investigations into the behaviour of displacement piles for offshore structures*, Ph.D. thesis, Ph. D. thesis, University of London Imperial College, London (1997).

[13] C. BCP, *Field tests on piles in sand,* Soils and Foundations 11, 29 (1971).

[14] J. Nauroy and P. Le Tirant, *Model tests of piles in calcarecus sands,* in *Geotechnical Practice in Offshore Engineering* (ASCE, 1983) pp. 356–369.

[15] P. Foray, J. Genevois, and S. Labenieh, *Effet de la mise en place sur la capacité portante des pieux dans les sables,* in *Proceedings of the 12th International Conference on Soil Mechanics and Foundation Engineering, Rio deJaneiro, Brazil* (1989) pp. 13–18.

[16] A. De Nicola and M. Randolph, *The plugging behaviour of driven and jacked piles in sand,* Geotechnique 47, 841 (1997).

[17] A. Deeks, D. White, and M. Bolton, *A comparison of jacked, driven and bored piles in sand,* in *Proceedings of the International Conference on Soil Mechanics and Geotechnical Engineering*, Vol. 16 (AA Balkema Publishers, 2005) p. 2103.

[18] J. Yang, L. Tham, P. Lee, S. Chan, and F. Yu, *Behaviour of jacked and driven piles in sandy soil,* Géotechnique (2006).

[19] G. G. Goble, *The analysis of pile driving-a state-of-the-art,* in *Proc. Int. Conf. on Application of Stress-wave Theory to Piles, Stockholm, 1980* (1980) pp. 131–161.

[20] R. I. Borja, *Dynamics of pile driving by the finite element method,* Computers and Geotechnics 5, 39 (1988).

[21] J. Lysmer and R. L. Kuhlemeyer, *Finite dynamic model for infinite media,* Journal of the Engineering Mechanics Division 95, 859 (1969).

[22] P.-A. von Wolffersdorff, *A hypoplastic relation for granular materials with a predefined limit state surface,* Mechanics of Cohesive-frictional Materials 1, 251 (1996).

[23] A. Niemunis and I. Herle, *Hypoplastic model for cohesionless soils with elastic strain range,* Mechanics of Cohesive-frictional Materials 2, 279 (1997).

[24] K. Mahutka, F. Konig, and J. Grabe, *Numerical modelling of pile jacking, driving and vibro driving.* in *International conference on Numerical Simulation of Construction Processes in Geotechnical Engineering for Urban Environment* (Bochum, Rotterdam, 2006).

[25] E. Ng, *Pile foundation. the behaviour of single pile in cohesionless soils,* Federal Highway Administration Report (1988).

[26] G. Axelsson, *Long-term set-up of driven piles in sand.*, Ph.D. thesis, Institutionen för anläggning och miljö (2000).

[27] J. Dijkstra, *On the modelling of pile installation*, Ph.D. thesis (2009).

6

7

Modelling rapid pile load testing

7.1. Rapid load test

In chapter 6 the hammered pile installation in dry and saturated sand was simulated. In this chapter an attempt is made to validate this type of simulations by numerical modelling of a number of Rapid Pile Load Tests (RLT) that were performed in a geotechnical centrifuge. Because in these tests the piles were installed in saturated sand and were loaded by impact. And moreover the conditions were well defined, regarding soil, loading and the deformations were measured as well as the pore pressures in the soil during loading.

In the following at first a short introduction of the different types of pile load tests and the Rapid test in particular is given.

7.1.1. Introduction

The purpose of a pile load test is to prove that a foundation fulfils requirements in terms of the stiffness under working load and the bearing capacity at the ultimate limit state. In general, there are three types of tests available, which are Static Load Test (SLT), Rapid Load Test (RLT) and Dynamic Load Test (DLT). The static load test is quite expensive due to its duration, which is about one day, and the requirements regarding the test facilities, dead weight, reaction frame, etc. The dynamic load test is much faster and cheaper; however, piles may experience tension during the test and the derivation of an equivalent static pile capacity is hampered by wave effects. The rapid pile load test method is conducted by exerting a long duration pulse load (between 50 and 200 milliseconds) on the pile head [1]. The long duration load of rapid pile load test, which is 10 to 20 times longer than the typical loading duration of a dynamic pile load test but still considered as a dynamic event. The long loading duration helps to significantly reduce stress-wave effects, thus leading to a less complex analysis method. Hence, rapid pile load testing methods which are less time consuming than the static load tests and less complicated to analyse than the dynamic load tests, are considered to be efficient alternatives for the prediction of

the static bearing capacity of the pile.

The rapid load testing method is distinguished from the other testing methods as it is based on the wave number N_w or the relative duration t_r. In which the relative duration t_r represents the ratio between the length of the applied pulse load and the length of the pile ([1]), t_r represents the ratio between the duration of the applied pulse load and the duration needed for a compression wave to propagate forwards and backwards through the pile ([2]). If N_w is in between 10 and 1000 or t_r is between 5 to 500, it is regarded as a rapid load test; if $N_w < 10$, it is regarded as a dynamic load test and if $N_w > 1000$, it is regarded as a static load test ([2]).

During the rapid load test, excess pore pressure is generated in the soil closed to the pile, even in sand [3] and the effect of generated excess pore pressure on the ultimate bearing capacity of the pile is uncertain. The Unloading Point Method (UPM) [4], which takes into account the soil viscous damping and the pile inertia but not the effect of pore pressure, is the most common method to derive an equivalent static pile capacity from a rapid test. McVay et al. [5] and Holscher et al. [6] confirmed that the derived capacity with UPM from a rapid load test overestimates the ultimate bearing capacity of piles in sand with about 10%.

Huy [7]and Holscher et al. [8] studied the effect of excess pore pressure by performing a number of rapid load tests on a model pile in sand in a geotechnical centrifuge. They found that, the maximum of pile tip resistance is higher in a rapid load test than in a static load test due to the rate effect (less than 10%) and the effect of excess pore pressure (maximum of about 30%).

7.1.2. Centrifuge rapid load tests

The centrifuge test was performed at Deltares (Delft, the Netherlands) based on a 1:40 scale test. Detail descriptions of the centrifuge test are given by Huy [7, 8] and Chi [9]. During the sample preparation, the pile was installed at a depth of 10D (for jacked pile) and 20D (for pile without installation effects) from the soil surface. The jacked pile was pushed down in flight 10D deeper to 20D depth from the soil surface. The objective is to have a pile installed without installation effects which is similar to a bored pile in comparison with a jacked pile. The load test sequence shown in Table 7.1 was applied after the centrifuge had been spun to an acceleration level of 40g.

The jacked pile (Test 2 and 3), the pile was pushed down in flight 10D deeper to 20D depth from the soil surface with a penetration velocity of 0.067 mm/s. After installation, the test programme was carried out and starting with a static load test. Then three sets of four RLTs were performed, with each set followed by another SLT. The duration of the load was shortened for each set of four RLTs. This led to an increasing test loading velocity. Each of the four RLTs was carried out with a constant duration (slow 50 ms, average 20 ms or fast 10 ms) and the amplitude was changed to achieve a different displacement of the pile (1%D, 2%D, 5%D and 10%D). For the pile without installation effects (Test 24), the RLTs began without the installation phase and the first static load test SLT - 1. All load tests were displacement-controlled with the displacement pattern shown in Figure 7.1. Experience with dynamic tests leads to a preference for displacement control since

Table 7.1: Loading scheme of considered tests.

	Name	Test 2 - Huy (2008)	Test 3 - Huy (2008)	Test 24 - Chi (2012)	RLT time & displacement		
Test information					RLT1	RLT2	RLT3
	Installation	Jacked pile	Jacked pile	wished in place pile	slow	medium	fast
	Dr	54%	36%	45%	50 ms	20 ms	10 ms
	Dpile	11.3 mm	11.3 mm	16 mm			
Step	1	Installation	Installation	x			
	2	SLT - 1	SLT - 1	x			
	3	RLT2 - 1 - 0,01D	RLT3 - 1 - 0,01D	RLT24 - 1 - 0,01D			
	4	RLT2 - 1 - 0,02D	RLT3 - 1 - 0,02D	RLT24 - 1 - 0,02D			
	5	RLT2 - 1 - 0,05D	RLT3 - 1 - 0,05D	RLT24 - 1 - 0,05D			
	6	RLT2 - 1 - 0,1D	RLT3 - 1 - 0,1D	RLT24 - 1 - 0,1D			
	7	SLT - 2	SLT - 2	SLT - 2			
	8	RLT2 - 2 - 0,01D	RLT3 - 2 - 0,01D	RLT24 - 2 - 0,01D			
	9	RLT2 - 2 - 0,02D	RLT3 - 2 - 0,02D	RLT24 - 2 - 0,02D			
	10	RLT2 - 2 - 0,05D	RLT3 - 2 - 0,05D	RLT24 - 2 - 0,05D			
	11	RLT2 - 2 - 0,1D	RLT3 - 2 - 0,1D	RLT24 - 2 - 0,1D			
	12	SLT - 3	SLT - 3	SLT - 3			
	13	RLT2 - 3 - 0,01D	RLT3 - 3 - 0,01D	RLT24 - 3 - 0,01D			
	14	RLT2 - 3 - 0,02D	RLT3 - 3 - 0,02D	RLT24 - 3 - 0,02D			
	15	RLT2 - 3 - 0,05D	RLT3 - 3 - 0,05D	RLT24 - 3 - 0,05D			
	16	RLT2 - 3 - 0,1D	RLT3 - 3 - 0,1D	RLT24 - 3 - 0,1D			
	17	SLT - 4	SLT - 4	SLT - 4			

0,1D   0,1D   0,1D
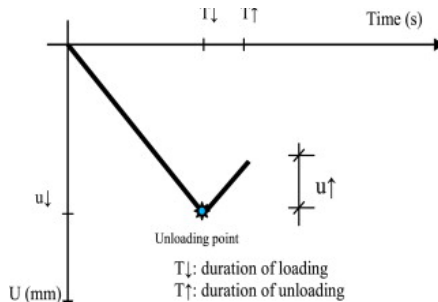
Figure 7.1: Displacement pattern of a rapid load test(after [7]).

it is more stable [8].

Pore pressure beneath the pile tip is measured by an integrated pore pressure transducer in the pile tip. Pore pressure in the sand model is measured in several different places beneath and at the flank of the loading location of the pile. The pore pressure transducers were positioned in the soil as shown in Figure 7.2.

Baskarp sand was used in the centrifuge test. Details of Baskarp sand properties as well as the sample preparation are described in Chapter 5. A viscous fluid is used, instead of water, in the considered tests with viscosities of up to 300 times the viscosity of water. The reason of using viscous fluid is in detail explained detailed in the following.
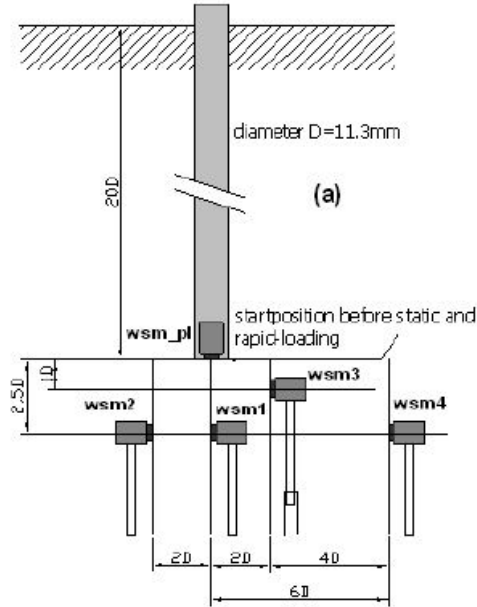
Figure 7.2: Positions of pore pressure transducers (after [7]). wsm_{pl} is the pore pressure transducer in the pile tip and $wsm1$, $wsm2$, $wsm3$, $wsm4$ are the pore pressure tranducers in the sand.

Scaling drainage conditions during the rapid load tests in sand

The effect of excess pore pressure in a rapid load test is expressed by a so-called dynamic drainage factor η [3, 10] as

$$\eta = \frac{GT}{g\rho R^2} k = \frac{GT}{\rho R^2} \frac{K}{\nu} \tag{7.1}$$

where G is the shear modulus [Pa], T is the duration of the loading [s], ρ is the water volumetric mass $[kg/m^3]$, k is the permeability of the sand $[m/s]$, K is the intrinsic permeability of the sand, g is the acceleration level and ν is the viscosity of the pore fluid.

In the centrifuge test with a scaling factor of $N = 40$, if water was used, the drainage factor would be N times smaller than in the prototype since time was scaled with factor $\frac{1}{N}$ and the radius with $\frac{1}{N^2}$. Hence, in order to have an identical drainage factor, a fluid with N times higher viscosity was used in the centrifuge tests. To compensate for the limitation of the loading duration in the centrifuge test, which was three times slower than the requirement, the viscosity of the fluid had to be increased three times (i.e. $3x40 = 120$ times higher than water). However, with this viscous fluid, the drainage factor of the fastest rapid load test was still too high to show any effect of excess pore pressure. Hence, it was decided to increase the fluid viscosity in order to slow down the drainage process and to render the phenomenon of interest more visible. Finally, the viscosity of the fluid in the centrifuge test was chosen to be 300 times higher than water viscosity and the drainage in the centrifuge was $300/40/3 = 2.5$ times slower than it would be in the prototype with Baskarp

sand.

7.1.3. Case study

In this chapter, the material point method is used to model the rapid load tests (RLT) for both the jacked pile as well as the pile without installation effect. The results are compared with the ones from the centrifuge test in order to validate the numerical method. After that, the effect of excess pore pressure is investigated in more detail.

The RLTs in test 2, test 3 (jacked pile) and test 24 (pile without installation effect) were chosen to be simulated. Due to the extensive computational time of the calculations and the limited time available, it was not possible to model all RLTs series in each test. For the pile without installation effects, the slow test 24 (step 3 to 6 in Table 7.1) is considered to be simulated. The results from the tests and the simulations were compared and described in section 7.2. The reason to choose test 24 is that no installation effect in the results of this first RLT. Hence, it is good to use the test results (of test 24) to calibrate several input parameters for the numerical model e.g. water stiffness or small strain stiffness of the hypoplastic model. For the pile without installation effect, there was no focus on fitting the results of MPM and the centrifuge tests. The goal of the comparison is rather on the jacked pile because the RLTs are strongly influenced by the installation process. MPM modelling of the RLT for the jacked pile is introduced in section 7.3.

In the centrifuge test, SLTs were carried out before and after each RLT. The comparison between the results of the SLTs provides information about changing soil conditions due to the RLTs performed in between SLTs. All force displacement curves during the SLTs are shown in Figure 7.3 for both the jacked pile and the pile without installation effects. In the case of the pile without installation effects, the deviation between each curve is significant, whereas a very small deviation can be seen in the SLTs curve of a jacked pile. It is assumed that the deviation is caused by the densification of sand due to RLTs performed in between two SLTs [7]. Therefore, the highest deviation is found in the results of the pile without installation effect, where the soil has not yet been compacted by the installation effect. Similarly, in the case of the jacked pile, the SLT curves of the pile in loose sand (Test 3) give a higher deviation than in medium dense sand (Test 2). For Test 2, SLT curves are almost the same, hence, it can be concluded that there is almost no change in soil condition due to RLTs performed in between two SLTs. Due to the fact that there are no soil condition changes, in section 7.3, the last rapid load test RLT2-3-0.1D with 10% of pile displacement (step 16 in Table 7.1) is chosen to model directly after the installation phase. It saved time and computational cost.
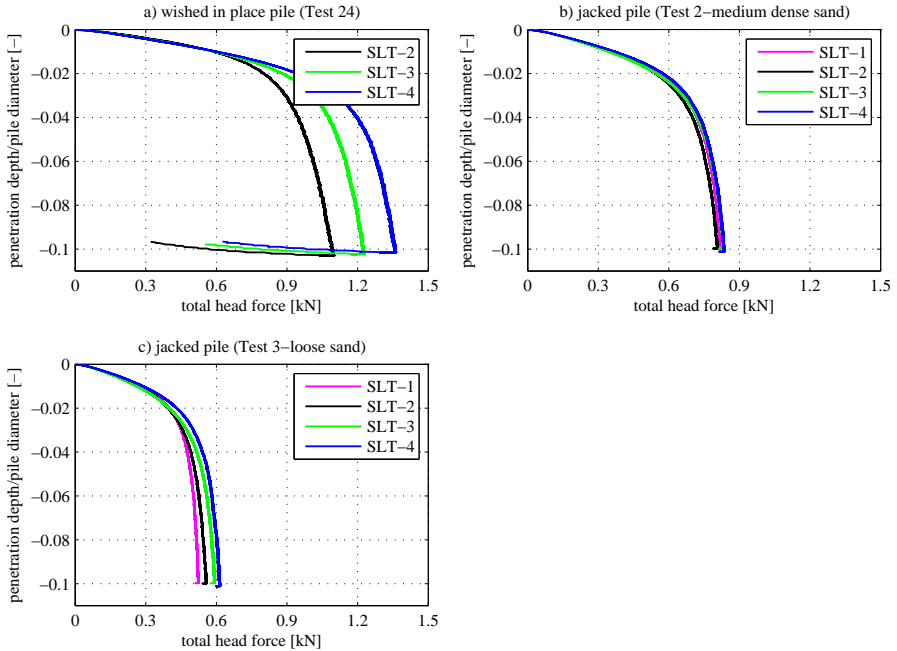
Figure 7.3: Force displacement curve during of SLTs after each set of RLT, results from centrifuge tests for medium dense sand $R_D = 54\%$ and pile diameter of 16 mm (comparison between wished in place pile and jacked pile).

7.2. MPM modelling of RLT for the pile without installation effects (Test 24)

In this section, a series of RLTs in Test 24, RLT24-1-1, RLT24-1-2, RLT24-1-3, RLT24-1-4 (step 3 to 6 in Table 7.1) are modelled by MPM. A detailed loading scheme was used in the centrifuge for the slow rapid load test, as shown in Table 7.2. In test 24, initial relative density of medium dense sand $R_D = 54\%$ was used.

7.2.1. Numerical model

Geometry

A prototype of a 0.64 m diameter pile in a fully saturated sand bed was modelled by a 16 mm model scale pile at an acceleration of $40 - g$ in the centrifuge test. In the numerical modelling, the geometry and results are scaled to prototype scale and used in simulations instead of applying an artificial acceleration field of $40 - g$. The problem geometry and the mesh discretization are shown in Figure 7.4. The length and depth of the investigated area are $18.5D$ and $35.4D$ respectively, in which $D = 0.64$ m is the pile diameter. Absorbing boundaries are placed along the lateral outer surface and along the base of the model to absorb waves travelling in both the solid and liquid phase. The detailed formulation of the absorbing boundary is presented in section 3.4.2.

For the simulations in this research, an implementation of MPM was applied in

Table 7.2: Loading scheme of slow rapid load tests for the pile without installation effects in Test 24 (model scale).

Number	Name	Direction	Displacement		Time	Velocity
			[% D]	[mm]	[ms]	[mm/s]
1	RLT24-1-1	Down	1	0.16	50	3.2
		up	0.5	0.08		1.6
		unloading				
2	RLT24-1-2	Down	2.5	0.4	50	8
		up	1	0.16		3.2
		unloading				
3	RLT24-1-3	Down	5	0.8	50	16
		up	1	0.16		3.2
		unloading				
4	RLT24-1-4	Down	10	1.6	50	32
		up	1	0.16		3.2
		unloading				
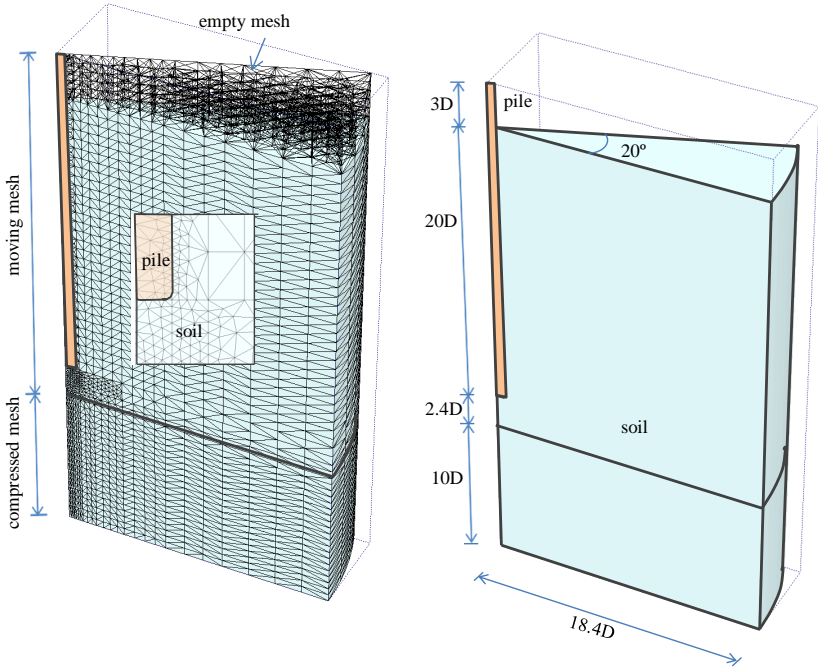
Figure 7.4: Mesh discretization and geometry of the considered problem for the pile without installation effects in Test 24.

which 4-noded tetrahedral elements with linear interpolation of displacements were used. The finite element mesh had a total of $28,005$ tetrahedral elements including the initially inactive elements, with a total $170,298$ of material points. The mesh

was refined near the pile. The inactive elements above the soil surface may be activated during the calculation process as material points are entering. Although the considered problem was axisymmetric, the simulations were three dimensional due to the nature of the MPM implementation. A $20°$ section of the axisymmetric problem was considered for discretization. A contact algorithm (section 3.4.3) was used to model the frictional contact between the pile and the soil. The chosen value of wall friction coefficient for all simulations in this study was assumed based on the characteristics of a polished steel pile surface, which was $\mu = tan\varphi = 0.194$. The simulations were done with two–phase material behaviour. The stresses in the soil were initiated using the so-called K0-procedure. The hydraulic conductivity of water k is $8.85E - 5$ m/s.

The pile was modelled as a rigid body. The shape of the pile tip was flat which is identical to the pile in the centrifuge test. However, the edge of the pile tip in the simulation was slightly curved to avoid numerical difficulties due to locking. The pile was initially embedded at $20D$ below the soil surface. The penetration of the pile into the soil was modelled by applying a prescribed velocity on the top of the pile. The amplitude of the prescribed velocity was generalized from the actual (measured) value by finding the mean value during the test as shown in Figure 7.5. To increase the accuracy of the results, the moving mesh concept was utilised in which the top part of the mesh moved together with the pile, while the lower part of the mesh was being compressed, ensuring that the refined elements are always located along the pile. More detail on the moving mesh concept is presented in Section 3.4.4.

Material parameters

Baskarp sand with a relative density of 45% (medium dense sand) is used in the centrifuge test. The hypoplastic constitutive model of Wolffersdorff [11], with the extension of intergranular strain by Niemunis and Herle [12], is used to model the soil behaviour.

For simulations of saturated soil, excess pore pressures can develop due to external loading. Soil has a time dependent behaviour which depends on permeability. To capture this behaviour and the development of excess pore pressure, a two-phase material with partially drained conditions is considered. The $v - w$ formulation is used, where the unknown primary variables are the solid velocity v and the fluid velocity w. The implementation of $v - w$ formulation in MPM is presented in Section 3.3. Additional parameters for modelling soil as a two phase material are listed in Table 6.1

For all calculations of RLT in this section, the original hypoplastic parameters of Baskarp sand listed in Table 5.3 are used. Parameter sets for small strain stiffness in the hypoplastic model are tabulated in Table 5.5.

In the following section, the influence of water stiffness K_w is studied to get a realistic behaviour of pore water pressure in comparison with the centrifuge test.
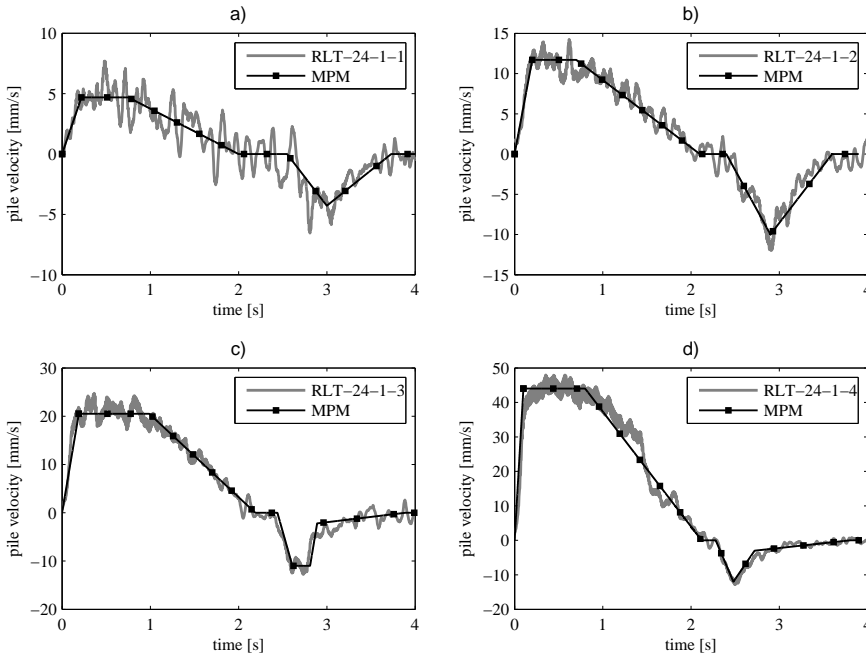
Figure 7.5: Prescribed velocity on the pile head during rapid load tests for wished in place pile with pile displacement of a) $1\%D$, b) $2\%D$, c) $5\%D$, d) $10\%D$.

7.2.2. Influence of water stiffness

In this section, the value of water stiffness K_w, hydraulic conductivity of water k and the initial stress K_0 are varied to investigate their influence on the rapid load test results, as well as on the generation of excess pore pressure, in order to get a realistic value of the excess pore pressure. The prescribed velocity used in this parametric study follows the pile velocity in test RLT-24-1-1, shown in Figure 7.5 a.

For the saturated soil, the compressibility of the water is related to the air content. Verruijt [13] introduced an equation to estimate a water bulk modulus K_w related to the degree of saturation as

$$K_w = \frac{p_{atm}}{1 - S_r} \tag{7.2}$$

with p_{atm} being the atmospheric pressure of approximately 100kPa. Hence, if assuming a degree of saturation of $S_r = 0.99$ the corresponding water bulk modulus K_w is estimated to be 10 MPa.

In Figure 7.6, the influence of the water stiffness on the generation of pore water pressure during the rapid load test is examined. Five different values of water stiffness $K_w = 81400$, 20000, 10000 8000 and 5000 kPa are chosen for comparison. As can be seen in Figure 7.6b, the water bulk modulus has a significant influence on the stiffness as well as the peak value of the excess pore pressure at tip. In fact, water is not fully incompressible, but a realistic value for the bulk modulus of water is very large. However, during the test preparation, the presence of a very small air bubble may significantly reduction of the water stiffness.

7

In conclusion, to attain a good match between the results of centrifuge tests and simulations regarding the generation of excess water pressure, the bulk modulus of water K_w is chosen as 8000 kPa for all rapid load test simulations.

7.2.3. Results and discussion

Changing of stress during the RLT-24-1-1

The horizontal and vertical stresses at different times during the rapid load test, $t = 0.75\,s$, $t = 2.55\,s$, $t = 3\,s$, and $t = 4\,s$, are plotted in Figure 7.7 and 7.8. From $t = 0 \rightarrow 0.75\,s$, the pile is pushed down fast with velocity of $v \approx 5\,mm/s$, then the increasing of both horizontal and vertical stresses, and positive excess pore water pressure is observed under the pile tip as shown in Figure 7.7 a, Figure 7.8 a, Figure 7.9 a, respectively. From $t = 0.75 \rightarrow 2.55\,s$, the pile is pushing down with decreasing velocity $v = 5 \rightarrow 0\,mm/s$, the pore water pressure around the pile tip is gradually dissipated. From $t = 3 \rightarrow 4\,s$, the pile is slightly pulled up, a minor negative excess pore pressure is observed under the pile tip. At the end of simulation, $t = 4\,s$, vertical effective stresses around the pile tip and pile shaft gradually reach zero (Figure 7.8 d).

Load-displacement curve during the RLT

Figure 7.10 shows the results of MPM simulation in comparison with the results of the centrifuge test. The simulation gives the peak value of the tip force and excess pore pressure which are similar as the ones of the centrifuge test. The simulated stiffness of the load displacement curve is slightly softer than in the result of centrifuge test. On the other hand, the generation of pore water pressure during the first second in the simulation is quite fast in comparison with the test result. In general, for the first rapid load test, RLT-24-1-1, both the simulation and test results are in good agreement.

After the first rapid load test with a pile displacement of $1\%D$, three additional rapid load tests were continuously modelled with a pile displacement of $2\%D$, $5\%D$ and $10\%D$ respectively. The results of load displacement curves during the simulations are plotted and compared with centrifuge test results in Figure 7.11.

Except the results of RLT-24-1-2, in which the simulation gives a slightly higher peak value of the pile tip force than in the centrifuge test, the pile tip forces in the other simulations are significantly smaller than in the centrifuge test (43% and 57% smaller in RLT-24-1-3 and RLT-24-1-4, respectively). One of the possible reasons for the lower tip force in the simulation after each cyclic loading might be that the constitutive model is not able to correctly model the cyclic behaviour. When compared a numerical triaxial of a compression test with the triaxial test on sand, Bauer and Wu [14] observed that a reversal from unloading to reloading, the stiffness becomes smaller while it should be larger. Other shortcoming in numerical simulation is that, cyclic loading with a given stress amplitude produces exactly identical stress strain cycles (ratcheting), which leads to the predicted strain in one-dimensional compression increase unlimitedly as the stress reaches infinity. The hypoplastic model in this thesis used the so-called "intergranular strain extension" to avoid excessive ratcheting in the case of cyclic loading (For more detail see Section 7.3.2).
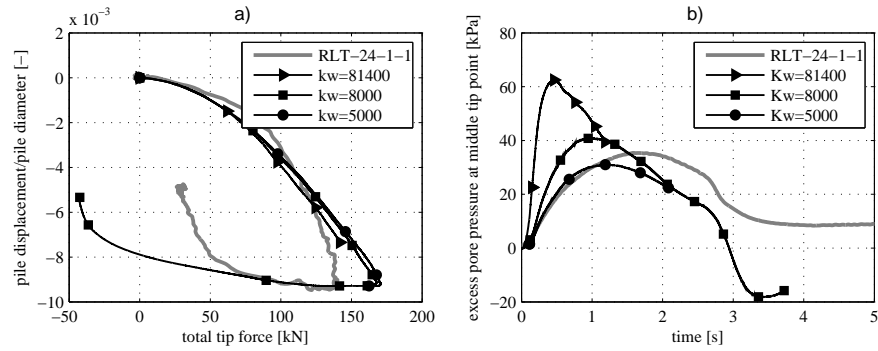
Figure 7.6: Influence of water bulk modulus K_w on the rapid load test results.(simulation with $K_0 = 0.46$ and $k = 8.85 x 10^{-5}$ m/s)
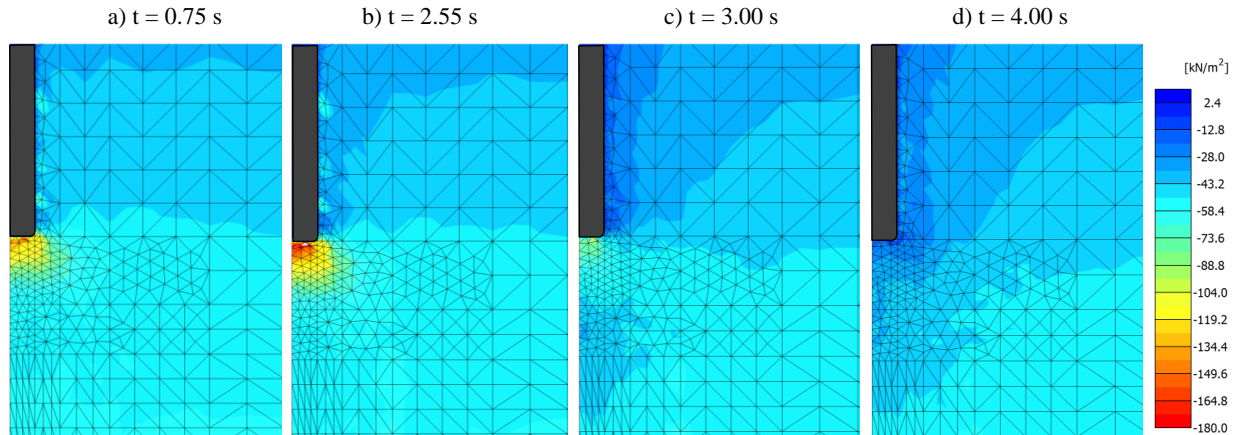

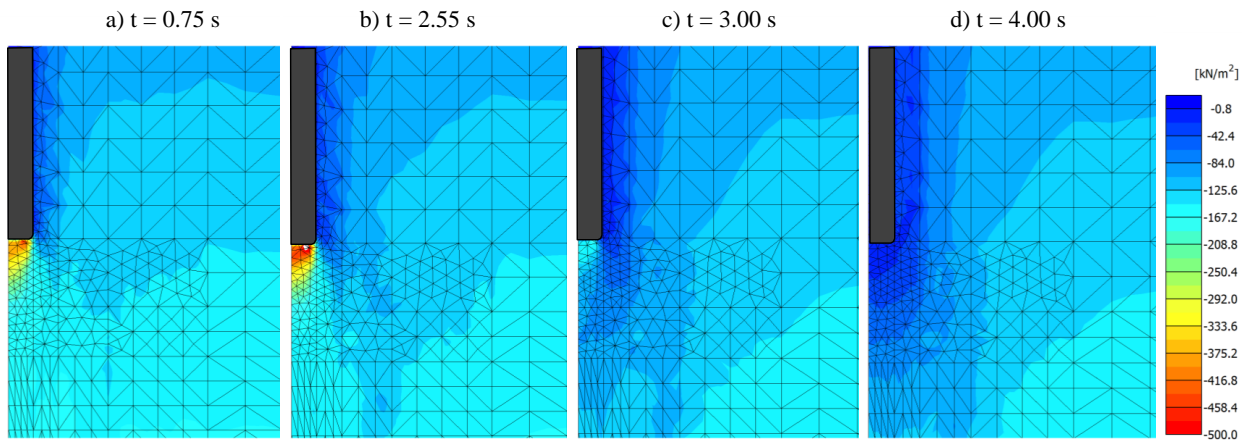Figure 7.7: Horizontal effective tress around the pile tip at different time during RLT 24-1-1

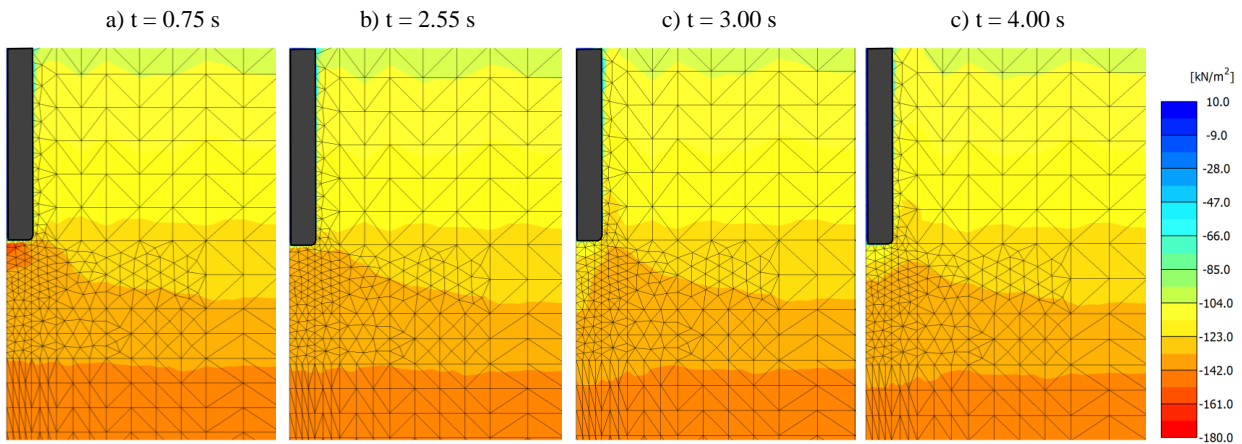Figure 7.8: Vertical effective stress around the pile tip at different time during RLT 24-1-1

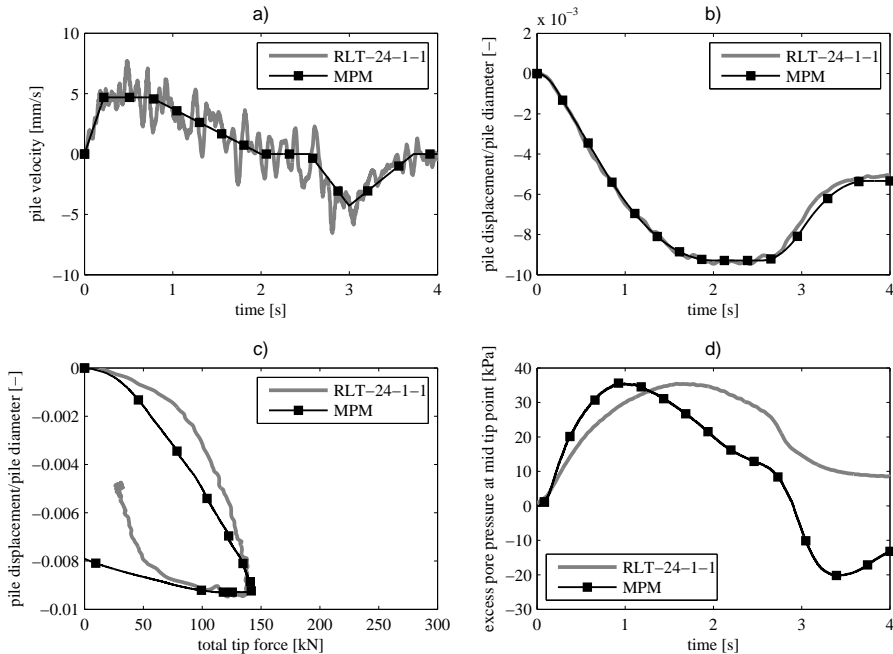Figure 7.9: Pore water pressure around the pile tip at different time during RLT 24-1-1

Figure 7.10: Comparison between centrifuge test and MPM for the first rapid load test RLT 24-1-1 (embedded pile with $1\%D$ displacement

As mentioned before, the purpose of this section is mainly to choose a good set of parameters for the validation of MPM with the centrifuge test. The numerical simulation of the centrifuge tests is focussed on the jacked pile with a 10%D pile displacement and will be discussed in the following section.

7.3. MPM modelling of RLT for jacked pile

In this section, the fast rapid load test RLT2-3-0.1D (medium dense sand) and RLT3-3-0.1D (loose sand) with 10% of pile displacement are simulated (step 1, 2 and 16 in Table 7.1).

7.3.1. Problem description

A prototype of a 0.452 m diameter pile in a fully saturated sand bed was modelled. The pile was initially embedded 10D below the soil surface and then pushed down 10D in flight to simulate the installation process. After this, the first SLT is modelled and followed by the RLT with 10%D of pile displacement. Details of the numerical model and the mesh discretization are similar as in Chapter 5 (Figure 5.2, 5.3). Absorbing boundaries are placed along the lateral outer surface and along the base of the model to absorb waves travelling in both the solid and the liquid phase. The detailed formulation of the absorbing boundary is described in section 3.4.2.

During the installation of the pile in the centrifuge test, the pile is pushed deeper in to the sand bed with a velocity of 0.167 mm/s. In the MPM simulation of the installation phase, a constant velocity of 20 mm/s is applied on the pile head. In
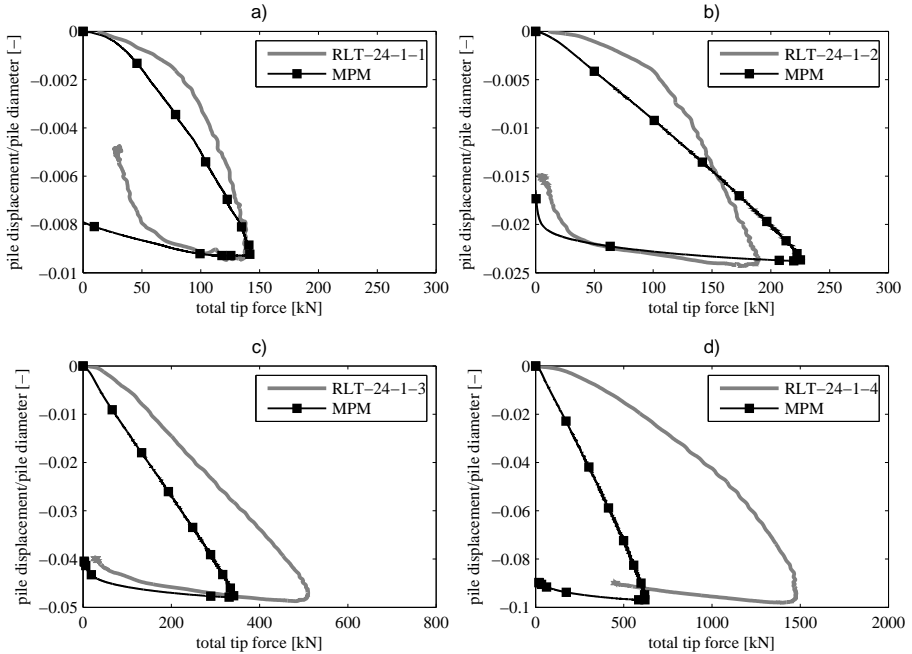
Figure 7.11: Load displacement curves during four rapid load test; comparison between centrifuge test and MPM for the pile without installation effect with pile displacement of a) $1\%D$, b) $2\%D$, c) $5\%D$, d) $10\%D$.
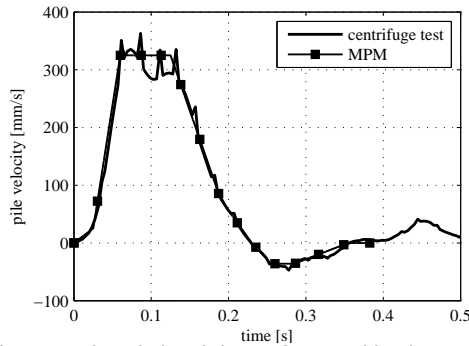

Figure 7.12: Prescribed velocity on the pile head during fast rapid load tests for jacked pile.

order to guarantee no excess pore pressure is generated during the installation, a higher value of hydraulic conductivity of $k = 8.85E-04$ m/s is used. This value is also used for the simulation of the SLT after the installation phase. Using a higher value of k also helps to increase the time step size and as a consequence, the computational cost reduces. The RLT is simulated with the same velocity and hydraulic conductivity as in the centrifuge test. A prescribed velocity, which is applied on the pile head during RLT is shown in Figure 7.12.

Baskarp sand with a relative density of 54% (medium dense sand) and 36% (loose sand) is used in the tests. The hypoplastic constitutive model of Wolffersdorff [11] with the extension of an intergranular strain by Niemunis and Herle [12] is used

to model the soil behaviour.

The $v - w$ formulation is used to simulate the saturated soil behaviour. Additional parameters for modelling soil as a two phase material are listed in Table 6.1. For all calculations of the rapid load test in this section, the original hypoplastic parameters of Baskarp Sand, listed in Table 5.3, are used. Parameter sets for small strain stiffness in the hypoplastic model are discussed in the following section.

As recommended in the previous section (7.2.2), the bulk modulus of water K_w is chosen as 8000 kPa, K_0 is 0.35 and hydraulic conductivity k is $8.85E - 5$ m/s for all rapid load test simulations.

7.3.2. Influence of small strain parameters on the results of RLT

As mentioned in Chapter 4, the hypoplastic model in this thesis is used with the so-called "intergranular strain extension" to avoid excessive ratcheting in the case of cyclic loading. Niemunis and Herle [12] proposed a method to determine the additional parameters for the extended model which is based on the theoretical considerations. The set of the parameters Niemunis and Herle gave for one sand was used successfully in many finite element simulations without further experimental investigations. Hence, this set IGS-3 (Table 7.3) is used in this thesis for most of the simulations in chapter 5 and 6 and section 7.2 of chapter 7. However, as shown in the previous section, after several loading cycles, the simulations of RLT gave significant lower values of total tip force in comparison with the centrifuge RLT. Furthermore, by evaluating the cyclic tests (resonant column, oedometric compression and triaxial shearing), Meier [15] revealed that the parameter m_R should depend on the stress state and density. In his calibration of a resonant column test on Karlsruhe sand together with post test calculation results, for $p_0' = 320$ kPa an $m_R = 6$ is obtained and for $p_0' = 20$ kPa an $m_R = 12$. Meier also found that, for the same stress $\sigma_v = -185$ kPa, an $m_R \approx 4.3$ was obtained for the loose sample ($e_0 = 0.9$) and $m_R \approx 3.0$ for the dense sample ($e_0 = 0.9$). Thus, it is concluded that a mean value should be taken for m_R, to fit the experimental results correctly in a relevant range of stress and density. The same stress and density dependence is conjectured for m_T, however, there has not been an experimental study with regard to determine the intergranular strain parameters. Meier [15] also suggested that $R = 10^{-4}$ can be treated as a independent material constant, and that $\chi = 1.0$ together with $\beta_\chi = 0.1$ are good starting values for calibration.

For Baskarp sand, no data is available on cyclic tests (e.g. oedometric compression tests with at least one unloading /reloading cycle) to calibrate m_R and $\beta_\chi = 0.1$ in order to realistically represent the increase in stiffness after a deformation reversal. Therefore in this section, the value of small strain parameters is taken as IGS-14 set in Table 7.3. Values of these parameters are chosen by trial and error to achieve the best fit with the centrifuge test. The influence of each small strain parameter on the results of RLT is individually investigated and shown in Appendix F.

Table 7.3: Small strain parameters for sand.

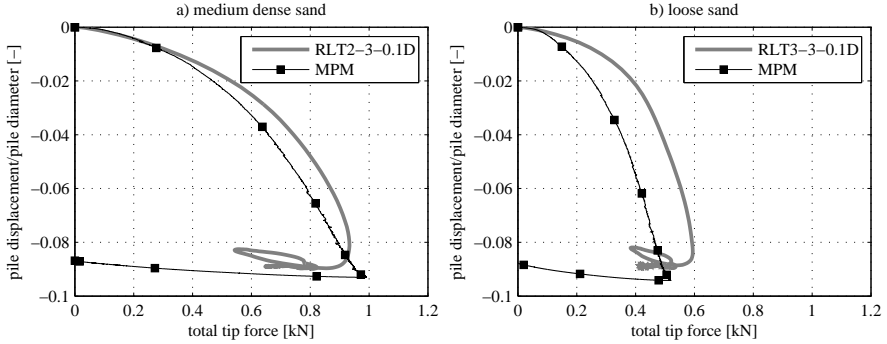| Name	R	m_R	m_T	χ	β_χ
IGS-3	10^{-4}	5	2	1	1
IGS-14	10^{-4}	7	7	1	0.2

Figure 7.13: Comparison between centrifuge test and MPM for a) medium dense sand and b)loose sand.

7.3.3. Results and discussion

Load displacement curve

The comparison between the results of the centrifuge test and the simulations using MPM are shown in Figure 7.13 for both medium dense sand and loose sand. A good fit between simulation and centrifuge results is found for medium dense sand. In loose sand, the simulation gives a bit lower peak value (about 16% less) and a softer behaviour than in centrifuge test. It may be related to the deviation of SLTs in between RLTs as explained in Section 7.1.3. In loose sand, a deviation of 16% is observed between the first and the last SLT, due to the densification of the soil during many RLTs from step 3-15 (in Table 7.1) in the centrifuge. Therefore, for loose sand, the omission of many RLTs in between, and the fact that only the last RLT in step 16 is modelled, causes the difference in results between the MPM and centrifuge test.

Pore water pressure generation during rapid load test

Figure 7.14 gives an overview of the change in pore pressure at the beginning of the RLT and the size of the influence zone. Close to the pile 1D, a high change in PWP and in the size of the influence zone up to 5D wide from the pile centre and about 5D depth under the pile tip is observed. Increasing pore pressure (positive excess pressures) is generated by a compression of soil and a decreasing pore pressure(under pressures) is caused by dilative soil behaviour during failure [8]. Under the pile tip, the soil is compressed during pile penetration and a nose cone is formed [16]. The formation of the nose cone is also confirmed in chapter 5 by MPM simulation. As the pile penetrates into the sand, the nose cone moves with the pile and the surrounding sand is sliding and sheared along the edge of the nose cone. The pore pressure response during the RLT is dependent on the deformation pattern and the existence of the pore flow in the soil region underneath the pile tip [7].
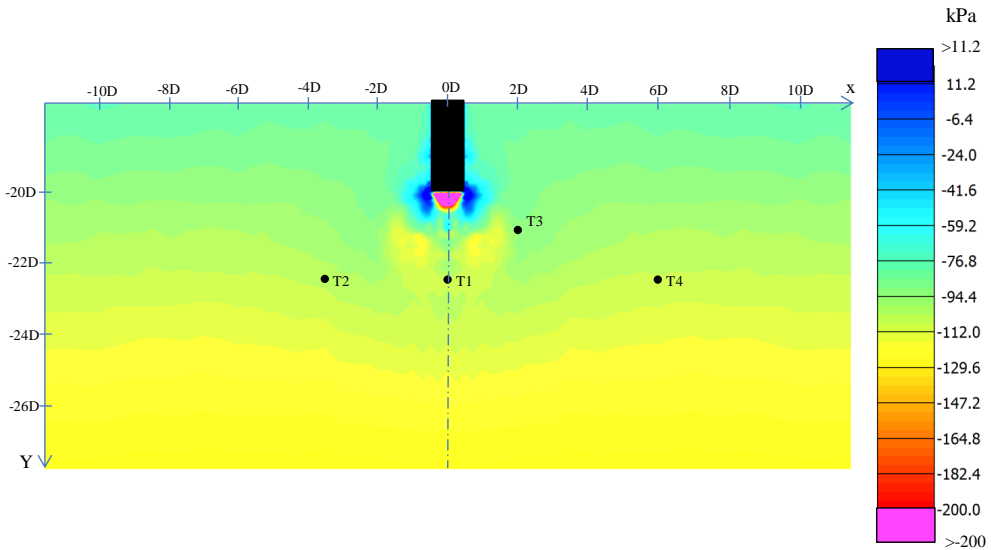
Figure 7.14: Pore pressure generated at time 4: t = 0.23 s in rapid load test for medium dense sand.

Figure 7.15 shows in detail how the pore pressure around the pile tip is changing at different loading times during RLT. The excess pore pressure inside the nose cone first increases to a maximum value then starts to dissipate when the pile is unloading. It may be due to the flow through the saturated soil, that the pore pressure equalises.

Along the edge of the nose cone and the pile shaft, the soil particles are sheared and slide, and this shear behaviour is dominant over the compression behaviour [16, 17]. Because of the dominance of the shear behaviour along the edge of the nose cone, the excess pore pressure in this zone is negative during most of the loading duration.

In the test set up, four pore pressure transducers (T1, T2, T3, T4) were placed at four different locations in the soil underneath the pile, and a fifth transducer was fitted on the pile tip to measure the response of pore pressure during the load tests. Figure 7.16 illustrates the changing of excess pore pressure at different locations in the centrifuge test in comparison with the MPM simulation for medium dense sand. As can be seen, the excess pore pressure observed at the pile tip (Figure 7.16 a) in the simulation is quite similar in evolution trend and the peak value with the change of pore water pressure in the centrifuge test. No excess pore pressure is observed at location T4 (Figure 7.16 d) for both simulation and measurement. For transducer T1 (Figure 7.16 b), placed at a distance 2,5D directly underneath the pile tip, MPM simulation gives positive excess pore pressure during the test, whereas the centrifuge test first gives a negative excess pore pressure during half of the time, then changes to a positive excess pore pressure. Huy [7] stated that, the decrease in pore pressure at the location of transducer T1 in centrifuge test seems very unrealistic. The pore water pressure would be expected to increase at the start of the test due to compression, and then to decrease but
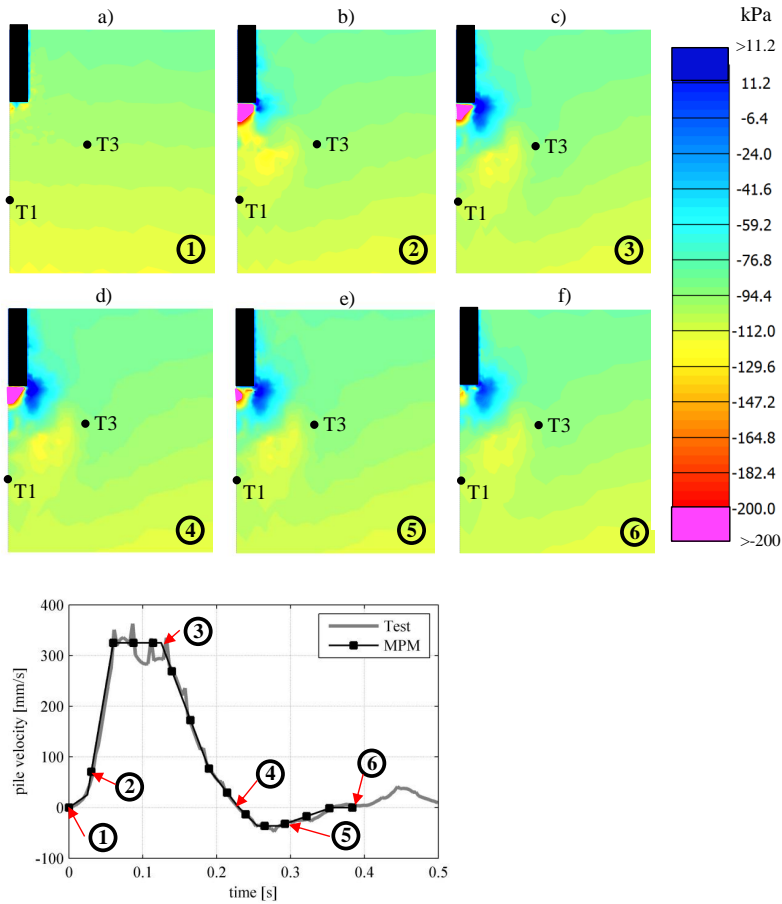
Figure 7.15: Pore pressure generated at different time during rapid load test for medium dense sand.

the measurement shows an opposite trend. An explanation for the appearance of negative excess pore pressure in the centrifuge test is due to the set-up and the size of the transducer (6 mm in diameter), which is large in comparison with the size of the pile tip [7]. When the pile is pushed down during the test, the transducer acts as an obstacle in the soil. Hence the soil particles slide around the transducer instead of moving straight downward and as a consequence, a shear surface is formed. At the location of transducer T3, a similar trend of increasing pore pressure at the start of the load test, which then decreases due to the sand dilatancy, is observed in both the centrifuge test as well as the MPM simulation (Figure 7.16 c). However the measurement shows a relatively higher increase in pore pressure in comparison with the result from the simulation. It is due to the horizontal displacement of sand particles in this region [16] and the set-up of the transducer that the compression of the soil in front of the porous stone increase [7]. Hence the set up causes pore pressure to increase more than the real value without the transducer.
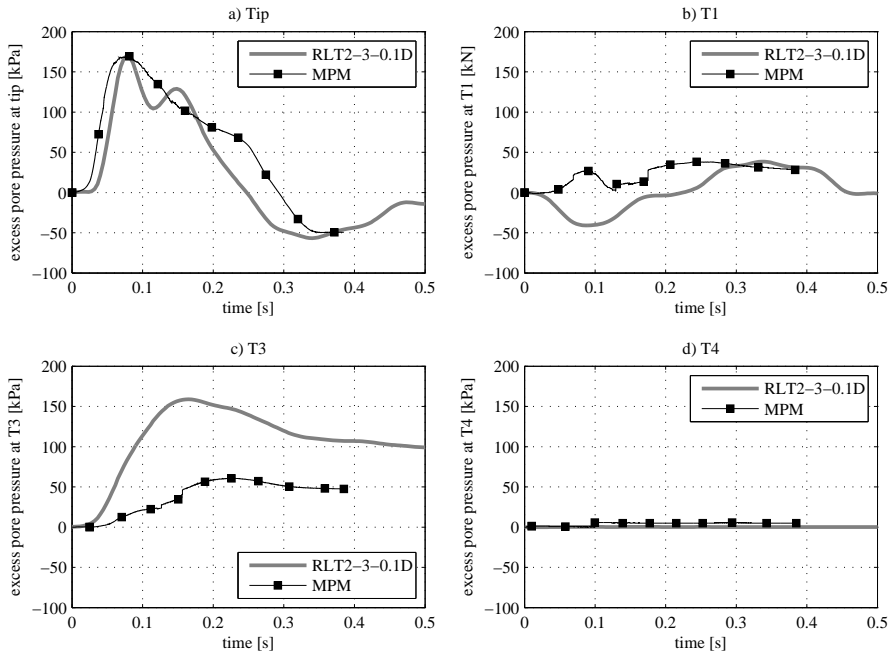
Figure 7.16: Pore pressure at different location during rapid load test for medium dense sand. Comparison between centrifuge test and MPM simulation.

7.4. Conclusions

Several RLTs are numerically simulated by the MPM-model. In this section the results are summarized.

A series of RLT in test 24 were simulated. The bulk modulus of water K_w is chosen as 8000 kPa to attain a good match between the results of centrifuge tests and and simulation regarding the generation of excess water pressure. For the first test RLT 24-1-1 with a pile displacement of $1\%D$, the simulations gives the peak value of the tip force and excess pore pressure are similar as the ones of the centrifuge test. However, in the test RLT 24-1-3 and RLT 24-1-4, the simulations result in significant smaller tip force values than in the centrifuge tests, which can be due to the constitutive model is not able to correctly model the cyclic behaviour.

In order to avoid excessive ratcheting in the case of cyclic loading, It is important to use the hypoplastic model with the intergranular strain extension. There are 5 input parameters in the intergranular strain extension, m_R, m_T, R, χ, β. The parameter m_R and m_T of the intergranular strain extension should depend on the stress state and density [15]. Hence a mean value should be taken for m_R and m_T to fit correctly the experimental results in a relevant range of stress and density. $R = 10^{-4}$ can be treated as a material independent constant, and that $\chi = 1.0$ together with $\beta_\chi = 0.1$ are good starting value for calibration. In this study, for Baskarp sand, the value of small strain parameters is taken as $R = 10^{-4}$, $m_R = 7$, $m_T = 7$, $\chi = 1.0$ and $\beta_\chi = 0.2$. The values of the parameters are chosen by trial and error to achieve the best fit with the centrifuge test since no cyclic test data

are available to calibrate.

The results of MPM simulations are compared with the results from the centrifuge tests. A good fit of a load displacement curve between simulation and centrifuge results is found for medium dense sand. In loose sand, the simulation gives a slightly lower peak value (about 16% less) and a softer behaviour than in centrifuge test. The observation of excess pore pressure at the pile tip in the simulation is quite similar in evolution trends as well as the peak value from centrifuge test.

Close to the pile $1D$, a high change in pore water pressure is observed and the size of the influence zone is up to $5D$ wide from the pile centre and about $5D$ depth under the pile tip.

Under the pile tip, the soil is compressed during the pile penetration and a nose cone is formed. The formation of the nose cone under the pile tip influences the generation of pore water pressure. As the pile penetrates into the sand, the nose cone moves with the pile and the surrounding sand is sliding and sheared along the edge of the nose cone. Increasing pore pressures are generated by a compression of soil and decreasing pore pressures are caused by dilative soil behaviour during failure. The excess pore pressure inside the nose cone first increases to a maximum value, then starts to dissipate when the pile is unloading. It may be due to the flow through the saturated soil that the pore pressure equalises. Along the edge of the nose cone and the pile shaft, the excess pore pressures in this zone are negative during most of the loading duration because of the dominance of the shear behaviour in this area.

7 References

[1] A. Holeyman *et al.*, *Technology of pile dynamic testing,* in *The 4th International Conference on the Application of Stress-Wave Theory to Piles* (1992).

[2] K. H. Karkee M., Horiguchi T., *Static and dynamic tests for evaluation of the vertical load bearing capacity of piles,* in *In 22nd Annual memeber's Conference, Deep Foundation institude* (1997) pp. 353–361.

[3] P. Holscher and F. Barends, *The relation between soil-parameters and one-dimensional models,* in *Proceedings of the Fourth International Conference on the Application of Stress-Wave Theory to Piles, The Hague, NL, 90 5410 082 6, Balkema, Rotterdam* (1992).

[4] P. Middendorp, P. Bermingham, and B. Kuiper, *Statnamic load testing of foundation piles,* in *Proceedings, Fourth International Conference of Applications of Stress-Wave Theory to Piles, The Hague, Netherlands* (1992) pp. 581–588.

[5] M. McVay, C. Kuo, and A. Guisinger, *Calibrating resistance factor in load and resistance factor design of Statnamic load testing. Florida Dept. of Transportation*, Tech. Rep. (March 2003, Research Report 4910-4504-823-12, 2003).

[6] P. Holscher, A. van Tol, and P. Middendorp, *European standard and guideline for rapid load test in santos, j.a,* in *the 8th International Conference on*

the Application of Stress-Wave Theory to Piles, Lisbon, Portugal (2008) pp. 699–705.

[7] N. Huy, *Rapid load testing of piles in sand: effect of loading rate and excess pore pressure*, Ph.D. thesis, Delft University of Technology (2008).

[8] P. Holscher, A. F. van Tol, and N. Huy, *Rapid pile load tests in the geotechnical centrifuge,* in *the 9th International Conference on Testing and Design Methods for Deep Foundations, Japanese Geotechnical Society* (2012) pp. 257–263.

[9] N. Chi, *Rapid pile loading centrifuge test - factual report*, Tech. Rep. (Deltares, 2012).

[10] N. Huy, A. Van Tol, and P. Holscher, *A numerical study to the effects of excess pore water pressure in a rapid pile load test,* in *Proceedings of the 14th European Conference on Soil Mechanics and Geotechnical Engineering* (2007) pp. 247–252.

[11] P.-A. von Wolffersdorff, *A hypoplastic relation for granular materials with a predefined limit state surface,* Mechanics of Cohesive-frictional Materials 1, 251 (1996).

[12] A. Niemunis and I. Herle, *Hypoplastic model for cohesionless soils with elastic strain range,* Mechanics of Cohesive-frictional Materials 2, 279 (1997).

[13] A. Verruijt, *An introduction to soil dynamics*, Vol. 24 (Springer Science & Business Media, 2009).

[14] E. Bauer and W. Wu, *A hypoplastic model for granular soils under cyclic loading,* (1993) pp. 247–258.

[15] T. Meier, *Application of hypoplastic and viscohypoplastic constitutive models for geotechnical problems* (Inst. für Bodenmechanik und Felsmechanik, 2009).

[16] D. J. White, *Investigation into the behaviour of pressed-in piles*, Ph.D. thesis, University of Cambridge (2002).

[17] E. Robinsky and C. Morrison, *Sand displacement and compaction around model friction piles,* Canadian Geotechnical Journal 1, 81 (1964).

7

8

Conclusion

8.1. Conclusion

This thesis presents a numerical modelling approach to investigate the stress and density change in the soil during pile installation of a jacked and driven pile in dry and saturated sand. The installation of displacement piles in sand leads to severe changes in the stress state, density and soil properties around the pile tip and shaft, and, therefore, has a significant influence on the pile bearing capacity. Most current numerical methods predicting pile capacity do not take installation effects into account, as large deformations can lead to mesh distortion and non-converging solutions. For a correct analysis of the pile installation and its consequential effects the numerical model should be able to deal with:

- large deformations

- adapted soil properties due to stress and density changes

- very high stresses and the related crushing

- a two phase medium, with the possibility of full liquefaction

8.1.1. Numerical model

Material point method

In this study, the Material Point Method (MPM) is applied to simulate the pile installation process and the subsequent static pile loading tests. MPM is an extension of the Finite Element Method (FEM), which is capable of modelling large deformations and soil-structure interactions. This study utilizes the moving mesh algorithm where a redefined computational mesh is applied in the convective phase. This allows a fine mesh to be maintained around the pile tip during the installation process and improves the accuracy of the numerical scheme, especially for the contact formulation. In chapter 5, several calculations were performed using the material point

method in order to model the installation process as well as the static pile load test of a jacked displacement pile in sand. The results of the simulations are compared with centrifuge experiments. It shows the capability of the used numerical scheme to simulate the installation process of jacked piles in sand. In order to successfully simulate the centrifuge test, it is necessary to account for a reduction of the friction and dilation angles at very high stress levels. With this reduction, the MPM simulations show good agreement with the centrifuge test results for both the installation process as well as the Static Load Test (SLT) after the installation both for the simulation with the Mohr Coulomb and the hypoplastic model. The pile capacity given by MPM simulations results in a good agreement with the load-displacement curve suggested in NEN-EN $9997 - 1, 2016$ the Dutch code for geotechnical design. In conclusion, MPM as applied in this study, instead of classical FEM, is well suited to model the large deformations and flow of material occurring during the pile installation process.

Constitutive model for crushed sand
In chapter 4, a constitutive model for granular materials which considers grain crushing effects, is developed in the framework of hypoplasticity. As grain crushing occurs, the behaviour of granular material can be significantly affected. In this study, several empirical relations between peak strength, uniformity coefficient and stiffness of sand, depending on stress level or amount of grain crushing have been derived for different sands based on experimental results in the literature. These relations are applied to improve a basic hypoplastic constitutive model based on the changes of stress level or grain size distribution. In the proposed modified hypoplastic model only two additional physical parameters, namely uniformity coefficient C_u and mean grain size d_{50} are incorporated. The afore mentioned parameters are crucial in the propose model. The empirical relations involving grain-crushing of the modified hypoplastic model are implemented in Plaxis, or in MPM, as a user-defined soil model. The validation of the modified model for three different types of sand under the triaxial test response with cell pressures up to 30 MPa is presented and shows a significantly better correspondence in both stress and strain in regard to the original basic hypoplastic model. The modified hypoplastic model for crushed sand is applied to model the installation process of a jacked pile in sand in chapter 5 (section 5.6). The importance of incorporating grain crushing effect into the hypoplastic model is confirmed by a significant improved load-displacement behaviour in simulation which is more closer with centrifuge result. Hence taking into account grain crushing in the hypoplastic constitutive model can be considered as one of the important factors to successfully model the pile installation as well as predicting the pile bearing capacity.

8.1.2. Installation effects
Installation of a jacked pile in dry sand
- The numerical analyses of a jacked pile installation in dry sand show significant differences of the soil stresses and strains around the pile after installation compared with the initial K_0-state. During installation, soil is pushed

aside by the pile, which leads to densification around the pile and a very high lateral stress at the pile tip. The influence of the installation extends to 8 pile diameters in horizontal direction from the centre of the pile and 7 pile diameters below the pile tip.

- Under the flat pile tip, the 'nose cone' is observed. The 'nose cone', which is referred to as a highly compressed region below the pile tip, has a central core that is stationary relative to the pile tip. The soil is sliding out from the nose cone and flowing around the shaft of the pile. Due to a highly densified 'nose cone' formed under flat pile tip, it generates a very high vertical stress underneath the pile. With the high vertical stresses, the flat pile tip results in a 25% higher total pile tip force than the triangular pile tip at the end of installation.

- A significant densification of the soil around the pile after jacked installation is observed for both medium dense and loose sand, except in a small dilative zone near the end of the pile shaft and around the corner of the pile. The dilative zone may be explained due to the high shear strains in the soil surrounding the corner pile. Hence, the compaction of the soil close to the pile is superimposed by the shearing process, while at a greater distance from the pile corner the compaction is dominant, which is in line with the findings of other researchers ([1]). For medium dense sand at a distance of $0.5D$ which is next to the pile shaft, a void ratio increase due to dilation is observed almost along the whole pile shaft, whereas, the dilation is only seen in the corner of the pile in the case of loose sand. For both medium dense and loose sand, the lowest void ratio value is found just under the pile tip which is considered as the highest densification zone. The densification gradually reduces when the distance from the pile increase.

- As a consequence of the change in soil state after installation, a significantly higher pile bearing capacity is observed during SLT as compared to simulations without installation effects and thus emphasizes the importance of accounting for installation effects when simulating the SLT. The results could be compared with findings in the literature regarding the ratio between pile capacity of non-displacement and displacement piles. The ratios between the base capacities ranges from 0.18 for loose to 0.33 for dense sand according to a data base in [2]. The ratios in this research are between 0.31 and 0.34 for the base capacity at a penetration of $10D$.

Installation of an impact driven pile in dry sand and saturated sand

- For impact driven piles in both dry and saturated sand, there is a significant reduction in the horizontal stress close to the pile shaft during dynamic pile installation. This behaviour has also been observed in various field tests [3, 4] and numerical studies [1, 5, 6].

- In dry sand simulations for driven piles, the compaction of the soil around the pile is much larger than that of the jacked pile due to the cyclic and dynamic

shearing resulting in a lower radial stress around the pile shaft. Generally, if the volume decrease caused by a densification of the soil is higher than the volume of soil pushed away by the pile, a relaxation of the radial stress at the shaft can be expected. If instead the densification is smaller than the displaced soil volume, the radial stress will increase [1]. Hence, in dry sand, jacked piles result in higher stiffness and capacity than driven piles due to the higher radial stress at both the pile shaft and the pile toe.

The disturbance zone is, due to pile driving, extended to a distance of about $5D$ from the pile centre and no change occurs in the void ratio below the distance of $8.5D$ from the pile tip. The largest compaction can be found at the position of $6.5D$ above the pile tip and close to the pile shaft.

- In saturated sand simulations, the influence of the pore water pressure on pile installation processes is significant. An increase of excess pore water pressure around the pile tip during installation is observed. As a consequence of the effective stress reaching zero value, the soil shows a tendency to liquefy in the area around the installed pile. Furthermore, there is almost no compaction of the soil around the driven pile during installation in comparison to the jacked pile.

  The zone, in which the radial stress is reduced to nearly zero, is extended to a distance of about $2.5D$ from the pile center. At a distance between $2.5D - 7D$ from the pile centre, a significant increase in radial stress is obtained. The peak value of stress in this zone is at the same level with the pile tip and has a value of about 2 times the initial stress. The influence zone is about $8D$ from the pile centre and $13.5D$ below the pile tip due to installation.

8.1.3. The generation and dissipation of excess pore pressure

For simulations of pile installation in saturated soil, excess pore pressures can develop due to external loading. Soil has a time dependent behaviour which is contingent on permeability. To capture the time dependent behaviour and the development of excess pore pressure, a two-phase material with partially drained conditions is considered. The $v - w$ formulation is used, where the unknown primary variables are the solid velocity v and the fluid velocity w.

Pore water pressure during pile installation

During the installation process of an impact driven pile, the excess pore water pressure is gradually built up. During the loading time of each blow, pore water pressure increases rapidly and then reduces during unloading time. Under the pile tip pore water pressure reduces significantly and tensile stress is observed after a few blows, especially at location $1D$ below the pile tip. For the residual particles in the zone around the pile tip (extended to a distance of about $2.5D$ from the pile centre), there still remains some excess pore pressure after each blow, which causes the excess pore water pressure around the pile tip to increase with time.

The generation of a negative excess pore water pressure, which appeared under the pile tip during each blow, results in an increase of the effective stresses and in

more difficulty for a deeper penetration of the pile. Therefore, according to these simulations, it is easier to hammer the pile in dry sand than in saturated sand, easier as well as in loose sand than in dense sand.

Pore water pressure during pile rapid load test

Several RLTs are numerically simulated by the MPM-model in chapter 7. The results from simulations are in good agreement with measurements in term of the load displacement curve as well as the generation and dissipation of excess pore pressure at the pile tip during RLT.

Closed to the pile $1D$, a high change in pore water pressure is observed and the size of the influence zone up to $5D$ wide from the pile centre and about $5D$ depth under the pile tip.

Increasing pore pressures (positive excess pressures) are generated by a compression of soil and a decreasing pore pressure(under pressures) are caused by dilative soil behaviour during failure [7]. Under the pile tip, the soil is compressed during pile penetration and a nose cone is formed [8]. As the pile penetrates into the sand, the nose cone moves with the pile and the surrounding sand is sliding and sheared along the edge of the nose cone. The pore pressure response during the RLT is dependent on the deformation pattern and the existence of pore flow in the soil region underneath the pile tip [9]. The excess pore pressure inside the nose cone first increases to a maximum value, then starts to dissipate when the pile is unloading, possibly due to the flow through the saturated soil that equalises the pore pressure. Along the edge of the nose cone and the pile shaft, the soil particles are sheared and slide and this shear behaviour is dominant over the compression behaviour [8, 10]. Because of the dominance of the shear behaviour along the edge of the nose cone, the excess pore pressures in this zone are negative during most of the loading duration.

8.2. Recommendation

A constitutive model for granular materials in the framework of hypoplasticity is developed which takes grain crushing effects into consideration. The importance of incorporating the crushing effects in the constitutive model is confirmed. This study considers stress dependency of five parameters $\alpha, \beta, e_i, e_c, e_d$ of the hypoplastic model. However, parameters h_s, n and φ_c are most likely influenced by grain crushing and by stress level as well [11]. Hence, further investigation should be carried out to improve the model, which may lead to a better correspondence with test data.

The stress/strain paths observed around the pile during penetration is complex. The constitutive models are known to have limitations for more complex problems. Further investigation of the physical test model utilizing photo-elastic measurements to observe the stress/strain paths.

The importance of including pile installation effects in numerical simulations, is demonstrated. However, simulating the entire penetration process of all piles of a practical application by means of MPM is expensive and not practical in engineering. Ideally, a method should be developed to incorporate the installation effects around

the wished-in-place pile to account for these effects [12]. It would leads to a significantly reduction in the computational demand, in particular for situations with more than one pile.

References

[1] K. Mahutka, F. Konig, and J. Grabe, *Numerical modelling of pile jacking, driving and vibro driving.* in *International conference on Numerical Simulation of Construction Processes in Geotechnical Engineering for Urban Environment* (Bochum, Rotterdam, 2006).

[2] T. A. Gavin K, Cadogan D and C. P, *The base resistance of non–displacement piles in sand. part i: field tests.* Proceedings of the Institution of Civil Engineers–Geotechnical Engineering 166, 540 (2013).

[3] E. Ng, *Pile foundation. the behaviour of single pile in cohesionless soils,* Federal Highway Administration Report (1988).

[4] G. Axelsson, *Long-term set-up of driven piles in sand.*, Ph.D. thesis, Institutionen för anläggning och miljö (2000).

[5] J. Grabe, T. Pucker, and T. Hamann, *Numerical simulation of pile installation processes in dry and saturated granular soils,* in *International Conference on Numerical Methods in Geotechnical Engineering, NUMGE, Delft, The Netherlands,*, Vol. 1 (CRC Press, 2014) pp. 663–668.

[6] V. Galavi, L. Beuth, B. Z. Coelho, F. S. Tehrani, P. Hölscher, and F. Van Tol, *Numerical simulation of pile installation in saturated sand using material point method,* Procedia Engineering 175, 72 (2017).

[7] P. Holscher, A. F. van Tol, and N. Huy, *Rapid pile load tests in the geotechnical centrifuge,* in *the 9th International Conference on Testing and Design Methods for Deep Foundations, Japanese Geotechnical Society* (2012) pp. 257–263.

[8] D. J. White, *Investigation into the behaviour of pressed-in piles*, Ph.D. thesis, University of Cambridge (2002).

[9] N. Huy, *Rapid load testing of piles in sand: effect of loading rate and excess pore pressure*, Ph.D. thesis, Delft University of Technology (2008).

[10] E. Robinsky and C. Morrison, *Sand displacement and compaction around model friction piles,* Canadian Geotechnical Journal 1, 81 (1964).

[11] I. Herle and G. Gudehus, *Determination of parameters of a hypoplastic constitutive model from properties of grain assemblies,* Mechanics of Cohesive-frictional Materials 4, 461 (1999).

[12] H. K. Engin, *Modelling pile installation effects: a numerical approach*, Ph.D. thesis (2013).

8

Solution procedure for a single time step of one-phase dynamic MPM

The implement of MPM solution procedure for one time step consists of the following phases and steps

1. Initialization phase

   In this phase, all the information of material points within the background mesh such as position, mass, body forces, tractions and other properties of continuum to material points is determined.

   Consider a tetrahedral element which has 1 or 4 or 8 or 10 or 20 material points inside. Each material point p is predefined an initial local position $\boldsymbol{\xi}_p$ inside the parent element. The global position $\mathbf{x}_p$ is calculated as:

$$\mathbf{x}(\boldsymbol{\xi}_p) \approx \sum_{i=1}^{n_{en}} N_i(\boldsymbol{\xi}_p)\mathbf{x}_i \tag{A.1}$$

   in which n_{en} is the number of nodes per element, $N_i(\boldsymbol{\xi}_p)$ is the shape function of node i which is evaluated at the local position of material point p and $\mathbf{x}_i$ is the global position of node i.

   All material points inside the same element have initially the same portion of the element volume, therefore the initial volume associated with material point p is obtained as

$$\Omega_p = \frac{1}{n_{ep}} \int_{\Omega_e} \mathrm{d}\Omega \approx \frac{1}{n_{eq}} \sum_{q=1}^{n_{eq}} \omega_q |\mathbf{J}(\boldsymbol{\xi}_q)| \tag{A.2}$$

   with n_{ep} and n_{eq} denote the number of material points and Gauss points in the element respectively, ω_q is the integration weight of Gauss point q and $\mathbf{J}$

is the Jacobian matrix. The mass of the material point m_p is then determined based on the volume associated with material point Ω_p and its density ρ_p,

$$m_p = \Omega_p \rho_p \tag{A.3}$$

The gravity force of particle p is calculated as

$$\mathbf{f}_p^{grav} = m_p \mathbf{g} \tag{A.4}$$

where $\mathbf{g}$ is gravitational acceleration vector.

2. Lagrangian phase, solution phase for a time step t to $t + \Delta t$

   (a) Mapping from material points to nodes
      i. Compute nodal mass

$$m_i^t \approx \sum_{p=1}^{n_{ep}} m_p N_i(\boldsymbol{\xi}_p^t) \tag{A.5}$$

      ii. Compute nodal momentum

$$m_i^t \mathbf{v}^t \approx \sum_{p=1}^{n_{ep}} m_p N_i(\boldsymbol{\xi}_p^t) \mathbf{v}_p^t \tag{A.6}$$

      iii. Compute traction force

$$\mathbf{f}_i^{trac,t} = \sum_{p=1}^{n_{ebp}} N_i(\boldsymbol{\xi}_p^t) \tilde{\mathbf{f}}_p^{trac}(\boldsymbol{\xi}_p^t) \tag{A.7}$$

      in which, n_{ebp} denotes the number of boundary particles inside the element which are located next to the loaded surface and $\tilde{\mathbf{f}}_p^{trac}$ is the traction force assigned to particle p. The way to calculate the traction force is detailed in section ??.
      iv. Compute gravity force

$$\mathbf{f}_i^{grav,t} \approx \sum_{p=1}^{n_{ep}} N_i(\boldsymbol{\xi}_p^t) \mathbf{f}_p^{grav} \tag{A.8}$$

      v. Compute internal force

$$\mathbf{f}_i^{int,t} = \sum_{p=1}^{n_{ep}} \Omega_p \boldsymbol{\sigma}_p^t \nabla N_i(\boldsymbol{\xi}_p^t) \tag{A.9}$$

      vi. Compute nodal force

$$\mathbf{f}_i^t = \mathbf{f}_i^{trac,t} + \mathbf{f}_i^{grav,t} - \mathbf{f}_i^{int,t} \tag{A.10}$$

(b) Solving equation 3.16

$$\mathbf{a}_i^t = \mathbf{f}_i^t / m_i^t \qquad \text{(A.11)}$$

(c) Mapping from nodes to material points

i. Update material point velocities

$$\mathbf{v}_p^{t+\Delta t} = \mathbf{v}_p^t + \sum_{i=1}^{n_{en}} \Delta t N_i(\boldsymbol{\xi}_p^t) \mathbf{a}_i^t \qquad \text{(A.12)}$$

ii. Update nodal velocities

$$\mathbf{v}_i^{t+\Delta t} = m_i^{t,-1} \sum_{p=1}^{n_{ep}} m_p N_i(\boldsymbol{\xi}_p^t) \mathbf{v}_p^{t+\Delta t} \qquad \text{(A.13)}$$

iii. Update nodal incremental displacements

$$\Delta \mathbf{u}_i^{t+\Delta t} = \Delta t \mathbf{v}_i^{t+\Delta t} \qquad \text{(A.14)}$$

iv. Update new position of material points

$$\mathbf{x}_p^{t+\Delta t} = \mathbf{x}_p^t + \sum_{i=1}^{n_{en}} N_i(\boldsymbol{\xi}_p^t) \Delta \mathbf{u}_i^{t+\Delta t} \qquad \text{(A.15)}$$

v. Update strain increment $\varepsilon_p^{t+\Delta t}$ and stresses $\boldsymbol{\sigma}_p^{t+\Delta t}$ of material points

$$\Delta \boldsymbol{\varepsilon}_p^{t+\Delta t} = \mathbf{B}(\boldsymbol{\xi}_p^t) \Delta \mathbf{u}_e^{t+\Delta t} \qquad \text{(A.16)}$$

$$\boldsymbol{\sigma}_p^t \xrightarrow[\text{constitutive relation}]{\Delta \boldsymbol{\varepsilon}_p^{t+\Delta t}} \boldsymbol{\sigma}_p^{t+\Delta t} \qquad \text{(A.17)}$$

vi. Update volumes associated with material points

$$\Omega_p^{t+\Delta t} = (1 + \Delta \varepsilon_{vol,p}^{t+\Delta t}) \Omega_p^t \qquad \text{(A.18)}$$

in which $\Delta \varepsilon_{vol,p}^{t+\Delta t}$ is the volumetric strain increment: $\Delta \varepsilon_{vol} = \Delta \varepsilon_{11} + \Delta \varepsilon_{22} + \Delta \varepsilon_{33}$

3. Convective phase

Reset the computational mesh or redefine the new one to the next time step. In the end of this step, the new number of material points per each finite element is determined and the new local position of each material point inside the element is obtained.

B

Solution procedure for a single time step of two-phase dynamic MPM

1. Initialization phase

   Knowing the local position $\boldsymbol{\xi}_p$, the global position $\mathbf{x}_p$ and the volume Ω_p associated with material point p are calculated in a similarly way as Equation A.1 and Equation A.2 of one-phase formulation. Noted that, the volume Ω_p is the total volume which contains both water and solid phase volume.

   The following masses are determined and assigned to the material point as

   $$m_{s,p} = \Omega_p \rho_{s,p}, \ \ m_{w,p} = \Omega_p \rho_{w,p} \ \text{and} \ m_p = \Omega_p \rho_{sat,p} \tag{B.1}$$

   The corresponding gravity forces associated with above masses are calculated as

   $$\mathbf{f}_{s,p}^{grav} = m_{s,p}\,\mathbf{g}, \ \ \mathbf{f}_{w,p}^{grav} = m_{w,p}\,\mathbf{g} \ \text{and} \ \mathbf{f}_p^{grav} = m_p\,\mathbf{g} \tag{B.2}$$

2. Lagrangian phase, solution phase for a time step t to $t + \Delta t$

   (a) Mapping from material points to nodes

       i. Compute nodal mass

   $$m_{w,i}^t \approx \sum_{p=1}^{n_{ep}} m_{w,p} N_i(\boldsymbol{\xi}_p^t) \tag{B.3}$$

   $$\bar{m}_{w,i}^t \approx \sum_{p=1}^{n_{ep}} n_p^t m_{w,p} N_i(\boldsymbol{\xi}_p^t) \tag{B.4}$$

   $$m_{s,i}^t \approx \sum_{p=1}^{n_{ep}} (1 - n_p^t) m_{s,p} N_i(\boldsymbol{\xi}_p^t) \tag{B.5}$$

ii. Compute nodal momentum

$$m_{s,i}^t \mathbf{v_s}^t \approx \sum_{p=1}^{n_{ep}} (1-n_p^t) m_{s,p} N_i(\boldsymbol{\xi}_p^t) \mathbf{v_s}_p^t \qquad \text{(B.6)}$$

$$m_{w,i}^t \mathbf{v_w}^t \approx \sum_{p=1}^{n_{ep}} n_p^t m_{w,p} N_i(\boldsymbol{\xi}_p^t) \mathbf{v_w}_p^t \qquad \text{(B.7)}$$

iii. Compute traction force

$$\mathbf{f}_i^{trac,t} = \sum_{p=1}^{n_{ebp}} N_i(\boldsymbol{\xi}_p^t) \tilde{\mathbf{f}}_p^{trac}(\boldsymbol{\xi}_p^t) \qquad \text{(B.8)}$$

$$\mathbf{f}_{w,i}^{trac,t} = \sum_{p=1}^{n_{ebp}} N_i(\boldsymbol{\xi}_p^t) \tilde{\mathbf{f}}_{w,p}^{trac}(\boldsymbol{\xi}_p^t) \qquad \text{(B.9)}$$

iv. Compute gravity force

$$\mathbf{f}_i^{grav,t} \approx \sum_{p=1}^{n_{ep}} N_i(\boldsymbol{\xi}_p^t) \mathbf{f}_p^{grav} \qquad \text{(B.10)}$$

$$\mathbf{f}_{w,i}^{grav,t} \approx \sum_{p=1}^{n_{ep}} N_i(\boldsymbol{\xi}_p^t) \mathbf{f}_{w,p}^{grav} \qquad \text{(B.11)}$$

v. Compute internal force

$$\mathbf{f}_i^{int,t} = \sum_{p=1}^{n_{ep}} \Omega_p \boldsymbol{\sigma}_p^t \nabla N_i(\boldsymbol{\xi}_p^t) \qquad \text{(B.12)}$$

$$\mathbf{f}_{w,i}^{int,t} = \sum_{p=1}^{n_{ep}} \Omega_p \delta p_p^t \nabla N_i(\boldsymbol{\xi}_p^t) \qquad \text{(B.13)}$$

where $\boldsymbol{\delta} = \begin{bmatrix} 1 & 1 & 1 & 0 & 0 & 0 \end{bmatrix}^T$

vi. Compute drag force

$$\mathbf{f}_{w,i}^{drag,t} = \mathbf{Q}^t(\mathbf{v_w}^t - \mathbf{v_s}^t) \qquad \text{(B.14)}$$

(b) Solving momentum Equation 3.41 and 3.42

$$\mathbf{a}_{w,i}^t = [\mathbf{f}_{w,i}^{trac,t} + \mathbf{f}_{w,i}^{grav,t} - \mathbf{f}_{w,i}^{int,t} - \mathbf{f}_{w,i}^{drag,t}]/m_{w,i}^t \qquad \text{(B.15)}$$

$$\mathbf{a}_{s,i}^t = [\mathbf{f}_i^{trac,t} + \mathbf{f}_i^{grav,t} - \mathbf{f}_i^{int,t} - \bar{m}_{w,i}^t \mathbf{a}_{w,i}^t]/m_{s,i}^t \qquad \text{(B.16)}$$

(c) Mapping from nodes to material points

i. Update material point velocities

$$\mathbf{v_s}_p^{t+\Delta t} = \mathbf{v_s}_p^t + \sum_{i=1}^{n_{en}} \Delta t N_i(\boldsymbol{\xi}_p^t)\mathbf{a}_{s,i}^t \tag{B.17}$$

$$\mathbf{v_w}_p^{t+\Delta t} = \mathbf{v_w}_p^t + \sum_{i=1}^{n_{en}} \Delta t N_i(\boldsymbol{\xi}_p^t)\mathbf{a}_{w,i}^t \tag{B.18}$$

ii. Update nodal velocities

$$\mathbf{v_s}_i^{t+\Delta t} = m_{s,i}^{t,-1} \sum_{p=1}^{n_{ep}} (1-n_p^t)m_{s,p}N_i(\boldsymbol{\xi}_p^t)\mathbf{v_s}_p^{t+\Delta t} \tag{B.19}$$

$$\mathbf{v_w}_i^{t+\Delta t} = \bar{m}_{w,i}^{t,-1} \sum_{p=1}^{n_{ep}} n_p^t m_{w,p}N_i(\boldsymbol{\xi}_p^t)\mathbf{v_w}_p^{t+\Delta t} \tag{B.20}$$

iii. Update nodal incremental displacements of the solid phase

$$\Delta\mathbf{u}_i^{t+\Delta t} = \Delta t \mathbf{v_s}_i^{t+\Delta t} \tag{B.21}$$

iv. Update new position of material points using the displacement of solid phase

$$\mathbf{x}_p^{t+\Delta t} = \mathbf{x}_p^t + \sum_{i=1}^{n_{en}} N_i(\boldsymbol{\xi}_p^t)\Delta\mathbf{u}_i^{t+\Delta t} \tag{B.22}$$

v. Update strain increment $\varepsilon_p^{t+\Delta t}$ and effective stresses $\boldsymbol{\sigma'}_p^{t+\Delta t}$ of material points

$$\Delta\varepsilon_p^{t+\Delta t} = \mathbf{B}(\boldsymbol{\xi}_p^t)\Delta\mathbf{u}_e^{t+\Delta t} \tag{B.23}$$

$$\boldsymbol{\sigma'}_p^t \xrightarrow[\text{constitutive relation}]{\Delta\varepsilon_p^{t+\Delta t}} \boldsymbol{\sigma'}_p^{t+\Delta t} \tag{B.24}$$

vi. update water pressure of particle p

$$p_p^{t+\Delta t} \approx p_p^t + \Delta t \frac{K_{w,p}}{n_p^t}\boldsymbol{\delta}^T[(1-n_p^t)\mathbf{B}(\boldsymbol{\xi}_p^t)\mathbf{v_s}_e^{t+\Delta t} + n_p^t\mathbf{B}(\boldsymbol{\xi}_p^t)\mathbf{v_w}_e^{t+\Delta t}] \tag{B.25}$$

vii. Calculate total stress at each particle

$$\boldsymbol{\sigma}_p^{t+\Delta t} = \boldsymbol{\sigma'}_p^{t+\Delta t} + p_p^{t+\Delta t} \tag{B.26}$$

viii. Update volumes associated with material points

$$\Omega_p^{t+\Delta t} = (1 + \Delta\varepsilon_{vol,p}^{t+\Delta t})\Omega_p^t \tag{B.27}$$

3. Reset the computational mesh or redefine the new one to the next time step. The book-keeping is updated using the new positions of material points

C

Baskarp sand and its hypoplastic parameters

[1] performed experiments on Baskarp sand to determine its hypoplastic material properties which are summarised in Table C.1

Table C.1: Hypoplastic parameters for for Baskarp sand ([1]

Parameter	ϕ_c	h_s	n	e_{d0}	e_{c0}	e_{i0}	α	β
Baskarp sand	31°	4000 MPa	0.42	0.548	0.929	1.08	0.12	0.96

C.1. Oedometer tests

Figure C.1 shows the oedometric response of different specimens with an initial void ratio varying between 0.657 (dense) and 0.823 (loose). In addition, simulated response from the element test is presented as well. First the oed simulations were done using h_s of 4GPa (Figure C.1a). At low axial pressures (<200 kPa) the numerical results match well the experimental results for both specimens. However, under high axial pressure (>200 kPa), the matching between experimental and numerical result is obtained only in dense and medium dense specimens. For loose specimens, numerical results give significantly stiffer response as compared to the experimental result. In the hypoplastic model, the parameter h_s denotes the granulate hardness. This parameter is determined and valid for certain pressure range. Occurrence of e.g. grain crushing at higher pressures changes the granular properties, thus the value of h_s, an attempt to get a better fit for the loose sand, h_s value of 2 GPa is used instead of 4 GPa (Figure C.1b).
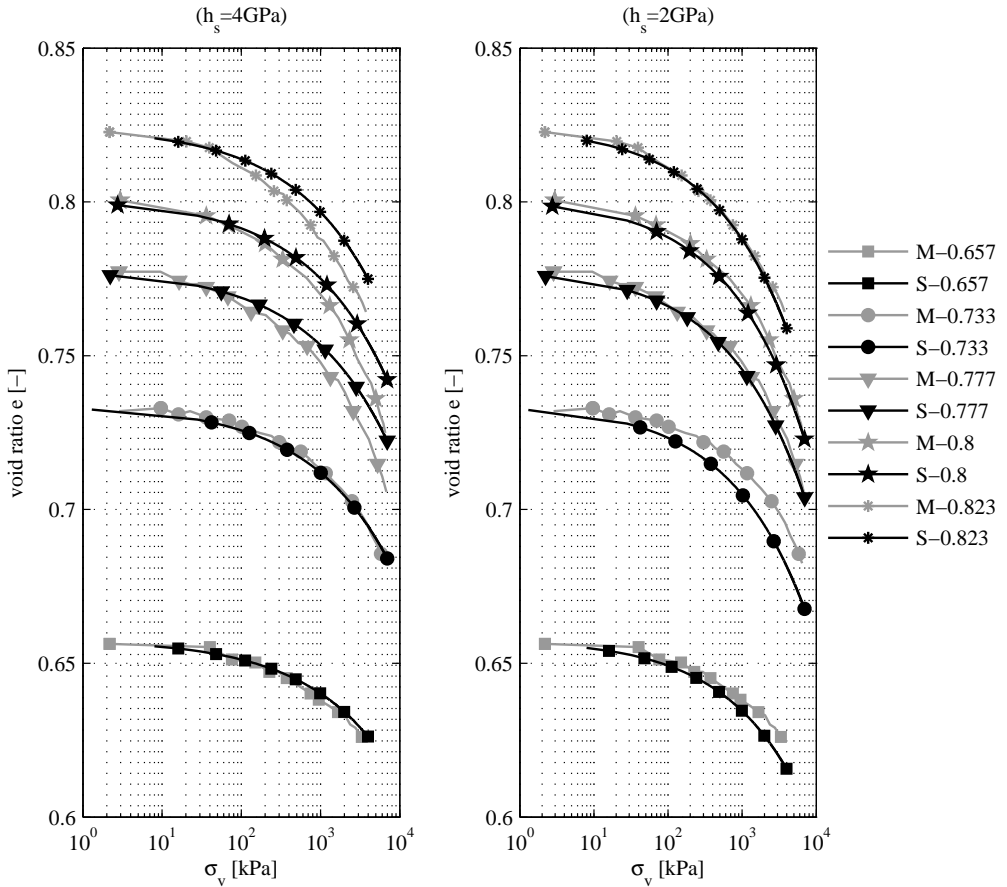
Figure C.1: Oedometric test on Baskarp sand, comparison between measurement and simulation.

C.2. Triaxial test

C.2.1. Dense sand

Tests on dense Baskarp samples were performed with three confining pressures:

- $\sigma = 50$ kPa, e = 0.59

- $\sigma = 100$ kPa, e = 0.6

- $\sigma = 200$ kPa, e = 0.6

The obtained experimental results and the numerical simulation of the drained triaxial compression tests performed on dense samples of Baskarp sand are shown in Figure C.2. The simulated peak shear strength and the residual shear strength are in accordance with laboratory experiments. The volumetric behaviour as simulated is qualitatively (shape) in accordance with the experimentally obtained results, however, simulated dilatancy angle is smaller as compared with the experimental
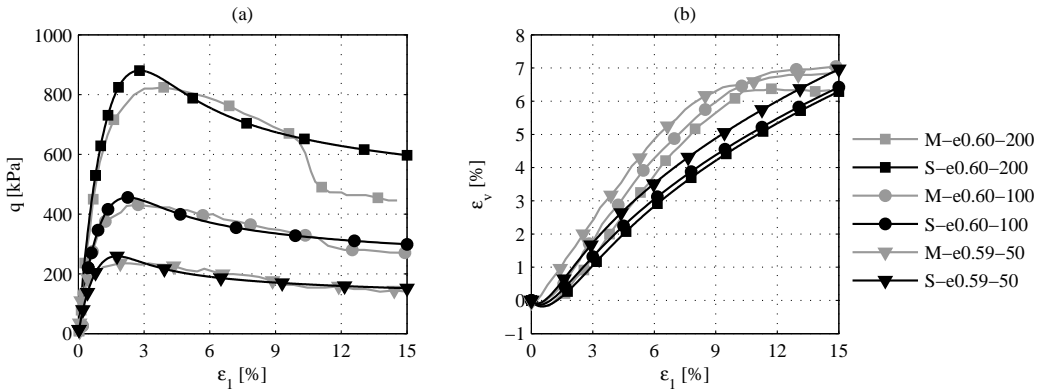
Figure C.2: Numerical simulation of triaxial compression test on dense sand specimens. (a) Deviatoric stress vs. axial strain and (b) Volumetric strain vs. axial strain. M-e0.60-200 means mesurement data for specimen with void ratio of 0.6 at confining pressure of 200 kPa; S-e0.60-200 means simulation data for specimen with void ratio of 0.6 at confining pressure of 200 kPa

results. According to [1], in the test with the initial effective confining pressure of 50 kPa, the initial stiffness behaviour as observed in the measurements is not representative and is merely due to logging error by the program. This logging error has also its effect on the simulated volumetric response. According to [1], the lower dilatancy angle in the element tests are probably linked to effects of lubricated ends and slenderness ratio. Conventional test conditions, i.e. slenderness ratio of 2 and no application of lubricated ends, lead to a pronounced stress peak. Shear banding occurs and simultaneously, the increase of the volumetric strain is abruptly stopped.

C.2.2. Loose sand
Tests on loose Baskarp samples were performed with three confining pressures:

- $\sigma = 50$ kPa, e = 0.70

- $\sigma = 100$ kPa, e = 0.84

- $\sigma = 200$ kPa, e = 0.81

The results of the triaxial tests on loose sand are plotted in Figure C.3. For loose sand, the initial stiffness response, peak shear strength and the residual shear strength of numerical simulations are quantitatively in accordance with the experimental data. However, in the experimental data, mobilisation of the peak shear strength, especially for high confining pressure, is more gradual compared to the numerical simulation. The volumetric behaviour as simulated is qualitatively (shape) in accordance with the experimentally obtained results. There is agreement in dilatancy angle between the simulation and the experiments, which is different from the case of the dense sand. This could be linked to the less pronounced peak in loose samples with a more ductile behaviour.
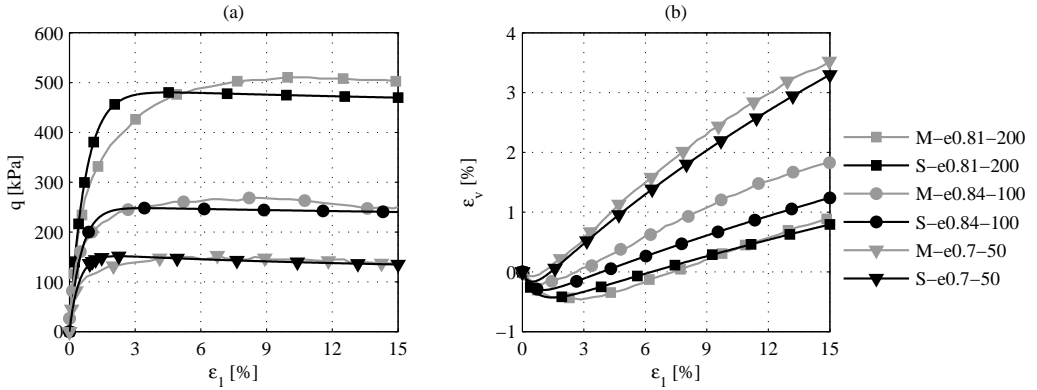
Figure C.3: Numerical simulation of triaxial compression test on loose sand specimens. (a) Deviatoric stress vs. axial strain and (b) Volumetric strain vs. axial strain. M-e0.81-200 means mesurement data for specimen with void ratio of 0.81 at confining pressure of 200 kPa; S-e0.81-200 means simulation data for specimen with void ratio of 0.81 at confining pressure of 200 kPa

C.3. Choosing small strain stiffness parameters

For jacking pile simulated in dymamic MPM, although no cyclic loading happened, ratcheting still has significant influences on the simulation results. It especially occurs in dynamic numerical models, as the wave propagation through the soil will be reflected at each material point. It means that the process of loading and unloading cycles always happens at material point level during simulation. Therefore, the use of hypoplastic model with IGS is neccessary for all MPM simulations in this thesis.

The intergranular strain model includes 5 parameters: m_R, m_T, R_{max}, β_R, χ([2]). However, the stiffness multipliers for shift in strain direction by 180 (m_R) and 90 (m_T) are usually taken 5 and 2 respectively and R_{max} is usually taken 0.0001. Therefore, this part only considers the influence of β_R and χ.

Proposed small strain stiffness parameters are given in Table C.2, in which IGS1, IGS2 are based on literature. Since there is no experimental data available on cyclic oedometer test, it is suggested for choosing suitable IGS parameters so that the initial stiffness of the oedometer response with IGS parameters should be nearly similar as the one without IGS. Figure C.4 gives results of cyclic oedometer element tests with and without IGS. Clearly, using IGS helps to reduce the effect of ratcheting for the modelling of small loading cycle in which elastic deformations occur. However the initial stiffness of the oedometric response in simulations with IGS1 and IGS2 is significantly stiffer than the one without IGS. Therefore, IGS3 is chosen to model the jacking pile problem in Chapter 5

Table C.2: Proposed parameter sets for small strain stiffness

Parameter	m_R	m_T	R_{max}	β_R	χ
IGS 1 [1]	5	2	$1e-4$	0.5	6
IGS 2 [2]	5	2	$1e-4$	1	2
IGS 3	5	2	$1e-4$	1	1
no IGS	0	0	0	0	0

[1] [2]
[2] [3]

C
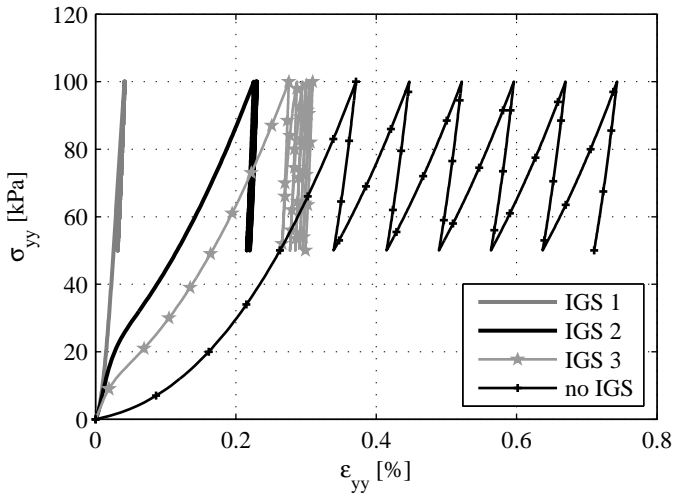
Figure C.4: Cyclic Odometric simulation on Baskarp sand with difference sets of small strain stiffness

References

[1] K. E. Anaraki, *Hypoplasticity investigated: parameter determination and numerical simulation*, Master's thesis, Delft University of Technology (2008).

[2] A. Niemunis and I. Herle, *Hypoplastic model for cohesionless soils with elastic strain range,* Mechanics of Cohesive-frictional Materials 2, 279 (1997).

[3] P. H. Dung, *Modelling of Installation Effect of Driven Piles by Hypoplasticity*, Master's thesis, TU Delft, Delft University of Technology (2010).

D

Parametric study

Several simulations have been performed to study the influence of prescribed velocity, contact algorithm and soil model parameters on the evolution of the load-displacement curve during penetration.

D.1. Inluence of precribed velocity

The penetration was performed with three different velocities of 0.02, 0.1, and 0.2 m/s to investigate the influence of penetration speed. Results are plotted in Figure D.1. As seen, the general behavior is of resemblance but when zooming in, local oscillations increase considerably with increasing velocity. In order to consider both the computational time as well as the oscillations of the results, the velocity of 0.02 m/s is chosen for all simulations of penetration into dry sand.
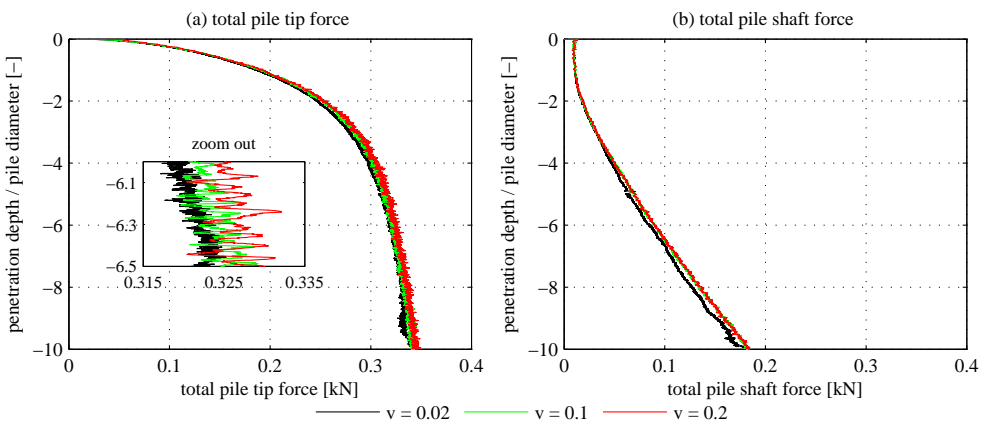
Figure D.1: Influence of installation velocity on analysis results. Simulations with Mohr-Coulomb model, E = 20 MPa, $\varphi = 30\circ$ and $\psi = 0\circ$.

D.2. Inluence of coefficient of friction of contact

Figure D.2 shows the influence of the coefficient of friction of contact μ on the load displacement curve during installation. Clearly, the value of μ plays an important role on the evolution of total pile shaft force, F_s rather than the evolution of total pile tip force, F_t. F_s increases significantly with the increase of μ. With smooth contact, $\mu = 0.0$, F_s is zero, whereas with fully rough contact, $\mu = 1$, the value of F_s is 1.5 times greater than F_t. The contact angle between polish steel and sand is about $10°$, therefore a coefficient of friction $\mu = \tan 10° = 0.176$ is used.
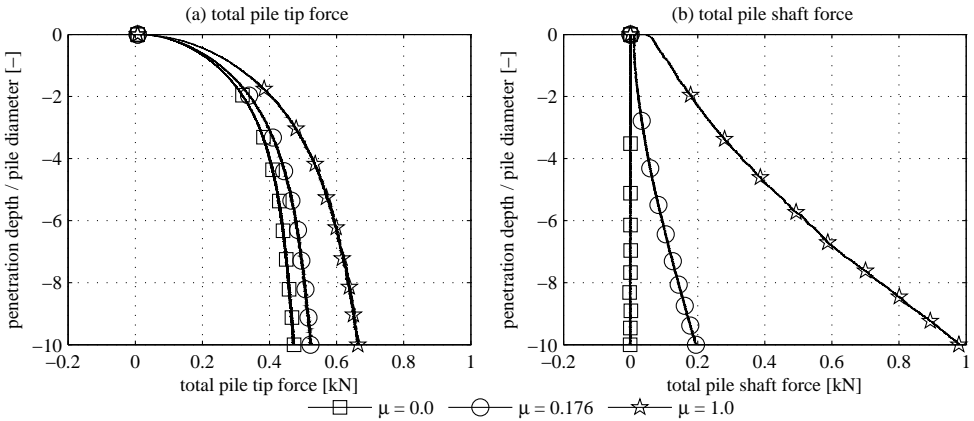
Figure D.2: Influence of coefficient of friction of contact μ on analysis results. Simulations with Mohr-Coulomb model, E = 22 MPa, $\varphi = 30°$ and $\psi = 0°$.

D.3. Influence of Mohr-Coulomb parameters on the load-displacement curve during penetration

D.3.1. Influence of stiffness value

Three different values of Young modulus of soil E = 30, 40 and 50 MPa are used to examine the influence of soil stiffness on the analysis results. Results are shown in Figure D.3. Higher value of Young modulus of the soil results in stiffer total pile tip force-displacement curve. The curve using low Young modulus value is fully mobilised at earlier depth than the others.
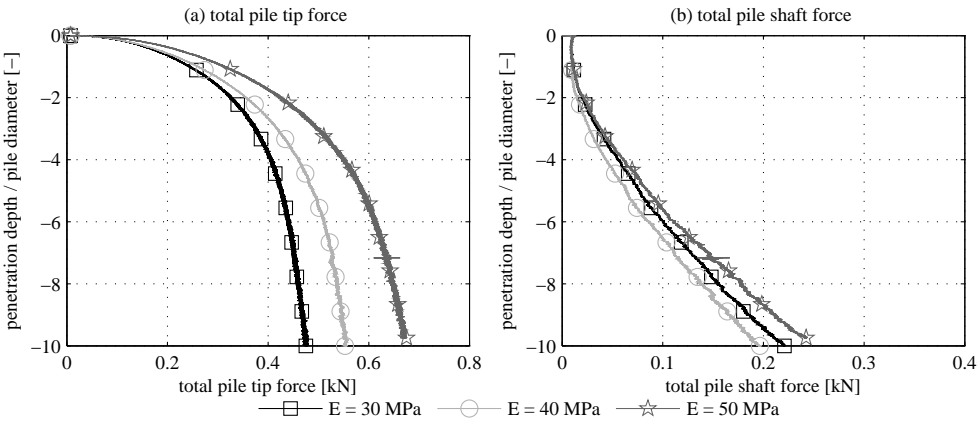
Figure D.3: Influence of soil stiffness on analysis results. Simulations with Mohr-Coulomb model, $\varphi = 30°$ and $\psi = 0°$.

D.3.2. Influence of strength parameter

In this section the influence of friction angle φ and dilation angle ψ is investigated. In Figure D.4 the friction angle is varied from $30°$ to $37°$ while soil stiffness and dilation angle are remained the same. The initial stiffness of the load displacement curve for the pile tip is increasing with the increase of friction angle. The higher value of friction angle, the higher capacity of the pile is get.
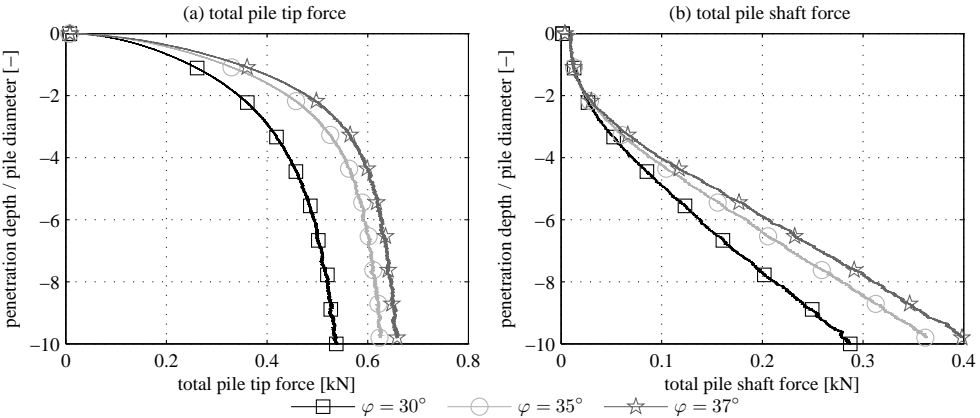
Figure D.4: Influence of friction angle on analysis results. Simulations with Mohr-Coulomb model, E = 30MPa and $\psi = 0\circ$.

Figure D.5 plot the load-displacement curve during penetration when using different value of dilation angle ψ from 0 to $10°$. As seen, the dilation angle has significant influence on the stiffness as well as mobilised depth of the load-displacement curve of the pile tip. The curve is much stiffer and fully mobilised at earlier depth when using higher value of dilation angle. The influence of dilation angle on shaft friction is not clear observed in this figure.
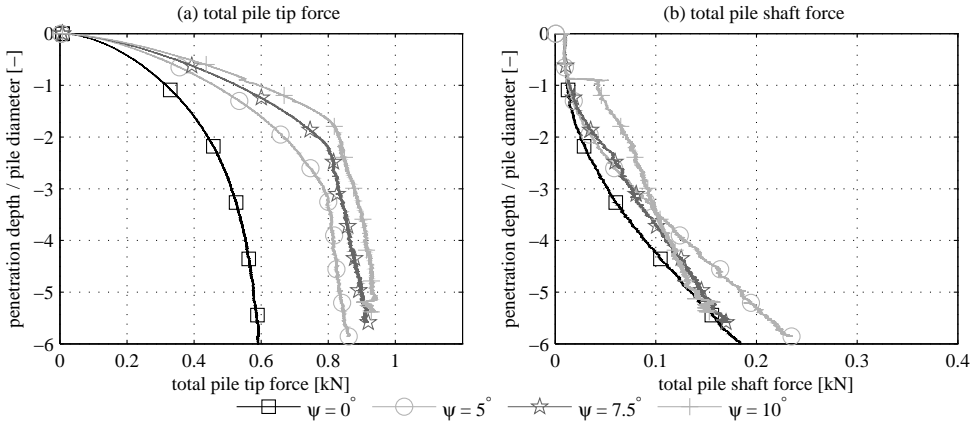
Figure D.5: Influence of dilation angle on analysis results. Simulations with Mohr-Coulomb model, E = 30 MPa and $\phi = 35°$.

D.4. Influence of hypoplastic parameters on the load-displacement curve during penetration

D.4.1. Influence of h_s and n

h_s and n are two parameters presenting the stiffness of soil in the hypoplastic model. The influences of these two parameters h_s and n are illustrated in Figure D.6 and D.7 respectively. As seen, the total pile tip force and total pile shaft force are both reduced with the reduction of h_s or n.
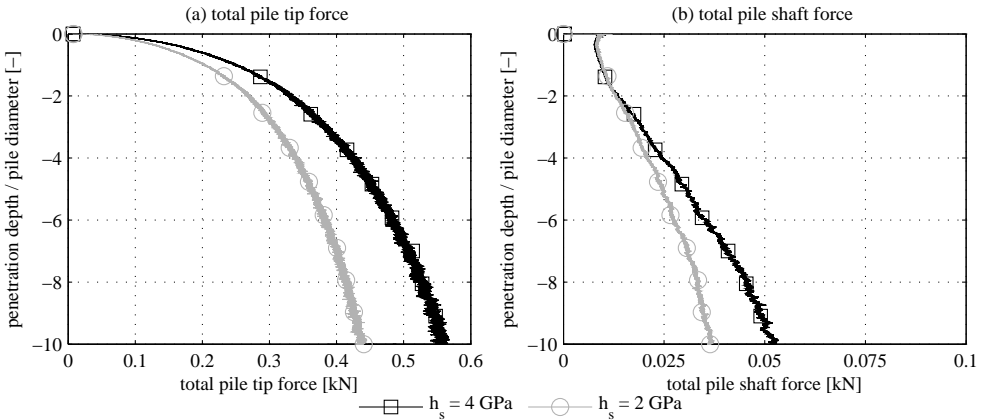
Figure D.6: Influence of h_s on analysis results.
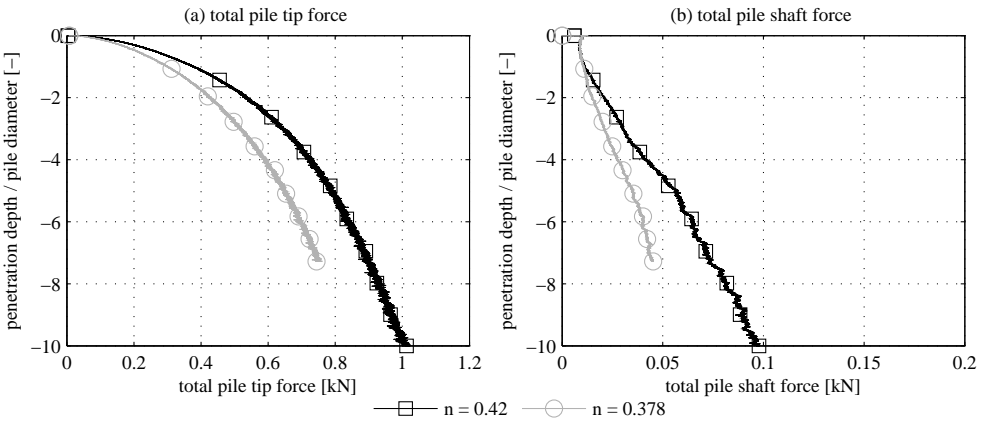
Figure D.7: Influence of n on analysis results.

D.4.2. Influence of α

As stated in previous chapter that the strength and dilatancy of soil in hypoplastic model can reduce by the decrease of parameter α. Therefore, the use of lower α reduces the total pile tip force, F_t significantly as shown in Figure D.8. However, it has almost no influence on the total pile shaft force.
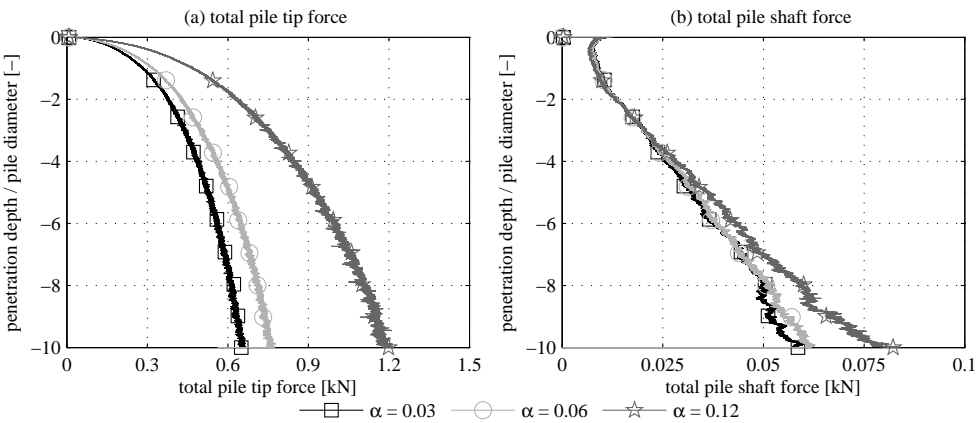
Figure D.8: Influence of α on analysis results.

D.4.3. Influence of initial void ratio

Figure D.9 plots the load-displacement curves during penetration process for simulations using hypoplastic model with three different initial void ratios. Clearly, the denser the soil, the more pile capacity is obtained.

D

D
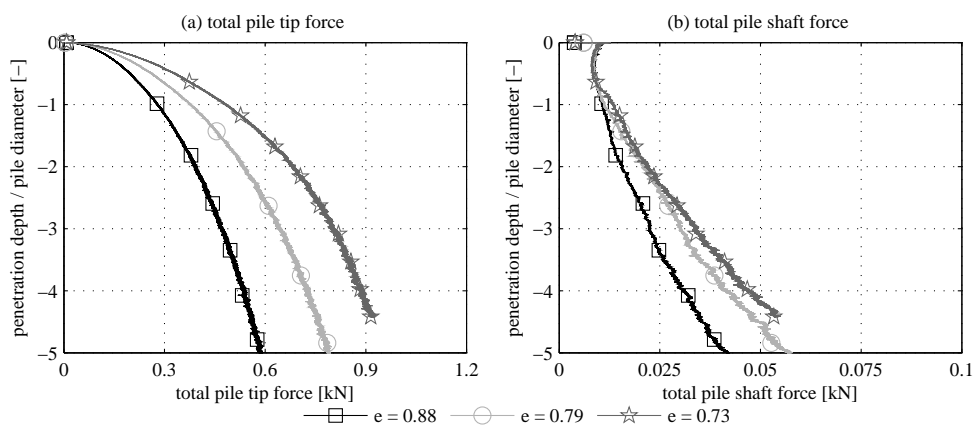
Figure D.9: Influence of initial void ratio on analysis results.

E

Parametric study for pile hammering

This work has been performed in collaboration with Jassim [1]. A pile driving problem for deep penetration is analysed in this section.

The pile with a diameter of $0.3m$ was initially embedded in the soil to a height of 0.4 m from its tip point. It was assumed to behave according to the linear elastic relation.

Detail of geometry and boundary condition, problem description, finite element mesh and constitutive model are refereed to Jassim[1].

E.1. Varying pile damping

Computations are carried out with different values of the local damping factor α to study the effect of damping on the installation process of an elastic pile. The frequency dependent Rayleigh damping was adopted in the work of Mabsout and Tassoulas [2] with a damping ratio of $\zeta_d = 3\%$ estimated at the natural frequency of the pile. The local damping factor α is related to the damping ratio ζ_d as $\alpha = \pi\zeta_d$. Three value of $\alpha = 0\%, 6\%$ and 10% are selected. The coefficient of friction between the sand and the pile was fixed to $\mu = 0.5$, an initial relative density of $R_D = 30.4\%$ and the peak pressure at the pile head is $p_{max} = 2000[kN/m^2]$. Figure E.1 shows the number of blows versus penetration depth for the considered cases. The results confirm the importance of good estimation of the damping factor for predicting realistic installation process of a pile.
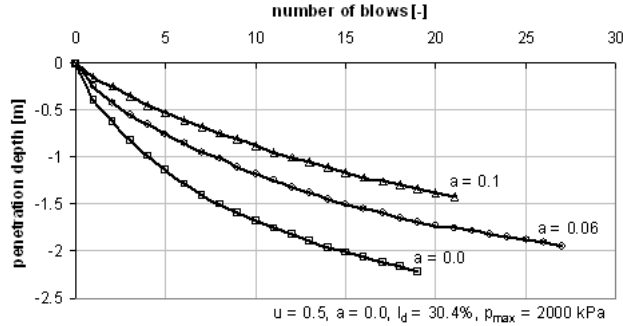
Figure E.1: Influences of damping on the load displacement curve.

E.2. Varying skin friction

The effect of skin friction μ which is the friction between the soil and the pile is studied. Two value of the friction coefficient $\mu = 0$ (fully smooth contact and $\mu = 0.5$ (which is realistic for concrete piles) are considered. All computations are carried out with a fixed damping factor of $\alpha = 0\%$ for pile and initial relative density of $R_D = 63.4\%$ for sand. Figure E.2 illustrate considerable differences in the result of pile penetration depth per blow.
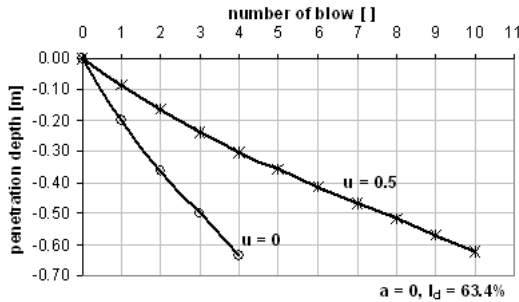
Figure E.2: Influences of skin friction on the load displacement curve.

E.3. Varying sand density

Simulations with different value of relative density $R_D = 30.4\%$ and 63.4% are carried out. The simulations are performed with $\mu = 0.5$ and $\alpha = 6\%$. Figure E.3 shows that for driving the pile to a penetration depth of 0.6 m in loose and dense sand, it requires 4 and 14 blows respectively, which indicates the need for heavier hammer for deeper penetration of dense sand.
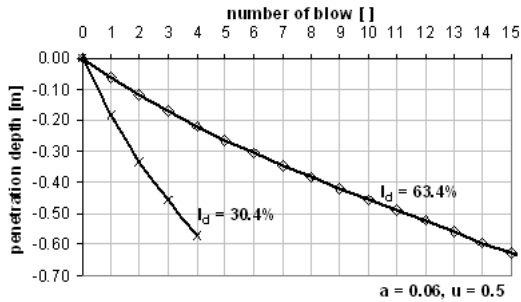
Figure E.3: Influences of sand density on the load displacement curve.

E.4. Varying driving pressure

Two different driving pressure $p_{max} = 1000$ and $2000[kN/m^2]$ are considered in this problem. Simulations are carried out with $\alpha = 0$, $\mu = 0.5$ and $R_D = 30.4\%$. The results of penetration depth per blow are shown in Figure E.4
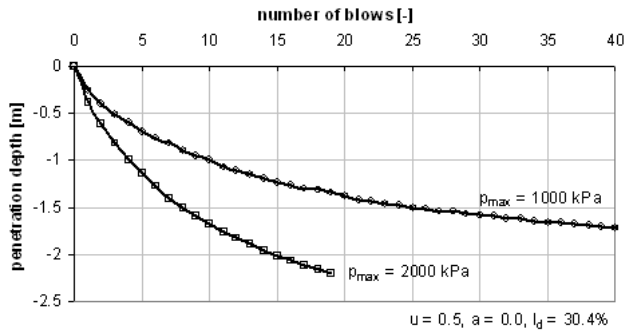
Figure E.4: Influences of driving pressure on the load displacement curve.

References

[1] I. K. Jassim, *Formulation of a Dynamic Material Point Method (MPM) for Geomechanical Problems*, Ph.D. thesis, University of Stuttgart (2013).

[2] M. E. Mabsout and J. L. Tassoulas, *A finite element model for the simulation of pile driving,* International Journal for numerical methods in Engineering 37, 257 (1994).

F

Influence of small strain parameters on the result of RLT

In this section, the influence of small strain parameters on the result of rapid load test (RLT) is examined. Prescribed velocity is applied on the pile head for all case studies. The value of prescribed velocity is approximated from the centrifuge test value and shown in Figure F.1.
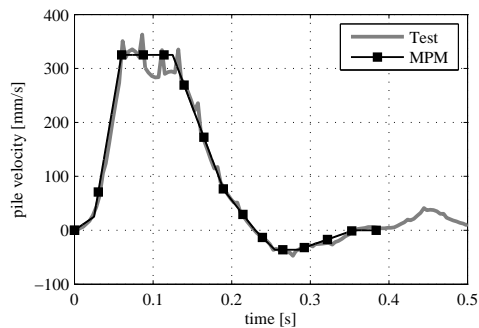
Figure F.1: Prescribed velocity applied on the pile head during rapid load test.

Figure F.2 → F.5 illustrate the influences of parameter χ, β_χ, m_R, m_T, respectively, on the results of load-displacement curve during the rapid load test.
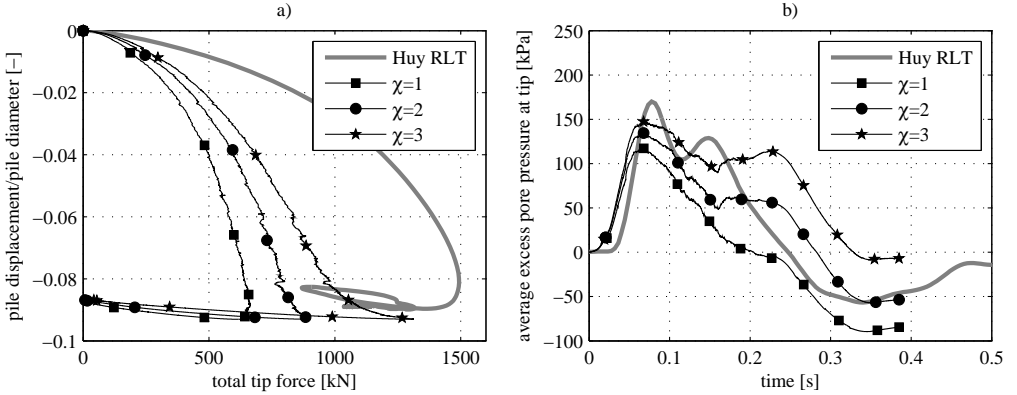
Figure F.2: Influence of different values of χ, $\chi = 1,\, 2\, and\, 3$ on the results of load-displacement curve during the rapid load test.
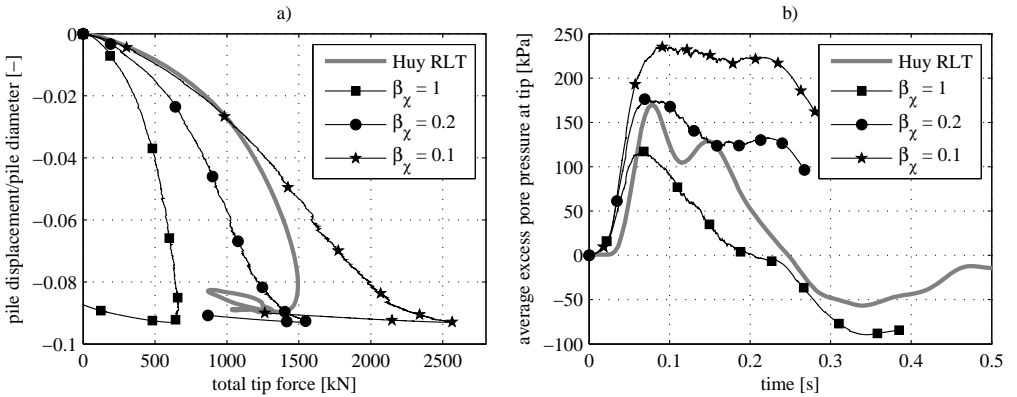
Figure F.3: Influence of different values of β_χ, $\beta_\chi = 1,\, 0.2\, and\, 0.1$ on the results of load-displacement curve during the rapid load test.
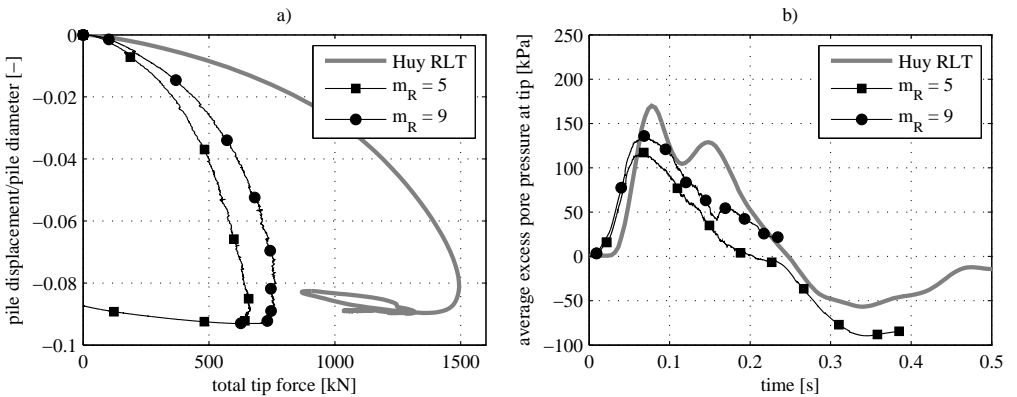
Figure F.4: Influence of different values of m_R, $m_R = 5,\, and\, 9$ on the results of load-displacement curve during the rapid load test.

F
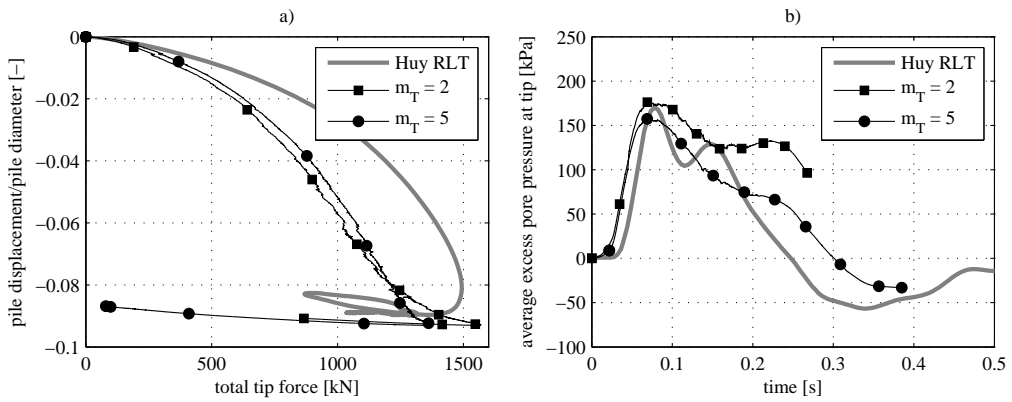
Figure F.5: Influence of different values of m_T, $m_T = 2$, and 5 on the results of load-displacement curve during the rapid load test.

Acknowledgements

Curriculum Vitæ

Phuong NGUYEN THI VIET

13-07-1984   Born in Hanoi, Vietnam.
Email   phuongnguyenviet137@gmail.com

Education

2002–2007   BSc in Hydraulic Engineering
Thuy Loi University, Viet Nam

2008–2010   MSc in Coastal Engineering
Unesco IHE - Institute for water education, Delft, The Netherlands

2011–2019   PhD in Geotechnical Engineering
Delft University of Technology, The Netherlands

List of publication

5. N. Phuong, A. F. van Tol, A. Elkadi and A. Rohe, *Modelling of pile installation using the material point method (MPM)*, In: Proc. 8th European Conference on Numerical Methods in Geotechnical Engineering (NUMGE 2014), Delft, The Netherlands, pp. 271-276 (2014).

4. N. Phuong, A. F. van Tol, A. Elkadi and A. Rohe, *Numerical investigation of pile installation effects in sand using material point method*, Computers and Geotechnics, Elsevier, 73, pp.58-71(2016).

3. F. S. Tehrani, N. Phuong, R. B. J. Brinkgreve and A. F. van Tol, *Comparison of press-replace method and material point method for analysis of jacked piles*, Computers and Geotechnics, Elsevier 78, pp. 38-53(2016).

2. N. Phuong, A. Rohe, R. B. J. Brinkgreve and A. F. van Tol, *Hypoplastic model for crushable sand*, Soils and Foundations, Elsevier 58(3), pp. 615-626 (2018).

1. A. Rohe and N. Phuong, *Jacked pile installation in sand*, The Material Point Method for Geotechnical Engineering: A Practical Guide, CRC Press, pp. 297-310 (2018).